Scattering Theory and Radiative Transfer in Spherically Symmetric Moving Atmospheres

A Thesis Submitted to

The Department of Physics

Pondicherry University, Puducherry - 605 014, India

For the Award of Degree of

Doctor of Philosophy

Submitted by

A. Megha

Thesis Supervisor

M. Sampoorna

Indian Institute of Astrophysics

Bengaluru - 560 034, India

May 2020

Title of the thesis	:	**Scattering Theory and Radiative Transfer in Spherically Symmetric Moving Atmospheres**
Name of the author	:	**A. Megha**
Address	:	Indian Institute of Astrophysics II Block, Koramangala Bengaluru - 560 034, India
Email	:	megha@iiap.res.in
Name of the supervisor	:	**Prof. M. Sampoorna**
Address	:	Indian Institute of Astrophysics II Block, Koramangala Bengaluru - 560 034, India
Email	:	sampoorna@iiap.res.in

Declaration

I hereby declare that the material presented in this thesis, submitted to the Department of Physics, Pondicherry University, for the award of a Ph.D. degree, is a result of the investigations carried out by me at Indian Institute of Astrophysics, Bengaluru, under the joint supervision of Prof. M. Sampoorna, late Prof. K. N. Nagendra and Dr. K. Sankarasubramanian. The results presented herein have not been subject to scrutiny for the award of a degree, diploma, associateship or fellowship whatsoever, by any university or institute. Whenever the work described is based on the findings of other investigators, due acknowledgment has been made. Any unintentional omission is sincerely regretted.

A. Megha
(Ph.D. Candidate)
Indian Institute of Astrophysics
2nd Block, Koramangala
Bengaluru 560 034
India
May 2020

Certificate

This is to certify that the thesis entitled **'Scattering Theory and Radiative Transfer in Spherically Symmetric Moving Atmospheres'** submitted to the Pondicherry University by Ms. A. Megha for the award of the degree of Doctor of Philosophy, is based on the results of the investigations carried out by her under my supervision and guidance, at the Indian Institute of Astrophysics. This thesis has not been submitted in whole or part for the award of any other degree, diploma, associateship, fellowship, etc. of any other university or institute.

Prof. M. Sampoorna
Thesis Supervisor
Indian Institute of Astrophysics
2nd Block, Koramangala
Bengaluru 560 034
India
May 2020

Dedicated to late Prof. K. N. Nagendra,

without whom this journey would not have been possible

Acknowledgements

I wish to express my deepest gratitude to my supervisor, Prof. M. Sampoorna, who guided and encouraged me to do my best in this journey. She was immensely patient with me during my learning phase and taught me basics of the subject and coding. Her valuable inputs for writing the scientific papers were of great help and made me confident about the same. She is always an inspiration to me to work hard and solve the tough problems with persistence. She always welcomed me to ask any type of questions and guided me thoroughly in every step. I am indebted to her for her support in shaping me as a researcher. I am extremely grateful to my co-guide late Prof. K. N. Nagendra, without whose encouragement I would not have chosen to work on this beautiful subject of spectropolarimetry. He was a fatherly figure to me who constantly supported me to have a work-life balance. He made me learn that science can only be enjoyed when it is shared. He always encouraged me to motivate and help other budding young students and researchers. He encouraged me to pursue my other interests (such as learning music and reading books). He was a perfect model for me to follow in the field of research. He and Prof. Sampoorna have together put a lot of effort and time in shaping me in various aspects. They both have introduced me to the eminent researchers like Prof. Jan Olof Stenflo, Prof. Hélène Frisch, and Prof. Véronique Bommier who are always my greatest inspirations in the field of research. I am extremely thankful to my co-guide Prof. K. Sankarasubramanian for his continuous encouragement and inspiration. A heartfelt thanks to him for forgoing his sleep during my three months course work project period and for his efforts in teaching me the observational aspects related to solar magnetic fields. His ability to do extensive hard work and dedication to science have been a source of inspiration to me. I have benefited through meetings related to Aditya-L1 conducted by him at U. R. Rao Satellite center and also through late night student discussions at

Indian Institute of Astrophysics (IIA). Our discussions regarding how we can take science to the public platforms and inspire young students, have helped me to boost my ideas on outreach activities.

I am grateful to the Director, IIA, Prof. Annapurni Subramaniam, the Dean, IIA, Prof. G. C. Anupama, the Chairperson, Board of Graduate Studies (BGS), Prof U. S. Kamath, and members of BGS, for providing me with exquisite research facilities and immense support during my stay. I thank the former Directors of IIA, Prof. Sreekumar and Prof. Jayant Murthy, former Chairpersons of BGS, Prof. Aruna Goswamy, Prof. R. T. Gangadhara and Prof. Annapurni Subramaniam for their support in various academic matters.

I sincerely thank my doctoral committee members Prof. Dipankar Banerjee and Prof. K. Sivakumar for their valuable suggestions and for evaluating the progress of my research work. I thank the Dean, School of Physical, Chemical & Applied Sciences, Pondicherry University (PU), Head of the Department of Physics, PU, and also staff members of PU for their help and cooperation during various occasions.

I am specially grateful to Prof. Jan Olof Stenflo, for checking the initial draft on 'Hanle-Zeeman scattering matrix for magnetic dipole transitions', and for his valuable inputs that helped to improve the presentation. My sincere thanks to Prof. Véronique Bommier for the fruitful discussions on the scattering polarization in the presence of dipolar field. Her insights on the subject helped me in understanding some difficult concepts. My special thanks to Prof. Oskar Steiner and Dr. Michele Bianda for organizing a fruitful SOLARNET school on spectropolarimetry and taking us for an inspiring visit to IRSOL at Locarno, Switzerland. I am grateful to Prof. Dipankar Banerjee for organizing many solar physics conferences and workshops in India. I thank him for providing me an opportunity to attend IAU symposium-340 and Solar Physics school. He has always encouraged me to attend his group meetings for sharing and discussing new science amongst his PhD students.

I thank foreign travel committee of IIA for providing sufficient financial support for attending conferences and schools. I also thank CSIR for their travel grant TG/10856/19-HRD and organizers of Solar Polarization Workshop-9 (SPW9) for their partial financial support to take part in SPW9.

I greatly appreciate the computing facility provided by IIA, namely, the NOVA and HYDRA clusters, FORNAX and KASPAR servers, that helped in performing several computations presented in this thesis. I thank the computer center staff at IIA, specially Mr. Anish, Mr. Fayaz and Mr. Ashok for their timely help during several occasions. My special thanks to the Library staff, IIA, for their swift response in providing me all the references requested, specially Mr. Mohan and Mr. Prabhakar. I thank Mr. Arumugam Pichai (Librarian) and Mrs. Sandra Rajeev (past Librarian) for providing the fine library facility. I thank all the outreach committee members, specially Dr. Kathiravan, Prasanna Deshmukh, Ramya, Nirmal, Sandeep, Anirban and Phanindra for involving me in many activities, in particular teaching basic physics and astronomy to the high school students that greatly cheered me. I thank all the staff members of Vainu Bappu Observatory, Kodaikanal Observatory, and Gauribidanur Observatory for hosting me during various occasions. I sincerely thank Mr. K. Sankaranarayanan, Section officer, BGS, for his help in various official matters. I thank Mr. K. Sripathi, Administrative officer, IIA, and Mr. S. B. Ramesh, Principal Staff officer, IIA, and all the administration staff, IIA, for helping me in various administrative matters. I thank all the staff members of Stores, IIA, for providing me necessary stationaries and procuring many indented materials. I thank Mr. Suresh, dispatch section for taking care of all my documents and mails. I am grateful to the Kannada Rajyothsava Samithi, IIA, who always organized the best Rajyothsava events in the campus and provided me an opportunity every year during my stay at IIA to present Carnatic classical music along with Mridangam artist Mr. Ramakrishna, which greatly inspirited me.

I express my heartfelt gratitude to Prof. G. C. Anupama, In-charge of Bhaskara guest house who took special care of me and made me have a comfortable stay in the hostel. My special thanks to Mr. Selvakumar, Mr. Chandrashekhar and Mr. Manjunath, for helping me to address day to day problems in the Bhaskara guest house. I sincerely thank all the house keeping staff both at Bhaskara and IIA campus, for their timely help and garden maintenance staff with whom I had nice conversations and for also providing me beautiful plants. I appreciate the help provided by all the cooking staff of both IIA canteen and Bhaskara, for always providing healthy food. I am extremely grateful for all the support provided by IIA and Bhaskara staff during corona virus outbreak. A special thanks to the cooking and helping staff of Bhaskara, Mr. Vimalan, Mr. Satish, Mr. Lakshminarayan, Mr. Ramesh and Mr. Rayappa.

I am extremely grateful to all my teachers who helped me in each and every crucial steps that I have taken, specially my BSc professors at DVS college, Kuvempu University, Prof. Sunanda, Prof. Umesh, Prof. Venkateshmurthy, Prof. Papanna, Prof. Chandrashekhar, and my MSc professors at Mysore University, Prof. Mallesh, Prof. Umesh, Prof. Krishnaveni, and Prof. Sridhar. I am grateful to Prof. Nageswara Rao for helping and influencing me in clearing most of the competitive examinations. Special thanks to Prof. Sudha, Kuvempu University, for her constant inspiration and help. I thank all my PhD course work mentors of IIA, Indian Institute of Science (IISc), Raman Research Institute (RRI), and U. R. Rao Satellite center, for teaching basics of astronomy and astrophysics.

I thank my senior, Dr. L. S. Anusha, for sharing her knowledge in her busy schedule. She also has inspired me to pursue research by her extensive hard work. She and her husband, Mr. Sandeep accompanied me and Prof. Nagendra for a tour to see all the Nobel laureates' houses and monuments in Göttingen during SPW9. They also invited me for a dinner with other scientists to their home, where I had really a memorable time discussing about science, fitness, politics, and early days of Prof. Stenflo, Prof. Nagendra and Prof. Michele Bianda. I also thank my senior Dr. K. Sowmya for helping me for VISA letter from MPS, she being on the LOC of SPW9. I thank my senior Dr. H. D. Supriya for encouraging me in my research and sharing the necessary documents when required.

I thank all my wonderful friends in Bhaskara with whom I spent wonderful time. I am deeply indebted to my best friend Anirban for helping me in studies, research, and providing me mental and emotional support without fail during various occasions. Thanks to my roommates Vidhya and Tanya, who always made me have a comfortable stay. I thank all my batch mates Anirban, Samrat, Snehalata, Dipanweeta, Chayan, Tridib for sharing their thoughts, keeping me happy and helping me during course work. I also thank my JAAP friends Avinash, Siddhartha, Akanksha, Sandeep, Raj, and Shina, who made my course work memorable. I am deeply grateful to Anirban, Tanya, Snehalata, Sireesha, Ramya, Pavana, Vishnu, Avinash, Akanksha, Souvik, Pavan, Aritra, Shejeela, Meenakshi, Maya, and Samrat for standing by my side during difficult times. I thank my best friend Shwetha and her husband Dr. Ganapati for their warm hospitality and extreme care in Darmstadt during my conference visit. Their son Kishan kept me very happy during this visit. I thank all my seniors at IIA who helped and guided me in many ways. Special thanks to my seniors Vaibhav and Tanmoy for clearing

many of my doubts on IDL programming and also observational aspects of solar physics. I thank all my juniors at IIA for the best time I had with all of them. Special thanks to my junior Dinesh for his hospitality and care in Göttingen. I also thank my friend Shwetha and MSc juniors Subramanya and Smitha for wonderful Physics discussions.

I am indebted and owe my deepest gratitude to my parents Ananda Rao and Madhura for their continuous support and vast freedom to choose everything on my own. They were very patient with me in this long journey and profoundly encouraged me with all my choices. Special thanks to my little sister Manya who has brought lot of joy in my life and cheered me all the time. I am immensely thankful to my brother and music teacher, Arun Kumar for guiding me at right instances and helping in many ways. I thank all my extended family members for their support during several occasions. I am grateful to Annapurneshwari hostel, DVS committee, Mr. Sridhar Sharma, Mr. Sudhindra and many other sources for extending financial help throughout my BSc and MSc terms without which I would have never reached this level. I thank my fitness trainer Rajesh and fitness partner Kalpana for lot of support and care, that has made me physically fit and mentally strong during my stressful days. Finally, I thank each and every person who has influenced, encouraged, and supported me to follow my dream in various ways.

Bengaluru A. Megha
May 2020

List of Publications

This Thesis is based on the following publications

In International Journals

1. Hanle-Zeeman Scattering Matrix for Magnetic Dipole Transitions
Megha, A, Sampoorna, M., Nagendra. K. N., & Sankarasubramanian, K. 2017, **ApJ**, 841, 129 (14 pages)

2. Polarized Line Formation in Spherically Symmetric Atmospheres with Velocity Fields
Megha, A, Sampoorna, M., Nagendra. K. N., Anusha, L. S., & Sankarasubramanian, K. 2019, **ApJ**, 879, 48 (18 pages)

3. Fast Iterative Techniques for Polarized Radiative Transfer in Spherically Symmetric Moving Media
Megha, A, Sampoorna, M., Nagendra. K. N., Anusha, L. S., & Sankarasubramanian, K. 2020, **ApJ**, 903, 6 (10 pages)

4. Polarized Line Formation in Spherically Symmetric Expanding Atmospheres with Weak Field Hanle Effect
Megha, A, Sampoorna, M., Nagendra. K. N., Anusha, L. S., & Sankarasubramanian, K. 2020, **ApJ** (Under preparation)

In Refereed Conference Proceedings

1. Coronal magnetic field measurements using forbidden emission lines
Megha, A, Sampoorna, M., Nagendra. K. N., & Sankarasubramanian, K. 2018, in Proceedings of **IAUS No. 340**, Long term datasets for the understanding of solar and stellar magnetic cycles, eds. Dipankar Banerjee, Jie Jiang, Kanya Kusano, & Sami Solanki, (Cambridge: Cambridge University Press), 61-62

2. Polarized Line Formation in Spherically Symmetric Expanding Atmospheres
Megha, A, Sampoorna, M., Nagendra. K. N., Anusha, L. S., & Sankarasubramanian, K. 2019, in **ASPCS**, 519, Radiative signatures from the cosmos: A meeting in honor of Ivan Hubeny, eds. K. Werner, C. Stehle, T. Rauch, & T. M. Lanz (San Francisco: ASP), 27-32

3. Resonance Line Polarization in Spherically Symmetric Moving Media: a Parametric Study
Megha, A, Sampoorna, M., Nagendra. K. N., Anusha, L. S., & Sankarasubramanian, K., 2019, in Proceedings of 9th Solar Polarization workshop SPW9, eds. A. Gandorfer, A. Lagg, & K. Raab (Göttingen:MPS), 1-10 (DOI: 10.17617/2.3186650)

4. Polarized Scattering Matrix for Magnetic Dipole Transitions
Megha, A, Sampoorna, M., Nagendra. K. N., & Sankarasubramanian, K. 2020, in **ASPCS**, Solar Polarization 8, eds. L. Belluzzi, J. Trujillo Bueno, R. Casini, & M. Romoli (San Francisco: ASP), 207-214

Abstract

Magnetic fields are ubiquitous in astrophysical plasmas. They are responsible for most of the stellar activities and they manifest in numerous ways in the stellar atmospheres. The Sun being our nearest star is the natural laboratory to understand the causes and effects of the magnetic fields. The solar magnetic field couples the solar interior with its atmosphere. It drives the dynamic phenomena such as coronal mass ejections (CMEs) and solar flares. The magnetic field also plays a critical role in heating the solar upper chromosphere and corona as well as in accelerating the solar wind. A variety of techniques are used to infer these magnetic fields and subsequently map them into the layers of the solar atmosphere, from where the concerned observable originates.

Studies of polarization properties of spectral lines formed in solar atmosphere serve as one of the best methods to determine the nature of solar magnetic fields (Stenflo 1994). The polarization is the result of breaking of symmetry in the source region. This symmetry breaking in the line forming regions can be attributed to the anisotropic illumination of the atoms and presence of magnetic fields. In the presence of magnetic fields the energy levels of the atoms split into different magnetic m sub-states. The transition from these split magnetic sub-states results in circularly or linearly or elliptically polarized light depending on the strength and orientation of the magnetic field with respect to the chosen line-of-sight (LOS). This effect discovered by Zeeman in the laboratory in 1896, is popularly known as Zeeman effect. It was first seen on Sun by Hale (1908) in sunspots. Using Zeeman effect in spectral lines it became possible to measure both the strength and orientation of the magnetic field vector (especially the strong fields of few kG).

Zeeman effect cannot be used effectively in the presence of very weak fields

(due to extremely small splitting) and also, it is not suitable to measure the turbulent fields (due to cancellation of the opposite polarities of the magnetic field within the finite spectral resolution). Under such conditions the magnetic field in the solar atmosphere can be determined by the linear polarization measurement of spectral lines with appropriate sensitivity to Hanle effect. Hanle effect is the result of quantum interferences between different magnetic m sub-states of a given atomic level involved in the transition. It is the modification: depolarization or repolarization and rotation of plane of linear polarization, of resonance scattering in the presence of weak magnetic fields. Therefore Zeeman and Hanle effects can be used to diagnose the magnetic field of the Sun in a very different and complementary parameter regimes.

The aim of this thesis is to develop pure theoretical tools required for the determination of the solar magnetic fields using polarized spectral line formation theory. The thesis is divided into two parts. In the first part (Chapters 2 and 3) we develop the scattering theory for magnetic dipole (M1) transitions and study the forbidden emission lines formed in solar coronal conditions or any other astrophysical objects with diffuse media. In the second part (Chapters 4–8) we consider the problem of polarized line formulation in spherically symmetric moving atmospheres, for the case of optically thick permitted (electric dipole allowed) lines. Chapter 1 gives a general introduction to the thesis, wherein we describe the basic physical concepts required in both parts of the thesis. Chapter 9 summarizes the work carried out in this thesis and also gives the future outlook on the problems described in both the parts of the thesis.

Part-I: Scattering Theory for Magnetic Dipole (M1) Transitions

In Chapter 2, we derive the Hanle-Zeeman scattering matrix for M1 transitions. It can be used to study the forbidden emission lines that are formed in any diffuse astrophysical media such as solar corona. Because the Einstein A coefficient is small for the forbidden lines, the magnetic splitting is much larger than the natural line width even for very weak coronal magnetic fields. Thus, we mainly remain in the regime of saturated Hanle effect in forbidden lines, in the solar corona. Thus, Hanle effect in forbidden lines provides an important means of diagnosing the topology of coronal magnetic fields. The earlier formulation of the problem of scattering on forbidden lines in magnetic fields is limited to the regime of saturated Hanle effect. Our aim here is to present a new alternative formulation of the required scattering theory that covers the entire field strength regime.

In Chapter 3, we apply the theoretical formalism developed in Chapter 2 to understand the effects of density distributions, magnetic field configurations, and velocity fields on the emergent Stokes profiles of the [Fe XIII] 10747 Å coronal forbidden line. We also describe the procedures to perform the integration over the solid angle of incident cone of radiation and the LOS integration, to conduct the above mentioned empirical studies.

Part-II: Polarized Radiative Transfer in Spherically Symmetric Moving Atmospheres

The plane-parallel approximation of the stellar atmospheres can not be applied to model the formation of several optically thick lines in extended atmospheres. To a good approximation these atmospheres can be represented by a spherically symmetric medium. Furthermore the extended stellar atmospheres are known to be highly dynamic, with low to high speed stellar wind originating in these layers. Such velocity fields present in the line forming regions produce Doppler shift, aberration of photons, and also give rise to advection. All these effects can modify the amplitudes and shapes of the emergent Stokes profiles. Thus our aim here is to develop numerical techniques to solve the polarized line transfer equation in spherically symmetric extended atmosphere with velocity fields and also magnetic fields.

In Chapter 4, we develop modern iterative techniques based on operator perturbation to solve the polarized transfer equation in a spherically symmetric static atmosphere. Apart from the Jacobi based polarized accelerated lambda iteration (PALI) method, in this chapter we also develop the fast iterative techniques based on Gauss-Seidel (GS) and successive overrelaxation (SOR). These latter methods are known to be superior over the traditional Jacobi iterative scheme. We describe the numerical steps for the Jacobi, GS, and SOR techniques and study their convergence behavior in the presence of both partial frequency redistribution (PFR) and complete frequency redistribution (CFR) scattering mechanisms.

In Chapter 5, we include the effects of radial velocity fields to the problem of polarized line formation in spherically symmetric atmospheres. We describe both observer's frame and comoving frame (CMF) methods to solve the problem under consideration. We describe the Jacobi based CMF-PALI method in detail as this method is computationally much superior than the observer's frame method. We also discuss the inclusion of GS and SOR techniques in the CMF-PALI method

and study their convergence behavior in the presence of velocity fields for both CFR and PFR.

In Chapters 6 and 7, we discuss in detail the numerical results obtained for the problem of polarized line formation in spherically symmetric static and expanding non-magnetic atmospheres. With the help of contribution function and Stokes source vector, we explain the nature of the polarized line profiles formed in both static and moving atmospheres in presence of both CFR and PFR (Chapter 6). We also vary the model parameters both the atmospheric and atomic parameters one at a time (keeping the other parameters as constants) and study the dependence of the linearly polarized line profiles on the model parameters for both static and moving atmospheres (Chapter 7).

In Chapter 8, we extend the Jacobi based CMF-PALI method developed in Chapter 5 to include the weak magnetic fields. In the presence of weak fields, Hanle effect comes into play. Unlike the non-magnetic case the physical quantities involved in the problem now become radiation field azimuth dependent. We take into account the approximation-III of Bommier (1997b) to represent angle-averaged PFR in the presence of weak magnetic fields. We also discuss the polarized line profiles formed in the presence of both magnetic and velocity fields for the case of CFR and PFR.

List of Abbreviations

The list of abbreviations used in this thesis along with their expansions are listed below.

AA	**A**ngle-**A**veraged
ALI	**A**ccelerated **L**ambda **I**teration
ARF	**A**tmospheric **R**eference **F**rame
CFR	**C**omplete **F**requency **R**edistribution
CLE	**C**oronal **L**ine **E**mission
CLV	**C**enter-to-**L**imb **V**ariation
CMF	**C**o**M**oving **F**rame
CPU	**C**entral **P**rocessing **U**nit
CS	**C**oherent **S**cattering
1D	One-**D**imensional
2D	Two-**D**imensional
3D	Three-**D**imensional
DH	**D**omke-**H**ubeny
DI	**D**isk **I**ntegrated
DOM	**D**iscrete **O**rdinate **M**ethod
DOME	**D**iscrete **O**rdinate **M**atrix **E**xponential
E1	**E**lectric dipole
EMF	**E**lectro**M**otive **F**orce
EUV	**E**xtreme-**UV**
FBF	**F**requency-**B**y-**F**requency
FOV	**F**ield-**O**f-**V**iew
GS	**G**auss-**S**eidel

HFS	**H**yper**F**ine **S**tructure
IR	**I**nfra**R**ed
ISM	**I**nter**S**tellar **M**edium
LDD	**L**atitude **D**ependent **D**ensity
LOS	**L**ine-**O**f-**S**ight
LTE	**L**ocal **T**hermodynamic **E**quilibrium
M1	**M**agnetic dipole
MALI	**M**ultilevel **ALI**
MHD	**M**agneto**H**ydro**D**ynamics
MKH	**M**ihalas-**K**unasz-**H**ummer
MRC	**M**aximum **R**elative **C**hange
MRF	**M**agnetic **R**eference **F**rame
MUGA	**MU**ltilevel **G**auss-**S**eidel
NLTE	**N**on-**LTE**
PA	**P**osition **A**ngle
PALI	**P**olarized-**ALI**
PFR	**P**artial **F**requency **R**edistribution
QED	**Q**uantum **E**lectro**D**ynamics
SEM	**S**cattering **E**xpansion **M**ethod
SOR	**S**uccessive **O**ver**R**elaxation
SS	**S**ingle **S**cattering
SSD	**S**pherically **S**ymmetric **D**ensity
UV	**U**ltra **V**iolet
VELC	**V**isible **E**mission **L**ine **C**oronagraph
ZIMPOL	**Z**urich **IM**aging **POL**arimeter

Contents

Chapter 1

General Introduction

According to the spectral classification of stars, the Sun is a G-type main-sequence star. It is also the nearest star, whose disk can be resolved, thereby, allowing us to understand it in a greater detail. Noticing the shape of solar corona during the solar eclipse, Hale concluded that the Sun must be magnetized and proved the same by observing the Zeeman splitting of spectral lines in a sunspot for the first time (Hale 1908). The magnetic fields are frozen-in in the photosphere (Alfvén 1943) due to high electrical conductivity of the plasma. On the other hand, the fields are nearly force-free in the upper solar atmosphere since the magnetic energy density is higher than the kinetic energy density of the plasma. Hence, it appears that the magnetic field acquires a life of its own in the upper atmosphere, thereby controlling the dynamics of hot, tenuous plasmas. Therefore, a study of nature of magnetic fields in the solar atmospheres is the first step towards understanding the global picture of magnetism in other astrophysical systems. It is well-known that both the distribution of energy (intensity) in terms of wavelength and vector properties (polarization) of the electromagnetic radiation emitted from the astrophysical systems can be measured with highest possible accuracy and resolution with the use of spectropolarimetry. Therefore, spectropolarimetry is one of the powerful tools to diagnose the Sun's magnetic field through remote sensing. In the following sections, we qualitatively describe the basic terminologies and the relevant physical phenomena that are useful for understanding the contents presented in this thesis.

1.1 Representation of polarized light

In a seminal paper, G. G. Stokes for the first time established an ideal mathematical formalism to describe the state of polarization of a photon beam (Stokes 1852). He also demonstrated important properties of the polarized light and showed that the state of mixed streams of polarized light can be completely determined by the values of four constants, which are now popularly known as Stokes parameters I, Q, U, and V. Here, I is the specific intensity, Q and U are a measure of the degree and plane of linear polarization, and V is a measure of circular polarization. This theory was ignored almost for 80 years by the scientific community until Soleillet (1929) used the Stokes parameters to study the partial polarization of light. Still the use of Stokes parameters to represent the polarized light was unknown to the astrophysical community for next 18 years. It was S. Chandrasekhar who demonstrated the usefulness of the Stokes parameters to formulate the polarized radiative transfer equation in stellar atmospheres (see the series of papers by Chandrasekhar 1946a,b, 1947, also the monograph on radiative transfer by Chandrasekhar 1950).

Alternatively, R. C. Jones presented a formalism to describe a 100 % polarized light (Jones 1941). The Jones formalism cannot describe partially polarized light which arises due to the incoherent superposition of mutually uncorrelated photons with different polarization states, that is very common in atomic processes. Mueller (1948) developed a classic approach for dealing with partially polarized light. He derived a 4×4 matrix which contains the effects of the medium and helps to transform the Stokes parameters when the light travels from one medium to the other. We also adopt this approach in part-I of this thesis. Stenflo (1994) has described these different representations of the polarized light along with the corresponding mathematical expressions. Here we recall few of those equations which are relevant for this thesis. If $\boldsymbol{e}_1$ and $\boldsymbol{e}_2$ are two orthogonal basis vectors in a plane perpendicular to the direction of propagation, then the electric vector $\boldsymbol{E}$ at any point in space is given by

$$\boldsymbol{E} = Re(E_1\boldsymbol{e}_1 + E_2\boldsymbol{e}_2), \tag{1.1}$$

where $E_k = E_{0k}e^{-\mathrm{i}(\omega t - \phi_k)}$ with $k = 1, 2$, E_{0k} are the complex amplitudes, ω, and ϕ_k are the frequency and phase of the electromagnetic radiation. The Stokes

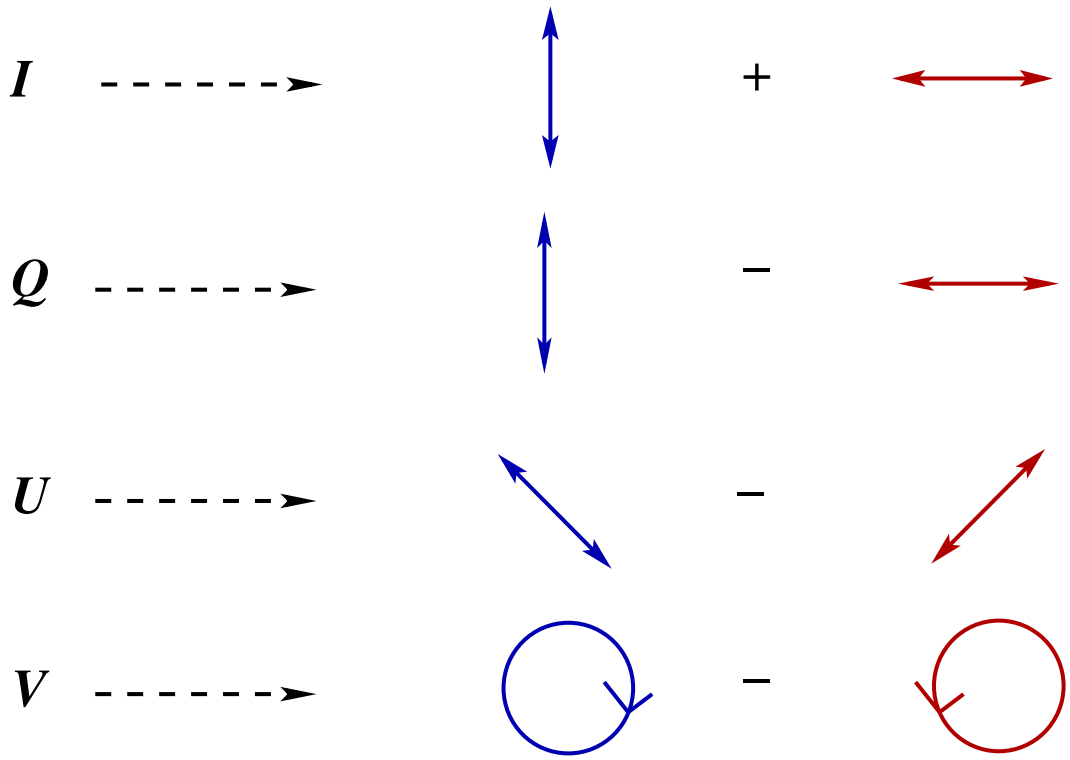

FIGURE 1.1: A pictorial representation of Stokes parameters I, Q, U, and V (reproduced by the author based on Figure 1 of Landi Degl'Innocenti 2002).

parameters are defined as

$$\begin{aligned} I &= \langle E_{01}^2 + E_{02}^2 \rangle; & Q &= \langle E_{01}^2 - E_{02}^2 \rangle, \\ U &= \langle 2E_{01}E_{02}\cos(\phi_1 - \phi_2) \rangle; & V &= \langle 2E_{01}E_{02}\sin(\phi_1 - \phi_2) \rangle. \end{aligned} \tag{1.2}$$

Here the angular brackets represent averaging over a statistical ensemble of uncorrelated photons. A pictorial representation of the Stokes parameters is shown in Figure 1.1. The quantities I, Q, U, and V are not independent but they are related to each other as, $I^2 = Q^2 + U^2 + V^2$ for a completely polarized light, $I^2 > Q^2 + U^2 + V^2$ for the partially polarized light, and $Q = U = V = 0$ for an unpolarized light. For a linearly polarized light $V = 0$. In this case, the degree of linear polarization is defined as

$$P = \frac{\sqrt{Q^2 + U^2}}{I}, \tag{1.3}$$

and the position angle (which defines the rotation of linear polarization with respect to the reference direction) is defined as

$$\mathrm{PA} = \frac{1}{2}\tan^{-1}\frac{U}{Q}. \tag{1.4}$$

Having defined the Stokes parameters, we now define the Jones vector $\boldsymbol{J}$ as

$$\boldsymbol{J} = \begin{pmatrix} E_1 \\ E_2 \end{pmatrix}. \tag{1.5}$$

If we now consider a light beam that enters a medium with Jones vector $\boldsymbol{J'}$ and exits as $\boldsymbol{J}$, then the relation between these two Jones vectors can be described by a complex 2×2 Jones matrix $\boldsymbol{w}$, which contains the information of interaction of light with the medium. Mathematically this is represented as

$$\boldsymbol{J} = \boldsymbol{w}\boldsymbol{J'}. \tag{1.6}$$

Since Jones matrix can only represent a 100 % polarized light, to handle the general partially polarized light, the coherency matrix formalism of the radiation field has to be used, which can be derived from Jones vectors as

$$\boldsymbol{D} = \langle \boldsymbol{J}\boldsymbol{J'} \rangle, \tag{1.7}$$

and the coherency matrix transforms as

$$\boldsymbol{D} = \boldsymbol{w}\boldsymbol{D'}\boldsymbol{w}^{\dagger}. \tag{1.8}$$

The relation between the coherency matrix and the Stokes parameters is given by

$$\mathbf{D} = \frac{1}{2}\begin{pmatrix} I+Q & U+\mathrm{i}V \\ U-\mathrm{i}V & I-Q \end{pmatrix}. \tag{1.9}$$

If $\boldsymbol{I'}$ represents the incident Stokes vector on a medium, then the transformation of this Stokes vector by the medium can be described by the 4×4 Mueller matrix $\boldsymbol{M}$ as

$$\boldsymbol{I} = \boldsymbol{M}\boldsymbol{I'}. \tag{1.10}$$

Using Equation (1.9), the Mueller matrix is expressed in terms of the Jones matrix $\boldsymbol{w}$ as

$$\boldsymbol{M} = \boldsymbol{T}\boldsymbol{W}\boldsymbol{T}^{-1}, \tag{1.11}$$

where the physical properties of the medium are contained in

$$\boldsymbol{W} = \boldsymbol{w} \otimes \boldsymbol{w}^* = \begin{pmatrix} w_{11}w_{11}^* & w_{11}w_{12}^* & w_{12}w_{11}^* & w_{12}w_{12}^* \\ w_{11}w_{21}^* & w_{11}w_{22}^* & w_{12}w_{21}^* & w_{12}w_{22}^* \\ w_{21}w_{11}^* & w_{21}w_{12}^* & w_{22}w_{11}^* & w_{22}w_{12}^* \\ w_{21}w_{21}^* & w_{21}w_{22}^* & w_{22}w_{21}^* & w_{22}w_{22}^* \end{pmatrix}. \tag{1.12}$$

The symbols $\otimes$ and $*$ denote tensor product and complex conjugation respectively. $\boldsymbol{T}$ and $\boldsymbol{T}^{-1}$ are purely mathematical transformation matrices without any physical contents and they are given by

$$\boldsymbol{T} = \begin{pmatrix} 1 & 0 & 0 & 1 \\ 1 & 0 & 0 & -1 \\ 0 & 1 & 1 & 0 \\ 0 & -\mathrm{i} & \mathrm{i} & 0 \end{pmatrix}; \quad \boldsymbol{T}^{-1} = \frac{1}{2}\begin{pmatrix} 1 & 1 & 0 & 0 \\ 0 & 0 & 1 & \mathrm{i} \\ 0 & 0 & 1 & -\mathrm{i} \\ 1 & -1 & 0 & 0 \end{pmatrix}. \tag{1.13}$$

Mueller calculus discussed above is an important flexible tool in spectropolarimetry. Mueller's approach has been extensively used in radiative transfer calculations involving Zeeman effect, coherent and incoherent scattering and the Hanle effect (see Stenflo 1994). The Mueller matrix can also be used to describe each component of the telescope system such as the spectrograph, retarders, polarizers, modulators etc., hence help in calculating the instrumental polarization. For such an optical system, the total Mueller matrix $\boldsymbol{M}$ is computed through simple matrix multiplication of Mueller matrices ($\boldsymbol{M_i}$, with $i = 1, 2, ..., m$, m being the total number of optical components) of each individual optical component as

$$\boldsymbol{M} = \boldsymbol{M}_m\boldsymbol{M}_{m-1}.....\boldsymbol{M}_2\boldsymbol{M}_1. \tag{1.14}$$

The matrices defined in Equations (1.11) and (1.12) are for the case of polarized light arising from electric dipole (E1) transitions. In part-I of this thesis we discuss the magnetic dipole (M1) transitions for which the above definitions are slightly modified and are given in detail in Chapter 2.

1.2 Origin of polarized radiation

Polarization is an intrinsic property of the transverse electromagnetic radiation. The nature of variation of electric field or magnetic field components of the radiation with time defines the state of polarization. Depending on the state of polarization (variation of tip of the field vector of the radiation), the light can be categorized as linearly, circularly, or elliptically polarized. Breaking of spatial symmetry in the physical processes is the reason for production of observed polarized radiation (Stenflo 2002). Some of the important symmetry breaking processes are Zeeman and Hanle effects (seen in spectral lines in the presence of magnetic fields), Stark effect (in the presence of electric fields), anisotropic illumination of atoms or molecules, collisions with a collimated beam of fast particles (impact polarization), reflection, refraction (e.g., rainbows, solar and lunar halos), Rayleigh scattering (e.g., on air molecules leading to blue color of the sky, scattering on bound electrons which can produce 100 % linearly polarized light in a 90° scattering), Mie scattering (when scatterer's dimension is larger than the wavelength of light), radiating charged particle, Thomson scattering (on free electrons), Bremsstrahlung (breaking radiation due to a fast moving electron near the Coulomb potential of a nucleus), cyclotron radiation (non-relativistic electron moving in the presence of a magnetic field), synchrotron radiation (relativistic electron moving in the presence of a magnetic field). For a detailed discussion of all the mentioned processes which generate polarization, see Rybicki and Lightman (1979), Collett (1993), and Landi Degl'Innocenti (2002). In this thesis we mainly focus on the polarization as observed on Sun which is mainly produced by a magnetic field (Zeeman effect), and by coherent scattering of an anisotropic radiation (namely, the resonance scattering in the absence of magnetic field and Hanle scattering in the presence of a weak magnetic field).

1.2.1 The Zeeman effect

Michael Faraday was interested in understanding the effect of magnetic fields on the linearly polarized light during the middle of nineteenth century which led to the discovery of the Faraday effect (namely, rotation of plane of polarization of the plane polarized light as it propagates through a medium, with non-zero magnetic

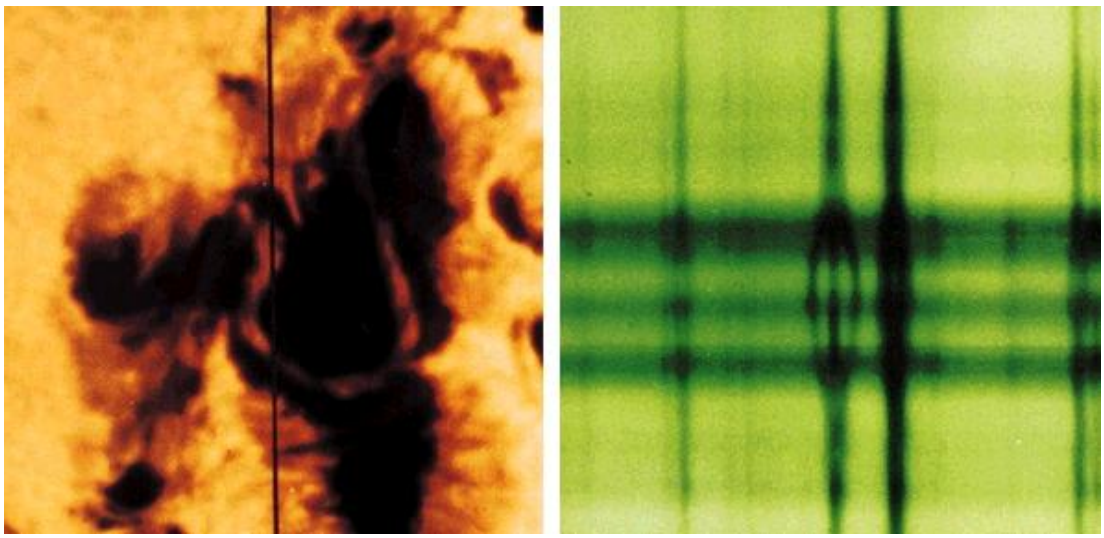

FIGURE 1.2: A complex sunspot picture obtained in Fe I 5250.22 Å line, taken at 15:30 hours UT, indicating a field strength of 4.13 kG in the region of maximum splitting in the lines. The vertical black line on the white light image (left) indicates the location of the slit for the spectrograph recording shown on the right. The splitting of one spectral line into three components is a clear demonstration of the Zeeman effect (shown on the right). This picture was taken at the McMath-Pierce Solar Facility on Kitt Peak. Courtesy: National Optical Astronomy Observatory (NOAO).

fields). It was not until 1896 that this relationship between light and magnetism was more concretely demonstrated by Pieter Zeeman through lab experiments, which were inspired by the collected works of Maxwell and Faraday. Zeeman was able to obtain the broadening of the sodium D lines in the presence of an electromagnet (Zeeman 1897) and a classical theory was immediately provided by Lorentz to explain this experimental result, which led them to share the Nobel Prize in Physics in 1902. This discovery is now popularly known as Zeeman effect. It describes splitting of a spectral line by an external magnetic field into differently polarized components. Prior to the laboratory works, Lockyer (1866) obtained the spectroscopic observation of the sunspot, but failed to interpret the results. It was George Ellery Hale who successfully observed the Zeeman effect in Hα photographs of sunspot and hence triggered the new era of astrophysical magnetism via spectropolarimetry. Figure 1.2 illustrates the Zeeman effect observed in a complex sunspot. For a historical account on solar magnetic fields we refer the reader to Stenflo (2017).

Lorentz introduced the classical oscillator theory for electric dipole (E1) transitions to describe the Zeeman effect. In Chapter 2 we discuss the classical oscillator theory for the case of M1 transitions. Therefore, here we briefly recall the classical description of the interaction of a bound electron with the electric field component $\boldsymbol{E}$ of the electromagnetic radiation, in the presence of an external magnetic field that can be applied for the electric dipole (E1) transitions. An excellent and detailed classical description of the Zeeman effect is presented in Stenflo (1994) (see also Collett 1993; Jefferies *et al.* 1989). For the corresponding quantum picture see Landi Degl'Innocenti and Landolfi (2004).

Lorentz used a simple model of Sodium atom (which has a single electron in the outermost orbit) and considered that the electron is bound to the nucleus. The motion of this bound electron about the nucleus is governed by the Hooke's law with a frequency of oscillation ω_0. Using Maxwell's theory, Lorentz predicted that broadened Zeeman line actually consists of 2 to 3 split lines with different polarization states (linear, circular or elliptical). This theory can successfully explain only normal Zeeman triplet, namely, it is equivalent to a quantum mechanical $J = 0 \rightarrow 1 \rightarrow 0$ transition. The oscillator equation which describes the motion of the bound electron in an atom in the presence of external magnetic field $\boldsymbol{B}$ and illuminated by the electromagnetic radiation with electric field component $\boldsymbol{E}_{\rm in}$ is given by

$$\ddot{\boldsymbol{r}} + \gamma\,\dot{\boldsymbol{r}} + \frac{e}{m}\,\dot{\boldsymbol{r}} \times \boldsymbol{B} + \omega_0^2 \boldsymbol{r} = -\frac{e}{m}\boldsymbol{E}_{\rm in}, \tag{1.15}$$

where $\boldsymbol{r}$ is the relative position vector of the bound electron, γ is the damping constant, e and m being the charge and mass of the electron respectively. The above coupled equation can be decoupled into component form by introducing the spherical vectors $\boldsymbol{e}_q$, with $q = 0, \pm 1$, where

$$\boldsymbol{e}_0 = \boldsymbol{e}_z; \quad \boldsymbol{e}_\pm = \mp(\boldsymbol{e}_x \pm \mathrm{i}\boldsymbol{e}_y)/\sqrt{2}. \tag{1.16}$$

Here $\boldsymbol{e}_{x,y,z}$ are Cartesian unit vectors with the z-axis along the direction of the magnetic field. Equation (1.15) in component form can be written as

$$\ddot{r}_q - (2\,q\,\mathrm{i}\,\omega_B - \gamma)\dot{r}_q + \omega_0^2 r_q = -\frac{e}{m}E_q^{\rm in}, \tag{1.17}$$

where $\omega_B = eB/2m$ is the Larmor frequency. Solution of the above equation gives

the trajectory of the bound electron in an external magnetic field. Clearly, we have three mutually perpendicular oscillators with oscillating frequency $\omega_0 - q\omega_B$. For $q = 0$, the resonating frequency is ω_0 and the oscillation is along the field direction, thereby representing a linear polarization in this direction and it is referred to as unshifted π-component. For $q = \mp 1$, the oscillators resonate at frequencies $\omega_0 \pm \omega_B$ and they represent left and right circular polarization and are referred to as σ-components (σ_r for $q = +1$: a redshifted component, σ_b for $q = -1$: a blueshifted component). Classically, these three types of oscillators represent electric dipoles and emit dipole radiation. The polarization properties of the radiation observed in a given direction is simply determined by the geometrical projection of the oscillating dipole vector on a plane perpendicular to the line-of-sight (LOS). Thus, if the field is directed along the LOS, contribution from the π-component vanishes, while the σ-components remain, giving rise to right and left circularly polarized light, namely the longitudinal Zeeman effect. If the field is oriented perpendicular to the LOS, then the σ and π-components are linearly polarized perpendicular and parallel to the field direction which is termed as transverse Zeeman effect. For an arbitrary field orientation, the Zeeman line components are elliptically polarized. A pictorial representation of longitudinal and transverse Zeeman effect are shown in Figure 1.3.

We now briefly discuss the quantum picture of Zeeman effect by considering the transition between atomic levels with total angular momentum quantum numbers J_l and J_u corresponding to the lower and upper levels respectively. Then the transition between these energy levels in the presence of an external magnetic field will give rise to spectral lines whose wavelength shifts can be determined by the following expression:

$$\lambda_{m_u m_l} = \lambda_0 - \Delta\lambda_B(g_u m_u - g_l m_l), \tag{1.18}$$

where g_u, g_l and m_u, m_l are the Landé factors and magnetic quantum numbers of the upper and lower levels, respectively. The Zeeman splitting factor $\Delta\lambda_B$ is given by

$$\Delta\lambda_B = 4.67 \times 10^{-10} \lambda_0^2 B, \tag{1.19}$$

where $\Delta\lambda_B$ is in mÅ, unperturbed wavelength is λ_0 in Å, and magnetic field strength B is in Gauss. Left panel of Figure 1.4 depicts the quantum picture of

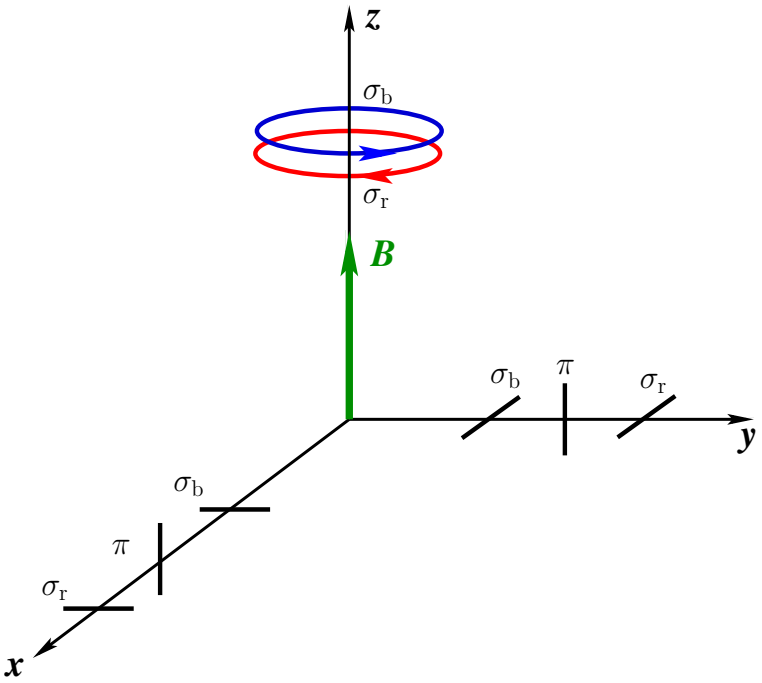

FIGURE 1.3: A representation of longitudinal and transverse Zeeman effects. Along the direction of magnetic field we see only σ-components which are right (σ_b) and left (σ_r) circularly polarized and along the LOS perpendicular to the magnetic field, we see both π and σ-components which are linearly polarized. This figure is made by the author following Figure 3.1 of Landi Degl'Innocenti and Landolfi (2004).

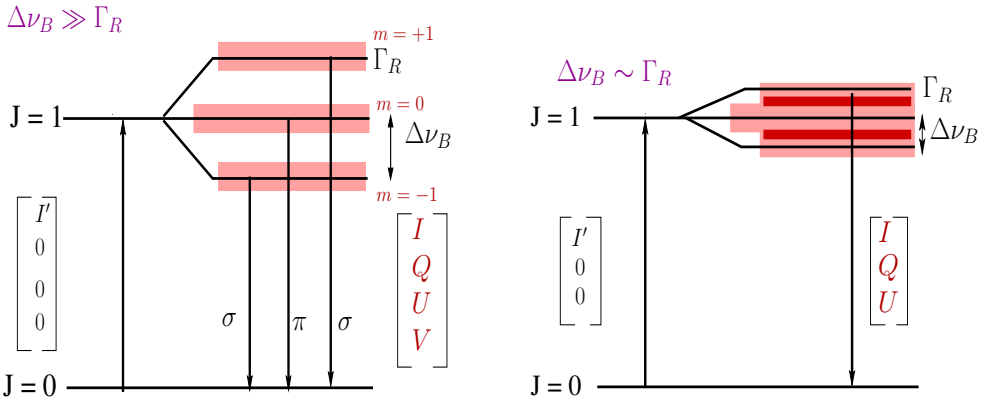

FIGURE 1.4: Level diagram in the presence of a strong (left panel) and a weak (right panel) magnetic field for a $J = 0 \rightarrow 1 \rightarrow 0$ transition. Γ_R is the radiative width of the upper level. When Zeeman splitting $\Delta\nu_B$ is much larger than Γ_R, we are in the Zeeman regime (left panel). On the other hand, if the splitting is comparable to Γ_R, then the Zeeman sublevels (here $m = 0, \pm 1$) superimpose or interfere giving rise to Hanle effect (right panel).

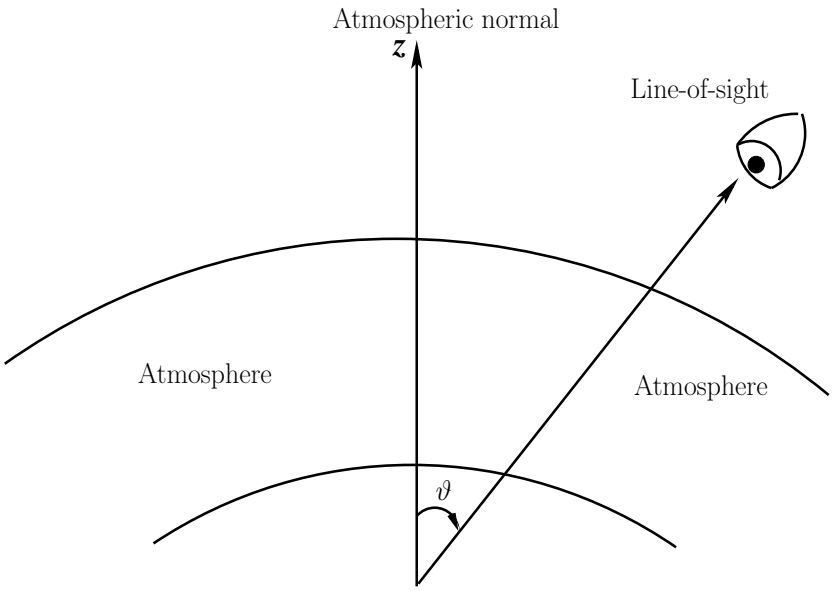

FIGURE 1.5: A 1D atmosphere with z-axis along the atmospheric normal. The line-of-sight makes an angle ϑ with respect to the z-axis.

Zeeman effect for a $J = 0 \rightarrow 1 \rightarrow 0$ transition. For a $J = 0 \rightarrow 1 \rightarrow 0$ transition, the upper level splits into three sublevels with $m = 0, \pm 1$. Only limited number of Zeeman components arise depending on the selection rule. For an E1 transition, the selection rule is given by

$$\Delta m = m_u - m_l = 0, \pm 1. \tag{1.20}$$

Clearly Equation (1.19) shows that the Zeeman splitting is more complete when longer wavelengths are considered (as $\Delta\lambda_B \propto \lambda_0^2$). Therefore Zeeman effect can be used to determine the vector magnetic field (both field strength and orientation) in Sun and stars using full Stokes polarimetry (namely, determining I, Q, U, and V) particularly when strong fields (about few hundreds to kG) are present in the observing region. Thus it serves as a diagnostic tool to determine the solar and stellar magnetic fields.

1.2.2 Scattering polarization

Solar spectrum observed near the limb is linearly polarized even in the absence of magnetic fields due to coherent scattering processes (Stenflo *et al.* 1983a,b). This

non-magnetic scattering polarization is zero at the disk center ($\mu = \cos\vartheta = 1$, see Figure 1.5) due to the axisymmetry of the radiation field there. The scattering polarization increases as the LOS is moved towards the limb and reaches the maximum near the limb ($\mu = 0$). This polarization arises due to an anisotropic radiative excitation of atoms or molecules in the solar atmosphere immediately followed by spontaneous emission. In the absence of velocity fields, the main contribution to this anisotropy is from the limb darkening. The degree of anisotropy in the solar atmosphere being smaller (Stenflo 2005) gives rise to smaller degree of scattering polarization of a few percent. Such weak signals have been recorded (Stenflo and Keller 1996, 1997) with the advent of high-precision polarimetric instrument such as the Zurich IMaging POLarimeter (ZIMPOL; Povel *et al.* 1990; Povel 1995), which has a polarimetric accuracy of 10^{-5}. This linearly polarized spectrum of Sun which completely differs from the intensity spectrum is called the "Second Solar Spectrum" (Ivanov 1991; Stenflo and Keller 1997). An atlas of the Second Solar Spectrum covering the wavelength range from 3160-6995 Å recorded near the solar limb (at $\mu = 0.1$) is presented in graphical form by Gandorfer (2000, 2002, 2005).

Rayleigh and Raman scatterings are two important types of scattering processes. If the quantum numbers n, L, J associated with an atomic transition are the same for both the initial and final states involved in the scattering process, then such a scattering phenomenon is termed as the Rayleigh scattering. Any difference in these quantum numbers between the initial and final atomic states leads to Raman scattering. Thomson scattering on free electrons and Rayleigh scattering on hydrogen atom mainly contribute to the polarized continuum spectra of the Sun. On the other hand, resonance scattering on atoms and molecules, gives rise to polarized line spectra. It is a special case of Rayleigh scattering, wherein the incident photon has a frequency equivalent to the energy difference between the atomic levels, particularly involving the ground state. A similar special case of Raman scattering is called fluorescent scattering.

The scattering phenomenon can be understood using a classical picture based on Maxwell's theory. Here we qualitatively describe the origin of scattering polarization by using a classical harmonic oscillator model for an atom. For this let us consider a simple 90° scattering event as shown in panel (a) of Figure 1.6. An unpolarized beam of radiation is incident on an atom (held at the center of

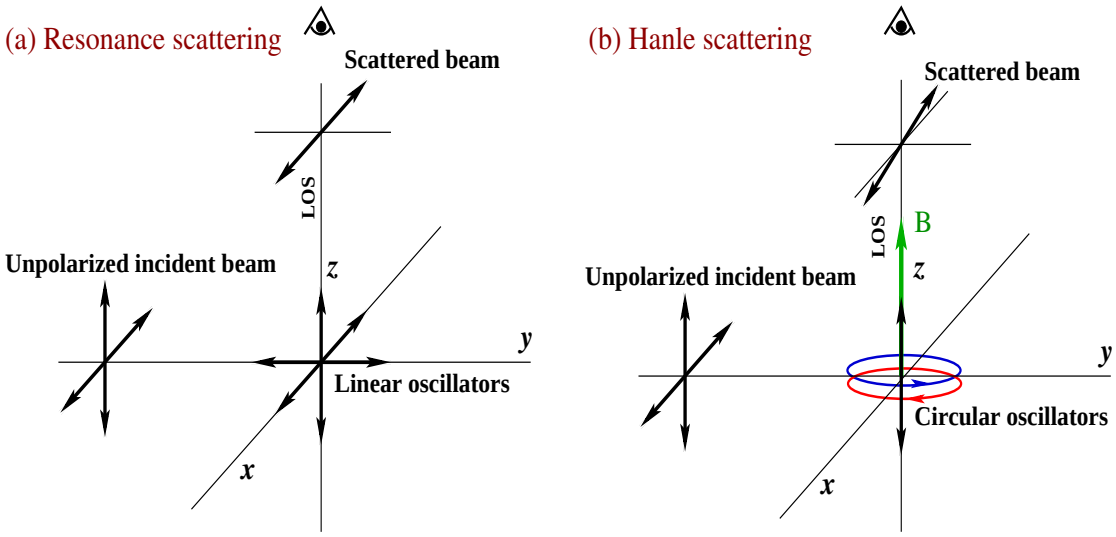

FIGURE 1.6: Classical picture of a 90° scattering event: (a) resonance scattering (in the absence of external magnetic field), and (b) Hanle scattering in the presence of a weak external magnetic field parallel to z-axis or LOS.

the coordinate system) along the y-axis. In the absence of the magnetic field, the atom can be represented by three mutually perpendicular independent linear oscillators vibrating at angular frequency ω_0. Since the incident radiation beam is along y-axis, only the x and z oscillators are excited. These two oscillating dipoles radiate independently in all directions except along the axis of the dipole, and they decay spontaneously with a damping constant γ in an extremely short time. The scattered radiation is linearly polarized and the degree of polarization depends on the LOS. For a 90° scattering geometry (LOS along the z-axis in Figure 1.6) the degree of polarization is maximum (100 %) and linearly polarized along the x-axis. For forward scattering (i.e., LOS along the y-axis) the degree of polarization is minimum (0 %). The same conclusion can also be attained by considering the x-oscillator as resulting from the coherent superposition of two counter-rotating circular oscillators that are oscillating in phase with respect to each other at frequency ω_0 in the x-y plane. It is interesting to note that in the Zeeman effect, only the state of polarization varies depending on the LOS but not the total degree of polarization.

A two-level atom having a lower level of angular momentum $J_l = 0$ and an upper level of angular momentum $J_u = 1$ can be used as the quantum analogue of above described classical harmonic oscillator model. The excitation of one of the classical oscillator is equivalent to excitation of one of the Zeeman sublevels of

the upper level. In this analogy, the linear oscillator corresponds to the sublevel $m_u = 0$, while the circular oscillators correspond to the sublevels $m_u = \pm 1$, respectively. When the field is zero, magnetic sublevels are degenerate and the atom can exist in a coherent superposition of these levels. Thus, the photons emitted from $m_u = +1$ and $m_u = -1$ levels (by two different atoms) are highly coherent (i.e., identical in frequency and phase), and oppositely circularly polarized. These photons interfere to give 100 % linearly polarized light (which explains the resonance scattering). Clearly the polarization produced is due to the population imbalances and quantum interferences among the Zeeman sublevels, which is referred to as 'atomic polarization' (Trujillo Bueno 2001). The presence of weak magnetic fields can modify the resonance polarization produced by coherent scattering, which we discuss in the next section.

1.2.3 The Hanle effect

Hanle effect is the modification of the scattering polarization produced by the resonance scattering in the presence of an external magnetic field. The presence of a magnetic field mainly causes the rotation of plane of polarization (i.e., generation of Stokes U), and modifies the degree of linear polarization (usually a depolarization in the line core leading to reduced Stokes Q) of the scattered radiation.

Wood (1908) for the first time observed the polarization of the fluorescent light of gases and molecules (mainly in the white light fluorescence of sodium and iodine vapor). Wood (1912) also observed that the light scattered from mercury vapor was completely polarized under non-resonant conditions, while the 2536.7Å resonant radiation was not always completely polarized. Rayleigh (1922) observed in multiple experiments that the resonant line of mercury was differently linearly polarized. Wood and Ellett (1923a,b) explained that the discrepancies observed in Rayleigh's experiments were because of the presence of earth's magnetic field (which was not compensated for). Wood and Ellett (1924) realized that the depolarization observed in resonant mercury line was not due to the Zeeman effect, because the field strength measured was $B \lesssim 1$ G (for which expected Zeeman splitting is negligible compared to the line width). They conducted experiments with both mercury and sodium D lines and concluded that the observed phenomenon was a new magneto-optic effect. A first correct interpretation (also eliminating

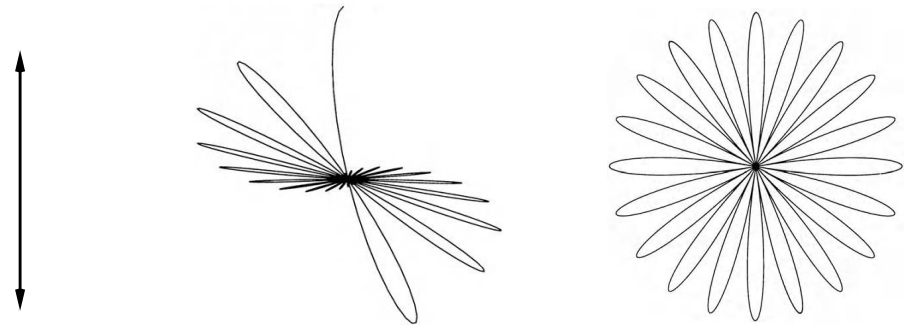

(a) Resonance scattering $B = 0$

(b) Hanle effect $B \neq 0$, $\omega_B \sim \gamma$ (weak field)

(c) Zeeman effect $B \neq 0$, $\omega_B \gg \gamma$ (strong field)

FIGURE 1.7: Trajectory of a bound electron obtained using a damped classical oscillator model. Here the LOS and the direction of magnetic field are parallel to each other and the motion of electron is in a plane transverse to the direction of magnetic field. Panels (b) and (c) are taken from Moruzzi and Strumia (1991).

Faraday effect) of the experimental results of Wood and Ellett (1924) was given by Hanle (1923, 1924, 1925), which formed his PhD thesis work titled "Magnetic field influence on the polarization of the resonance fluorescence of mercury". His interpretation (both classical and quantum) of the observed phenomenon, which was later called as the 'Hanle effect' is briefly discussed below (for greater details see Mitchell and Zemansky 1934; Moruzzi and Strumia 1991).

For the classical description, we again consider the geometry shown in Figure 1.6 with a quasi-elastically bound electron in a mercury atom. An unpolarized beam of incoming radiation along the y-axis is incident on the mercury atom. The scattered resonance light is observed along the z-axis. The polarization of the scattered radiation is determined in the xy-plane. An external magnetic field is applied along the z-axis (which is also along the LOS). Now the electron oscillations in the xy-plane can be decomposed into two counter rotating circular motions each having slightly different oscillating frequencies ($\omega_0 \pm \omega_B$) because of the non-zero magnetic field. The resulting trajectory of the electron in the xy-plane (obtained by solving the Eq. (1.15) by setting the RHS to zero) is given by

$$\begin{aligned} x(t) &= e^{-\gamma t/2} \cos(\omega_{\rm B} t) \cos(\omega_0 t), \\ y(t) &= e^{-\gamma t/2} \sin(\omega_{\rm B} t) \cos(\omega_0 t). \end{aligned} \tag{1.21}$$

The bound electron thus describes in the xy-plane a complicated pattern called the "rosette" pattern (see Figure 1.7). Based on the ratio $\omega_{\rm B}/\gamma$, the shape of the rosette varies, which can be mainly divided into three cases.
(i) $\omega_{\rm B} \gg \gamma$ (strong field regime): here the bound electron precesses about the magnetic field several times before being affected by the damping, thereby describing a perfect rosette as shown in Figure 1.7c. For the geometry considered (cf. Figure 1.6), the scattering polarization (along the z-axis) is zero. However in this regime, the longitudinal Zeeman effect produces circular polarization.
(ii) $\omega_{\rm B} \ll \gamma$ (zero field regime): if the applied field is very weak, the electron performs a highly damped oscillation with hardly any precession and emits linearly polarized light, which is the case of resonance scattering (see Figure 1.7a).
(iii) $\omega_{\rm B} \approx \gamma$ (weak field or Hanle effect regime): if the applied field is weak, such that $\omega_{\rm B} \approx \gamma$, then there can be two competing processes, i.e., a) the applied field forces the electron to precess about the magnetic field and b) the radiation damping tries to suppress this precessing motion. Thus, the bound electron exhibits a damped rosette motion as shown in Figure 1.7b, thereby giving rise to a depolarization and a small rotation of plane of polarization with respect to the corresponding non-magnetic case. This is the regime of the Hanle effect.

To interpret the Hanle effect in terms of quantum mechanics, Hanle noted that when the magnetic splitting of the excited energy level of a quantum system is on the order of, or smaller than, $h/t_{\rm life}$ (here h is Planck's constant and $t_{\rm life}$ the lifetime of the atomic level under consideration), the excited level can exist in a quantum superposition of magnetic sublevels. From Heisenberg's uncertainty principle, we know that, $h/t_{\rm life}$ is the natural width or radiative width ($\Gamma_{\rm R}$, which is equivalent to damping constant γ of the classical theory) of the excited level. In the absence of external magnetic field, these magnetic sublevels are fully degenerate leading to a resonant polarization. On the other hand, in the presence of weak magnetic fields (field strength within 0 to few hundred Gauss), the magnetic sublevels are not fully separated (see Figure 1.4b), but they are superimposed giving rise to a mixed state. Resonant scattering taking place from such superimposed states gives rise to the Hanle effect. The field for which Hanle effect is sensitive is quantitatively determined by the Hanle gamma parameter

$$\Gamma_B \approx 8.79 \times 10^6 B\, g_J\, t_{\rm life}, \tag{1.22}$$

where $t_{\rm life}$ is inversely proportional to the damping constant γ and g_J is the Landé g-factor of the upper or lower level. Clearly, sensitivity regime of Hanle effect varies depending on the spectral line of interest and it is optimum when $\Gamma_B \sim 1$. For a known field strength, Hanle effect plays an important role in spectroscopy in determining the lifetimes of the excited states of atoms and molecules (Moruzzi and Strumia 1991). In astrophysics, Hanle effect is a very useful tool to determine the weak magnetic fields (see reviews by Leroy 1985; Kazantsev 1983; Stenflo 1991). Basic theoretical concepts required for applying Hanle effect in astrophysics are given in greater detail in Stenflo (1994) and Landi Degl'Innocenti and Landolfi (2004).

The Hanle effect is sensitive to weaker fields in the range of 1 mG to 100 G which can be found in the solar surface (Trujillo Bueno 2001). Therefore Hanle effect has been extensively used to determine the weak magnetic field on the Sun, to name a few: deterministic fields in prominences (see, e.g., Leroy *et al.* 1977; Leroy 1977; Sahal-Bréchot *et al.* 1977; Sahal-Bréchot 1981; Landi Degl'Innocenti 1982; Leroy *et al.* 1983; Athay *et al.* 1983; Querfeld *et al.* 1985; Bommier *et al.* 1986; Landi Degl'Innocenti *et al.* 1987), turbulent magnetic fields in the solar photosphere (wherein circular polarization signals due to Zeeman effect cancels out within each spatial resolution element containing mixed polarity fields; see, e.g., Stenflo 1982; Faurobert-Scholl 1993, 1996; Faurobert *et al.* 2001; Trujillo Bueno *et al.* 2004; Bommier *et al.* 2005; Faurobert *et al.* 2009), and in chromosphere, transition region and corona (see, e.g., Stenflo 1982; Bommier and Sahal-Bréchot 1982; Sahal-Bréchot *et al.* 1986; Faurobert-Scholl 1992; Bianda *et al.* 1998a,b; Derouich *et al.* 2010; Trujillo Bueno *et al.* 2011; Anusha *et al.* 2011a). See Stenflo (2013) and Trujillo Bueno *et al.* (2017) for a review on the diagnostic potential of Hanle and Zeeman effects to determine the nature of solar magnetic fields. Hanle effect can also be used to study the stellar magnetic fields (see, e.g., Ignace *et al.* 1997; Ignace 2001; López Ariste *et al.* 2011; Bommier 2012; Manso Sainz and Trujillo Bueno 2011; Manso Sainz and Martínez González 2012).

In part-I of this thesis we describe the application of Hanle effect to determine the coronal magnetic fields using optically thin forbidden emission lines. In part-II, we discuss the application of Hanle effect to study the optically thick permitted lines formed in the spherically symmetric moving atmospheres.

1.3 Coronal magnetic fields

Coronal magnetic field measurement is still a challenging problem in solar physics because the fields are intrinsically weak (few Gauss) and the corona contains optically thin, high temperature (up to few million Kelvin) tenuous plasma leading to thermally broadened weak signals. Coronal magnetic field is one of the major sources affecting the space weather. Therefore, a variety of methods have been applied to determine the same. We list few methods that are used for measuring magnetic fields at different heights using different wavelengths: direct magnetometer measurements based on induced currents (Mariani and Neubauer 1990), using Bremsstrahlung and Faraday rotation in radio waves (Bird and Edenhofer 1990; Gelfreikh 1994; Sakurai and Spangler 1994), using gyroresonance emission (Akhmedov *et al.* 1982), using longitudinal Zeeman effect (Lin *et al.* 2000), using resonance polarization (Arnaud and Newkirk 1987), using Hanle effect (Sahal-Bréchot 1981; Landi Degl'Innocenti 1982; Raouafi *et al.* 2016), using magneto acoustic waves (Jess *et al.* 2016), using MHD modeling (Mackay and Yeates 2012; Wiegelmann *et al.* 2014; Inoue 2016), using vector tomographic inversion technique (Kramar *et al.* 2016), and using multi-wavelength studies (Gibson *et al.* 2016) etc.

Among different techniques mentioned above, the spectropolarimetry of coronal forbidden emission lines undergoing M1 transitions can provide one of the best constraints on both the plane-of-sky (POS) field direction and LOS field strength, thereby serving as a diagnostic tool to determine the vector magnetic field in the solar corona.

1.3.1 Coronal forbidden emission lines

During total solar eclipse of 7 August 1869, Young and Harkness independently observed the 5303 Å coronal emission line for the first time using a spectrograph. This line was called 'green line' and was assumed to be produced by an unknown element called 'coronium'. Campbell and Moore (1919) presented the spectrum of solar corona mentioning them as bright lines. Grotrian (1939) solved this puzzle of green line and concluded that this line was originated from the highly ionized state of iron [Fe XIV] and also gave the tentative identifications for red coronal lines

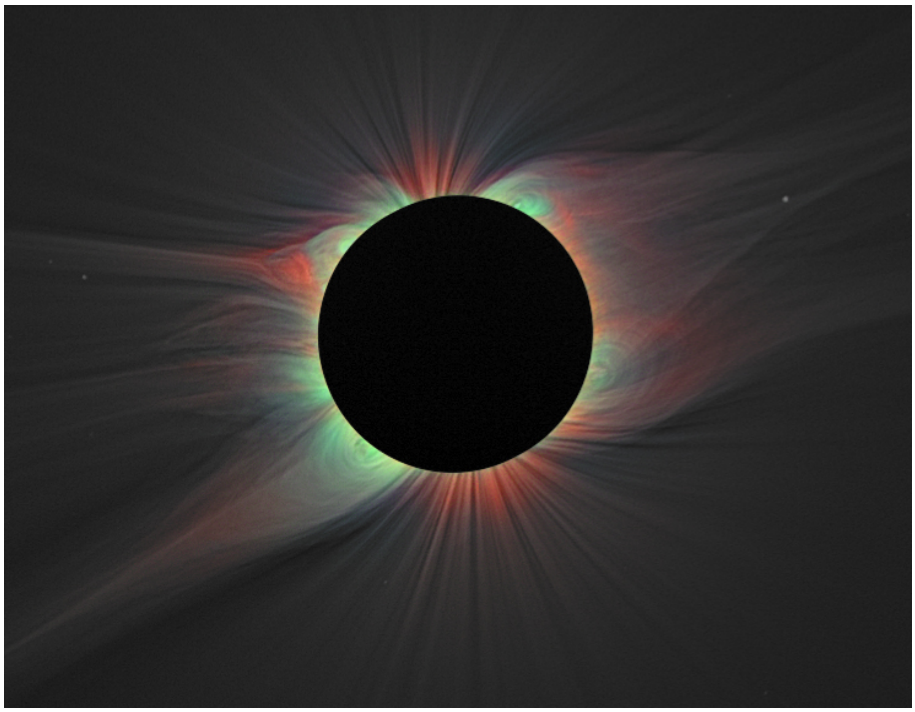

FIGURE 1.8: Solar corona during the total solar eclipse of 2008 displaying emission from forbidden Fe lines combined with white light. [Fe XI] is shown in red, [Fe XIII] in blue, and [Fe XIV] in green, taken from Habbal *et al.* (2010).

[Fe X] 6374 Å and [Fe XI] 7892 Å. Lyot (1939) developed a coronagraph and found unidentified lines such as the famous infrared (IR) [Fe XIII] 10747 Å and 10797 Å forbidden lines, which initiated the new era of coronal magnetometry (Waldmeier 1957). Coronal observations require natural eclipses (see Figure 1.8 displaying the coronal forbidden emission lines during the total solar eclipse of 2008) or coronagraphs. Some of the ground based coronagraphic measurements are made at Sacramento Peak (New Mexico), Norikura (Japan), Haleakala (Hawaii), Pic du Midi (France), Kislovodsk (Russia) and Mauna Loa Solar Observatory (High Altitude Observatory, Boulder). The Visible Emission Line Coronagraph (VELC) payload onboard Aditya-L1[1], is the first Indian space based solar coronagraph intended to study the corona of Sun. This payload also includes a spectropolarimetric channel in IR for 10747 Å line (see the energy level diagram in Figure 1.9). Aditya-L1 is expected to be launched in 2020-2021.

Coronal forbidden lines arise from M1 transitions. In other words, they are not electric dipole (E1) allowed transitions. Because of the low density and high

[1]https://aditya.iiap.res.in/

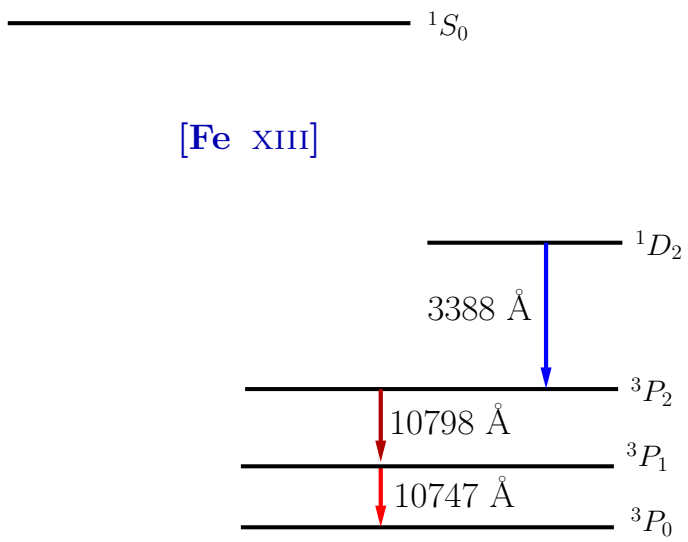

FIGURE 1.9: Energy level diagram of [Fe XIII] ion showing IR transition lines 10747 Å and 10798 Å.

temperature of the coronal plasma, they naturally occur in such conditions. They have small values of Einstein spontaneous emission coefficient A (whose classical analogue is the damping constant γ) or extremely high lifetime. For most of the forbidden lines in the corona, A value lies between 10 s^{-1} to 100 s^{-1}, which is about 10^6 times smaller compared to the lines undergoing E1 transitions. Because of low values of A, even for weak magnetic fields of strength 10^{-4} G, Equation (1.22) shows that Γ_B will be much larger than unity. This means that measurement of magnetic field strength is impossible from linear polarization measurement of these lines. However, these lines continue to be sensitive to the orientation of field vector on POS. This asymptotic regime of Hanle effect, where the scattered linearly polarized light has become insensitive to the magnetic field strength, but sensitive to the field orientation is called the 'strong field regime' or 'saturated Hanle regime'.

Landi Degl'Innocenti (1983a) has given a classification scheme for the formation of polarization in spectral lines based on four important parameters. They are: (i) the ratio of anisotropic (R_a) to isotropic (R_i) contributions to the radiative excitation rate, i.e., R_a/R_i, (ii) the ratio of Larmor frequency to the Doppler width of the line, i.e., $\nu_B/\Delta\nu_D$, (iii) the radio of Larmor frequency to the spontaneous deexcitation rate, i.e., ν_B/A, and (iv) the ratio of collisional depolarizing rate (D) to the radiative isotropic excitation rate, i.e., D/R_i. For the observed visible or IR M1 lines, $\nu_B/\Delta\nu_D$ is about 10^{-3} or less, while E1 lines observed at extreme ultra

violet (EUV) wavelengths will show even lesser values in the corona. The critical particle density for E1 transitions to occur is about 10^{15} cm^{-3}, whereas for M1 transitions it is close to 10^{8} cm^{-3} (see Judge *et al.* 2001). Therefore, anisotropy in the case of visible and IR wavelengths is substantial for the M1 transitions, which is also modified by the depolarizing collisions ($R_a \sim D$). Thus, forbidden emission lines undergoing M1 transitions fit well into this classification scheme and are very useful for the determination of topology of coronal magnetic fields.

In part-I of this thesis, we derive the Hanle-Zeeman scattering matrix for M1 transitions (in Chapter 2) and present its application to the case of [Fe XIII] 10747 Å coronal forbidden emission line (in Chapter 3).

1.4 Polarized line radiative transfer

Part-I of this thesis is dedicated to the optically thin forbidden (M1) lines formed in the corona. There are several optically thick UV and EUV allowed (E1) lines which form in the upper chromosphere, transition region and above (e.g., Lyα lines of H I, He II etc). For the quantitative analysis of the Stokes profiles of optically thick lines, it is necessary to solve the polarized radiative transfer equation. Before describing the transfer equation, we briefly discuss the redistribution mechanism in scattering which is a fundamental physical phenomena in the line transfer theory. We remark that, for an optically thin M1 lines considered in part-I of the thesis, frequency coherent scattering in the laboratory frame suffices to represent the scattering mechanism. However, for optically thick E1 lines (particularly for strong resonance lines) it is necessary to account for frequency redistribution in scattering which is discussed in the following subsections.

1.4.1 Redistribution in line scattering

Scattering process may change the frequency, direction, and polarization of the scattered photon relative to that of the incident photon. It contributes to the formation of both line and continuous part of the spectrum. Here we discuss only the redistribution mechanisms in line scattering. For a discussion on redistribution

mechanism for scattering on electrons (which contributes to both line and continuum scattering) we refer the reader to Chandrasekhar (1950). A redistribution function $R(\nu, \boldsymbol{n}, \nu', \boldsymbol{n}')$ gives the joint probability of a photon with a frequency ν' and direction $\boldsymbol{n}'$ being absorbed by an atom and then being re-emitted (or scattered) with outgoing frequency ν and direction $\boldsymbol{n}$. If the frequency and direction of the scattered photon are correlated to the corresponding quantities of the incident one then the redistribution mechanism is called the partial frequency redistribution (PFR). On the other hand, absence of such correlation in the scattering mechanism is called the complete frequency redistribution (CFR). CFR mechanism is usually sufficient to describe the weak resonance lines and subordinate lines and it is numerically much easier to handle. However, PFR is numerically complex to handle in radiative transfer problems, but it is very important and necessary ingredient to model the polarized profiles of strong resonance lines.

Hummer (1962) derived the scalar redistribution function for a 2-level atom, in the absence of collisions. Further studies on the frequency redistribution in resonance and subordinate lines including collisions were done by Oxenius (1965); Heinzel (1981); Heinzel and Hubeny (1982); Hubeny (1982); Heinzel and Hubeny (1983); Hubeny *et al.* (1983a,b); Hubeny and Heinzel (1984); Hubeny and Cooper (1986); and Hubeny and Lites (1995). For a detailed mathematical description and a historical account on the theory of PFR, we refer the reader to Hubeny and Mihalas (2014).

The calculation of redistribution function is a two step process. First the redistribution function is calculated in the rest frame of the atom. Since the transfer calculations are done in the laboratory (or observer's) frame, the atomic redistribution has to be convolved with a velocity distribution corresponding to the thermal motion of the scattering atoms which give rise to Doppler shifts. When calculating the laboratory frame redistribution function it is usually assumed that the atomic velocity is unchanged during the scattering process and also the velocity distribution is given by a Maxwellian. The scalar redistribution function in the atomic frame may be written as

$$R_0(\xi, \boldsymbol{n}, \xi', \boldsymbol{n}') = r(\xi, \xi') p(\boldsymbol{n}, \boldsymbol{n}'), \tag{1.23}$$

where the subscript "0" identifies the quantities in the atomic rest frame. ξ, ξ' are the frequencies of the scattered and incident photons in the atomic frame. The $p(\boldsymbol{n}, \boldsymbol{n}')$ is the angular phase function which describes the probability that the photon is scattered from solid angle $d\boldsymbol{n}'$ in direction $\boldsymbol{n}'$, into solid angle $d\boldsymbol{n}$ in direction $\boldsymbol{n}$. We now briefly discuss the Hummer's type-II and type-III frequency redistribution functions which are relevant for a resonance line considered in part-II of this thesis.

The type-II redistribution mechanism in the atom's frame involves an atomic transition between an infinitely sharp lower level and radiatively broadened upper level. In the atomic frame, the emitted photon has the same frequency as the incident photon and the corresponding frequency redistribution is given by

$$r_{\rm II}(\xi, \xi') = \mathcal{L}(\xi')\delta(\xi - \xi'), \tag{1.24}$$

where δ is the Dirac distribution and $\mathcal{L}(\xi')$ is the rest frame absorption profile, which is a Lorentzian. This is called "frequency coherent scattering" in the atomic frame. $r_{\rm II}(\xi, \xi')$ is convolved with a Maxwellian velocity distribution to get the laboratory frame redistribution function $R_{\rm II}(\nu, \boldsymbol{n}, \nu', \boldsymbol{n}')$ (wherein ν and ν' are the frequencies of the scattered and incident photons in the laboratory frame).

The type-III redistribution mechanism in the atom's frame involves an atomic transition between an infinitely sharp lower level and radiatively as well as collisionally broadened upper level. Here the elastic collisions are assumed to be more frequent so that all the excited electrons are randomly reshuffled over the substates of the upper state before the occurrence of emission. Therefore, in the atomic frame, the emitted photon's frequency is uncorrelated to that of the incident photon and the corresponding frequency redistribution is given by

$$r_{\rm III}(\xi, \xi') = \mathcal{L}(\xi')\mathcal{L}(\xi). \tag{1.25}$$

Since the correlation between the incident and emitted frequencies is lost, this redistribution is called "frequency incoherent scattering" or "complete frequency redistribution" (CFR) in the atomic frame. Again, $r_{\rm III}(\xi, \xi')$ is convolved with a Maxwellian velocity distribution to get the laboratory frame redistribution function $R_{\rm III}(\nu, \boldsymbol{n}, \nu', \boldsymbol{n}')$. The explicit form of both $R_{\rm II}$ and $R_{\rm III}$ functions can be found

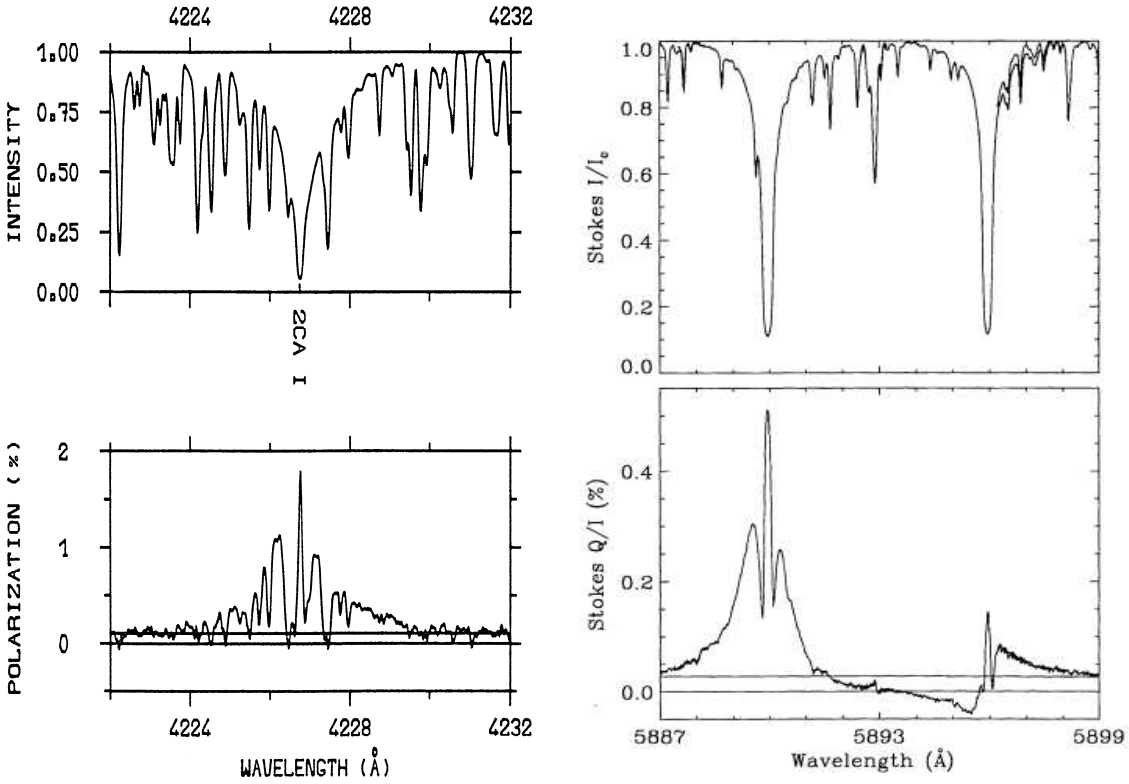

FIGURE 1.10: Intensity and linear polarization profiles of Ca I 4227.74 Å resonance line (to the left) taken from Stenflo (1994) and Na I D_1 5890 Å and D_2 5896 Å lines (to the right) taken from Stenflo (1996) showing the PFR effects in both intensity and polarization.

in Mihalas (1978).

1.4.2 A brief historical overview of PFR theories with polarization

The redistribution function becomes a 4×4 redistribution matrix when polarization of incident and scattered photons is taken into account. In this case, the PFR effects are described by a 4×4 redistribution matrix $\mathbf{R}(\nu, \boldsymbol{n}, \nu', \boldsymbol{n}')$ in the absence of a magnetic field and $\mathbf{R}(\nu, \boldsymbol{n}, \nu', \boldsymbol{n}', \boldsymbol{B})$ in the presence of a magnetic field. As already mentioned PFR plays an important role in the formation of the polarized line profiles of strong resonance lines. In general PFR produces large damped wings in the intensity profile and gives rise to a typical triple peak structure in the linear polarization (see Figure 1.10, also see, for eg., Rees and Saliba 1982).

A classical theory of PFR using a forced damped oscillator model was introduced by Zanstra (1941a,b) to explain the polarized profiles of resonance lines in a non-magnetic condition. Stenflo (1994, 1996, 1998) and Bommier and Stenflo (1999) developed a modern approach to the classical theory with the inclusion of respectively, the coherent scattering and atomic frame PFR in the presence of arbitrary strength magnetic fields. A first quantum electrodynamic (QED) treatment of this problem was given by Omont *et al.* (1972) in the absence of magnetic fields and Omont *et al.* (1973) including the effects of magnetic fields. Based on the formulation of Omont *et al.* (1972), the functional forms of the non-magnetic redistribution matrix was derived by Domke and Hubeny (1988), which proved useful for practical applications. Bommier (1996) made a first attempt to derive the PFR matrix using the density matrix formalism. Later, Bommier (1997a,b) developed the master equation theory to derive the collisional PFR matrix both in the absence and presence of arbitrary magnetic fields. For more details see the reviews by Hubeny (1985); Frisch (1988); Stenflo (1996); Frisch (1996); Frisch *et al.* (2001).

Based on the classical theory of Bommier and Stenflo (1999), Sampoorna *et al.* (2007a,b) derived the Hanle-Zeeman PFR matrix in the laboratory frame. They also showed the equivalence between the QED approach (Bommier 1997a,b) and the classical oscillator approach (Bommier and Stenflo 1999) for the case of $J = 0 \rightarrow 1 \rightarrow 0$ scattering transition. Sampoorna (2011) extended this work to the transitions with arbitrary quantum numbers. Based on the Kramer-Heisenberg scattering approach of Stenflo (1994, 1998), the two-term atom PFR matrix was derived by Smitha *et al.* (2011, 2013) considering the interference between the upper fine-structure J-states (in the linear Zeeman regime). This work was extended to the case of arbitrary field strengths (including the Paschen-Back effect regime) by Sowmya *et al.* (2014a). The PFR matrix for a two-level atom with hyperfine structure splitting (HFS) was derived in Smitha *et al.* (2012) in the linear Hanle-Zeeman regime and in Sowmya *et al.* (2014b) including also Paschen-Back effect regime of field strength. Sowmya *et al.* (2015) have derived the PFR matrix for a two-term atom with HFS accounting for combined $J-$ and $F-$state interferences in arbitrary fields. For a more complete set of references we refer the reader to the reviews by Nagendra (2014, 2015, 2019).

Based on a metalevel approach, Landi Degl'Innocenti *et al.* (1997) extended the multi-level and multi-term atom density matrix formalism to include collisionless PFR. Recently Casini *et al.* (2014) presented a new quantum mechanical theory for the frequency redistribution in a two-term atom with arbitrary magnetic fields. This was also extended to three-term atom by Casini and Manso Sainz (2016a,b). Bommier (2016a) extended the master equation theory to handle polarized PFR in multilevel and multiline atom. Using this theory Bommier (2016b) attempted to model the observed linearly polarized profiles of the Na I D_1 and D_2 lines. Explicit expressions of the collisional PFR matrix for a two-term atom are derived in Bommier (2017). The Kramer-Heisenberg approach has been extended by Stenflo (2015, 2016) to handle multi-level atomic systems. In this thesis we use the non-magnetic and weak field Hanle angle-averaged PFR matrix of Bommier (1997a,b, see also Domke and Hubeny 1988) to study the effects of the velocity fields in the extended spherical atmospheres.

1.4.3 Polarized radiative transfer in plane-parallel geometry

The equation of transfer is a mathematical formulation to express the conservation of radiation energy when a light ray passes through a medium by incorporating the effects of emission, absorption, and scattering. The polarized transfer equation for a ray passing through a 1D plane-parallel atmosphere (Figure 1.11a) is given by

$$\mu \frac{\partial \boldsymbol{I}(z,\mu,x)}{\partial z} = -\chi(z,x)[\boldsymbol{I}(z,\mu,x) - \boldsymbol{S}(z,\mu,x)], \tag{1.26}$$

where $\boldsymbol{I}$ is the Stokes vector, $\boldsymbol{S}$ is the source vector, χ is the total absorption coefficient, z is the vertical distance along the atmospheric normal, $\mu = \cos\vartheta$, with ϑ is inclination of the ray (or LOS) with respect to the atmospheric normal, and $x = (\nu - \nu_0)/\Delta\nu_D$ is the non-dimensional frequency measured in Doppler width ($\Delta\nu_D$) units, with ν_0 being the line center frequency.

The source vector being the ratio of emission to the absorption coefficient plays an important role in describing the interaction of the radiation field with the medium as the light propagates through it. Thus, the source vector $\boldsymbol{S}$ depends on

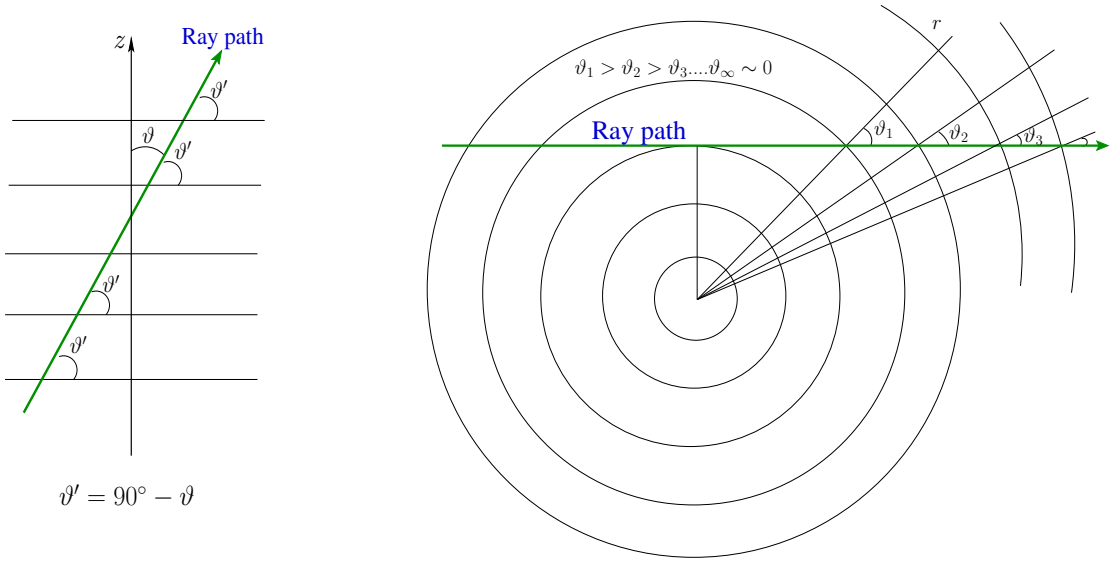

(a) Planar Geometry (b) Spherical Geometry

FIGURE 1.11: Represention of a ray (or LOS) passing through a 1D plane-parallel atmosphere (panel a) and a spherically symmetric atmosphere (panel b).

the physical processes involved in the medium. If the matter is in thermal equilibrium with itself (but not with the radiation field), then the matter can be said to be in local thermodynamic equilibrium (LTE). Under LTE, the source vector is given by unpolarized Planck function at the line center $B_{\nu_0}(\mathrm{T})$, which depends only on the local temperature T of the medium. The regions where collisions dominate (e.g., in the lower photosphere of Sun), one can use LTE approximation for $\boldsymbol{S}$ namely, $\boldsymbol{S} = B_{\nu_0}(\mathrm{T})\boldsymbol{U}$ (where $\boldsymbol{U}$ is the unity vector). However, scattering (which depends on the incident radiation) is another common physical process (e.g., in the upper photosphere, chromosphere of Sun), which introduces the non-local coupling of the atmosphere over distances that are of the order of one photon mean free path. Thus scattering dominated atmospheres are in non-local thermodynamic equilibrium (NLTE). Under NLTE, the source vector becomes decoupled from the local temperature and depends on the radiation field itself from non-local points. Chandrasekhar (1950) was the first to set-up the NLTE polarized radiative transfer equation for the resonance scattering in the absence of magnetic field.

1.4.4 Polarized radiative transfer in spherical geometry

The approximation of plane-parallel stratification for the radiative transfer problems is an excellent choice when dealing with stellar atmospheres having a density scale-height much smaller than the radius of the star. However, there are several stars, like Wolf-Rayet stars and supergiants with the atmospheric thickness which is an appreciable fraction of their radius. Under such situations, their atmosphere can be represented by a spherically symmetric medium to a good approximation. The polarized transfer equation for a 1D spherically symmetric atmosphere in divergence form is given by

$$\mu\frac{\partial \boldsymbol{I}(r,\mu,x)}{\partial r} + \frac{(1-\mu^2)}{r}\frac{\partial \boldsymbol{I}(r,\mu,x)}{\partial \mu} = -\chi(r,x)[\boldsymbol{I}(r,\mu,x) - \boldsymbol{S}(r,\mu,x)]. \qquad (1.27)$$

Comparing Equations (1.26) and (1.27), we see that the spherical transfer equation contains an extra term involving the μ derivative of the Stokes vector. This derivative with respect to μ comes into play due to sphericity or curvature effects (clearly depicted in Figure 1.11b). Thus the transfer equation in a spherically symmetric atmosphere is a first order 'partial differential equation' involving explicitly two independent variables. Details on numerically solving such an equation are presented in Chapter 4 of this thesis. Because of the above mentioned differences, the solution of the spherical transfer equation differs from that of plane-parallel atmosphere and exhibits three important characteristics. These characteristics (discussed in detail in Kunasz and Hummer 1974a) are (i) the 'bias' in scattering toward the larger radius: This means a photon which is scattered from a certain radius will more often end its flight at a larger radius than at the smaller radius unlike in plane-parallel geometry, where the photon travels with equal probability to both larger or smaller depths. Kunasz and Hummer (1974a) show that for a homogeneous sphere (power law opacity index $\tilde{n}$=0), the bias is more important only in the inner regions, while for $\tilde{n} \geq 2$, the bias is largest in the outer regions of the sphere, constituting larger portion of the atmosphere. This is because for $\tilde{n} \geq 2$, the opacity decreases in the outward atmospheric direction, thereby increasing the photon mean free path.

(ii) The 'dilution' of diffuse radiation field: In the spherical atmosphere, for a fixed optical thickness T, and for $\tilde{n} \geq 2$, the opacity decreases as the radius increases, so that for a sufficiently large outer radius R, a substantial part of the atmosphere

remains optically thin (i.e., diluted) at all the frequencies. This dilution factor is given by (see Nagendra 1989)

$$W = \frac{1}{2}[1 - \sqrt{(1 - 1/R^2)}]. \tag{1.28}$$

Clearly for values of R even slightly exceeding unity, there is a rapid decrease in W and it gradually saturates for larger values of R. This suggests that even a small departure from plane-parallel limit leads to significant amount of weakening of the mean radiation field.

(iii) The 'peaking' of the radiation in the radial direction for larger spherical extensions: A ray emitted in any direction at a deeper region of the atmosphere, and traversing in the outward direction, makes smaller and smaller angles with respect to the radius vector (as shown in Figure 1.11b). This phenomenon which is also called 'curvature' scattering, leads to numerical difficulties in the problems requiring highly extended systems (as it demands the use of a large number of angular grid points).

The above discussed characteristics of the spherical radiative transfer will have minimum effects as $\mu \to 1$. In other words, solutions obtained from both spherical and plane-parallel geometries nearly coincide for $\mu = 1$.

In part-II of this thesis, we discuss the polarized line formation in both static and expanding spherically symmetric atmospheres.

1.5 Methods to solve the polarized radiative transfer problems

The two well established theoretical formulations of the problem of polarized line transfer are: the 'density matrix approach' and the 'scattering matrix approach'. In the following sections we briefly discuss both these approaches and present an overview of the numerical methods developed.

1.5.1 The density matrix approach

Density matrix approach is based on QED formalism. In this approach, the atomic states are described by the diagonal and non-diagonal elements of the density matrix and the atomic polarization is considered to be due to the population imbalances in the magnetic sublevels (represented by the diagonal elements) and/or due to the quantum interferences or coherences between the different magnetic sublevels (represented by the non-diagonal elements). Here the atomic polarization is represented by the irreducible spherical statistical tensors and the polarized radiation field is represented by nine irreducible radiation field tensors (see Trujillo Bueno 2001; Landi Degl'Innocenti and Landolfi 2004 for details). This approach is based on the Markovian assumption and flat spectrum approximation, namely the spectrum of the incident radiation should be flat across a frequency range which is wider than both the radiative width and the Larmor frequency of the upper level. As a result this approach is limited to CFR in scattering. In this approach, the key role is played by the statistical equilibrium equations which are coupled to the radiative transfer equation.

Bommier and Sahal-Bréchot (1978) developed the density matrix approach and derived the statistical equilibrium equations to determine the linear polarization in the case of optically thin helium D_3 line formed in prominences. This work was extended to determine the vector magnetic field including circular polarization by Landi Degl'Innocenti (1982). Landi Degl'Innocenti (1983a,b, 1984, 1985) gave a more general formalism which can describe the resonance polarization for a multi-level atom in a magnetized, and multi-dimensional optically thick medium. Landi Degl'Innocenti (1987) used the perturbation method to solve the resulting coupled system of equations for the case of Hanle effect. For more details on the density matrix approach see the monograph by Landi Degl'Innocenti and Landolfi (2004).

Trujillo Bueno and Landi Degl'Innocenti (1997) extended the operator-splitting method developed in Trujillo Bueno and Landi Degl'Innocenti (1996) for solving the NLTE Zeeman line transfer equation, to include the lower-level polarization in the absence of magnetic fields. The Jacobi based approximate lambda iteration (ALI) method of Olson *et al.* (1986) was generalized to include the scattering polarization by Trujillo Bueno and Manso Sainz (1999). For solving the scalar

NLTE problems, fast iterative techniques based on Gauss-Seidel (GS) and successive overrelaxation (SOR) schemes were developed by Trujillo Bueno and Fabiani Bendicho (1995). Trujillo Bueno and Manso Sainz (1999) and Manso Sainz and Trujillo-Bueno (1999) extended these methods respectively to the case of resonance scattering and Hanle effect in 1D, 2D, and 3D atmospheres for a two-level atom without lower-level polarization. Trujillo Bueno (1999); Manso Sainz and Trujillo Bueno (2003) and Štěpán and Trujillo Bueno (2013) have further extended these methods to handle multi-level atoms including both upper and lower-level polarization.

As already mentioned in Section 1.4.2, QED theory including both density matrix formalism and PFR has been developed recently by several authors. A lambda iteration method to solve the resulting set of equations have been developed by Bommier (2016b) for the case of Na I D_1 and D_2 lines, by del Pino Alemán *et al.* (2016) for studying the Mg II h and k lines, and del Pino Alemán *et al.* (2020) for the case of three-term atom (namely, the Mg II h and k lines and the associated subordinate UV triplet).

Most of the papers cited above consider 1D planar atmospheres for computing the emergent polarized radiation field. Asensio Ramos and Trujillo Bueno (2006) have developed the Jacobi, GS, and SOR based multi-level ALI methods to solve the NLTE polarized transfer problems based on density matrix formalism in spherically symmetric atmospheres.

1.5.2 The scattering matrix approach

Computation of the scattering contribution to the source vector in the transfer equation (1.26) or (1.27) is the central problem in the scattering approach. The traditional direct solution methods to solve the transfer equation in the unpolarized case in both planar and spherical geometries are discussed in Hubeny and Mihalas (2014, see also Peraiah 2002). An NLTE theory for the problem of resonance line polarization in the non-magnetic case was developed by Stenflo (1976), who also showed that his theory can be extended to multi-level atom. Furthermore, he gave explicit formulas for the special case of a two-level atom in spherically symmetric atmosphere. Assuming a two-level atom model and CFR, this theory

was used in Stenflo and Stenholm (1976) to explore the UV emission lines formed in both plane-parallel and spherically symmetric solar atmosphere. They solved this problem using Rybicki's core saturation method and by considering the Stokes Q parameter as a perturbation. The same problem was solved using the integral equation technique by Rees (1978) for both finite and semi-infinite plane-parallel atmosphere.

Dumont *et al.* (1977) considered the effects of type-I angle-dependent PFR on NLTE non-magnetic resonance line polarization. They used Feautrier method to solve this problem in a semi-infinite plane-parallel atmosphere accounting for Doppler frequency redistribution effects in the line core (namely, type-I PFR of Hummer 1962). The effects of type-II angle-averaged PFR were considered by Rees and Saliba (1982) who used a Feautrier method with Stokes Q treated as perturbation. For the same problem, McKenna (1984, 1985) used the moment integral equation method and also accounted for both type-II and type-III angle-averaged as well as angle-dependent PFR functions. Faurobert (1987, 1988) used a non-perturbative Feautrier method and accounted for type-II angle-averaged and angle-dependent PFR. Nagendra (1988, 1989) used a non-perturbative discrete space method together with type-II angle-averaged PFR. The non-magnetic collisional redistribution matrix derived by Domke and Hubeny (1988) was used in the polarized line transfer computations by Nagendra (1994, 1995) again using the discrete space method for solution. While all the above-cited papers used plane-parallel atmospheres, Nagendra (1988, 1989, 1994, 1995) used spherically symmetric atmospheres.

In the NLTE scattering matrix approach, the total source vector can be written as the weighted average of both line and continuum contributions, namely

$$\boldsymbol{S}(r,\mu,x) = \frac{\phi(x)\boldsymbol{S}_l(r,\mu,x) + \beta_c \boldsymbol{S}_c}{\phi(x) + \beta_c}, \tag{1.29}$$

where $\boldsymbol{S}_c = B_{\nu_0}(\mathrm{T})\boldsymbol{U}$ is the unpolarized continuum source vector, $\phi(x)$ is the profile function, and β_c is the continuous absorption parameter. For a two-level atom with infinitely sharp and unpolarized lower-level, the line source vector in the absence of magnetic field is given by

$$\boldsymbol{S}_l(r,\mu,x) \;=\; \epsilon B_{\nu_0}\boldsymbol{U} + \int_{-\infty}^{+\infty} dx' \frac{1}{2}\int_{-1}^{+1} d\mu' \frac{\mathbf{R}(x,\mu,x',\mu')}{\phi(x)}\boldsymbol{I}(\tau,\mu',x'), \tag{1.30}$$

where ϵ is the thermalization parameter. Clearly, the second part of the above equation is the NLTE part of the total source vector and is called the 'scattering integral', which involves the integration over all the incoming angles and frequencies. Using the 'hybrid approximation' of Rees and Saliba (1982) in which the frequency redistribution and polarization parts get completely decoupled, the angle-dependent redistribution matrix may be written as

$$\mathbf{R}(x, \boldsymbol{n}, x', \boldsymbol{n}') = R(x, \boldsymbol{n}, x', \boldsymbol{n}')\mathbf{P}_{\rm R}(\boldsymbol{n}, \boldsymbol{n}'), \tag{1.31}$$

where $\mathbf{P}_{\rm R}(\boldsymbol{n}, \boldsymbol{n}')$ is the Rayleigh phase matrix (Chandrasekhar 1950). For resonance lines, $\mathbf{R}(x, \boldsymbol{n}, x', \boldsymbol{n}')$ is usually given by type-II PFR function of Hummer (1962). To avoid the use of computationally expensive angle-dependent function, one usually assumes the angle-averaged form for $R(x, \boldsymbol{n}, x', \boldsymbol{n}')$. Thus, according to the hybrid approximation of Rees and Saliba (1982), we can re-write Equation (1.31) as

$$\mathbf{R}(x, \boldsymbol{n}, x', \boldsymbol{n}') = R(x, x')\mathbf{P}_{\rm R}(\boldsymbol{n}, \boldsymbol{n}'). \tag{1.32}$$

Here $R(x, x') = \phi(x)\phi(x')$ for CFR and $R(x, x') = R_{\rm II}(x, x')$ for PFR. Furthermore, in a planar or spherically symmetric non-magnetic atmospheres the radiation field is axisymmetric and hence $\mathbf{P}_{\rm R}(\boldsymbol{n}, \boldsymbol{n}')$ can be replaced by $\mathbf{P}_{\rm R}(\mu, \mu')$, so that Equation (1.32) can be re-written as

$$\mathbf{R}(x, \mu, x', \mu') = R(x, x')\mathbf{P}_{\rm R}(\mu, \mu'). \tag{1.33}$$

We use this approximation in Chapters 4–7.

Stenflo (1978) developed the NLTE theory for weak field Hanle effect applicable to the case of multi-level atoms, including also the effects of collisions. He derived the Hanle phase matrix in the magnetic reference frame (magnetic field is along the z-axis, see Figure 2.3). Landi Degl'Innocenti and Landi Degl'Innocenti (1988) obtained the analytical expressions for the Hanle phase matrix elements for a more general geometry (namely, magnetic field inclined to the z-axis, see Figure 2.4). Based on the fact that the Hanle effect is operative only in the line core, Faurobert-Scholl (1991) introduced a 1D-domain based Hanle redistribution matrix to solve

the Hanle PFR transfer problems, namely

$$\mathbf{R}(x,\boldsymbol{n},x',\boldsymbol{n}',\boldsymbol{B}) = R_{\rm II}(x,x') \times \begin{cases} \mathbf{P}_{\rm H}(\boldsymbol{n},\boldsymbol{n}',\boldsymbol{B}) & \text{for } |x| < x_c, \\ \mathbf{P}_{\rm R}(\boldsymbol{n},\boldsymbol{n}') & \text{for } |x| > x_c, \end{cases} \tag{1.34}$$

where $\mathbf{P}_{\rm H}(\boldsymbol{n},\boldsymbol{n}',\boldsymbol{B})$ is the Hanle phase matrix (with $\boldsymbol{B}$ denoting the vector magnetic field) and x_c is the cut-off frequency. Bommier (1997b) derived the correct form of Hanle redistribution matrix including collisions. She provided a 2D-domain based PFR matrices, referred to as "Approximation II" (which uses Hummer's angle-dependent PFR functions) and "Approximation III" (which uses the corresponding angle-averaged redistribution functions). In Chapter 8, we use the Approximation III of Bommier (1997b) for solving the polarized radiative transfer equation in the presence of weak fields (Hanle effect) in spherically symmetric expanding media.

The above mentioned numerical methods are computationally expensive requiring considerable CPU time and memory. A novel iterative method based on the operator perturbation was developed by Cannon (1973) for the scalar transfer problem. This method is called Accelerated or Approximate Lambda Iteration (ALI) method (see reviews by Hubeny 1992, 2003; Hubeny and Mihalas 2014). It was Olson *et al.* (1986) who demonstrated that the diagonal of the actual Lambda operator provides an optimum choice for the approximate Lambda operator. This ALI method was extended to include the polarization by Faurobert-Scholl *et al.* (1997) for the case of resonance scattering with CFR in a 1D axisymmetric planar medium. This method is called PALI (polarized-ALI). The PALI method was extended to include PFR effects by Paletou and Faurobert-Scholl (1997). Nagendra *et al.* (1998) developed the PALI method to handle Hanle effect with CFR, which was extended to include a 1D-domain based PFR by Nagendra *et al.* (1999) and Nagendra *et al.* (2000). Fluri *et al.* (2003) included the 2D-domain based PFR (given by Approximation III of Bommier 1997b) in the PALI method. Sampoorna *et al.* (2008) extended the PALI method to handle non-domain based Hanle PFR matrix (given by Approximation-I of Bommier 1997b). They used the decomposition technique of Frisch (2007). PALI method has been generalized to include angle-dependent PFR in Sampoorna *et al.* (2011) and Supriya *et al.* (2012). PALI method with angle-averaged PFR matrices corresponding to two-level atom with

and without HFS, and two-term atom without HFS have been developed in Sampoorna and Trujillo Bueno (2010); Smitha *et al.* (2011, 2012, 2013) and Belluzzi and Trujillo Bueno (2014). For a complete review on the development of PALI method see Nagendra (2003, 2019, 2014, see also Nagendra and Sampoorna 2009).

All the papers cited above consider 1D planar atmospheres. For multidimensional media including angle-averaged PFR the relevant PALI method is presented in Anusha and Nagendra (2011); Anusha *et al.* (2011b). A Lambda iteration method to solve the polarized transfer equation in spherical geometry for molecular lines formed with CFR is presented in Milić and Faurobert (2012). In part-II of this thesis, we extend the PALI method to solve the polarized transfer equation in spherically symmetric expanding atmospheres in both absence and presence of weak magnetic fields, and including angle-averaged PFR.

1.5.3 Observer's and comoving frame methods: a brief historical background

It is well known that the solar and stellar atmospheres are dynamic due to the presence of macroscopic velocity fields especially in their outer layers. These velocity fields strongly affect the polarized line profiles formed in these regions. Therefore, including the velocity fields in the polarized transfer problem is necessary. A straight forward method to solve this problem is the observer's frame method. However, due to angle and frequency coupling involved in the problem, the observer's frame method quickly becomes computationally very expensive particularly when large velocity fields need to be accounted for. Alternatively, the effects of velocity fields can be handled without much computational difficulty when comoving frame (CMF) method is used. The advantages of CMF over observer's frame is listed for e.g., in Noerdlinger and Rybicki (1974); Mihalas (1978) and Hubeny and Mihalas (2014) for the unpolarized case.

Sengupta (1993) and Rangarajan (1997) used the discrete space theory (Peraiah 1984, see also Peraiah 2002) to study the effects of a velocity field on resonance line polarization. While the former solved the relevant problem in the CMF, the latter used the observer's frame. Carlin *et al.* (2012, 2013) used the density matrix approach in the observer's frame to study the formation of scattering polarization

of Ca II IR triplet in hydrodynamical models of the solar chromosphere. Carlin and Asensio Ramos (2015) presented forward modeling approach to forward scattering Hanle effect in Ca II IR triplet using a realistic magneto-hydrodynamical simulations. All these works considered CFR in scattering. Nagendra (1996) developed the CMF method using the discrete space theory to solve the problem of resonance line polarization including PFR and velocity fields. Sampoorna and Nagendra (2015a) considered the same problem, but taking also into account the effects of a weak magnetic field. They solved this problem in the observer's frame using a PALI method. Sampoorna and Nagendra (2015b, 2016) developed a CMF-PALI method to solve the above mentioned problem, including both monotonic and non-monotonic velocity fields. In all the above cited papers a plane-parallel geometry was used for solving this problem.

A wide variety of the astrophysical objects show evidence of outflowing gas in their extended atmospheres. These extensions can be treated using the spherically symmetric geometry to a first approximation. There are several methods to treat the radiative transfer in the static spherical atmospheres since the beginning of the 19th century (to name a few: McCrea 1928; Chandrasekhar 1934; Kosirev 1934; Wilson and Sen 1965; Chapman 1966; Hummer and Rybicki 1971; Cassinelli and Hummer 1971; Grant and Peraiah 1972; Peraiah and Grant 1973; Kunasz and Hummer 1974a; Nagendra 1988, 1989, 1994, 1995; Asensio Ramos and Trujillo Bueno 2006; Cernicharo *et al.* 2006; Daniel and Cernicharo 2008; Anusha *et al.* 2009 etc.). McCrea and Mitra (1936) were the first to correctly formulate the line transfer problem for optically thick atmospheres with radial velocity fields. The first approximate solutions were then provided by Chandrasekhar (1945b,a). Noerdlinger and Scargle (1972) gave the analytic solution for transfer in expanding spherical atmospheres with coherent scattering in the CMF. Kunasz and Hummer (1974b) developed a direct numerical solution method for the linear system of equations that are obtained by generalizing the method of Rybicki (1971, namely, the modified Feautrier's finite difference method). They solved the scalar transfer problem in spherically symmetric atmosphere with radial velocity fields in the observer's frame. Mihalas *et al.* (1975) also used a Feautrier's finite differencing scheme with Rybicki-type elimination (Rybicki 1971) along with a frequency-by-frequency elimination method to solve the partial differential equations representing the unpolarized radiation field in CMF. Baschek *et al.* (1997)

presented exact analytical solutions of the transfer equation for differentially moving plane-parallel and spherical geometries, including the general 3D case of arbitrary velocity fields. Hauschildt (1992); Hauschildt *et al.* (1994) used the ALI method in the CMF to solve the spherical transfer equation with fully relativistic monotonic velocity fields. Hauschildt and Baron (2004) extended this work by introducing a second order discretization scheme for the wavelength derivative. Baron and Hauschildt (2004) further extended this CMF-ALI method to include fully relativistic non-monotonic velocity fields.

Most of the papers cited above (excepting those of Nagendra) considered CFR in line scattering. The effects of angle-averaged PFR on the solution of unpolarized transfer in spherically symmetric atmospheres with radial velocity flows were considered by Mihalas *et al.* (1976b). They solved this problem in the CMF using a Feautrier's elimination scheme together with variable Eddington-factor method. We remark that the review of the literature presented in this section is not complete and we refer the reader to Hubeny and Mihalas (2014) for a detailed review of the subject. Furthermore, most of the above cited papers considered unpolarized radiation field. In part-II of this thesis, we extend the CMF-ALI method of Hauschildt and Baron (2004) to include resonance polarization (hence we call it CMF-PALI) and the effects of angle-averaged PFR in spherically symmetric geometry with and without weak magnetic fields (Hanle effect).

1.6 Outline of the thesis

In this thesis we aim at developing the theoretical tools required for the determination of the solar magnetic fields using polarized spectral line formation theory. For this we divide the thesis into two parts. Chapters 2 and 3 constitute Part-I of the thesis and deals with developing the scattering theory for M1 transitions and applying the same to study the forbidden emission lines formed in solar coronal conditions. Chapters 4–8 constitute Part-II of the thesis which is dedicated to develop the numerical techniques to solve the problem of polarized line formulation in spherically symmetric moving atmospheres and apply them to study the polarized line profiles of optically thick permitted (E1) lines in both the absence and presence of weak magnetic fields.

Outline on part-I of the thesis

In Chapter 2, we develop a theoretical framework to handle the forbidden lines arising from M1 transition and formed in any diffuse astrophysical media such as solar corona, in the presence of magnetic fields. In particular, we derive the Hanle-Zeeman scattering matrix for M1 transitions. The Einstein A coefficient for the forbidden lines is nearly 10^6 times smaller than that for the permitted lines. Therefore, the magnetic splitting between the excited atomic levels is much larger than the natural line width of each level, even for very weak magnetic fields. Thus, the forbidden lines remain in the saturated Hanle regime, even for field strengths of few mG. Therefore, these lines are not sensitive to the variation of field strengths. However, the linear polarization produced by the scattering in these lines are very sensitive to the field orientations. Thus, Hanle effect in forbidden lines can be effectively used for diagnosing the topology of coronal magnetic fields. The earlier formulation of the problem of scattering on forbidden lines in magnetic fields is limited only to the regime of saturated Hanle effect. Therefore, here we aim at presenting a new alternative formulation of the required scattering theory that covers the entire field strength regime (namely, the Hanle regime: field strength of few μG, the saturated Hanle regime: few mG $\lesssim B \sim$ 200 G, the Hanle-Zeeman regime: 250 G $\lesssim B <$ 1 kG, and the pure Zeeman regime: $B \gtrsim$ 1 kG).

The theoretical formalism developed in Chapter 2, is used in Chapter 3 to study the effects of density distributions, magnetic field configurations, and velocity fields on the emergent Stokes profiles of the forbidden line. We use the [Fe XIII] 10747 Å coronal forbidden line for these studies. Theses ions present in the corona are illuminated by the flat limb-darkened radiation coming from the photosphere. Also the Stokes signal received at the Earth is affected by the density variation along the LOS. Therefore here we describe the procedures to conduct the integration over the solid angle of incident cone of radiation and also the LOS integration to obtain the polarized profiles and study their dependence on the above mentioned physical quantities.

Outline on part-II of the thesis

Mass loss is common in most of the astrophysical objects due to the presence of velocity fields in the extended regions of their atmospheres. The polarized spectral lines formed in such regions strongly get affected in both amplitude and shape by

the presence of velocity fields (which produces Doppler shift, aberration of photons, and also gives rise to advection) and also by the curvature of the atmosphere. Therefore, in part-II of this thesis, we consider the problem of polarized line transfer in a spherically symmetric static and expanding atmospheres. Our aim here is to develop numerical techniques to solve this problem including velocity fields and also magnetic fields.

In Chapter 4, we develop modern iterative techniques based on operator perturbation to solve the non-magnetic polarized transfer equation in a static spherically symmetric atmosphere. In the literature the polarized accelerated lambda iteration (PALI) method is mostly used with Jacobi iterative scheme, which has a slower convergence rate. However, these are fast iterative techniques based on Gauss-Seidel (GS) and successive overrelaxation (SOR) that are known to be superior than the traditional Jacobi iterative scheme. We describe in detail the numerical implementation of the Jacobi, GS and SOR techniques for the problem at hand and study their convergence behavior in the presence of both angle-averaged PFR and CFR scattering mechanisms.

In Chapter 5, we consider the problem of non-magnetic polarized line transfer in spherically symmetric atmospheres in the presence of radial velocity fields. We describe both the observer's frame and comoving frame (CMF) methods to solve the problem under consideration. We describe in detail the CMF-PALI method based on Jacobi, GS, and SOR schemes and the formal solution in the CMF. We study the convergence behavior of all these schemes in the presence of velocity fields for both CFR and angle-averaged PFR. We also present the convergence behavior of CMF-PALI method for varying optical thickness (T) and extension (R) with PFR.

In Chapter 6 and 7 we discuss the numerical solutions to the problem of polarized line formation in spherically symmetric static and expanding non-magnetic atmospheres. We interpret the emergent polarized line profiles formed in both static and moving atmospheres in the presence of both CFR and PFR using contribution functions and Stokes source vector (Chapter 6). In Chapter 6, we also study the center-to-limb variation (CLV) of the emergent polarized line profiles relative to the plane-parallel atmosphere. We also discuss the dependence of polarized line profiles on the variation of extension R of the spherical atmosphere.

The atmospheric and atomic model parameters are varied in Chapter 7, one at a time (keeping the other parameters as constants) to study the dependence of the linearly polarized line profiles on the model parameters for both static and moving atmospheres.

The Jacobi based CMF-PALI method developed in Chapter 5 is extended to include the weak magnetic fields in Chapter 8. Unlike the non-magnetic case the physical quantities involved in the problem now become radiation field azimuth dependent due to Hanle effect. We apply the core-wing method of Fluri *et al.* (2003) developed for approximation-III of Bommier (1997b) (representing the angle-averaged PFR) in the presence of weak magnetic fields. We also discuss the emergent polarized line profiles formed in the presence of both magnetic and velocity fields for the cases of CFR and PFR.

Chapter 9 summarizes the thesis and also presents the possible future prospects of the work presented in this thesis.

Part-I

Scattering Theory for Magnetic Dipole (M1) Transitions

Chapter 2

Hanle Zeeman Scattering Matrix for M1 Transitions[1]

An overview

The polarization of the light scattered by the coronal ions is influenced by the anisotropic illumination from the photosphere and the magnetic field structuring in the solar corona. The properties of the coronal magnetic fields can be well studied by understanding the polarization properties of coronal forbidden emission lines which arise from magnetic dipole (M1) transitions in the highly ionized atoms present in the corona. We present the classical scattering theory of the forbidden lines for a more general case of arbitrary-strength magnetic fields. We derive the scattering matrix for M1 transitions using the classical magnetic dipole model of Casini and Lin (2002) and applying the scattering matrix approach of Stenflo (1998). We consider a two-level atom model and neglect collisional effects. The scattering matrix so derived is useful for studying the Stokes profiles formed in coronal conditions in those regions where the radiative excitations dominate over collisional excitations. We discuss the nature of the scattering matrix for M1 transitions and compare it with that for the E1 transitions.

[1]The contents of this chapter are based on the publication: Megha *et al.* (2017)

2.1 Introduction

The plasma β values being low in the inner corona of the Sun suggests that the magnetic fields emerging from subphotospheric layers control the dynamics and heating of the corona. Our ability to determine the properties of the coronal magnetic fields remains severely limited because the fields in the quiet-Sun corona are intrinsically weak. The influence of these fields on the electromagnetic radiation that is emitted by the coronal plasma is accordingly weak. One of the best ways to determine the properties of coronal magnetic fields is to study the polarization properties of coronal forbidden emission lines that are produced as the result of an anisotropic excitation of the ions that are present in the corona (see Figure 2.1). The quest for understanding the origin and formation of coronal emission line polarization dates back to the early part of the 20th century. The first attempt to measure the polarization in coronal lines, especially the green forbidden emission line (5303 Å), was made by Wood (1905). He reported that the polarization is lower than 1%. Öhman (1929) was the first to mention that the coronal lines might be polarized, but there was lack of information regarding the origin of the polarization in these lines. The first theoretical analysis of coronal emission line polarization was given by Charvin (1965, see also Hyder 1965), who studied the detailed interaction of anisotropic photospheric light with the radiating ions and showed how the linear polarization is related to the direction of the magnetic field projected onto the plane-of-sky (POS). House (1972) represents an important landmark in the theoretical calculation of the polarization of coronal forbidden lines. His treatment was restricted to pure scattering. Sahal-Bréchot (1974, 1977) and House (1977) included the collisional terms in the statistical equilibrium equation for the radiating atom. Based on the statistical equilibrium solutions of Sahal-Bréchot (1977) and House (1977) for the [Fe XIII] 10747 Å line, a simple analytic form of the line-of-sight (LOS) integrated Stokes vector was deduced by Querfeld (1982) which shows an explicit dependence of the Stokes vector on coronal electron density, magnetic field direction, and temperature. However, the circular polarization was neglected in the above-mentioned theoretical works. Casini and Judge (1999) provided a consistent theory treating both linear and circular polarizations of M1 lines. They also gave a generalized magnetograph formula for determining the longitudinal component of the vector magnetic field. Based on this theory, Judge and Casini (2001) developed a diagnostic code called Coronal

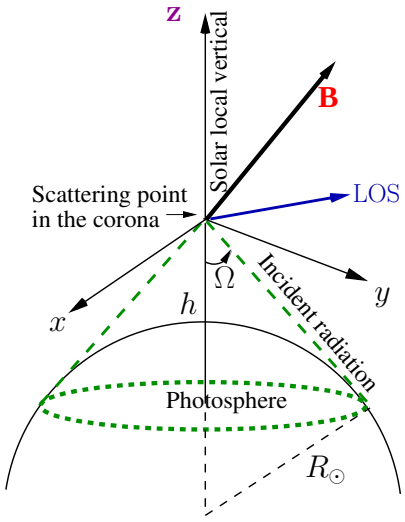

FIGURE 2.1: Geometry describing the anisotropic illumination of ions in the corona by the photospheric radiation field.

Line Emission (CLE), which is employed by Gibson *et al.* (2016) in a community resource toolset, namely FORWARD. It is extensively used for the magnetic field modeling and other studies of the solar corona.

A classical oscillator model for the magnetic dipoles was proposed by Casini and Lin (2002). Their model is based on a 3D L–C circuit analogy, which considers the magnetic field component of the incident radiation that induces the magnetic dipole (M1) transitions. Based on this model, Lin and Casini (2000) derived the polarization properties of the coronal forbidden emission lines in the collisionless regime. They particularly considered the case of the strong-field (or saturated Hanle) regime wherein the Larmor frequency is much larger than the natural width of the line. Their classical result coincides with the quantum mechanical result derived in Casini and Judge (1999) in the restricted case of the $J = 0 \rightarrow 1 \rightarrow 0$ transition. Stenflo (1998, hereafter called S98), presented a general approach to derive the Hanle-Zeeman scattering matrix for the electric dipole (E1) transitions. In the present chapter, starting from the solution of the classical damped M1 oscillator (Casini and Lin 2002), we derive the Hanle-Zeeman scattering matrix following the approach of S98. We consider coherent scattering in arbitrary-strength magnetic fields and a two-level atom with the $J = 0 \rightarrow 1 \rightarrow 0$ M1 transition. The scattering matrix for the coronal forbidden emission lines is retrieved from this general theory as a limiting case (strong-field limit). The effects of collisions and multilevel coupling are neglected in our formalism. Therefore the present approach

can be applied only to those regions in the corona where radiative excitations of ions are dominant.

In Sections 2.2 and 2.3 we derive the Jones scattering matrix and Mueller scattering matrix using the S98 approach. In Section 2.4 the Hanle-Zeeman scattering matrix for M1 transitions derived using S98 approach is expressed in terms of the irreducible spherical tensors of Landi Degl'Innocenti (1984) and the generalized profile functions defined by Landi Degl'Innocenti *et al.* (1991). In Section 2.5 we discuss the important similarities and differences between the E1 and M1 transitions using the polarization diagram. In Section 2.6 we present the concluding remarks.

2.2 Jones scattering matrix for M1 transitions

Here we derive the scattering amplitudes for the M1 transitions using the Jones calculus. For this we use a classical model for the damped, magnetic dipole oscillator proposed by Casini and Lin (2002). In this model they have considered a plane, circular L–C circuit with no applied electromotive force (EMF) that is irradiated by a monochromatic electromagnetic plane wave with its magnetic field component varying as $\boldsymbol{B}_{\rm in}(t) = \boldsymbol{B}_0 \exp(-{\rm i}\omega{\rm t})$. Here the dipole approximation is introduced by assuming that the radius of the L–C circuit r is much smaller than the wavelength of the incident radiation ($r \ll 2\pi c/\omega$). Because the net magnetic flux through the circuit includes flux due to radiation reaction current, the circuit behaves as an L–R–C circuit (see Figure 2.2). Using the theory of quasi-stationary currents (see Casini and Lin 2002 for details), the idea of L–R–C circuit is extended to three dimensions to construct a classical M1 oscillator model to represent an atomic system. Thus the atomic system is now schematized by considering the three atomic M1 oscillators describing the forbidden transition, $J = 0 \rightarrow 1 \rightarrow 0$, as three plane circular L–R–C circuits, oscillating orthogonally (so that the mutual inductance between the circuits can be neglected), and rigidly oriented with respect to some Cartesian basis $\boldsymbol{e}_x, \boldsymbol{e}_y, \boldsymbol{e}_z$. A homogeneous stationary external magnetic field $\boldsymbol{B} = B\boldsymbol{e}_z$ is applied to this 3D physical system. As a consequence, each circuit in the atomic model will generally be subjected to a torque. After some algebra, the complete oscillator equation for the classical damped M1 oscillator is

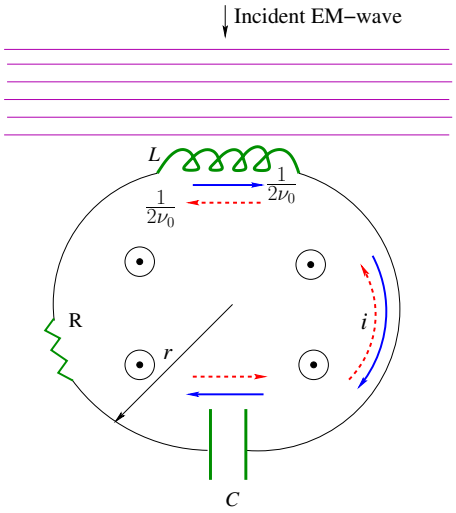

FIGURE 2.2: A plane circular L–R–C circuit irradiated by a monochromatic electromagnetic plane wave. This circuit represents a one-dimensional M1 oscillator when we consider the interaction of the circuit with the magnetic field component of the electromagnetic radiation incident from the top. The applied external magnetic field is perpendicular to the plane of the paper.

obtained as

$$\ddot{\boldsymbol{m}} + \gamma\dot{\boldsymbol{m}} + 2\omega_B\,\dot{\boldsymbol{m}} \times \boldsymbol{e}_z + \omega_0^2\boldsymbol{m} = \frac{\omega^2\sigma^2}{c^2 L}\boldsymbol{B}_{\rm in}, \tag{2.1}$$

where $\boldsymbol{m}$ is the magnetic dipole associated with the three circuits, L is the inductance, $\gamma = \mathrm{R}/L$ is the damping constant with R being the resistance, σ is the area of the circuit, $\omega_0 \approx 1/LC$ is the characteristic resonance frequency of the L–R–C circuit, and ω_B is the Larmor frequency. This equation is analogous to the corresponding damped electric dipole oscillator equation given in Equation (3.33) of Stenflo (1994, hereafter called S94, see also Equation (1.15)). The only difference is that the driving force in Equation (2.1) for the magnetic dipole is the magnetic vector component of the incident electromagnetic radiation, while it is the electric vector component for the electric dipole oscillator. Equation (2.1) decouples in the basis of spherical unit vectors, and the resulting solution in component form is given by

$$m_q(\omega) = \frac{\omega^2\sigma^2}{c^2 L}\,\frac{B_q^{\rm in}}{\omega_0^2 - \omega^2 - 2q\omega\omega_B - \mathrm{i}\gamma\omega}\,, \tag{2.2}$$

where $q = 0, \pm 1$ and $B_q^{\rm in}$ is the spherical component of the incident radiation. Hereafter, we refer to the magnetic field of the electromagnetic radiation as the radiation magnetic field. For a spectral line, $\omega \simeq \omega_0$ is satisfied and therefore

$| \omega_0 - \omega | \ll \omega_0$. This condition simplifies the resonant term in Equation (2.2) as

$$\frac{1}{\omega_0^2 - \omega^2 - 2q\omega\omega_B - \mathrm{i}\gamma\omega} \approx \frac{1/2\omega_0}{[\omega_0 - \omega - q\omega_B - \mathrm{i}\gamma/2]}\,. \tag{2.3}$$

Following Bommier and Stenflo (1999), we now define the area normalized profile function Φ_q as

$$\Phi_q = \frac{2/\mathrm{i}}{\omega_0 - \omega - q\omega_B - \mathrm{i}\gamma/2}. \tag{2.4}$$

Thus Equation (2.2) can be rewritten as

$$m_q(\omega) \sim \Phi_q B_q^{\mathrm{in}}. \tag{2.5}$$

We denote the spherical components of the scattered radiation magnetic field as B_q^{out}, which is proportional to the spherical components of the magnetic dipole vector amplitude m_q. Following S94, we can write $B_q = \sum_\alpha \varepsilon_q^\alpha B_\alpha$, where $\alpha = 1, 2$ are the linear polarization basis vectors and ε_q^α are the spherical vector components of the linear unit vector $\boldsymbol{e}_\alpha$. Thus the scattered radiation magnetic field can now be written as

$$B_\alpha^{\mathrm{out}} = \sum_q \varepsilon_q^{\alpha *} B_q^{\mathrm{out}} \sim \sum_q \varepsilon_q^{\alpha *} \Phi_q B_q^{\mathrm{in}}. \tag{2.6}$$

Simplifying further by a substitution for $B_q^{\mathrm{in}} = \sum_\beta \varepsilon_q^\beta B_\beta^{\mathrm{in}}$, we obtain

$$B_\alpha^{\mathrm{out}} = \sum_\beta w_{\alpha\beta}^B B_\beta^{\mathrm{in}}\,, \tag{2.7}$$

where

$$w_{\alpha\beta}^B = \sum_q \varepsilon_q^{\alpha *} \varepsilon_q^\beta \Phi_q\,, \tag{2.8}$$

are the components of the 2×2 Jones scattering matrix $\boldsymbol{w^B}$, which describes the interaction of radiation with the medium. The quantity $w_{\alpha\beta}^B$ given above has exactly the same form as that for the electric dipole transitions. However, it is derived considering the radiation magnetic field. Because the Stokes parameters are defined on the basis of the electric field components of the radiation, we also transform Equation (2.7) to the same basis. This can be achieved by using the relation between the radiation electric and magnetic field vectors, which is given by $\boldsymbol{E} = \boldsymbol{B} \times \hat{\boldsymbol{r}}$. Thus the relation between the radiation electric and magnetic

field vectors ($\boldsymbol{B} = -E_2\boldsymbol{e}_1 + E_1\boldsymbol{e}_2$) can be written in matrix form as

$$\boldsymbol{E} = \boldsymbol{\alpha}\boldsymbol{B} \;\; ; \;\; \boldsymbol{B} = \boldsymbol{\alpha}^\dagger \boldsymbol{E}, \tag{2.9}$$

where

$$\boldsymbol{\alpha} = \begin{pmatrix} 0 & 1 \\ -1 & 0 \end{pmatrix} \quad ; \quad \boldsymbol{\alpha}^\dagger = \begin{pmatrix} 0 & -1 \\ 1 & 0 \end{pmatrix}. \tag{2.10}$$

Using the above relation, Equation (2.7) can be rewritten in matrix form as

$$\boldsymbol{E}^{\rm out} = \boldsymbol{w}^{\boldsymbol{E}} \boldsymbol{E}^{\rm in}, \tag{2.11}$$

where

$$\boldsymbol{w}^{\boldsymbol{E}} = \boldsymbol{\alpha}\boldsymbol{w}^{\boldsymbol{B}}\boldsymbol{\alpha}^\dagger, \tag{2.12}$$

which is now defined using the radiation electric field vector.

2.3 Scattering matrix for M1 transitions

The Mueller scattering matrix $\boldsymbol{M}^{\rm M1}$, which describes the transformation from incident to the scattered Stokes vectors, is given by

$$\boldsymbol{M}^{\rm M1} = \boldsymbol{T}\boldsymbol{W}^{\rm M1}\boldsymbol{T}^{-1}, \tag{2.13}$$

where

$$\boldsymbol{W}^{\rm M1} = \boldsymbol{w}^{\boldsymbol{E}} \otimes \boldsymbol{w}^{\boldsymbol{E}*}. \tag{2.14}$$

The matrices $\boldsymbol{T}$, and $\boldsymbol{T}^{-1}$ are defined in Equation (1.13). The tensor product in Equation (2.14) has the same form as given in Equation (10) of S98 (see also Equation (1.12)), but with $\boldsymbol{w}$ there replaced by $\boldsymbol{w}^{\boldsymbol{E}}$ defined in Equation (2.12). In terms of the elements of $\boldsymbol{w}^{\boldsymbol{B}}$, the tensor product in Equation (2.14) can be written

as

$$\boldsymbol{W}^{\mathrm{M1}} = \begin{pmatrix} w^B_{22}w^{B*}_{22} & -w^B_{22}w^{B*}_{21} & -w^B_{21}w^{B*}_{22} & w^B_{21}w^{B*}_{21} \\ -w^B_{22}w^{B*}_{12} & w^B_{22}w^{B*}_{11} & w^B_{21}w^{B*}_{12} & -w^B_{21}w^{B*}_{11} \\ -w^B_{12}w^{B*}_{22} & w^B_{12}w^{B*}_{21} & w^B_{11}w^{B*}_{22} & -w^B_{11}w^{B*}_{21} \\ w^B_{12}w^{B*}_{12} & -w^B_{12}w^{B*}_{11} & -w^B_{11}w^{B*}_{12} & w^B_{11}w^{B*}_{11} \end{pmatrix}. \tag{2.15}$$

Comparing Equation (1.12) with Equation (2.15), one can clearly see the role played by $\boldsymbol{\alpha}$ and $\boldsymbol{\alpha}^{\dagger}$ (namely the change of signs as well as the changed positions of the elements in the matrix $\boldsymbol{W}^{\mathrm{M1}}$ with respect to the matrix $\boldsymbol{W}$ defined in Equation 1.12). Since $\boldsymbol{w^B}$ is identical to $\boldsymbol{w}$ corresponding to E1 transitions (namely that of S98), following S98 (see his Equation (12)), we define

$$\begin{aligned} A &= \mid w^B_{11} \mid^2; & B &= \mid w^B_{22} \mid^2; \\ C &= \mid w^B_{12} \mid^2; & D &= \mid w^B_{21} \mid^2; \\ a &= w^B_{11}w^{B*}_{22}; & b &= w^B_{11}w^{B*}_{12}; \\ c &= w^B_{11}w^{B*}_{21}; & d &= w^B_{12}w^{B*}_{21}; \\ e &= w^B_{12}w^{B*}_{22}; & f &= w^B_{21}w^{B*}_{22}. \end{aligned} \tag{2.16}$$

With these quantities the Mueller matrix for the magnetic dipole transitions can be organized as

$$\boldsymbol{M}^{\mathrm{M1}} = \boldsymbol{M}^{\mathrm{M1}}_{Q} + \Re\left(\boldsymbol{M}^{\mathrm{M1}}_{U}\right) + \Im\left(\boldsymbol{M}^{\mathrm{M1}}_{V}\right), \tag{2.17}$$

where

$$\boldsymbol{M}^{\mathrm{M1}}_{Q} = \frac{1}{2}\begin{pmatrix} A+B+C+D & -(A-B-C+D) & 0 & 0 \\ -(A-B+C-D) & A+B-C-D & 0 & 0 \\ 0 & 0 & 0 & 0 \\ 0 & 0 & 0 & 0 \end{pmatrix},$$

$$\boldsymbol{M}^{\mathrm{M1}}_{U} = \begin{pmatrix} 0 & 0 & -(b+f) & 0 \\ 0 & 0 & b-f & 0 \\ -(c+e) & c-e & a+d & 0 \\ 0 & 0 & 0 & a-d \end{pmatrix},$$

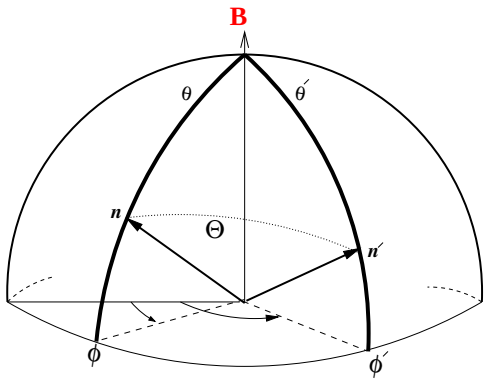

FIGURE 2.3: Geometry of scattering with magnetic field along the Z-axis: the magnetic reference frame (MRF). Incident ray $\boldsymbol{n}'$ with polar angles (θ', ϕ') is scattered into an outgoing ray $\boldsymbol{n}$ with polar angles (θ, ϕ). The scattering angle is denoted by Θ.

$$\boldsymbol{M}_V^{\rm M1} = \begin{pmatrix} 0 & 0 & 0 & -b-f \\ 0 & 0 & 0 & -(-b+f) \\ 0 & 0 & 0 & -(-a+d) \\ c+e & -(c-e) & -(a+d) & 0 \end{pmatrix}. \tag{2.18}$$

Comparing the elements of $\boldsymbol{M}^{\rm M1}$ given in Equation (2.18) with the corresponding elements in Equation (14) of S98, we see that the Mueller matrix for magnetic dipole transitions is exactly the same as that for the electric dipole transitions, except for the change in the signs of certain elements. These elements that have undergone sign change are $\boldsymbol{M}^{\rm M1}_{Q,12}$, $\boldsymbol{M}^{\rm M1}_{Q,21}$, $\boldsymbol{M}^{\rm M1}_{U,13}$, $\boldsymbol{M}^{\rm M1}_{U,31}$, $\boldsymbol{M}^{\rm M1}_{V,24}$, $\boldsymbol{M}^{\rm M1}_{V,42}$, $\boldsymbol{M}^{\rm M1}_{V,34}$, and $\boldsymbol{M}^{\rm M1}_{V,43}$. The analytical form of the Hanle-Zeeman scattering matrix for $J = 0 \rightarrow 1 \rightarrow 0$ M1 transition in the magnetic reference frame (MRF, see Figure 2.3) can be derived following Section 4 of S98. Indeed, the expressions turn out to be identical to those given in Section 4 of S98, with the sign changes already mentioned above. All the special cases discussed in Section 5 of S98 can also be recovered for the M1 transitions. In the following subsection we particularly discuss the strong-field regime of the Hanle effect, which is of relevance to coronal forbidden emission lines.

2.3.1 Saturated Hanle regime

For the coronal forbidden lines, the Einstein spontaneous emission coefficient A is very small (typically, $A \sim 10\,\mathrm{s}^{-1}$). Therefore excited states of these forbidden lines have extraordinarily long lifetimes, due to which the natural line widths of these lines are very small compared to the Zeeman splitting even for micro gauss fields. As the expected field strengths for the quiet-Sun corona are much stronger ($\sim 10\,\mathrm{G}$), for these lines $\omega_B \gg A$. Thus we are always in the saturated Hanle regime (or strong-field regime with respect to the traditional Hanle effect) in forbidden lines in the solar corona. Under this condition the separated magnetic substates of the upper level do not interfere and scatter the incident radiation incoherently (independently). The tensor product defined in Equation (2.14) has terms of the type $w^B_{\alpha\beta} w^{B*}_{\alpha'\beta'}$. This involves a coherent summation over q, q' (see Equation (2.8)). In the saturated Hanle regime we neglect the interference terms. In other words, an incoherent summation is performed ($q = q'$) when forming the tensor product. Thus the Mueller matrix for the coronal forbidden lines under the saturated Hanle regime is given by

$$\boldsymbol{M}^{\mathrm{M1}}_{\mathrm{corona}}/H_0 = \boldsymbol{E}_{11} + \frac{3}{8}\begin{pmatrix} \frac{1}{3}(1-3\mu^2)(1-3\mu'^2) & -(1-3\mu^2)(1-\mu'^2) & 0 & 0 \\ -(1-\mu^2)(1-3\mu'^2) & 3(1-\mu^2)(1-\mu'^2) & 0 & 0 \\ 0 & 0 & 0 & 0 \\ 0 & 0 & 0 & 4\mu\mu' \end{pmatrix}. \quad (2.19)$$

In the above equation $\mu = \cos\theta$, $\mu' = \cos\theta'$, where θ and θ' are the colatitudes of the scattered and incident radiation (see Figure 2.3). When deriving Equation (2.19), the reference direction for positive Stokes Q is chosen to be in the meridian plane containing the magnetic field and the propagation direction. Since the Zeeman splitting for the coronal forbidden lines is much smaller than the Doppler width, the Voigt functions for $q = \pm 1$ are taken as H_0 (namely, $H_\pm \approx H_0$). The notations used in the above expression are the same as those in S98. From Equation (2.19) it is clear that the linear polarization of the scattered radiation no longer depends on the strength of the magnetic field.

For an unpolarized beam of light incident on a point source, the fractional polarization (Q/I) resulting from a single scattering is given by (see Equation (2.19))

$$\frac{Q}{I} = -\frac{(1-3\mu'^2)(1-\mu^2)}{(8/3 + (1-3\mu^2)(1-3\mu'^2)/3)}. \quad (2.20)$$

This equation is the same as Equation (12) of House (1972), where the symbols θ and θ' are reversed for the linear polarization angle equal to zero and for the M1 transition with $J = 0 \rightarrow 1 \rightarrow 0$ (see Table I of House 1972 for details). Equation (2.20) clearly shows that when μ'^2=1/3, i.e., when $\theta' = 54.^\circ7$ which is called the Van Vleck angle, the linear polarization of the scattered ray becomes zero and undergoes a sign reversal about this angle. When $\theta' < 54.^\circ7$, the linear polarization is normal to the direction of $\boldsymbol{B}$ projected on POS and is parallel to projected $\boldsymbol{B}$ for $\theta' > 54.^\circ7$.

2.4 Spherical tensor representation of the scattering matrix

The spherical tensor representation introduced in Landi Degl'Innocenti (1984) allows us to develop a more compact mathematical formulation of the problem. In addition, the polarization properties of the emitted radiation are expressed in their simplest form in that basis. Hence in this section we express the Hanle-Zeeman scattering matrix derived in Section 2.3 in terms of the irreducible spherical tensors introduced in Landi Degl'Innocenti (1984) as well as in terms of the generalized profile function introduced by Landi Degl'Innocenti *et al.* (1991). The procedure for achieving this is described in Sampoorna *et al.* (2007a, hereafter SNS07). We apply this procedure originally written for E1 transitions, to the case of M1 transitions. Following Landi Degl'Innocenti and Landolfi (2004, hereafter LL04), we choose the linear polarization unit vectors as

$$\boldsymbol{e}_{-1}(\boldsymbol{n}) = \frac{1}{\sqrt{2}}[\boldsymbol{e}_a(\boldsymbol{n}) + \mathrm{i}\boldsymbol{e}_b(\boldsymbol{n})], \quad \boldsymbol{e}_{+1}(\boldsymbol{n}) = \frac{1}{\sqrt{2}}[-\boldsymbol{e}_a(\boldsymbol{n}) + \mathrm{i}\boldsymbol{e}_b(\boldsymbol{n})],$$
$$\boldsymbol{e}'_{-1}(\boldsymbol{n'}) = \frac{1}{\sqrt{2}}[\boldsymbol{e}'_a(\boldsymbol{n'}) + \mathrm{i}\boldsymbol{e}'_b(\boldsymbol{n'})], \quad \boldsymbol{e}'_{+1}(\boldsymbol{n'}) = \frac{1}{\sqrt{2}}[-\boldsymbol{e}'_a(\boldsymbol{n'}) + \mathrm{i}\boldsymbol{e}'_b(\boldsymbol{n'})], \quad (2.21)$$

where $[\boldsymbol{e}_a(\boldsymbol{n}), \boldsymbol{e}_b(\boldsymbol{n}), \boldsymbol{n}]$ form a right-handed coordinate system about the outgoing ray and similarly a primed system for the incoming ray. Here $\boldsymbol{e}_a(\boldsymbol{n})$ and $\boldsymbol{e}_b(\boldsymbol{n})$ represent the linear polarization basis vectors. The relation between radiation electric and magnetic field vectors depends on the choice of linear polarization basis vectors. In the classical derivation for M1 transitions presented in Section 2.3, the linear polarization basis vectors were $\boldsymbol{e}_a(\boldsymbol{n})$ and $\boldsymbol{e}_b(\boldsymbol{n})$ (which are denoted as $\boldsymbol{e}_\alpha$

with $\alpha = 1$, 2 in Section 2.3 following S98). In this basis the relation between the radiation electric and magnetic field vectors is given by Equation (2.9). In the present section we use the linear polarization basis vectors defined in Equation (2.21). Therefore to find the relation between the radiation electric and magnetic field vectors in the basis of $\boldsymbol{e}_{+1}(\boldsymbol{n})$ and $\boldsymbol{e}_{-1}(\boldsymbol{n})$, we use the relation $E_1\boldsymbol{e}_a + E_2\boldsymbol{e}_b = E_{+1}\boldsymbol{e}_{+1} + E_{-1}\boldsymbol{e}_{-1}$ and $\boldsymbol{E} = \boldsymbol{B} \times \hat{\boldsymbol{r}}$ and find that $\boldsymbol{B} = (\mathrm{i}E_{+1})\boldsymbol{e}_{+1} + (-\mathrm{i}E_{-1})\boldsymbol{e}_{-1}$. Therefore the spherical vector components of the radiation electric and magnetic fields are related through

$$B_\delta = \mathrm{i}\,\delta E_\delta \;\; ; \;\; E_\delta = -\mathrm{i}\,\delta B_\delta, \quad \delta = \pm 1. \tag{2.22}$$

Similar relations also hold good for the primed system. Following Equations (C1) and (C2) of SNS07, the magnetic field components of the scattered radiation can be written as

$$B^{\rm out}_\mu \sim \sum_{\rho q} \Phi_q [e_\mu(\boldsymbol{n})]^*_q [e'_\rho(\boldsymbol{n'})]_q B^{\rm in}_\rho. \tag{2.23}$$

Using Equation (2.22), we can rewrite the above equation as

$$E^{\rm out}_\mu \sim \sum_{\rho q} \mu\rho\Phi_q [e_\mu(\boldsymbol{n})]^*_q [e'_\rho(\boldsymbol{n'})]_q E^{\rm in}_\rho, \;\; \mu, \rho = \pm 1. \tag{2.24}$$

Following S94, we define the coherency matrix $I^S_{\mu\nu} = E^{\rm out}_\mu E^{\rm out*}_\nu$, where the superscript S stands for S94. From Equation (2.24) we can write $I^S_{\mu\nu}$ for M1 transitions as

$$I^S_{\mu\nu} = \sum_{\rho\sigma} T^{S,{\rm M1}}_{\mu\nu,\rho\sigma}(\omega, \boldsymbol{n}, \boldsymbol{n'}; \boldsymbol{B}) I'^S_{\rho\sigma}, \tag{2.25}$$

where

$$T^{S,{\rm M1}}_{\mu\nu,\rho\sigma}(\omega, \boldsymbol{n}, \boldsymbol{n'}; \boldsymbol{B}) = \sum_{qq'} \mu\nu\rho\sigma \;\; \Phi_q \Phi^*_{q'} [e_\mu(\boldsymbol{n})]^*_q \, [e_\nu(\boldsymbol{n})]_{q'} [e'_\rho(\boldsymbol{n'})]_q [e'_\sigma(\boldsymbol{n'})]^*_{q'}. \tag{2.26}$$

Similar to the E1 transitions (see LL04), we now define the reducible spherical tensor for the M1 transitions as

$$\mathcal{E}^{S,{\rm M1}}_{qq'}(\mu, \nu, \boldsymbol{n}) = \mu\nu [e_\mu(\boldsymbol{n})]^*_q [e_\nu(\boldsymbol{n})]_{q'}. \tag{2.27}$$

Therefore Equation (2.26) can be rewritten as

$$T^{S,\mathrm{M1}}_{\mu\nu,\rho\sigma}(\omega,\boldsymbol{n},\boldsymbol{n'};\boldsymbol{B}) = \frac{3}{2}\sum_{qq'}\Phi_q\Phi^*_{q'}\mathcal{E}^{S,\mathrm{M1}}_{qq'}(\mu,\nu,\boldsymbol{n})\mathcal{E}^{S,\mathrm{M1}}_{q'q}(\sigma,\rho,\boldsymbol{n'}), \tag{2.28}$$

where the factor 3/2 is the normalization constant (see S94). We now transform from coherency matrix basis to the Stokes vector basis (see S94 as well as Appendix C of SNS07). Thus the scattered Stokes vector S_i (with $i = 0, 1, 2, 3$) can be written as

$$S_i = \sum_{j=0}^{3} P^{\mathrm{M1}}_{ij}(\omega,\boldsymbol{n},\boldsymbol{n'};\boldsymbol{B})S'_j, \tag{2.29}$$

with S'_j being the incident Stokes vector, and the phase matrix P^{M1}_{ij} for the M1 transitions is given by

$$P^{\mathrm{M1}}_{ij}(\omega,\boldsymbol{n},\boldsymbol{n'};\boldsymbol{B}) = \frac{3}{4}\sum_{\mu\nu\rho\sigma qq'}\Phi_q\Phi^*_{q'}(\sigma_i)_{\nu\mu}(\sigma_j)_{\rho\sigma}\mathcal{E}^{S,\mathrm{M1}}_{qq'}(\mu,\nu,\boldsymbol{n})\mathcal{E}^{S,\mathrm{M1}}_{q'q}(\sigma,\rho,\boldsymbol{n'}), \tag{2.30}$$

where σ_i are the Pauli spin matrices. Following LL04, we define

$$\mathcal{T}^{S,\mathrm{M1}}_{qq'}(i,\boldsymbol{n}) = \sum_{\mu\nu}\frac{1}{2}(\sigma_i)_{\nu\mu}\mathcal{E}^{S,\mathrm{M1}}_{qq'}(\mu,\nu,\boldsymbol{n}). \tag{2.31}$$

Thus Equation (2.30) can be rewritten as

$$P^{\mathrm{M1}}_{ij}(\omega,\boldsymbol{n},\boldsymbol{n'};\boldsymbol{B}) = 3\sum_{qq'}\Phi_q\Phi^*_{q'}\mathcal{T}^{S,\mathrm{M1}}_{qq'}(i,\boldsymbol{n})\mathcal{T}^{S,\mathrm{M1}}_{q'q}(j,\boldsymbol{n'}). \tag{2.32}$$

For mathematical simplicity we express the product of profile functions as proportional to their sums (see S98), namely

$$\Phi_q\Phi^*_{q'} = \frac{1}{2\pi a}\cos\alpha_{q-q'}e^{\mathrm{i}\alpha_{q-q'}}(\Phi_q + \Phi^*_{q'}), \tag{2.33}$$

where $\alpha_{q-q'}$ is the Hanle angle given by $\tan\alpha_{q-q'} = (q-q')g_b\omega_B/\gamma$, with g_b being the Landé g-factor of the upper level, and $a = \gamma/4\pi\Delta\nu_D$ is the damping parameter with $\Delta\nu_D$ the Doppler width. Following LL04, we introduce the irreducible spherical tensor written in terms of the reducible spherical tensor:

$$\left[\mathcal{T}^{K,\mathrm{M1}}_{Q}(i,\boldsymbol{n})\right]^S = \sum_{qq'}(-1)^{1+q}\sqrt{3(2K+1)}\begin{pmatrix} 1 & 1 & K \\ q & -q' & -Q \end{pmatrix}\mathcal{T}^{S,\mathrm{M1}}_{qq'}(i,\boldsymbol{n}), \tag{2.34}$$

with the inverse relation given by

$$\mathcal{T}^{S,\mathrm{M1}}_{qq'}(i,\boldsymbol{n}) = \sum_{KQ}(-1)^{1+q}\sqrt{\frac{(2K+1)}{3}}\begin{pmatrix} 1 & 1 & K \\ q & -q' & -Q \end{pmatrix}\left[\mathcal{T}^{K,\mathrm{M1}}_{Q}(i,\boldsymbol{n})\right]^{S}. \quad (2.35)$$

Substituting Equations (2.33) and (2.35) in Equation (2.32) we obtain

$$\begin{aligned} P^{\mathrm{M1}}_{ij}(\omega,\boldsymbol{n},\boldsymbol{n'};\boldsymbol{B}) = \sum_{KK'Q}\cos\alpha_Q e^{\mathrm{i}\alpha_Q}\left[\mathcal{T}^{K,\mathrm{M1}}_{Q}(i,\boldsymbol{n})\right]^{S}\left[\mathcal{T}^{K',\mathrm{M1}}_{-Q}(j,\boldsymbol{n'})\right]^{S} \\ \times\Bigg\{\sum_{qq'}(-1)^{q+q'}\sqrt{(2K+1)}\sqrt{(2K'+1)}\begin{pmatrix} 1 & 1 & K \\ q & -q' & -Q \end{pmatrix} \\ \times\begin{pmatrix} 1 & 1 & K' \\ q' & -q & Q \end{pmatrix}\frac{1}{2}(\Phi_q+\Phi^*_{q'})\Bigg\}. \quad (2.36) \end{aligned}$$

We now express the profile function appearing in Equation (2.36) in terms of the generalized profile function defined in Landi Degl'Innocenti *et al.* (1991). For the sake of clarity, we recall the definition of the generalized profile function for the $J = 0 \rightarrow 1 \rightarrow 0$ transition:

$$\begin{aligned} \Phi^{KK'}_{Q}(0,\,1;\,\omega) = \sum_{MM'}(-1)^{Q-M-M'}\sqrt{(2K+1)(2K'+1)}\begin{pmatrix} 1 & 1 & K \\ M' & -M & Q \end{pmatrix} \\ \times\begin{pmatrix} 1 & 1 & K' \\ -M & M' & Q \end{pmatrix}\frac{1}{2}[\phi(\omega_{1M'00}-\omega)+\phi^*(\omega_{1M00}-\omega)]. \quad (2.37) \end{aligned}$$

In the above equation the profile function $\phi(\omega_{1M00}-\omega)$ is given by

$$\phi = \frac{-2/\mathrm{i}}{\omega_0-\omega+g_bM\omega_B+\mathrm{i}\gamma/2}. \quad (2.38)$$

For the two-level atomic system considered in this chapter $g_b = 1$. Comparing this equation with Equation (2.4), we see that $\Phi_q = \phi^*(\omega_{1-q00}-\omega)$. In Equation (2.36) we replace $-q$ by M, $-q'$ by M' as well as Q by $-Q$, and using the properties of 3-j symbols, we can identify the resulting term in the flower bracket of Equation (2.36) to be related to the generalized profile function given in Equation (2.37).

Thus Equation (2.36) can be rewritten as

$$P_{ij}^{\mathrm{M1}}(\omega,\boldsymbol{n},\boldsymbol{n'};\boldsymbol{B}) = \sum_{KK'Q}\cos\alpha_Q e^{-\mathrm{i}\alpha_Q}(-1)^Q\left[\mathcal{T}_{-Q}^{K,\mathrm{M1}}(i,\boldsymbol{n})\right]^S\left[\mathcal{T}_{Q}^{K',\mathrm{M1}}(j,\boldsymbol{n'})\right]^S \times(-1)^K\Phi_Q^{KK'}(0,1;\omega). \tag{2.39}$$

We now express $\left[\mathcal{T}_{Q}^{K,\mathrm{M1}}\right]^S$ in terms of the irreducible spherical tensors for the E1 transitions. The reducible tensor $\mathcal{E}_{qq'}^{S,\mathrm{M1}}(\mu,\nu,\boldsymbol{n})$ defined in Equation (2.27) can be rewritten in terms of the Wigner rotation matrices as

$$\mathcal{E}_{qq'}^{S,\mathrm{M1}}(\mu,\nu,\boldsymbol{n}) = \mu\nu\mathcal{D}_{\mu q}^1(R)^*\mathcal{D}_{\nu q'}^1(R), \tag{2.40}$$

where $R\equiv(0,-\theta,-\phi)$ is a rotation that brings the system $[\boldsymbol{e}_a(\boldsymbol{n}),\boldsymbol{e}_b(\boldsymbol{n}),\boldsymbol{n}]$ into the system, where the magnetic field is along the polar Z-axis. Substituting for $\mathcal{E}_{qq'}^{S,\mathrm{M1}}$ in Equation (2.31) and the resulting expression for $\mathcal{T}_{qq'}^{S,\mathrm{M1}}$ in Equation (2.34), we obtain

$$\left[\mathcal{T}_{Q}^{K,\mathrm{M1}}(i,\boldsymbol{n})\right]^S = (-1)^Q\sum_{Q'}\left[t_{Q'}^{K,\mathrm{M1}}(i)\right]^S\mathcal{D}_{Q'-Q}^K(R), \tag{2.41}$$

where

$$\left[t_{Q'}^{K,\mathrm{M1}}(i)\right]^S = \sum_{\mu\nu}\frac{1}{2}\mu\nu(\sigma_i)_{\mu\nu}\sqrt{3(2K+1)}\begin{pmatrix}1 & 1 & K\\ \mu & -\nu & -Q'\end{pmatrix}. \tag{2.42}$$

Defining the quantity

$$\zeta_i = (1,-1,-1,1),\ i=0,1,2,3, \tag{2.43}$$

corresponding to the Stokes parameters, Equation (2.42) can be rewritten as

$$\left[t_{Q'}^{K,\mathrm{M1}}(i)\right]^S = \zeta_i\sum_{\mu\nu}\frac{1}{2}(\sigma_i)_{\mu\nu}\sqrt{3(2K+1)}\begin{pmatrix}1 & 1 & K\\ \mu & -\nu & -Q'\end{pmatrix}. \tag{2.44}$$

Comparing this expression with the Equation (C21) of SNS07 (which is for electric dipole transitions), we can write

$$\left[t_{Q'}^{K,\mathrm{M1}}(i)\right]^S = \zeta_i\left[t_{Q'}^{K}(i)\right]^S. \tag{2.45}$$

With the above expression and Equation (C22) of SNS07, Equation (2.41) can be rewritten as

$$\left[\mathcal{T}^{K,\mathrm{M1}}_{Q}(i,\boldsymbol{n})\right]^{S} = \zeta_i \left[\mathcal{T}^{K*}_{Q}(i,\boldsymbol{n})\right]^{L}, \tag{2.46}$$

where the superscript 'L' stands for LL04. From the above equation it is clear that the irreducible spherical tensor for the M1 transition is related to that for the E1 transition by the factor ζ_i (see also Equation (13.25) of LL04). Therefore in terms of irreducible spherical tensor representation of LL04, Equation (2.39) therefore becomes

$$\begin{aligned} P^{\mathrm{M1}}_{ij}(\omega,\boldsymbol{n},\boldsymbol{n'};\boldsymbol{B}) = \quad & \zeta_i\zeta_j\Big[\sum_{KK'Q}\cos\alpha_Q e^{-\mathrm{i}\alpha_Q}(-1)^Q \\ & \mathcal{T}^{K}_{Q}(i,\boldsymbol{n})\mathcal{T}^{K'}_{-Q}(j,\boldsymbol{n'})(-1)^K\Phi^{KK'}_{Q}(0,1;\omega)\Big], \end{aligned} \tag{2.47}$$

where we have dropped the superscript L without loss of generality. The above equation represents the Hanle-Zeeman scattering matrix for the M1 transitions. The term in the square brackets in Equation (2.47) is identical to the right-hand side of Equation (52) in Bommier (1997b), when in the latter the collisions are ignored and only frequency coherent scattering is considered. Therefore the term in the square brackets represents the Hanle-Zeeman scattering matrix for E1 transitions. Thus we can write

$$P^{\mathrm{M1}}_{ij}(\omega,\boldsymbol{n},\boldsymbol{n'};\boldsymbol{B}) = \zeta_i\zeta_j\, P^{\mathrm{E1}}_{ij}(\omega,\boldsymbol{n},\boldsymbol{n'};\boldsymbol{B}). \tag{2.48}$$

The above relation between the phase matrices for M1 and E1 transitions is quite general. Indeed, they differ only through signs of certain matrix elements. The sign differences occur because the driving force for E1 and M1 transitions are the radiation electric and magnetic fields, respectively, which are independent of the J quantum numbers of the transition involved. Therefore Equation (2.48) can be used for an arbitrary $J_l \rightarrow J_u \rightarrow J_l$ scattering transition. The corresponding phase matrix P^{E1} can be derived using the Kramers-Heisenberg approach of S98 (see also LL04).

For our further discussions we would like to introduce the non-dimensional frequency in the laboratory frame which, is defined as

$$x = \frac{\omega_0 - \omega}{\Delta\omega_D}, \tag{2.49}$$

where $\Delta\omega_D = 2\pi\Delta\nu_D$. To account for thermal motion of radiating atoms, the profile function in the rest frame $\phi(\omega_{1M00} - \omega)$ is convolved with the Maxwellian velocity distribution. Thus the laboratory frame profile function is given by

$$\mathcal{H}(a, x_M) = H(a, x_M) + \mathrm{i}\, F(a, x_M), \tag{2.50}$$

where $H(a, x_M)$ is the normalized Voigt function describing absorption and $F(a, x_M)$ is the normalized Faraday-Voigt function describing dispersion with $x_M = x + g_b M \nu_B / \Delta\nu_D$ (see Section 2.3 of S98 for details).

2.5 Polarization diagram for E1 and M1 transitions

Equation (2.48) shows that the scattering matrix derived for M1 transition is related to that of E1 transition in a simple manner. To illustrate this, we consider a single scattering of an unpolarized beam of radiation incident on the scattering atom in the vertical direction. The Stokes parameters of the scattered radiation is then simply given by the first column of the phase matrix. Figure 2.5 shows the polarization diagram, namely the plot of U/I versus Q/I for $x = 0$ as a function of field strength parameter $\Gamma_B = g_b \omega_B / \gamma$ for different choices of magnetic azimuthal angles φ_B and a fixed field inclination angle $\vartheta_B = \pi/2$ (see Figure 2.4). From Equation (2.48), we see that Q/I and U/I for M1 transitions differ from those for E1 transitions by a negative sign. This is clearly reflected in Figure 2.5. For example, note that Q/I values are negative for E1 transitions, while they are positive for M1 transitions. As for U/I, let us take the example of $\varphi_B = 0°$. It is negative for all values of Γ_B in E1 transitions, while it is positive for M1 transitions. As expected, the magnitudes remain the same. The symmetry properties of the polarization diagram with respect to $\varphi_B = \pm\pi/2$, $\pm\pi/4$ and $\pm 3\pi/4$ are identical for both E1 and M1 transitions. Furthermore, for a given ϑ_B and φ_B, the U/I initially increases, reaches a maximum for $\Gamma_B = 0.5$, and then decreases and saturates for $\Gamma_B \gg 1$.

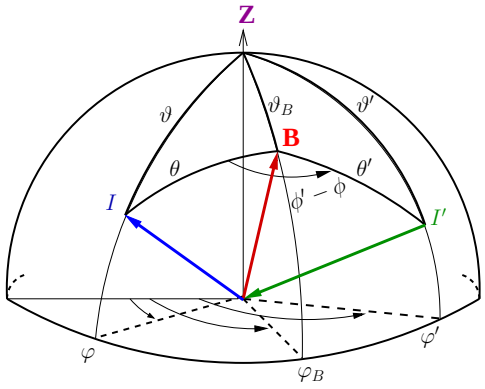

FIGURE 2.4: Geometry showing the scattering process in a coordinate system where the magnetic field makes an angle ϑ_B with respect to the polar Z-axis, and has an azimuth of φ_B . We refer to this as the atmospheric reference frame (ARF). In this frame (ϑ', φ') refer to the incident ray, and (ϑ, φ) to the scattered ray. (θ', ϕ') refer to the incident ray, and (θ, ϕ) to the scattered ray with respect to the magnetic field (MRF).

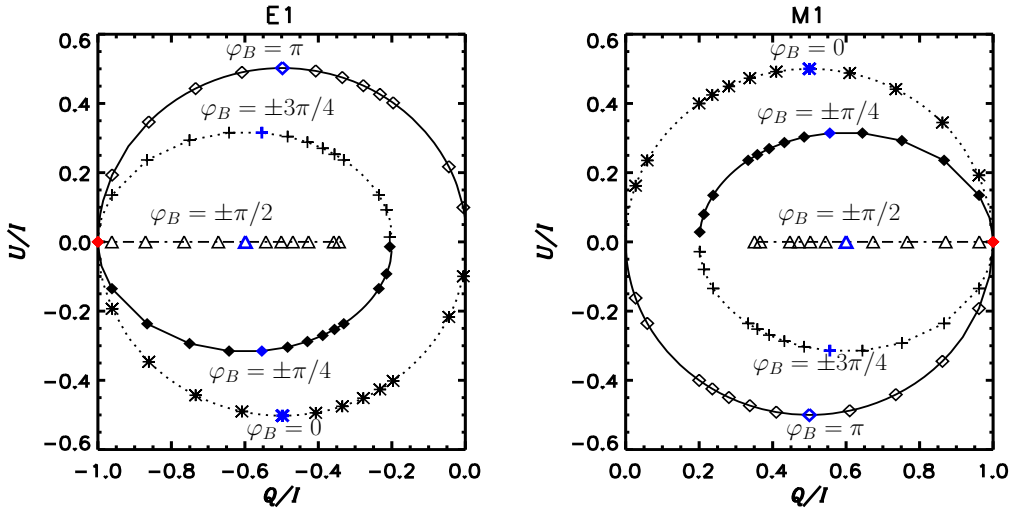

FIGURE 2.5: Polarization diagram for E1 (left) and M1 (right) $J = 0 \to 1 \to 0$ transitions. Fractional polarizations Q/I and U/I are plotted as a function of field-strength parameter Γ_B, for various values of the magnetic field azimuth angle φ_B and a fixed inclination angle $\vartheta_B = \pi/2$. An unpolarized beam of radiation is incident on the atom in the vertical direction ($\vartheta' = 0°$ and $\varphi' = 0°$). The scattered Stokes parameters are calculated in the horizontal plane ($\vartheta = 90°$ and $\varphi = 0°$). The symbols along the different curves correspond to different values of Γ_B (increasing from left to right for E1 transitions and from right to left for the M1 transitions). $\Gamma_B = 0$ is marked by the filled red symbol. The blue symbols correspond to $\Gamma_B = 0.5$.

2.6 Concluding remarks

In the present chapter we have derived the scattering matrix for the case of $J = 0 \rightarrow 1 \rightarrow 0$ M1 transitions in arbitrary-strength magnetic fields. For this purpose, we used the classical scattering matrix approach of Stenflo (1994, 1998) together with the classical damped magnetic dipole oscillator model of Casini and Lin (2002). This matrix describes various cases like Hanle, saturated Hanle, intermediate Hanle-Zeeman, and pure Zeeman regimes in a continuous way, hence the name Hanle-Zeeman scattering matrix. We also expressed the Hanle-Zeeman M1 scattering matrix in terms of the irreducible spherical tensors (Landi Degl'Innocenti 1984) and the generalized profile functions (Landi Degl'Innocenti *et al.* 1991). We showed that this matrix is related to the scattering matrix for E1 transitions in a simple manner, involving only sign changes of some of the matrix elements. This could then allow for a straightforward generalization of the M1 scattering matrix to arbitrary $J_l \rightarrow J_u \rightarrow J_l$ scattering transition. The differences and similarities between the scattering matrix for E1 and M1 transitions were also illustrated through polarization diagrams. This theoretical formalism may find application in modeling the polarization profiles of forbidden lines formed in the several astrophysical contexts such as: solar corona, interstellar medium (ISM), circumstellar regions, supernova remnants.

Chapter 3

Empirical Study of Polarized Profiles Formed in Solar Coronal Conditions[1]

An overview

A classical theory for the forbidden lines is presented in Chapter 2 for the case of arbitrary-strength magnetic fields. Here we apply this theoretical formalism to study the effect of density distributions, magnetic field configurations, and velocity fields on the Stokes profiles formed in solar coronal conditions. To this end, we take into account the integration over a cone of an unpolarized radiation from the solar disk incident on the scattering atoms. Furthermore, we also integrate along the line-of-sight (LOS) to calculate the emergent polarized line profiles. For our studies we adopt the atomic parameters corresponding to the [Fe XIII] 10747 Å coronal forbidden emission line.

3.1 Introduction

Coronal forbidden emission lines are formed due to the magnetic dipole (M1) transitions in highly ionized atoms in the solar corona. Polarization in these lines arises

[1]The contents of this chapter are based on the publications: Megha *et al.* (2017, 2018, 2020c)

due to the anisotropic excitation of ions in the corona. The polarization measurement of these lines is the most promising method of determining the direction of magnetic fields in the corona (House 1972, House 1977, Querfeld 1982, Judge 1998, Penn 2014, Plowman 2014, Dima *et al.* 2016, Li *et al.* 2017). Here we apply the classical theory for the forbidden lines which is presented in Chapter 2 for the case of arbitrary-strength magnetic fields, to study the polarized line profiles formed in solar coronal conditions. It is clear that an emitting atom in the corona is illuminated by the limb darkened anisotropic radiation from the photosphere. Following House (1972), here we describe a procedure for the integration over the solid angle of the incident cone of radiation to obtain the scattered radiation. Also since the corona is optically thin, the polarization of emission lines measured at the Earth contain the integrated contribution along the LOS. Therefore here we describe the steps to perform the LOS integration. For our studies we use both spherically symmetric and latitude dependent density distributions. For illustrations we use the atomic parameters of the [Fe XIII] 10747 Åcoronal forbidden emission line. We consider both radial and dipole field distributions of the magnetic field.

In Section 3.2, we describe a procedure to perform angular integration over the unpolarized incident cone of radiation from the solar photosphere. The resulting Stokes profiles from the scattering point are also presented. In Section 3.3, we describe the LOS integration technique and present emergent Stokes profiles for radial and dipole field distributions within the corona. In Section 3.4 we show the plane-of-sky (POS) polarization maps for different density and magnetic field configurations. In Section 3.5 we discuss the effect of a radial velocity field on the Stokes profiles formed in the corona. Conclusions are presented in Section 3.6.

3.2 Integration over the solid angle of the incident cone of radiation

For mathematical simplicity the phase matrix for M1 transitions was derived in Chapter 2 in the magnetic reference frame (MRF, with Z-axis along the magnetic field direction; see Figure 2.3). For practical purposes we need the scattering matrix in a more general geometry, called the atmospheric reference frame (ARF, see Figure 2.4). Following LL04 (see also Frisch 2007), Equation (2.47) can now

be written in ARF as

$$P_{ij}^{\mathrm{M1}}(x,\boldsymbol{n},\boldsymbol{n'};\boldsymbol{B}) = \zeta_i\zeta_j\Big[\sum_{KQ}(-1)^K\mathcal{T}_Q^K(i,\boldsymbol{n})\sum_{K'Q'}N_{QQ'}^{KK'}(x,\boldsymbol{B})(-1)^{Q'}\mathcal{T}_{-Q'}^{K'}(j,\boldsymbol{n'})\Big]. \tag{3.1}$$

Here, $\boldsymbol{n}$ and $\boldsymbol{n'}$ are now defined by their polar angles ϑ, φ and ϑ', φ' in the ARF. The magnetic kernel $N_{QQ'}^{KK'}(x,\boldsymbol{B})$ may be written as

$$N_{QQ'}^{KK'}(x,\boldsymbol{B}) = e^{\mathrm{i}(Q'-Q)\varphi_B}\sum_{Q''}d_{QQ''}^K(\vartheta_B)d_{Q''Q'}^{K'}(-\vartheta_B)\cos\alpha_{Q''}e^{-\mathrm{i}\alpha_{Q''}}\Phi_{Q''}^{KK'}(0,1;x), \tag{3.2}$$

where ϑ_B and φ_B are the polar angles of the magnetic field in ARF. Expressions for the reduced rotation matrices $d_{QQ'}^K$ can be found in LL04 (see their Table 2.1).

The scattering atom in the corona is illuminated by the unpolarized cone of radiation incident from the photosphere (see Figure 2.1). Thus the scattering matrix has to be integrated over the solid angle subtended by this cone at the sight of the atom. The resulting scattered Stokes parameters are given by

$$\mathcal{I}_i^{\mathrm{M1}}(x,\vartheta,\varphi;\boldsymbol{B}) = \int_0^{2\pi}\int_{\cos\Omega}^1 P_{i0}^{\mathrm{M1}}(x,\boldsymbol{n},\boldsymbol{n'};\boldsymbol{B})I'\frac{d\mu' d\varphi'}{4\pi}, \tag{3.3}$$

where $\mu' = \cos\vartheta'$. To perform the above integration, we consider a limb-darkening function to represent the angular distribution of incident radiation I' within the cone. This is given by

$$I' = I_0\left[1-u+\frac{\sqrt{\cos^2\vartheta'-\cos^2\Omega}}{\sin\Omega}u\right], \tag{3.4}$$

where u is an empirically determined limb-darkening coefficient, I_0 is the continuum intensity at the center of the disk which is taken to be unity in this chapter, and the solid angle Ω is defined as $\sin\Omega = R_\odot/(R_\odot+h)$, with h being the height of the scattering atom above the photosphere.

Following Frisch (2007), we write the irreducible spherical tensors

$$\mathcal{T}_Q^K(i,\boldsymbol{n}) = \tilde{\mathcal{T}}_Q^K(i,\vartheta)e^{\mathrm{i}Q\varphi}. \tag{3.5}$$

Introducing Equation (3.5) in Equation (3.1) and the resulting expression in Equation (3.3), we see that the integration over φ' will be non-zero only for $Q' = 0$.

Now expanding the summation over K', Equation (3.3) can be written as

$$\mathcal{I}_i^{\rm M1}(x,\vartheta,\varphi;\boldsymbol{B}) = \frac{\zeta_i}{2}\sum_{KQ}(-1)^K\mathcal{T}_Q^K(i,\boldsymbol{n})\Bigg[N_{Q0}^{K0}\int_{\cos\Omega}^{1}\tilde{\mathcal{T}}_0^0(0,\vartheta')\,I'\,d\mu' + N_{Q0}^{K2}\int_{\cos\Omega}^{1}\tilde{\mathcal{T}}_0^2(0,\vartheta')\,I'\,d\mu'\Bigg]. \quad (3.6)$$

After introducing the values for $\tilde{\mathcal{T}}_0^0(0,\vartheta')$ and $\tilde{\mathcal{T}}_0^2(0,\vartheta')$ from LL04 (Table 5.6, with a particular choice of the reference angle $\gamma = 0$), the two integrations appearing in Equation (3.6) can be performed analytically and the resulting expressions are given by

$$\int_{\cos\Omega}^{1}\tilde{\mathcal{T}}_0^0(0,\vartheta')\,I'\,d\mu' = (1-u)(1-\cos\Omega) + \frac{u}{2}\Bigg[1-\cot\Omega\cos\Omega\,\ln(\sec\Omega+\tan\Omega)\Bigg],$$

$$\int_{\cos\Omega}^{1}\tilde{\mathcal{T}}_0^2(0,\vartheta')\,I'\,d\mu' = \frac{1}{2\sqrt{2}}\Bigg\{(1-u)\,\cos\Omega\sin^2\Omega + 3\,u\Bigg[\frac{1}{4}-\frac{1}{8}\cos^2\Omega - \frac{1}{8}\cot\Omega\cos^3\Omega\,\ln(\sec\Omega+\tan\Omega)\Bigg] - \frac{u}{2}\Bigg[1-\cos\Omega\cot\Omega\,\ln(\sec\Omega+\tan\Omega)\Bigg]\Bigg\}. \quad (3.7)$$

From here on, for all the illustrations presented in this chapter, we consider scattering on the [Fe XIII] ion located at a height $h = 0.5\,R_\odot$ above the limb. In particular, we consider the 10747 Å line that results from ${}^3P_0 \rightarrow {}^3P_1 \rightarrow {}^3P_0$ scattering transition. We chose this line because it is expected to be used for the spectropolarimetric studies of the solar corona by the Visible Emission Line Coronagraph (VELC) payload on board Aditya-L1[2], an upcoming Indian space mission to study the Sun. VELC is designed to image the solar corona over a field-of-view (FOV) of 1.05 $R_\odot$ to 3 $R_\odot$ and further facilitates spectropolarimetric studies of the 10747 Å line over a FOV of 1.05 $R_\odot$ to 1.5 $R_\odot$.

We use two-level atom approximation and neglect collisions. The effects of collisions and multi-level coupling are discussed in detail in House (1977) and Sahal-Bréchot (1977). These authors show that the two-level atom approximation is insufficient particularly when electron densities are larger than $10^7\,{\rm cm}^{-3}$. This

[2]https://www.isro.gov.in/aditya-l1-first-indian-mission-to-study-sun

is because in such cases the collisional effects can not be neglected. Indeed, the ground configuration of the [Fe XIII] ion consists of five levels, namely, $^3P_0$, $^3P_1$, $^3P_2$, $^1D_2$, $^1S_0$. Sahal-Bréchot (1977) has demonstrated that the collisional transfer from the $^3P_2$ level (and also other higher levels) plays an important depolarizing role. In particular, the collisional effects decrease the degree of linear polarization of the [Fe XIII] 10747 Å line by about 10% (see also Figure 4(d) of House 1977). Therefore, the theoretical formalism presented in Chapter 2 can be applied to only those regions in the corona where the electron densities are lower than $10^7\,\mathrm{cm}^{-3}$. For the electron density model considered by House (1977, see his Table 2 and see also Equation (3.10) below), such densities are found for $h \gtrsim 0.5\,R_\odot$ above the limb. Thus, we present all the results for $h = 0.5\,R_\odot$ (which is the upper limit for spectropolarimetric observations of the Aditya-L1 mission). For $h < 0.5\,R_\odot$ it is essential to account for the collisional effects and thereby the multi-level coupling.

Although we use two-level atom approximation and neglect collisions, our theoretical formalism is able to handle a wide range of field strengths, unlike previous formalisms (Sahal-Bréchot 1977, House 1977, Casini and Judge 1999) which only considered the saturated Hanle regime. For our illustrations we therefore consider a range of field strengths from μG to 3 kG. However, the coronal magnetic fields are expected to fall in the range 1-30 G (Lin *et al.* 2000, Jess *et al.* 2016), which corresponds to the saturated Hanle regime for the [Fe XIII] 10747 Å line. In spite of this, we consider field strengths outside this range to demonstrate the applicability of our approach to arbitrary-strength fields. In the stellar case, the 10747 Å line has been observed by Zirin (1976) in R Aquarii, which is a symbiotic star. Extremely weak fields on the order of μG are expected to be found in diffuse media such as the interstellar medium (ISM), circumstellar regions, supernova remnants etc. (see eg. Yan and Lazarian 2006, Ferrière 2009, Reynolds *et al.* 2012). In such diffuse media, several forbidden lines of [O I], [O III], [Ne II], [Ne V], [Ca II], [S II], [Fe II], [Fe XIV], [Fe X] (Kraus *et al.* 2010, Dopita *et al.* 2016) are formed. Indeed, the IR forbidden lines of neon are formed in the winds of Wolf-Rayet stars (Ignace and Brimeyer 2006), where fields as strong as 1.5 kG are expected (de la Chevrotière *et al.* 2014). More recently, the polarization of [O I] 6300 Å line formed in the solar photosphere has been observed (de Wijn *et al.* 2017). Our theoretical formalism can be applied to compute the linear polarization profiles of any M1 forbidden line (see the text below Equation (2.48)) in the presence

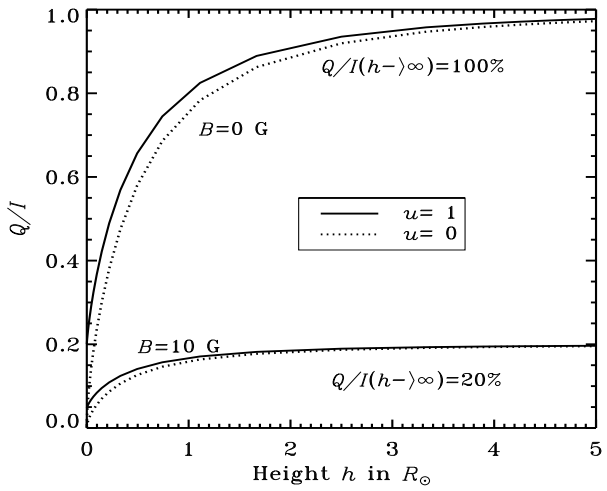

FIGURE 3.1: Line integrated Q/I versus height after integration over the incident cone of radiation from the photosphere. The model parameters are $(A,\, \vartheta,\, \varphi,\, \vartheta_B,\, \varphi_B,\, \Delta\lambda_D) = (14.04\,\mathrm{s}^{-1},\, 90^\circ,\, 0^\circ,\, 90^\circ,\, 45^\circ,\, 0.87\text{Å})$. The reference direction for the positive Stokes Q lies in the meridian plane containing the Z-axis of the atmospheric reference frame and the propagation direction.

of arbitrary-strength magnetic fields (that are found in the ISM, stellar winds, and also in solar and stellar atmospheres), provided the collisions and multi-level couplings are negligible.

Figure 3.1 shows the plot of line integrated Q/I as a function of the height above the photosphere, after integrating over a cone of radiation incident from the photosphere (see Equations (3.6) and (3.7)). For the chosen geometry and the reference direction for the linear polarization measurement U/I=0. This can be explained by using Equation (3.6) for $i = 2$, i.e., for Stokes U as follows: For $\vartheta = 90^\circ$ and $\varphi = 0^\circ$, the only non-zero $\mathcal{T}^K_Q(2, \boldsymbol{n})$'s are $\mathcal{T}^2_{\pm1}(2, \boldsymbol{n}) = -\mathrm{i}\sqrt{3}/2$. For these values of $K = 2$ and $Q = \pm1$, $N^{20}_{\pm10} = N^{22}_{\pm10} = 0$ implying that $U = 0$. As the height increases, the solid angle of the incident cone at the scattering atom decreases. Thus, the anisotropy of the incident radiation increases, thereby resulting in an increase of line integrated Q/I with height. Indeed, in the limit of $h \to \infty$, the cone can be mimicked by a vertically incident ray. Thus we reach the configuration corresponding to maximum Q/I, which is 100% in the non-magnetic case and 20% in the magnetic case. We remark that the line integrated Q/I is nearly the same for all field strengths. For lower heights ($h \leqslant 1\,R_\odot$) the line integrated Q/I has some sensitivity to the choice of limb-darkening coefficient u.

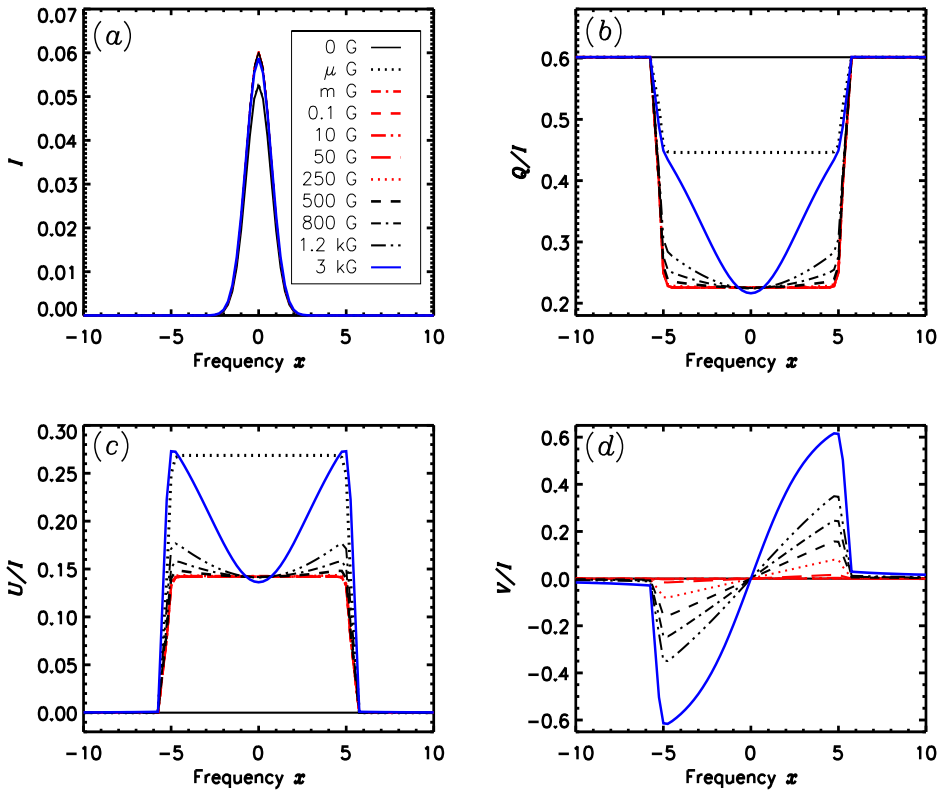

FIGURE 3.2: Scattered Stokes profiles from a height of 0.5 $R_\odot$ above the limb after the integration over the incident cone of radiation from the photosphere. The model parameters are (A, ϑ, φ, ϑ_B, φ_B, $\Delta\lambda_D$, u) = (14.04 s^{-1}, 90°, 90°, 30°, 60°, 0.87 Å, 0.34).

For heights above 1 $R_\odot$ the anisotropy is mainly due to the geometrical effects, thereby making the line integrated Q/I insensitive to u.

Figure 3.2 shows the scattered Stokes profiles obtained after integrating over a cone of radiation incident from the photosphere. The limb-darkening coefficient $u = 0.34$ is used (see Pierce 2000). The field strength is varied in a wide range from μG to 3 kG. Because the Einstein A coefficient for the chosen transition is very small (about 14.04 s^{-1}), the field strength parameter Γ_B (see Section 2.5 for a definition of Γ_B) is very large, so that the profiles remain in the saturated Hanle regime for a wide range of field strengths (shown as red curves covering the range from mG to 250 G). At a coronal temperature of 2 MK, the Doppler width is large (about 0.87 Å) therefore the intensity profiles become insensitive to the field strength variation. As the field strength increases, the Q/I profiles become depolarized in the line core and reach a saturated value (with no variation with

field strength up to 250 G). Similar to Q/I, the U/I first increases (for μG field) and then decreases (for mG field) and remains in the saturated regime up to 250 G. For fields larger than 250 G, the Q/I and U/I profiles exhibit typical Zeeman-like behavior. The V/I profiles exhibit a typical antisymmetric shape with increasing amplitudes as a function of field strength.

3.3 Line-of-sight (LOS) integration

The polarization of the coronal emission lines measured by an observer at Earth is influenced by the density variation of the scattering ions along the LOS. As the corona is optically thin, it is sufficient to integrate the scattering contributions from atoms along the LOS. The geometry chosen for the LOS integration is shown in Figure 3.3. In this geometry the primed coordinate system $x'y'z'$ is fixed to the Sun with the $x'z'$ plane describing the POS and y' axis is chosen along the LOS. The unprimed coordinate system xyz is oriented at an angle χ with respect to $x'y'z'$ system with x' parallel to x. This xyz system describes the ARF where the atom is considered to be fixed at its origin at a height h above the limb. The LOS makes an angle $\vartheta = 90^\circ - \chi$ with respect to the z-axis and has an azimuth $\varphi = 90^\circ$. ψ is the angle between $\boldsymbol{B}$ and LOS. The distance along the LOS as measured from the mid-plane ($\chi = 0$) in units of $R_\odot$ is given by

$$l = (1 + \rho_0) \tan \chi, \tag{3.8}$$

where $\rho_0 = h_0/R_\odot$. The solid angle subtended by the cone of incident radiation at the scattering point can now be defined as $\sin \Omega = 1/(1 + \rho)$, where $\rho = h/R_\odot$. This can also be written in terms of χ using $\cos \chi = (1 + \rho_0)/(1 + \rho)$, which then gives $\sin \Omega = \cos \chi/(1 + \rho_0)$. The integration along the LOS can now be expressed in the following form:

$$I_i^{\mathrm{M1}}(x, \rho_0) = \int_{-\pi/2}^{\pi/2} \mathcal{I}_i^{\mathrm{M1}}(x, \vartheta, \varphi; \boldsymbol{B}) N(\rho, \chi) \frac{(1 + \rho_0)}{\cos^2 \chi}\, d\chi, \tag{3.9}$$

where $N(\rho, \chi)$ is the relative density distributions of the scattering ions along the LOS.

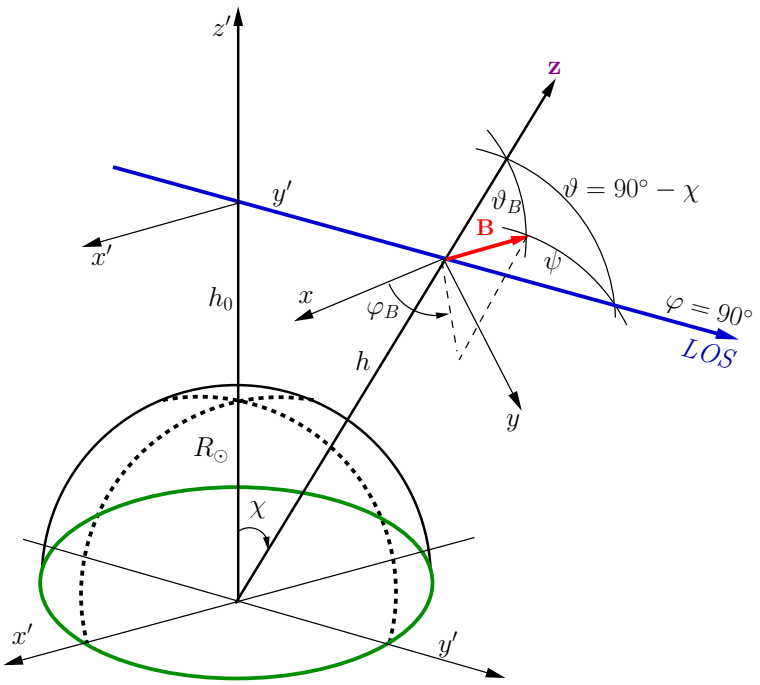

FIGURE 3.3: Geometry used for integration along the LOS (see the text for details).

The LOS integral in Equation (3.9) is performed numerically using Simpson's $1/6^{\text{th}}$ integration formula along with equally spaced points in the χ-grid. We find that 11 points χ-grid is sufficient to accurately evaluate the LOS integral. For the purpose of comparison, we have used all the five different density variations that are listed as Cases 1–5 in House (1972). We find that the variation of degree of linear polarization with height above the limb for all the five cases given in Tables II and III of House (1972) can be reproduced with an accuracy of 2-8% for the limb-darkening coefficient value $u = 1$ and for a $J = 0 \rightarrow 1 \rightarrow 0$ scattering transition. For illustration, in Figure 3.4 we plot the frequency-integrated degree of linear polarization as a function of height above the limb for the density distribution in Case 5 of House (1972) given by $N \propto k_4 \exp(-\beta_4 \rho)$ with $k_4 = 1$, $\beta_4 = 0$ and for a radial field. The small differences between the P computed by House (1972) and our computations could be due to different methods of LOS and frequency integration.

For further studies presented in this chapter (excepting Section 3.4) we adopt the spherically symmetric density (SSD) distribution model used in House (1972),

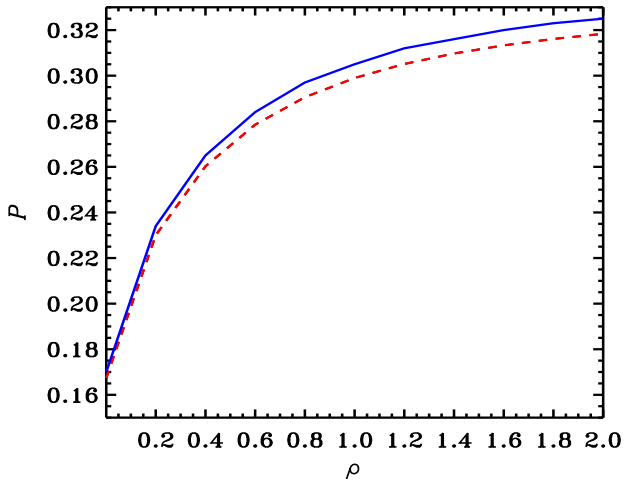

FIGURE 3.4: Degree of linear polarization ($P{=}\sqrt{Q^2+U^2}/I$) as a function of height above the limb in $R_\odot$ units for density distribution in Case 5 of House (1972) for $u = 1$. The blue solid line corresponds to the data given in Table III of House (1972) and the red dashed line corresponds to P computed by us.

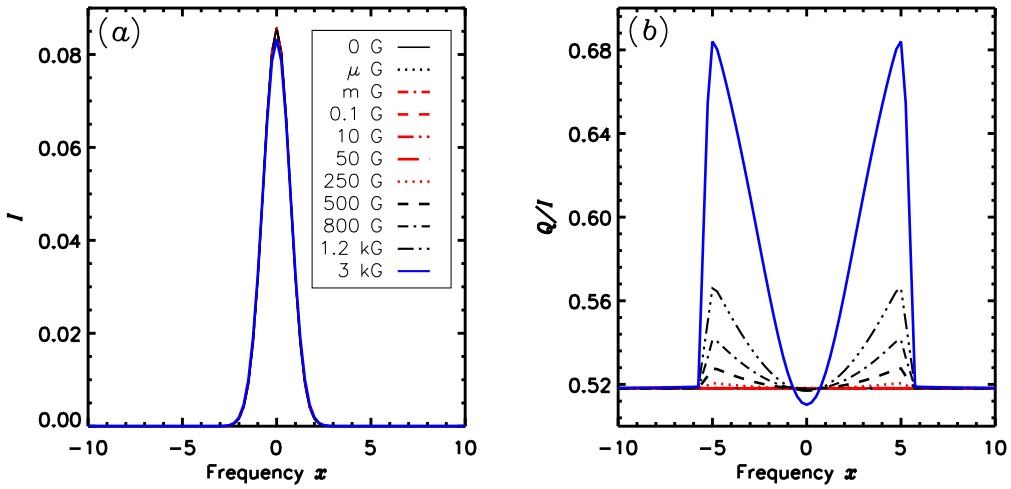

FIGURE 3.5: The LOS-integrated Stokes profiles at $h_0 = 0.5R_\odot$ for the radial field. The model parameters are (A, ϑ_B, φ_B, $\Delta\lambda_D$, u) = (14.04 s^{-1}, 0°, 0°, 0.87 Å, 0.34). The density distribution is given by Equation (3.10).

which is given by

$$N = \sum_{i=1}^{3} k_i \, (1+\rho)^{-\beta_i}, \tag{3.10}$$

where $k_1 = 7.55$, $k_2 = -1.68$, $k_3 = 1.04{\times}10^3$, $\beta_1 = 5.35$, $\beta_2 = 14.74$ and $\beta_3 = -20.45$. These values are taken from Newkirk *et al.* (1970).

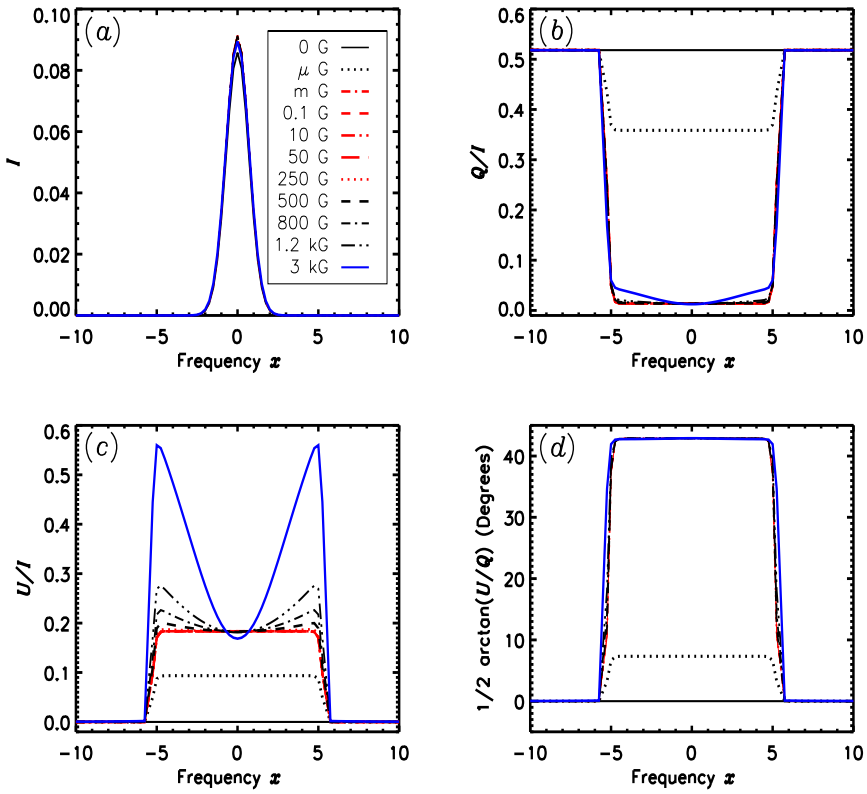

FIGURE 3.6: The LOS-integrated Stokes profiles (panels a, b, c) and the position angle, PA $= 1/2 \arctan(U/Q)$ as a function of frequency for the dipole field with a colatitude of 60° (panel d). The LOS is at a height of $0.5\,R_{\odot}$ above the limb. The model parameters are $(A,\ \vartheta_B,\ \varphi_B,\ \Delta\lambda_D,\ u) = (14.04\ s^{-1},\ 40°.89,\ 0°,\ 0.87\,\text{Å},\ 0.34)$. The density distribution is given by Equation (3.10). The dipole axis is in the POS which makes an angle of 90° with respect to the LOS.

3.3.1 Radial and dipole magnetic field configurations

Using the density distribution given in Equation (3.10) we compute the LOS-integrated Stokes profiles for the radial field ($\vartheta_B = 0°$ and $\varphi_B = 0°$, see Figure 3.5) and also for the dipole field (see Figure 3.6) with a fixed colatitude of 60° at all the spatial points along the LOS. For simplicity we consider the case where the dipole field axis and the stellar rotation axis are aligned and remain vertical in the POS. The field strength is varied as discussed in Section 3.2. The limb-darkening coefficient is fixed at 0.34.

For a radial field, the magnetic field is along the radius vector at each spatial point along the LOS. Thus the azimuthal symmetry of the problem is retained. In this case, Q/I remains at the non-magnetic (Rayleigh) scattering value throughout

the line profile for fields of up to 250 G (see Figure 3.5) and the U/I is zero. This can be understood using Equations (3.2) and (3.6). From Equation (3.2) we see that for radial field ($\vartheta_B = 0^\circ$ and $\varphi_B = 0^\circ$), $N^{KK'}_{QQ'}$ is non-zero only for $Q = Q' = 0$ and depends on the magnetic field strength only through the generalized profile function (and not through the Hanle angles as $Q'' = 0$). For fields weaker than 250 G, the profile functions corresponding to different Zeeman components are nearly the same, namely $\mathcal{H}(a, x_{\pm 1}) \approx \mathcal{H}(a, x_0)$. Therefore $N^{KK'}_{00}(x, \boldsymbol{B})$ is nearly equal to the corresponding Rayleigh value. Furthermore, in Equation (3.6), $\mathcal{T}^K_0(i, \boldsymbol{n})$ alone contributes for the radial field case. For our choice of reference angle $\gamma = 0$, $\mathcal{T}^2_0(2, \boldsymbol{n})$ is zero (see Table 5.6 of LL04), thereby giving rise to $U = 0$ for the radial field case. For fields beyond 250 G we enter the Zeeman regime, resulting in Zeeman-like Q/I profiles. U/I profiles are zero due to the reasons explained above. The LOS-integrated V/I profile is zero for radial field due to exact cancellation of the V/I in the forward part of the hemisphere ($\chi > 0^\circ$) by the V/I formed at the corresponding spatial points in the backward part of the hemisphere ($\chi < 0^\circ$). This is due to the opposite signs of the longitudinal component of the radial magnetic field in the forward and backward parts of the hemisphere.

For a dipole field, the azimuthal symmetry is broken, because of which both Q/I and U/I are non-zero. For very weak fields (μG) typical Hanle-like signatures are obtained (see black dotted line in Figure 3.6) which then saturate for mG to 250 G fields. Again, Zeeman signatures are observed for fields stronger than 250 G. Like in the case of radial field, the LOS-integrated V/I is zero because the values of V/I at the χ-grid points along the LOS are perfectly antisymmetric about the mid-plane ($\chi = 0^\circ$, see Figure 3.7). Figure 3.6(d) shows the position angle plotted as a function of frequency. It can be clearly observed that the position angle remains constant within the line core at 43° in the saturated Hanle regime. In the line wings the position angle is zero because of the Rayleigh scattering at those frequencies. To study the variation of profiles along the grid points along the LOS, we plot the profiles as a function of angle χ (see Figure 3.7). We have plotted this for the dipole field case. It shows that the $(I, Q/I, U/I)$ are symmetric, while V/I is antisymmetric about $\chi = 0^\circ$, i.e., when the direction of the field is in the POS.

Figure 3.8 shows a plot of a frequency-integrated degree of polarization $P = \sqrt{Q^2 + U^2}/I$ as a function of height above the limb. To illustrate the effect of LOS

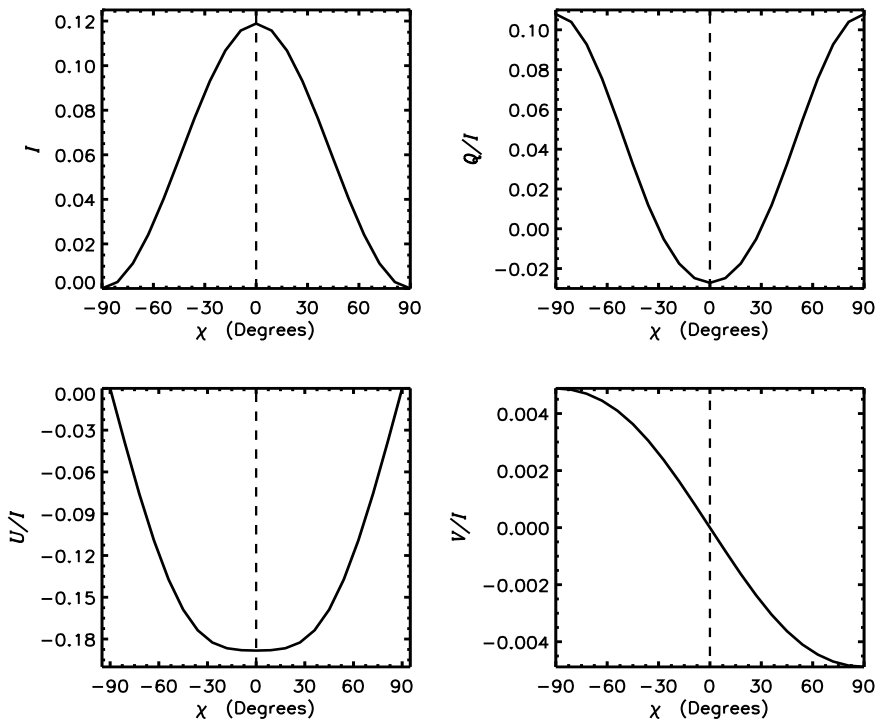

FIGURE 3.7: Variation of I, Q/I, and U/I at line center ($x = 0$) and V/I at the frequency corresponding to its peak value at different spatial points (represented by different values of χ) along the LOS. A dipole field with a colatitude of 60° is considered. Note that I, Q/I, and U/I are symmetric about $\chi = 0°$, while V/I is antisymmetric. A constant field strength of $B = 10\,\mathrm{G}$ is used.

integration, we plot P computed with (blue lines) and without (red lines) LOS integration. We consider three different cases, namely, (a) a magnetic field with $\vartheta_B = 30°$ and $\varphi_B = 60°$, (b) a radial field, and (c) a dipole field with a colatitude of 60°. When LOS integration is neglected, the P simply represents the emission from a given point in the corona. The effect of LOS integration starts to show up for $\rho > 0.4$. The LOS integration results in a decrease of P because of a mixing of (Q/I, U/I) contributions from various spatial points along the LOS. In Figure 3.8(d) we plot LOS-integrated $\log(I)$ as a function of height for the dipole field case. We clearly see the sharp decrease of intensity with height. This decrease in brightness across the disk basically represents the center-to-limb variation in the corona.

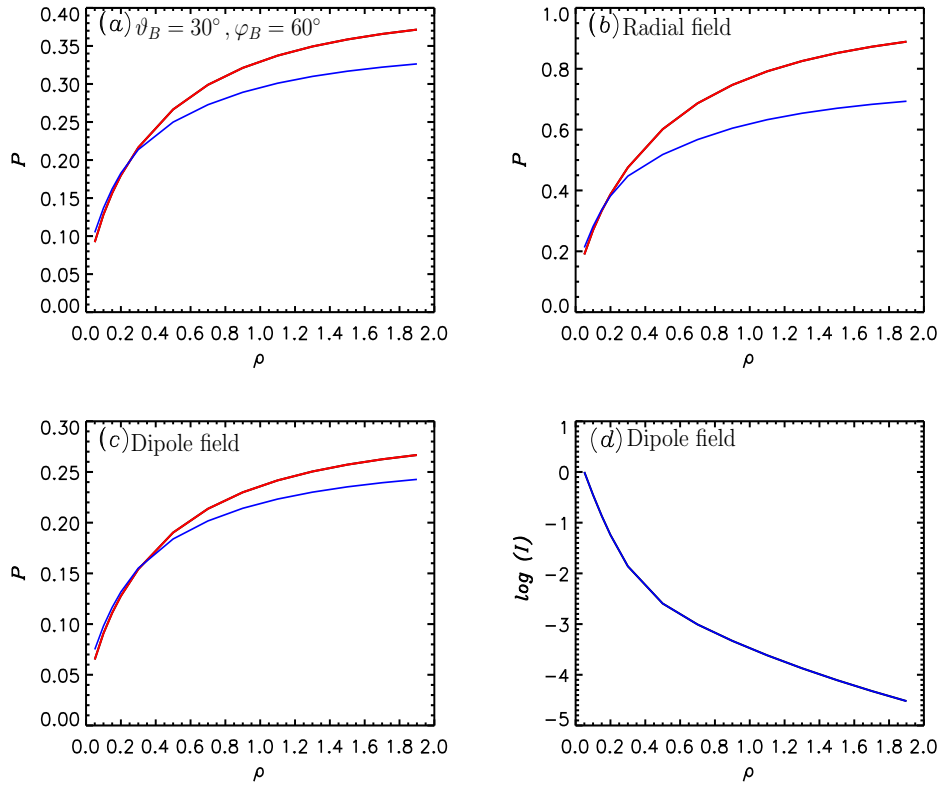

FIGURE 3.8: Frequency-integrated degree of linear polarization ($P = \sqrt{Q^2 + U^2}/I$) (panels a–c) and $\log(I)$ (panel d) as a function of height above the limb. P computed with (blue line) and without (red line) LOS integration are shown. For all the points a constant field strength of $B = 10\,\mathrm{G}$ is used.

3.3.2 Symmetry properties of M1 scattering matrix

We study the symmetry properties of M1 scattering matrix by considering the variation of the magnetic field orientation on the POS. Figure 3.9 shows the polarization diagram as a function of field azimuth φ_B, which is varied in the full range 0° to 360°, for different field inclination ϑ_B. We consider ϑ_B in the range $[0°, 90°]$ in steps of 10°. The LOS-integrated U/I and Q/I at $x = 0$ are plotted. For $\vartheta_B = 0°$, from Equations (3.2) and (3.6) we obtain $U/I = 0$ and Q/I takes the Rayleigh scattered value (φ_B independent). Thus this case represents a point (denoted by plus symbol) in the polarization diagram. For $\vartheta_B \neq 0°$, the breaking of the azimuthal symmetry results in open solid curves in the polarization diagram. As ϑ_B increases, the curvature of these open solid curves increases. The curves are open because we are in the regime of the saturated Hanle effect. The size of the curves initially increases with ϑ_B and then decreases as ϑ_B approaches the

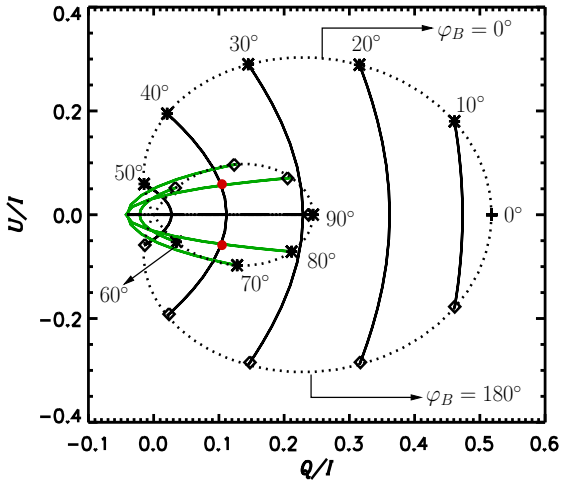

FIGURE 3.9: Polarization diagram for varying $\vartheta_B \in [0°, 90°]$ and $\varphi_B \in [0°, 360°]$ for a constant field strength of $B = 10\,\mathrm{G}$. The LOS is at $h_0 = 0.5\,R_\odot$. The case of $\vartheta_B = 0°$ is represented by the plus symbol and the following curves correspond to different values of ϑ_B increasing in steps of 10°. The points corresponding to $\varphi_B = 0°$ and 360° are marked by an asterisk and $\varphi_B = 180°$ are marked by diamonds. As φ_B increases from 0° to 180° in steps of 10°, we move along the curve from asterisk to diamond. For φ_B between 180° and 360°, the curve is retraced from diamond to asterisk.

Van Vleck angle (54°.7). For ϑ_B larger than the Van Vleck angle, the $(Q/I,\, U/I)$ change their sign and the sense of variation with φ_B is reversed (shown by the green solid lines in Figure 3.9). Furthermore, the size of the polarization diagram also increases. Finally, for $\vartheta_B = 90°$ the polarization diagram becomes a straight line $(U/I = 0)$ with a periodicity of $\varphi_B = 90°$ with respect to the φ_B variation.

The polarization diagrams overlap for $(\vartheta_B,\, \varphi_B)$ and $(180° - \vartheta_B,\, -\varphi_B)$. This symmetry property is observed in both the Hanle regime (figure not shown) and in the saturated Hanle regime. In the latter regime, an additional symmetry is seen with respect to φ_B, namely, for any ϑ_B the polarization diagrams overlap for φ_B and $180° - \varphi_B$. These symmetry properties result in the ambiguity in the pair of Stokes parameters $(Q/I,\, U/I)$, namely, the same values of $(Q/I,\, U/I)$ are obtained for four different choices of the field orientations mentioned above. These are the traditional 180° ambiguities arising due to the symmetry properties of the scattering matrix. In addition to these ambiguities, there is another source of ambiguity in the Stokes parameters that formed in the saturated Hanle regime. This is the so-called Van Vleck ambiguity that was originally noted by House

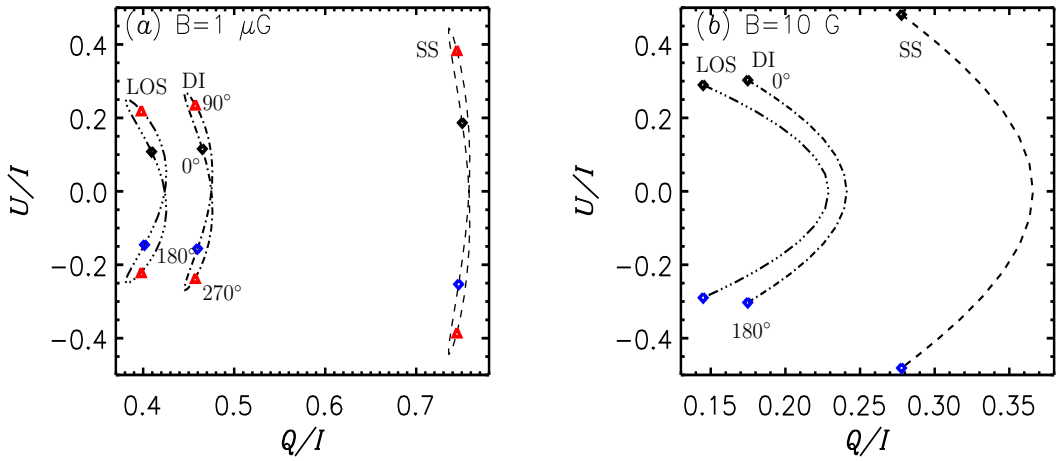

FIGURE 3.10: Polarization diagram for (a) $B = 1\,\mu$G and (b) $B = 10\,$G with $\vartheta_B = 30°$, $\varphi_B \in [0°, 360°]$. Different curves correspond to: dashed (single scattering: SS), dot-dashed (disk integrated: DI), and dash-triple-dotted (LOS-integrated). Black symbols mark both $\varphi_B = 0°$ and 360°.

(1977, see also Casini and Judge 1999), which occurs in a narrow angular range of field orientations around the Van Vleck angle (54.°7). For example, the curves for $\vartheta_B = 40°$ and $\vartheta_B = 80°$ in the polarization diagram (Figure 3.9) intersect at two points that are marked as red dots. This ambiguity adds to the traditional ambiguity discussed above. Thus there could be six pairs of (ϑ_B, φ_B) values that produce the same values of (Q/I, U/I).

Figure 3.10 shows the polarization diagram for a very weak field of $1\,\mu$G (panel a) in the Hanle regime and for 10 G (panel b) in the saturated Hanle regime. The field inclination is fixed at $\vartheta_B = 30°$ and φ_B is varied from 0° to 360°. In the Hanle regime the polarization diagram executes Lissajous figures (namely, closed loops), in comparison to open curves in saturated Hanle regime. In Figure 3.10 we present the polarization diagrams computed using (i) pure single scattering (SS) of an incident vertical beam of radiation in the mid-plane (dashed curves), (ii) after integrating over a cone of incident photospheric radiation (also called disk integrated in the literature – DI) at a height of $h = 0.5\,R_\odot$ (dot-dashed curves), and (iii) the same as case (ii), but performing an integration along the LOS (dash-triple-dotted curves). The size of the polarization diagram decreases from case (i) to case (iii). This is expected as the SS represents a case of the highest degree

of anisotropic scattering, while the anisotropy decreases successively for the other two cases.

3.4 Maps of degree of linear polarization and position angle

In this section, we consider radial and dipole field configurations with an average coronal field strength of 10 G. In order to study the effects of density distributions on the degree of linear polarization formed in the coronal conditions, we consider two types of density distributions namely, (i) spherically symmetric density (SSD) model of House (1972) shown in Figure 3.11a, and is given in Equation (3.10) and (ii) the latitude (λ) dependent density (LDD) model of Saito *et al.* (1970) for sunspot minimum shown in Figure 3.11b and given by

$$\begin{aligned} N(r,\lambda) = \quad & 10^8 \times \{3.09(1-0.5\sin\lambda)(1+\rho)^{-16} + 1.58(1-0.95\sin\lambda)(1+\rho)^{-6} \\ & +0.025(1-\sqrt{\sin\lambda})(1+\rho)^{-2.5}\}, \end{aligned} \tag{3.11}$$

where $\rho = h/R_\odot$. Figure 3.11 clearly depicts the relative intensity (normalized with respect to the maximum calculated intensity) which is proportional to the density distribution under consideration. For the model given above, we calculate the LOS-integrated degree of linear polarization $P = \sqrt{Q^2+U^2}/I$ and position angle, PA $= 0.5\tan^{-1}(U/Q)$. Figure 3.12 shows the map of P and PA for SSD and LDD for the radial field configuration. For the case of SSD, P increases with height and reaches a maximum of 73.3%. Here PA lies along the radius vector. Unlike the SSD case, the map of P for LDD is asymmetric and reaches a maximum of 73.29 % in the polar region. However PA continues to be along the radius vector. The differences in magnitude of degree of linear polarization for SSD and LDD cases start to occur at heights larger than $2R_\odot$. Figure 3.13 shows the map of P and PA for the dipole field configuration with LDD. The Van Vleck effect is observed when P becomes identically zero (symmetric black regions in map) i.e., when ϑ_B= ϑ_V=54°.7 (namely, $\lambda = 19°.5$ and ϑ_V=Van Vleck angle). The PA follows the field lines for $\vartheta_B < \vartheta_V$ and becomes perpendicular to field lines for $\vartheta_B > \vartheta_V$ (radial). For a given radius, P is maximum near the poles and uniformly decreases until

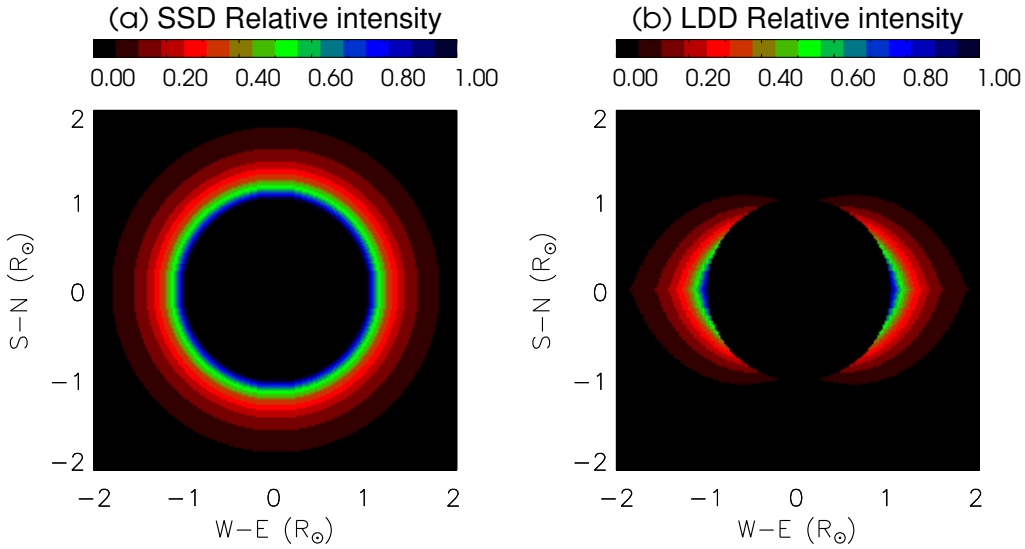

FIGURE 3.11: Maps of relative intensity corresponding to SSD (panel a) and LDD (panel b) with radial field configuration.

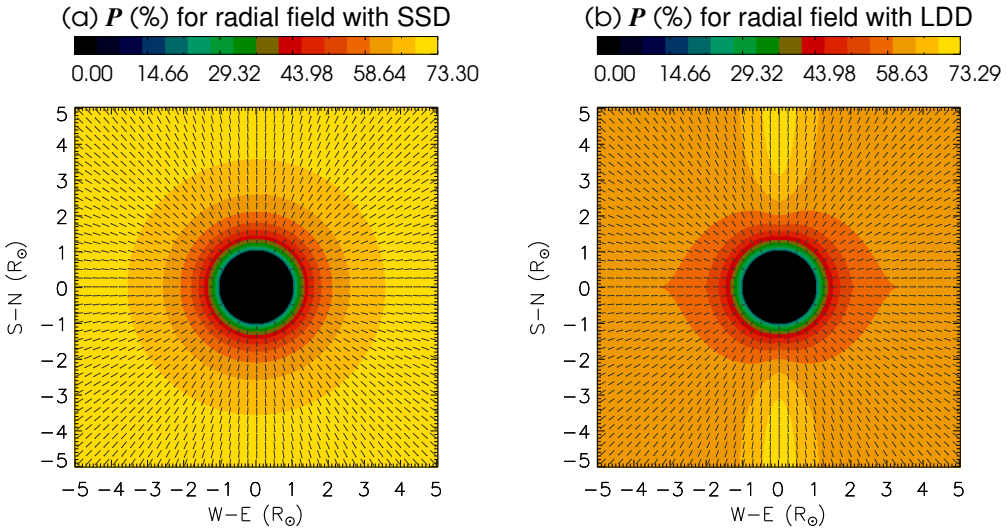

FIGURE 3.12: Maps of degree of linear polarization. Short bars represent the position angle (PA). Panels (a) and (b) correspond respectively to SSD and LDD configurations with radial field.

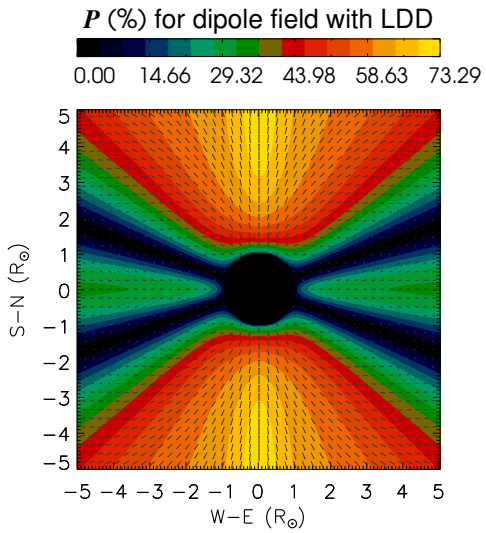

FIGURE 3.13: Maps of degree of linear polarization for the dipole field configuration with LDD. Short bars represent the PA.

the Van Vleck region and then increases marginally until the equator, showing a symmetry about N-S and E-W directions.

3.5 Effect of a constant radial velocity field $V(r)$ on Stokes profiles

Solar corona is known to be dynamic, with solar wind originating in the corona. Thus in this section we study the effects of a non-zero velocity field on the Stokes profiles formed in the solar coronal conditions. Here the velocity field is assumed to be radial and constant throughout the corona. We parameterize the velocity field through the non-dimensional parameter $V(r) = v(r)/v_{\rm th}$, where $v(r)$ is the radial velocity field and $v_{\rm th}$ is the mean thermal velocity. Figure 3.14 shows the spatial variation of the Stokes I, Q/I, U/I, and V/I profiles as a function of the non-dimensional frequency x. This clearly depicts that as the height above the photosphere increases, intensity decreases, while polarization increases which is expected. Figure 3.15 shows the LOS-integrated Stokes profiles for different $V(r)$. These profiles exhibit a broadening that increases with $V(r)$. This is because for $-\pi/2 \leqslant \chi < 0$ (see Figure 3.3) the profiles are redshifted and for $0 < \chi \leqslant \pi/2$ the profiles are blueshifted. Q/I and U/I profiles show significant changes in the

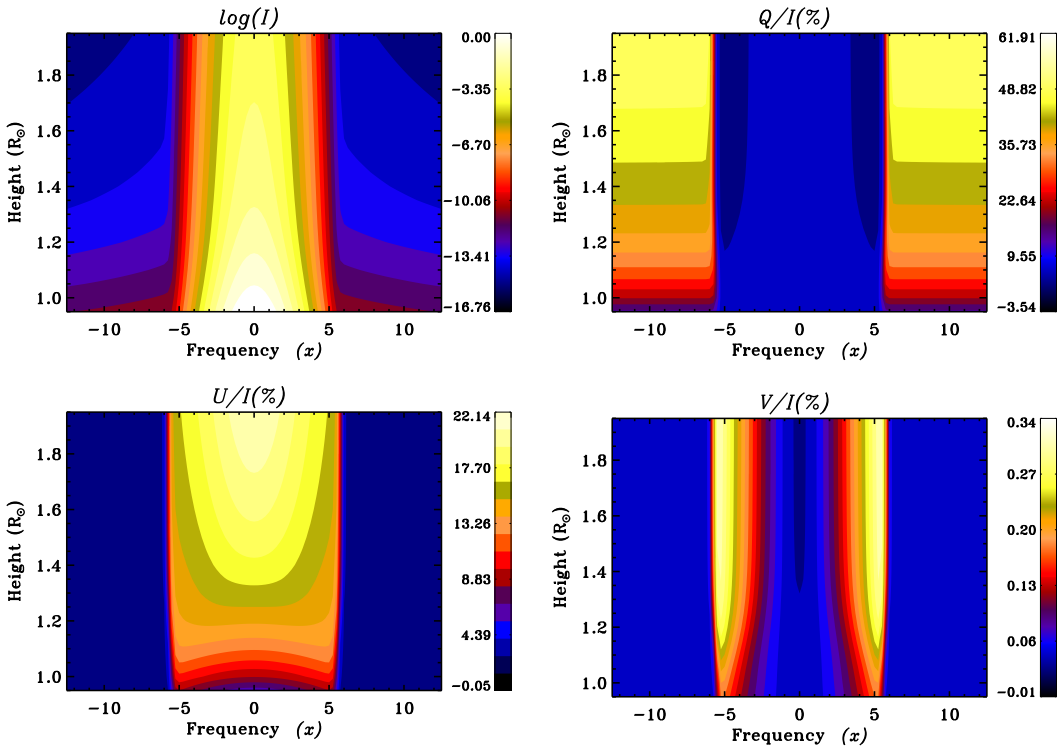

FIGURE 3.14: Spatial variation of Stokes profiles as a function of frequency x for a radial velocity field $V(r) = 1$ mean thermal units and with SSD.

line core. $V/I = 0$ in the static case (due to opposite signs of V/I in the forward and backward lobes with respect to mid-plane $\chi = 0°$). In the presence of velocity fields V/I exhibit a non-zero double-peaked shape. These changes are due to the combined effects of spherical geometry (radius vector making smaller and smaller angles with respect to the LOS, as we move away from the mid-plane) and the projected velocity field.

3.6 Concluding remarks

Here we applied the theory developed in Chapter 2 to study the dependence of polarized forbidden M1 lines on density, magnetic field, and velocity distributions in coronal conditions. For illustrations we considered scattering on the [Fe XIII] ion placed at a height of h above the solar limb. We approximated the [Fe XIII] ion by a two-level atom model. In particular, we were interested in the [Fe XIII] 10747 Å

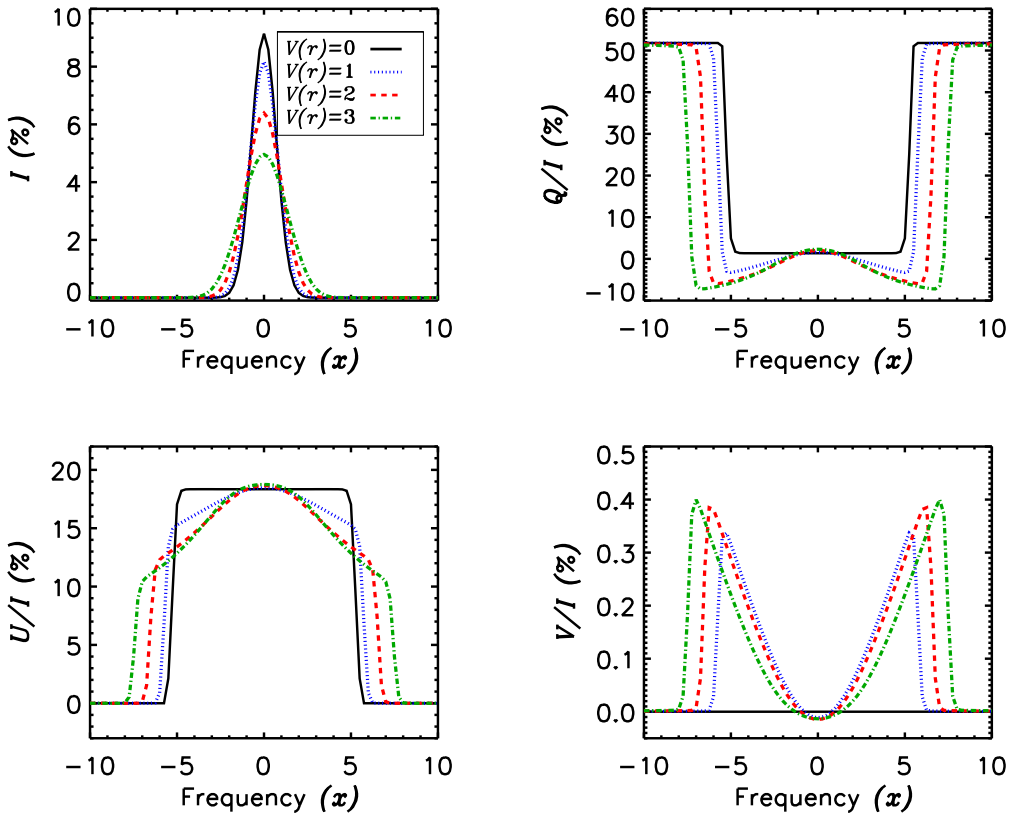

FIGURE 3.15: Plot of Stokes profiles as a function of frequency x for $r = 1.5R_\odot$, for radial velocity fields $V(r) = 0, 1, 2, 3$ mean thermal units. The results are shown for a dipole field with a colatitude of 60°

.

line. We chose this particular line as it will be used for spectropolarimetric measurements in the solar corona by Aditya-L1 mission. However, as demonstrated in Sahal-Bréchot (1977) and House (1977), the two-level atom approximation is insufficient when collisions are important. Indeed, they show that only when electron densities are lower than $10^7\,\mathrm{cm}^{-3}$, the two-level atom approximation suffices to model the polarization profiles of [Fe XIII] 10747 Å line. For the electron density model considered in this chapter (following House 1977), this occurs at heights larger than 0.5 $R_\odot$ above the limb. However, the heights at which the transition from collision-dominated excitation to radiative-dominated excitation takes place depend on the electron density model and also on the spectral line under consideration (see Habbal *et al.* 2011). For example, electron densities in coronal holes may drop below $10^7\,\mathrm{cm}^{-3}$ around $0.2\,R_\odot$ above the limb (see Figure 2 of Doschek *et al.* 1997). Clearly, our formalism can be applied to those regions in the solar

corona where radiative excitations dominate. Near the solar limb, where collisions cannot be neglected, one should resort to the density matrix formalism developed by the previous authors (Sahal-Bréchot 1977; House 1977; Casini and Judge 1999) which is however limited to the saturated Hanle regime. Therefore we showed the behavior of the Stokes profiles emerging from a height $h = 0.5\,R_\odot$ above the solar limb. We considered different cases such as single scattering, integration over a cone of incident radiation from the photosphere (also called disk integration), and integration along the LOS for an atom in conditions typical of the solar corona. We have explored a broad range of field strengths and different field orientations. As expected, the [Fe XIII] 10747 Å line remains in the saturated Hanle regime for a rather wide range of field strengths. We also presented frequency-integrated degree of linear polarization for different field distributions (such as radial and dipole fields). Furthermore, we studied the symmetry properties of the M1 scattering matrix through polarization diagrams.

For our studies we have varied the field strength from μG to kG ranges. However, only fields on the order of 1–30 G are expected in the solar corona (Lin *et al.* 2000). Magnetic fields as low as μG can be found in diffuse media such as the ISM, circumstellar regions, and supernova remnants (Yan and Lazarian 2006, Ferrière 2009, Reynolds *et al.* 2012). In these regions several forbidden lines are observed that in principle may respond to the μG field through the Hanle effect. Fields in the range of a few hecto-Gauss to kG are found in stellar atmospheres (Landstreet 2015). Indeed, the Hanle effect in allowed lines (E1 transitions) can be used as a tool to diagnose such stellar magnetic fields (see e.g., López Ariste *et al.* 2011, Ignace *et al.* 2011, Bommier 2012, Manso Sainz and Martínez González 2012). As for the forbidden lines, they are also formed in the stellar winds, where field strengths as large as kG can be found (de la Chevrotière *et al.* 2014). Our theoretical formulation may find application in modeling the polarization profiles of forbidden lines formed in the above-mentioned astrophysical contexts.

The intensity and degree of linear polarization maps showed that, for the chosen density distribution, the intensity is more sensitive to the density gradient than degree of polarization P for $1 \lesssim R < 2R_\odot$. For $R \gtrsim 2R_\odot$ the P continues to be sensitive to density distribution. Thus, polarization measurements provide a better diagnostic tool to detect density and magnetic field variations in the corona.

We showed that the Stokes profiles are sensitive to the velocity fields in the corona, thereby serving as diagnostic tools.

Part-II

Polarized Radiative Transfer in Sperically Symmetric Moving Atmospheres

Chapter 4

Iterative Techniques to Solve Polarized Line Formation in Spherically Symmetric Static Atmospheres [1]

An overview

A more precise modeling of polarized spectral lines formed in extended stellar atmospheres requires the solution of the radiative transfer equation for the Stokes vectors in a spherical geometry than in a planar geometry. In this chapter we present the modern iterative techniques based on operator perturbation, to solve the spherically symmetric polarized radiative transfer equation. We consider scattering on a two-level atom accounting for partial frequency redistribution (PFR). It is well-known that the numerical solution to such problems requires higher grid resolution. Consequently Jacobi-based methods lead to somewhat smaller convergence rate. The convergence rate can be improved by a factor of 2 or more when highly convergent iterative schemes based on Gauss-Seidel (GS) and successive overrelaxation (SOR) methods are used over Jacobi-based method. Here we present the Jacobi, GS, and SOR iterative techniques for solving polarized line

[1] This chapter is based on the publications: Megha *et al.* (2019b, 2020a)

formation in spherically symmetric atmospheres, and discuss their convergence behavior.

4.1 Introduction

It is well-known that extended stellar atmospheres cannot be represented by plane-parallel stratification, but by a spherically symmetric medium. Therefore to study the spectral lines formed in extended atmospheres it is necessary to develop numerical methods to solve the radiative transfer equation in spherically symmetric medium. Furthermore, to model strong resonance lines it is necessary to account for partial frequency redistribution (PFR) in scattering. Early attempts for solving the transfer equation in spherical geometry were by McCrea (1928), Chandrasekhar (1934) and Kosirev (1934) who used the Eddington approximation. A variable Eddington factor method which uses the Feautrier solution along rays of constant impact parameter in the spherical geometry were developed by Hummer and Rybicki (1971), Kunasz and Hummer (1974a,b), and Mihalas (1978). For a more complete list of references on numerical methods to solve spherical scalar (unpolarized) radiative transfer equation we refer the reader to Peraiah (2002) and Hubeny and Mihalas (2014, see also Anusha *et al.* 2009).

Cannon (1973) developed an iterative technique based on operator splitting or perturbation for the planar geometry and introduced the concept of approximate lambda operator. Olson *et al.* (1986) proposed that an optimum choice for the approximate lambda operator is the diagonal of the actual lambda operator. This method which is popularly knows as approximate or accelerated lambda iteration (ALI) method was also used to solve the transfer problem in spherical geometry (see reviews by Hubeny 2003; Hamann 2003). The ALI method which was initially developed to solve unpolarized planar transfer equation for a two-level atom with complete frequency redistribution (CFR) was extended to include PFR by Paletou and Auer (1995, see also initial attempts by Vardavas and Cannon 1976, Scharmer 1983). The ALI method discussed above is based on the Jacobi iterative scheme, which exhibits slower convergence rates as the number of spatial points per decade is increased. Since there are wide varieties of astrophysical objects with different

types of environment, understanding and studying them require challenging radiative transfer computations. Therefore it is necessary to develop fast iterative techniques to solve such radiative transfer problems.

Fast iterative techniques based on GS and SOR methods were developed by Trujillo Bueno and Fabiani Bendicho (1995) for solving unpolarized, one dimensional, planar transfer problem for a two-level atom model with CFR. These iterative schemes have a convergence rate which is equivalent to that corresponding to upper or lower triangular approximate lambda operators, however without requiring construction and inversion of such operators. Therefore, the computing time per iteration is similar to that of the Jacobi scheme, but the number of iterations needed to reach convergence is an order of magnitude smaller. A Jacobi based multilevel ALI (MALI) method to solve unpolarized radiative transfer for multilevel atoms with CFR was developed by Rybicki and Hummer (1991, 1992). This MALI method was extended by Uitenbroek (2001) to include PFR in scattering. Auer *et al.* (1994) generalized the Jacobi based MALI of Rybicki and Hummer (1991) to multi-dimensions along with grid doubling technique. Fabiani Bendicho *et al.* (1997); Fabiani Bendicho and Trujillo Bueno (1999) extended the MALI to include GS and SOR schemes along with non-linear multi-grid techniques (Hackbush 1985) and they called it a MUlti-level Gauss-Seidel (MUGA) method. Paletou and Léger (2007) described step-by-step implementation of GS and SOR schemes to multi-level atom models in 1D planar geometry and provided practical description of implementing these schemes in short-characteristics (Olson and Kunasz 1987) formal solver. Léger *et al.* (2007) aimed at providing all the necessary elements required for a successful implementation of GS and SOR schemes in a 2D Cartesian geometry to study the solar prominences.

Extension of Jacobi based ALI methods to solve polarized planar transfer equation including non-magnetic resonance scattering on a two-level atom with CFR were by Faurobert-Scholl *et al.* (1997), Trujillo Bueno and Manso Sainz (1999); and with PFR was by Paletou and Faurobert-Scholl (1997). Extensions of GS and SOR methods to non-magnetic resonance scattering polarization were done by Trujillo Bueno and Manso Sainz (1999) for the case of CFR and Sampoorna and Trujillo Bueno (2010) with the inclusion of all the three angle-averaged (AA) redistribution functions of Hummer (1962).

On the other hand the MUGA method was extended to handle scalar spherical transfer by Asensio Ramos and Trujillo Bueno (2006), Cernicharo *et al.* (2006) and with the inclusion of line overlap problem by Daniel and Cernicharo (2008). Jacobi, GS, and SOR methods along with preconditioned bi-conjugate gradient method was presented in Anusha *et al.* (2009) for the case of scalar 1D spherical geometry with CFR. A discrete space method was developed in Nagendra (1988, 1989, 1994, 1995) to solve the polarized resonance line transfer problem in spherically symmetric medium including both CFR and PFR. In the present chapter, we extend the scalar Jacobi, GS, and SOR methods to solve the polarized line transfer equation in 1D spherical geometry including both CFR and PFR in the absence of magnetic fields. Following Nagendra *et al.* (1998), we refer to these ALI based methods as polarized ALI (PALI) methods. To determine the accuracy of the extended iterative scheme we determine the true error following Auer *et al.* (1994). A study of true error of such iterative techniques has also been presented in: Trujillo Bueno and Fabiani Bendicho (1995); Trujillo Bueno and Manso Sainz (1999); Chevallier *et al.* (2003); Asensio Ramos and Trujillo Bueno (2006); Anusha *et al.* (2009); Sampoorna and Trujillo Bueno (2010); Sampoorna and Nagendra (2016).

This chapter is organized as follows. In Section 4.2 we set up the basic polarized transfer equation in spherically symmetric medium and describe the necessary terms. In Section 4.3 we present in detail the iterative techniques to solve the problem in hand. In Section 4.5 we present a comparison of the Jacobi, GS, and SOR iterative techniques by studying the maximum relative change (MRC) and the surface true error. Conclusions are drawn in Section 4.6.

4.2 Polarized line transfer equation in spherical atmospheres

We consider an isothermal one-dimensional spherically symmetric atmosphere along with a two-level atom model having an infinitely sharp and unpolarized lower level. The polarized PFR transfer equation for a spherically symmetric

medium in divergence form is given by

$$\mu\frac{\partial \boldsymbol{I}(r,\mu,x)}{\partial r}+\frac{(1-\mu^2)}{r}\frac{\partial \boldsymbol{I}(r,\mu,x)}{\partial \mu}=-\chi(r,x)[\boldsymbol{I}(r,\mu,x)-\boldsymbol{S}(r,\mu,x)], \qquad (4.1)$$

where $\boldsymbol{I}=(I,Q)^{\mathrm{T}}$ is the polarized intensity vector, $\boldsymbol{S}$ is the total source vector, r is the radial distance, $x=(\nu-\nu_0)/\Delta\nu_D$ is the non-dimensional frequency measured in Doppler width ($\Delta\nu_D$) units with ν_0 being the line center frequency, and $\mu=\cos\vartheta$ with ϑ being the inclination of the ray with respect to the local radius vector. The total absorption coefficient is defined as $\chi(r,x)=\chi_l(r)\phi(x)+\chi_c(r)$ where χ_l and χ_c are, respectively, the line center and continuum absorption coefficients. The line profile function $\phi(x)=H(a,x)$ is the normalized Voigt function, where a is the damping parameter.

The polarized transfer equation (4.1) is a partial differential equation in r and μ. The numerical complexity of solving such an equation can be reduced by using characteristic rays along which the polarized transfer equation becomes an ordinary differential equation involving a single derivative with respect to the path length along that ray. Furthermore, to effectively treat the outward peaking of the radiation field inherent in a spherically symmetric atmosphere, we transform the transfer equation (4.1) which is given in (r,μ) coordinate system to (p,z) representation (Hummer and Rybicki 1971). The (p,z) coordinate system is shown in Figure 4.1. The impact parameter p is the perpendicular distance of a ray from a parallel ray passing through the center of the star. The impact parameter rays are taken to be tangent to spherical shells (see Figure 4.1). z is the distance along a given impact parameter ray, measured from the plane through the center of the star perpendicular to the central ray. It is zero at the mid-line (see Figure 4.1) and is positive towards the observer and negative away from the observer. This method of solving the transfer equation along each ray of constant impact parameter is termed as ray-by-ray approach. The rays which intersect the core are called core rays and the rest of them are called lobe rays. In the (p,z) coordinate system we define a central core which is a sphere of radius $r=1$ in units of the core radius R_{c}. The surface is a sphere of radius $r=R$ in units of R_{c}. In the (p,z) representation, the radius r is related to p and z as $r(z,p)=\sqrt{z^2+p^2}$ and therefore $z=\sqrt{r^2-p^2}$. Thus along a given characteristic ray (or tangent ray),

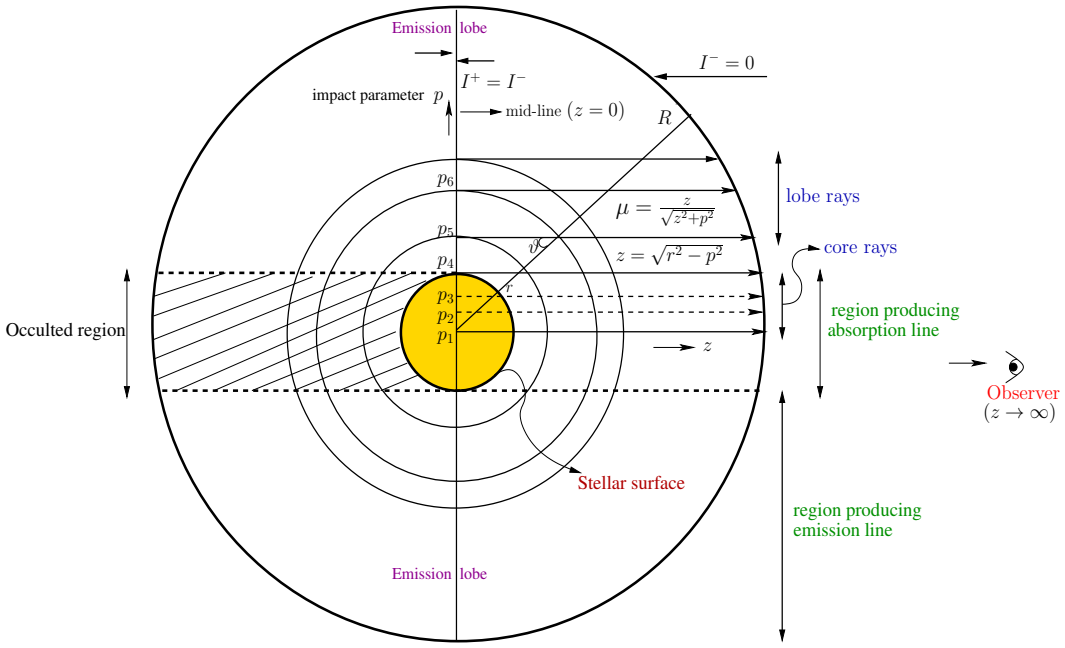

FIGURE 4.1: The (p, z) coordinate system used to solve the transfer equation in the spherically symmetric atmosphere.

the differential operator in z can be written as

$$\frac{\partial}{\partial z} = \mu \frac{\partial}{\partial r} + \frac{1-\mu^2}{r} \frac{\partial}{\partial \mu}. \tag{4.2}$$

The optical depth scale along the tangent rays is computed using $d\tau_z = d\tau_r/\mu$, where $d\tau_r$ is the optical depth along the radius vector defined as $d\tau_r = -\chi_l(r)dr$. Using Equation (4.2) the transfer equation in the (p, z) coordinate system can be written as

$$\pm \frac{\partial \boldsymbol{I}^{\pm}(z,p,x)}{\partial \tau(z,x)} = \boldsymbol{I}^{\pm}(z,p,x) - \boldsymbol{S}(z,p,x), \tag{4.3}$$

for outgoing $(+)$ and incoming $(-)$ rays, respectively. The monochromatic optical depth along the tangent rays is given by $d\tau(z,x) = [\phi(x) + \beta_c]d\tau_z$, with $\beta_c = \chi_c(r)/\chi_l(r)$. For a given spherical shell of radius r, the direction cosines $\mu(r,p) = \sqrt{1-(p^2/r^2)}$ with $\mu \in [0,1]$. The total source vector is defined as

$$\boldsymbol{S}(z,p,x) = \frac{\phi(x)\boldsymbol{S}_l(z,p,x) + \beta_c \boldsymbol{S}_c}{\phi(x) + \beta_c}, \tag{4.4}$$

where $\boldsymbol{S}_c = B_{\nu_0}\boldsymbol{U}$ is the unpolarized continuum source vector, with B_{ν_0} the Planck function at the line center, and $\boldsymbol{U} = (1,0)^{\mathrm{T}}$. For a two-level atom with an infinitely

sharp and unpolarized lower-level, the line source vector has the form

$$\boldsymbol{S}_l(z,p,x) \;=\; \epsilon B_{\nu_0}\boldsymbol{U} + \int_{-\infty}^{+\infty} dx' \frac{1}{2}\int_{-1}^{+1} d\mu' \frac{\mathbf{R}(x,\mu,x',\mu')}{\phi(x)}\boldsymbol{I}(\tau,\mu',x'), \quad (4.5)$$

where ϵ is the thermalization parameter. Here the primed symbols x', μ' refer to the incoming photons and the unprimed ones to scattered photons. $\mathbf{R}(x,\mu,x',\mu')$ is the collisional redistribution matrix for the non-magnetic case (Domke and Hubeny 1988, Bommier 1997a). The angle-averaged (AA) version of this redistribution matrix for the static case can be written as

$$\mathbf{R}(x,\mu,x',\mu') = \sum_{K=0,2} W_K(J_l,J_u)\{\alpha R_{\mathrm{II,AA}}(x,x') + [\beta^{(K)}-\alpha]R_{\mathrm{III,AA}}(x,x')\} \times \mathbf{P}^K_{\mathrm{R}}(\mu,\mu'), \quad (4.6)$$

where the coefficient $W_0(J_l,J_u)=1$, with J_l and J_u being the total angular momentum quantum numbers of the lower and upper levels, respectively. The coefficient $W_2(J_l,J_u)$ characterizes the maximum linear polarization that can be produced in the line. $R_{\mathrm{X,AA}}$ with X=II, III are the AA redistribution functions of Hummer (1962). $\mathbf{P}^K_{\mathrm{R}}(\mu,\mu')$ denote the multipolar components of the Rayleigh phase matrix (see Landi Degl'Innocenti 1984). The branching ratios α and $\beta^{(K)}$ are given by

$$\alpha = \frac{\Gamma_{\mathrm{R}}}{\Gamma_{\mathrm{R}}+\Gamma_{\mathrm{I}}+\Gamma_{\mathrm{E}}}, \quad (4.7)$$

$$\beta^{(K)} = \frac{\Gamma_{\mathrm{R}}}{\Gamma_{\mathrm{R}}+\Gamma_{\mathrm{I}}+D^{(K)}}, \quad (4.8)$$

where Γ_{I} is the inelastic collisional deexcitation rate, Γ_{R} is the radiative deexcitation rate, Γ_{E} and $D^{(K)}$ are elastic and depolarizing collisional rates respectively.

From Equation (4.5) it is clear that the line source vector depends on both frequency x and impact parameter p. To reduce the computational cost, it is beneficial to factorize the Rayleigh phase matrix into a product of two 2×2 matrices that depend separately on μ and μ'. Such a factorization comes out naturally if we use the irreducible tensors $\mathcal{T}^K_Q(i,\boldsymbol{n})$ (see Landi Degl'Innocenti 1984) to derive the Rayleigh phase matrix. Here for each K, the value of Q varies from $-K$ to $+K$ in steps of one, $\boldsymbol{n}=(\vartheta,\varphi)$ denote the ray direction with respect to the local radius vector, and $i=0,1$. Frisch (2007) provided an elegant way to decompose the

Stokes vector components into the irreducible components in the weak field regime of Hanle effect. These irreducible components are cylindrically symmetric when CFR or angle-averaged PFR is chosen as the frequency redistribution mechanism. The numerical methods developed based on these cylindrically symmetric components are superior to those based on the Stokes vector representation. Following Frisch (2007), the Stokes vector can be decomposed as

$$I_i^{\pm}(z,p,x) = \sum_{K=0,2} \tilde{\mathcal{T}}_0^K(i,\vartheta)\mathcal{I}_0^{K,\pm}(z,p,x), \tag{4.9}$$

where $i = 0, 1$ denote the Stokes parameters I, Q and $\mathcal{T}_Q^K(i,\boldsymbol{n})=\tilde{\mathcal{T}}_Q^K(i,\vartheta)\mathrm{e}^{\mathrm{i}Q\varphi}$. A decomposition similar to Equation (4.9) can be written relating U_i, $S_i(z,p,x)$, and $S_{l,i}(z,p,x)$ to $\mathcal{U}_0^K$, $\mathcal{S}_0^K(z,x)$, and $\mathcal{S}_{l,0}^K(z,x)$, respectively. $\mathcal{I}_0^{K,\pm}(z,p,x)$ and $\mathcal{S}_0^K(z,x)$ are the irreducible tensor components of the Stokes and the source vectors respectively. The transfer equation in the irreducible basis can be written as

$$\pm \frac{\partial \boldsymbol{\mathcal{I}}^{\pm}(z,p,x)}{\partial\tau(z,x)} = \boldsymbol{\mathcal{I}}^{\pm}(z,p,x) - \boldsymbol{\mathcal{S}}(z,x), \tag{4.10}$$

where $\boldsymbol{\mathcal{I}}^{\pm} = [\mathcal{I}_0^{0,\pm}, \mathcal{I}_0^{2,\pm}]^{\mathrm{T}}$ and $\boldsymbol{\mathcal{S}} = [\mathcal{S}_0^0, \mathcal{S}_0^2]^{\mathrm{T}}$. Clearly, $\boldsymbol{\mathcal{S}}$ is now independent of p and has a form similar to Equation (4.4), but with the irreducible line source vector given by

$$\boldsymbol{\mathcal{S}}_l(z,x) = \epsilon B_{\nu_0}\boldsymbol{\mathcal{U}} + \overline{\boldsymbol{\mathcal{J}}}_x, \tag{4.11}$$

where $\boldsymbol{\mathcal{U}} = [1,0]^{\mathrm{T}}$ and the frequency-averaged PFR mean intensity vector is given by

$$\overline{\boldsymbol{\mathcal{J}}}_x = \int_{-\infty}^{+\infty} dx' \frac{\boldsymbol{\mathcal{R}}(x,x')}{\phi(x)}\,\boldsymbol{\mathcal{J}}_{x'}, \tag{4.12}$$

where

$$\boldsymbol{\mathcal{J}}_{x'} = \frac{1}{2}\int_{-1}^{+1} d\mu' \boldsymbol{\Psi}(\mu')\boldsymbol{\mathcal{I}}(\tau,\mu',x'). \tag{4.13}$$

Here $\boldsymbol{\Psi}(\mu)$ is the (2×2) Rayleigh phase matrix in the irreducible basis (Frisch 2007) and $\boldsymbol{\mathcal{R}}(x,x')$ is the PFR matrix in the irreducible basis. The latter is given by

$$\boldsymbol{\mathcal{R}}(x,x') = \mathbf{W}\{\alpha\mathbf{E}R_{\mathrm{II,AA}}(x,x') + (\boldsymbol{\mathcal{B}} - \alpha\mathbf{E})R_{\mathrm{III,AA}}(x,x')\}, \tag{4.14}$$

where $\mathbf{E}$ is a (2×2) identity matrix, $\mathbf{W} = \mathrm{diag}[\mathrm{W}_0, \mathrm{W}_2]$ and $\boldsymbol{\mathcal{B}} = \mathrm{diag}[\beta^{(0)}, \beta^{(2)}]$ are (2×2) diagonal matrices. It is useful to re-write Equation (4.13) as

$$\boldsymbol{\mathcal{J}}_{x'} = \boldsymbol{\mathcal{J}}^{-}_{x'} + \boldsymbol{\mathcal{J}}^{+}_{x'}, \tag{4.15}$$

where

$$\boldsymbol{\mathcal{J}}^{-}_{x'} = \frac{1}{2}\int_{-1}^{0} d\mu' \boldsymbol{\Psi}(\mu')\boldsymbol{\mathcal{I}}^{-}(\tau, \mu', x') \quad \text{and} \quad \boldsymbol{\mathcal{J}}^{+}_{x'} = \frac{1}{2}\int_{0}^{+1} d\mu' \boldsymbol{\Psi}(\mu')\boldsymbol{\mathcal{I}}^{+}(\tau, \mu', x'). \tag{4.16}$$

4.3 Iterative methods to solve polarized spherical radiative transfer equation

An iterative method is initiated by first assuming a given value for the line source vector $\boldsymbol{\mathcal{S}}_l(z, x)$, which is either zero or the thermal source vector. Once the total source vector is known the transfer equation (4.10) can be solved by applying a short-characteristic formal solution method of Olson and Kunasz (1987). Such a formal solution gives the irreducible Stokes vector $\boldsymbol{\mathcal{I}}^{\pm}$ at every z, p, x values, which can be used to compute new values of $\overline{\mathcal{J}}_x$ and consequently $\boldsymbol{\mathcal{S}}(z, x)$. This process is repeated until the irreducible source vector and Stokes vector converges. Thus an iterative method involves the computation of a series of formal solution of transfer equation. The convergence of this iterative method is accelerated by using the Jacobi, GS, and SOR schemes, which will be discussed in this section. For a more detailed physical and mathematical insights into the iterative methods based on operator splitting the reader is referred to Hubeny (2003, see also Hubeny 1992).

4.3.1 Formal solution

The formal solution of Equation (4.10) can be written as

$$\boldsymbol{\mathcal{I}}^{\pm}(p, x) = \boldsymbol{\Lambda}^{\pm}(p, x)[\boldsymbol{\mathcal{S}}(x)] + \boldsymbol{T}^{\pm}(p, x), \tag{4.17}$$

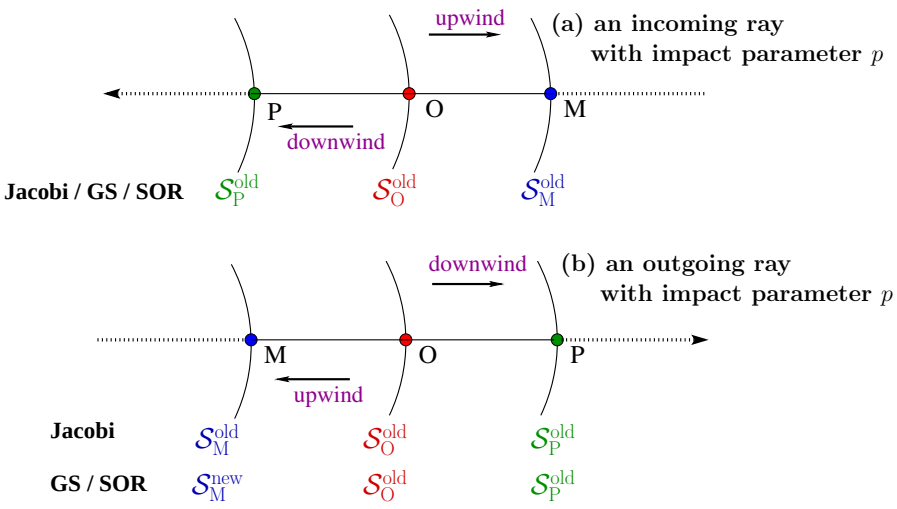

FIGURE 4.2: A schematic representation of the one-dimensional short-characteristic formal solution on an MOP stencil along both incoming (a) and outgoing (b) characteristic rays with a given impact parameter p in the spherical atmosphere.

where for notational brevity we suppress the dependence on z. $\boldsymbol{T}^{\pm}(p,x)$ is the directly transmitted two-component Stokes vector due to the incident radiation given at the boundaries and $\boldsymbol{\Lambda}^{\pm}(p,x)$ is a $2N \times 2N$ integral operator whose elements depend on the optical distances between the grid points, with N being the number of spatial grid points. We implement the short-characteristic integration technique of Olson and Kunasz (1987) for obtaining the formal solution. We use parabolic interpolation with coefficients $\Psi_{\rm M}^{\pm}$, $\Psi_{\rm O}^{\pm}$, and $\Psi_{\rm P}^{\pm}$ for $\boldsymbol{\mathcal{S}}$, on a stencil of short-characteristic MOP (with O being a given point, M and P being the upwind and downwind points, respectively, see Figure 4.2). Using this, the short-characteristic formal solution for a spherically symmetric atmosphere at a given point "O" along a given ray of impact parameter p and frequency x can be written as

$$\boldsymbol{\mathcal{I}}_{\rm O}^{\pm}(p,x) = e^{-\Delta\tau_{\rm MO}}\boldsymbol{\mathcal{I}}_{\rm M}^{\pm}(p,x) + \Psi_{\rm M}^{\pm}(p,x)\boldsymbol{\mathcal{S}}_{\rm M}(x) + \Psi_{\rm O}^{\pm}(p,x)\boldsymbol{\mathcal{S}}_{\rm O}(x) + \Psi_{\rm P}^{\pm}(p,x)\boldsymbol{\mathcal{S}}_{\rm P}(x), \tag{4.18}$$

where $\Delta\tau_{\rm MO}$ is the optical distance on the segment MO. Substituting Equation (4.13) in (4.17), the mean intensity vector can be written as

$$\boldsymbol{\mathcal{J}}_x = \boldsymbol{\Lambda}_x[\boldsymbol{\mathcal{S}}_x] + \boldsymbol{T}_x, \tag{4.19}$$

where for notational brevity "x" appears as subscript and monochromatic Lambda operator is given by

$$\mathbf{\Lambda}_x = \frac{1}{2}\int_{-1}^{+1} \mathbf{\Psi}(\mu)\mathbf{\Lambda}^{\pm}(p,x)d\mu. \tag{4.20}$$

Also $\boldsymbol{T}_x$ is given by

$$\boldsymbol{T}_x = \frac{1}{2}\int_{-1}^{+1} \mathbf{\Psi}(\mu)\boldsymbol{T}^{\pm}(p,x)d\mu. \tag{4.21}$$

Following Sampoorna and Trujillo Bueno (2010) we now write the two-component mean intensity vector at given depth point index k as

$$\begin{aligned}\boldsymbol{\mathcal{J}}_{x,k} = \quad & \mathbf{\Lambda}_{x,k1}\boldsymbol{\mathcal{S}}^a_{x,1} + ... + \mathbf{\Lambda}_{x,kk-1}\boldsymbol{\mathcal{S}}^a_{x,k-1} + \mathbf{\Lambda}_{x,kk}\boldsymbol{\mathcal{S}}^b_{x,k} + \mathbf{\Lambda}_{x,kk+1}\boldsymbol{\mathcal{S}}^c_{x,k+1} + ... \\ & + \mathbf{\Lambda}_{x,kN}\boldsymbol{\mathcal{S}}^c_{x,N} + \boldsymbol{T}_{x,k}. \end{aligned} \tag{4.22}$$

In the above equation a, b, and c are symbols which indicate whether the source vector values we choose are "old" or "new".

4.3.2 Jacobi iterative scheme

The Jacobi iterative scheme for the scalar and polarized PFR transfer problems are respectively discussed in Paletou and Auer (1995) and Paletou and Faurobert-Scholl (1997). According to this scheme $a = c =$ old and $b =$ new is chosen in Equation (4.22) (see also Figure 4.2 for clarity) and we obtain

$$\overline{\boldsymbol{\mathcal{J}}}_{x,k} = \overline{\boldsymbol{\mathcal{J}}}^{\,\mathrm{old}}_{x,k} + \int_{-\infty}^{+\infty} dx' \frac{\boldsymbol{\mathcal{R}}(x,x')}{\phi(x)}\, p_{x'}\mathbf{\Lambda}_{x',kk}\delta\boldsymbol{\mathcal{S}}_{lx',k}, \tag{4.23}$$

where $p_x = \phi(x)/[\phi(x)+\beta_c]$ and the line source vector corrections at a given depth point k are given by

$$\delta\boldsymbol{\mathcal{S}}_{lx,k} - \int_{-\infty}^{+\infty} \frac{\boldsymbol{\mathcal{R}}(x,x')}{\phi(x)} p_{x'}\mathbf{\Lambda}_{x',kk}\delta\boldsymbol{\mathcal{S}}_{lx',k}dx' = \boldsymbol{r}_{x,k}, \tag{4.24}$$

where the residual vector $\boldsymbol{r}_{x,k}$ is

$$\boldsymbol{r}_{x,k} = \epsilon B\boldsymbol{\mathcal{U}} + \overline{\boldsymbol{\mathcal{J}}}^{\,\mathrm{old}}_{x,k} - \boldsymbol{\mathcal{S}}^{\mathrm{old}}_{lx,k}. \tag{4.25}$$

Equation (4.24) can be solved either using a frequency-by-frequency (FBF) method (Paletou and Auer 1995; Sampoorna *et al.* 2008) or a core-wing method (Paletou and Auer 1995; Paletou and Faurobert-Scholl 1997; Nagendra *et al.* 1999; Fluri *et al.* 2003). FBF method involves inversion of a matrix which can become computationally expensive when large frequency bandwidths are used, whereas the core-wing method approximates Equation (4.23) by a set of algebraic equations that can be solved faster without requiring much computing power. The core-wing method for the redistribution matrix given in Equation (4.14) is discussed in Sampoorna and Trujillo Bueno (2010). We follow this method for the case of spherical atmosphere.

4.3.3 GS and SOR iterative schemes

Here we first recall the GS and SOR methods presented in Sampoorna and Trujillo Bueno (2010) for the case of polarized line transfer with PFR in polarized planar atmospheres and then extend them to the case of spherical atmospheres. For the GS iterative scheme we set c = old and $a = b$ = new in Equation (4.22) and we obtain

$$\overline{\boldsymbol{\mathcal{J}}}_{x,k} = \overline{\boldsymbol{\mathcal{J}}}^{\text{old+new}}_{x,k} + \int_{-\infty}^{+\infty} dx' \frac{\boldsymbol{\mathcal{R}}(x,x')}{\phi(x)} \boldsymbol{\Lambda}_{x',kk} \delta\boldsymbol{\mathcal{S}}_{x',k}, \tag{4.26}$$

where $\delta\boldsymbol{\mathcal{S}}_{x,k} = p_x \delta\boldsymbol{\mathcal{S}}_{lx,k}$ is the total source vector correction. $\overline{\boldsymbol{\mathcal{J}}}^{\text{old+new}}_{x,k}$ is the PFR mean intensity vector calculated using the "new" values of the source vector at grid points 1, 2, $\ldots, k-1$ and the "old" values at points k, $k+1$, $\ldots, N$. The line source vector corrections at a given depth point k are given by Equation (4.24) but now the residual vector has the form

$$\boldsymbol{r}_{x,k} = \epsilon B\boldsymbol{\mathcal{U}} + \overline{\boldsymbol{\mathcal{J}}}^{\text{old+new}}_{x,k} - \boldsymbol{\mathcal{S}}^{\text{old}}_{lx,k}. \tag{4.27}$$

For the case of SOR iterative scheme the line source vector corrections are calculated from the $\delta\boldsymbol{\mathcal{S}}^{\text{GS}}_{lx,k}$ at the nth iterate as

$$\delta\boldsymbol{\mathcal{S}}^{\text{SOR},n}_{lx,k} = \omega \delta\boldsymbol{\mathcal{S}}^{\text{GS},n}_{lx,k}, \tag{4.28}$$

where ω is given by

$$\omega = \frac{2}{1+\sqrt{1-\delta}}. \tag{4.29}$$

Here δ is the spectral radius of the GS iteration. ω takes an optimum value between 1 and 2. A detailed description of the method to fix the optimum value of ω is discussed in Section 2.4 of Trujillo Bueno and Fabiani Bendicho (1995). We now discuss the implementation of GS and SOR algorithms for the case of spherical geometry (see also Anusha *et al.* 2009).

1. Incoming part for the incoming rays ($\mu < 0$):

(a) This calculation begins at the radial shell with depth index $k = 1$, namely at the outer boundary for all the impact parameter rays (see Figure 4.2a).

(b) The irreducible Stokes vector $\boldsymbol{\mathcal{I}}^-$ at the next radial shell is then determined using the short-characteristic formal solver (Equation (4.18)). For the incoming rays at any point k, Equation (4.18) uses $\boldsymbol{\mathcal{S}}^{\rm old}_{x,k+1}$, $\boldsymbol{\mathcal{S}}^{\rm old}_{x,k}$, and $\boldsymbol{\mathcal{S}}^{\rm old}_{x,k-1}$ to compute $\boldsymbol{\mathcal{I}}^-$ at that point k.

(c) Before moving to the next radial shell, $\overline{\boldsymbol{\mathcal{J}}}^{-}_{x,k}$ is computed. Therefore at the end of the incoming block, the contribution from the incoming rays to the frequency-averaged PFR mean intensity vector $\overline{\boldsymbol{\mathcal{J}}}^{-}_{x,k}$ would have been computed at all the radial shells until the inner boundary is reached or until the ray becomes tangent to the radial shell.

2. Outgoing part for the outgoing rays ($\mu > 0$):

(d) Once $\overline{\boldsymbol{\mathcal{J}}}^{-}_{x,k}$ is determined in the incoming part, we now start at the depth index $k = N$, namely at the inner boundary. Since the irreducible Stokes vector $\boldsymbol{\mathcal{I}}^+$ is known at this point (as it being the boundary condition), the total PFR mean intensity vector $\overline{\boldsymbol{\mathcal{J}}}_{x,N}$ can be computed, using which $\delta\boldsymbol{\mathcal{S}}_{lx,N}$ and $\delta\boldsymbol{\mathcal{S}}_{x,N}$ are also determined.

(e) Now the new total source vector $\boldsymbol{\mathcal{S}}^{\rm new}_{x,N}$ is updated at the inner boundary using

$$\boldsymbol{\mathcal{S}}^{\rm new}_{x,N} = \boldsymbol{\mathcal{S}}^{\rm old}_{x,N} + \delta\boldsymbol{\mathcal{S}}_{x,N}. \tag{4.30}$$

(f) For the next radial shell $k = N - 1$, GS uses $\boldsymbol{\mathcal{S}}^{\rm new}_{x,N}$, $\boldsymbol{\mathcal{S}}^{\rm old}_{x,N-1}$, and $\boldsymbol{\mathcal{S}}^{\rm old}_{x,N-2}$ in Equation (4.18) (see Figure 4.2(b)) to calculate $\boldsymbol{\mathcal{I}}^+$ at $k = N - 1$ and thereby we obtain $\overline{\boldsymbol{\mathcal{J}}}_{x,N-1}$.

(g) It is important to note that for the incoming part, $\overline{\boldsymbol{\mathcal{J}}}^{-}_{x,N-1}$ is calculated using $\boldsymbol{\mathcal{S}}^{\rm old}_{x,N}$, $\boldsymbol{\mathcal{S}}^{\rm old}_{x,N-1}$, and $\boldsymbol{\mathcal{S}}^{\rm old}_{x,N-2}$, whereas $\overline{\boldsymbol{\mathcal{J}}}^{+}_{x,N-1}$ is calculated using $\boldsymbol{\mathcal{S}}^{\rm new}_{x,N}$, $\boldsymbol{\mathcal{S}}^{\rm old}_{x,N-1}$, and $\boldsymbol{\mathcal{S}}^{\rm old}_{x,N-2}$. Therefore, for the actual computation of $\overline{\boldsymbol{\mathcal{J}}}^{\rm old+new}_{x,N-1}$, we need to add the

following correction:

$$\Delta\overline{\boldsymbol{\mathcal{J}}}^{-}_{x,N-1} = \int_{-\infty}^{+\infty} dx' \frac{\boldsymbol{\mathcal{R}}(x,x')}{\phi(x)} \Delta\boldsymbol{\mathcal{J}}^{-}_{x',N-1}, \tag{4.31}$$

where

$$\Delta\boldsymbol{\mathcal{J}}^{-}_{x,N-1} = \frac{1}{2}\int_{-1}^{0} \Delta\boldsymbol{\mathcal{I}}^{-}_{x,N-1} d\mu, \tag{4.32}$$

with

$$\Delta\boldsymbol{\mathcal{I}}^{-}_{x,N-1} = \Psi^{-}_{\mathrm{N}}(p,x)\delta\boldsymbol{\mathcal{S}}_{x,N}. \tag{4.33}$$

Once the actual $\overline{\boldsymbol{\mathcal{J}}}^{\mathrm{old+new}}_{x,N-1}$ is computed, $\delta\boldsymbol{\mathcal{S}}_{lx,N-1}$ is calculated and the new total source vector $\boldsymbol{\mathcal{S}}^{\mathrm{new}}_{x,N-1}$ is updated. Since $\boldsymbol{\mathcal{S}}^{\mathrm{new}}_{x,N-1}$ is now available, before going to the next radial shell, the $\boldsymbol{\mathcal{I}}^{+}$ at the present shell i.e., at $N-1$ needs to be updated by adding the following correction:

$$\Delta\boldsymbol{\mathcal{I}}^{+}_{x,N-1} = \Psi^{+}_{\mathrm{N-1}}(p,x)\delta\boldsymbol{\mathcal{S}}_{x,N-1}. \tag{4.34}$$

Once the $\boldsymbol{\mathcal{I}}^{+}$ is updated at $k = N-1$, the above procedure is then repeated for the subsequent shells. Clearly unlike the Jacobi, GS, and SOR schemes require particular ordering of the loops to implement the above mentioned steps. The outermost loop is over iterations, the next loop is over directions (first the incoming and then the outgoing), following this there is loop over radial shells with index k (running from $k = 1, ..., N$ for incoming rays and in the reverse order for outgoing rays), and then the loop over impact parameter rays p. The innermost loop is over the frequency points.

4.4 Model parameters

We consider an isothermal, spherically symmetric atmosphere with inverse square law opacity distribution for both line and continuum, i.e., $\chi_{l,c} \propto r^{-\tilde{n}}$, with the power law opacity index $\tilde{n}$=2, outer radius R, and a line integrated total radial optical thickness of T. We apply reflecting boundary condition, which is also known as hollow-core or planetary nebula boundary condition, given by $\boldsymbol{\mathcal{I}}^{+}(\tau = T, p, x) = \boldsymbol{\mathcal{I}}^{-}(\tau = T, p, x)$ for both core and lobe rays. The outer boundary

condition is given by $\boldsymbol{\mathcal{I}}^{-}(\tau = 0, p, x) = 0$. The isothermal atmosphere is characterized by the following set of input parameters: $T = 10^6$, $R = 300$, $\beta_c = 10^{-6}$, $\epsilon = 10^{-4}$, $a = 10^{-3}$, $B_{\nu_0} = 1$, and $\Gamma_{\rm E}/\Gamma_{\rm R}$=0. A logarithmically spaced τ_r-grid with 20 points per decade, and with the first depth point at $\tau_{r,1} = 10^{-4}$ is used. A logarithmically spaced r-grid is constructed from the $\tau(r)$ grid using the relation (Kunasz and Hummer 1974a)

$$\tau(r) = T\ \frac{r^{-\tilde{n}+1} - R^{-\tilde{n}+1}}{R_c^{-\tilde{n}+1} - R^{-\tilde{n}+1}}, \tag{4.35}$$

where R_c=1 is the core radius and $\tilde{n} = 2$ for inverse square law opacity. The p-grid is constructed as in Hummer *et al.* (1973). Typically we have seven core rays, and as many lobe rays as the r-grid points (see Anusha *et al.* 2009 for more details). The angle grid is then constructed using $\mu(r, p) = \sqrt{1 - (p^2/r^2)}$. The weights corresponding to the angle (μ) grids are constructed using the method devised by Hummer *et al.* (1973) in the range $[0 < \mu \leqslant 1]$. Equally spaced points with a step size of 0.125 Doppler widths in the line core (up to 4 Doppler widths) and logarithmically spaced points in the wings (up to 1000 Doppler widths) are used in the frequency grid construction. The maximum frequency $x_{\rm max}$ is chosen such that $\phi(x_{\rm max})T \ll 1$ is satisfied. We typically have 153 points in the interval $[-x_{\rm max}, +x_{\rm max}]$.

4.5 Comparison of Jacobi, GS, and SOR iterative schemes

It is always necessary to use high-resolution grids to obtain solutions of higher accuracy (Chevallier *et al.* 2003). This is particularly true in the case of spherical transfer problems which demand finer spatial grid to obtain accurate solutions. It is well established that the Jacobi-based ALI methods show lower convergence rates when the spatial grid resolution is increased. Thus, the GS and SOR methods turn out to be far superior than the Jacobi method for handling the spherical radiative transfer problems. Therefore here we aim at studying the robustness of the GS and SOR schemes over the Jacobi scheme by considering the MRC and

the surface true error which determine the characteristics of any iterative method in hand.

For a given level of grid resolution g at the nth iterative stage, the MRC of irreducible components of the source vector is defined as

$$(c_0^K)^n = \max_{z,x}\left\{\frac{\mid (\mathcal{S}_0^K)(n,g) - (\mathcal{S}_0^K)(n-1,g) \mid}{(\mathcal{S}_0^K)(n,g)}\right\}. \tag{4.36}$$

and the surface true error on $\mathcal{S}_0^K$ at $z = z_{\max}$ is defined as

$$T_e(S_0^K) = \max_{x}\left\{\frac{\mid (\mathcal{S}_0^K)(n,g) - (\mathcal{S}_0^K)(\infty,\infty) \mid}{(\mathcal{S}_0^K)(\infty,\infty)}\right\}. \tag{4.37}$$

Here $(n, g) = (\infty, \infty)$ indicates that the true solution corresponds to the fully converged solution on a grid of infinite resolution. A fully converged solution on a grid resolution level g is obtained when $\max[(c_0^0)^n, (c_0^2)^n] < 10^{-8}$.

Figure 4.3 shows a plot of $(c_0^0)^n$ (top panels) and $(c_0^2)^n$ (bottom panels) as a function of iteration number for the case of CFR (panel (a)) and PFR (panel (b)) for Jacobi (solid lines), GS (dotted lines), and SOR (dashed lines) schemes. For obtaining the variation of MRC with iteration number, the iterations are continued until we find the fully converged solution on a grid resolution of $g = 20$ points per decade. Clearly, the Jacobi iterative scheme exhibits the lowest convergence rate. In the case of CFR, the Jacobi scheme takes about 315 iterations for the convergence of $\mathcal{S}_0^0$ (see top panel in Figure 4.3(a)). Whereas GS scheme takes about 125 iterations, which is about two and half times smaller than the Jacobi scheme. In the case of the SOR scheme, to achieve the highest convergence rate we find that the optimum value of the factor ω is 1.22 for both CFR and PFR. For this choice of ω, the SOR scheme takes only about 70 iterations for the convergence of $\mathcal{S}_0^0$ with CFR. Therefore, SOR scheme is even more robust than the GS. $(c_0^2)^n$ also exhibits a behavior similar to $(c_0^0)^n$ for all the three iterative schemes. In the case of PFR, the rate of convergence is somewhat slower than that for CFR. This is expected because of photon-trapping in the wings in the case of PFR leading to relatively higher number of iterations for the convergence. However, the convergence behavior of PFR remains almost similar to that of CFR for all the three iterative schemes.

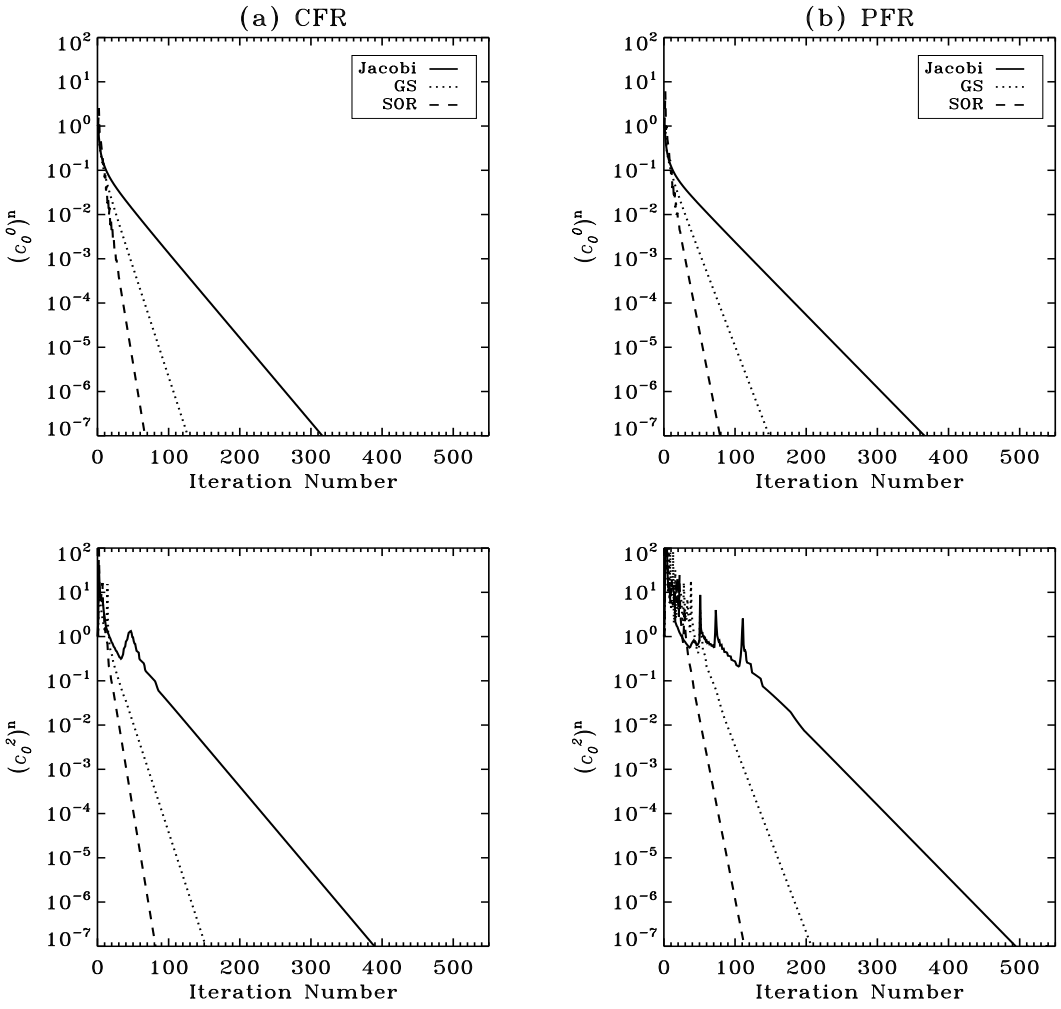

FIGURE 4.3: Maximum relative change of irreducible source vector components $(c_0^0)^n$ (top panels) and $(c_0^2)^n$ (bottom panels) as a function of iteration number. The case of CFR is considered in panel (a) an PFR in panel (b). Model parameters are given in Section 4.4.

The numerical accuracy of the solutions obtained from the Jacobi, GS, and SOR schemes is determined by the true error (Auer *et al.* 1994). Therefore, in Figure 4.4 we show a plot of the surface true error on $\mathcal{S}_0^0$ (top panels) and $\mathcal{S}_0^2$ (bottom panels) as a function of iteration number for the case of CFR (panel (a)) and PFR (panel (b)) for Jacobi (solid lines), GS (dotted lines), and SOR (dashed lines) schemes. The true solution required to calculate the surface true error is obtained by using a grid whose resolution is twice finer (40 points/decade in this case) compared to the one on which we determine the true error (20 points/decade). From Figure 4.4 we see that the true error for the case of PFR is somewhat larger than that for CFR as obtained also in Sampoorna and Trujillo Bueno (2010) in the

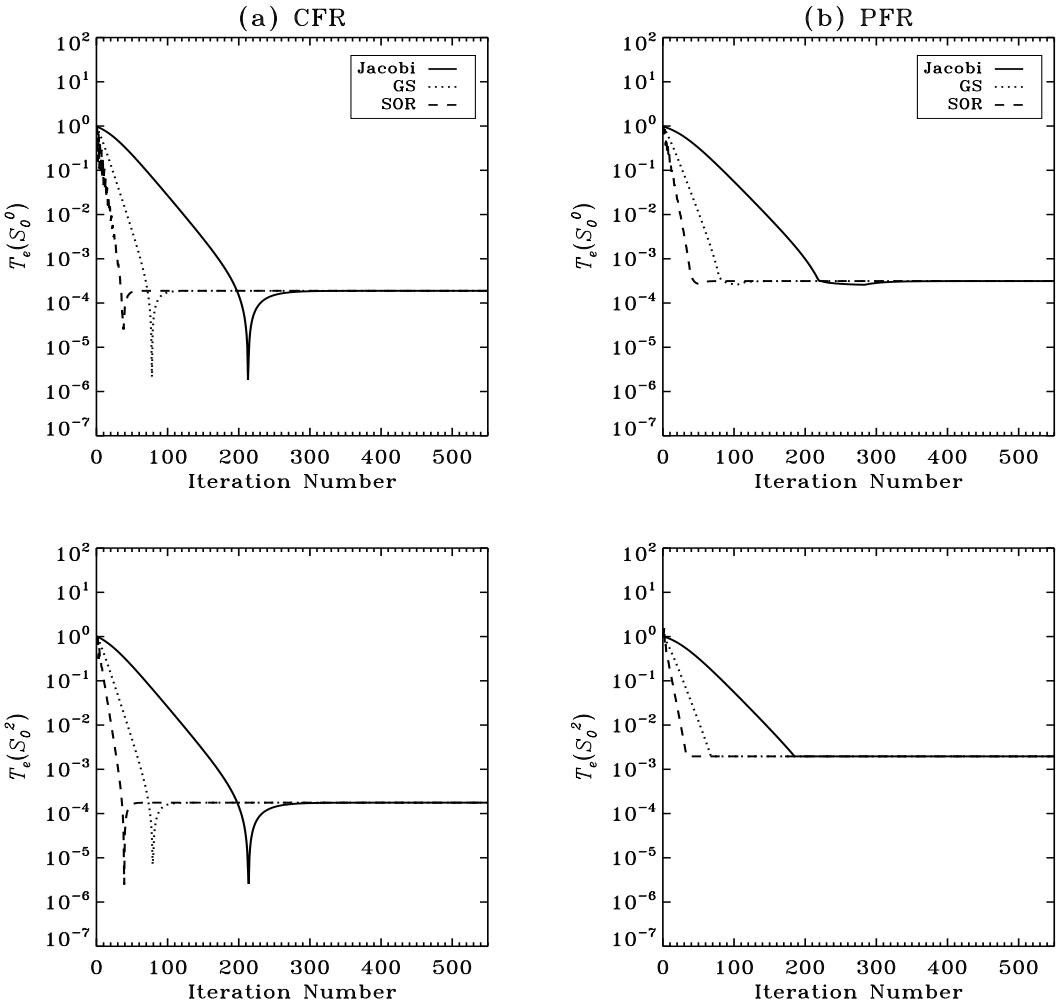

FIGURE 4.4: The surface true error on $\mathcal{S}_0^0$ (top panels) and $\mathcal{S}_0^2$ (bottom panels) as a function of iteration number. Panel (a) corresponds to the case of CFR, while panel (b) to PFR. Model parameters are given in Section 4.4.

planar case. In the case of CFR, the surface true error is on the order of 0.018 % on $\mathcal{S}_0^0$, and 0.017 % on $\mathcal{S}_0^2$. On the other hand, for PFR it is 0.031 % on $\mathcal{S}_0^0$ and 0.19 % on $\mathcal{S}_0^2$. The true error on $\mathcal{S}_0^0$ and $\mathcal{S}_0^2$ are somewhat of similar magnitudes in the case of CFR. Whereas in the case of PFR, the true error on $\mathcal{S}_0^2$ is larger than $\mathcal{S}_0^0$ by about 10 %. All the three iterative schemes give same values for the surface true error. This is expected as the true error is determined by the grid resolution which is assumed to be the same for all the three schemes. However, lesser number of iterations are taken by the GS and SOR schemes to attain these true error values, thereby demonstrating their superiority over the Jacobi scheme.

4.6 Concluding remarks

In this chapter we have generalized the Jacobi, GS, and SOR iterative schemes to solve the problem of polarized radiative transfer in spherically symmetric static medium including both CFR and PFR in scattering. As shown in previous works for planar atmospheres (see e.g., Trujillo Bueno and Fabiani Bendicho 1995, Trujillo Bueno and Manso Sainz 1999, Sampoorna and Trujillo Bueno 2010), even in the case of spherical atmospheres, we find that the GS and SOR iterative schemes are more robust and superior than the Jacobi-based ALI method (see also Asensio Ramos and Trujillo Bueno 2006, Anusha *et al.* 2009 for the corresponding unpolarized version). These methods can be used to solve the complicated NLTE problems rapidly and effectively. They also have excellent smoothing capabilities. The computing time per iteration is nearly the same as the Jacobi scheme. However, for the GS scheme, the number of iterations required for convergence is about half that for the Jacobi scheme. The SOR scheme takes even less number of iterations for convergence when an optimum value for ω factor is used. For the numerical studies presented in this chapter $\omega = 1.22$ turns out to be an optimum value. Therefore, GS and SOR methods are very useful techniques for problems requiring fine grids such as the spherical radiative transfer. In the next chapter we further generalize the Jacobi, GS, and SOR methods to handle expanding spherical atmospheres.

Chapter 5

Iterative Techniques to Solve Polarized Line Formation in Spherically Symmetric Moving Atmospheres[1]

An overview

It is well-known that the extended stellar atmospheres are in general dynamic, due to the systematic motions present in their layers. Macroscopic velocity fields present in the spectral line forming regions produce Doppler shift, aberration of photons, and also give rise to advection. All of these effects can modify the amplitudes and shapes of the emergent Stokes profiles. In the present chapter we consider the problem of polarized line formation in spherically symmetric media, in the presence of velocity fields. Solving the radiative transfer problem in the observer's frame is a straightforward approach to handle the presence of velocity fields. This method, however, becomes computationally prohibitive when large velocity fields are considered, particularly in the case of the line formation with partial frequency redistribution (PFR). For the solution of the concerned polarized transfer equation we use the comoving frame (CMF) formulation, and apply the appropriately modified Jacobi, GS, and SOR based polarized accelerated

[1]This chapter is based on the publications: Megha *et al.* (2019b, 2020a)

lambda iteration (PALI) methods. We consider non-relativistic radial velocity fields, thereby accounting only for Doppler shift effects and neglecting advection and aberration of photons. We study the convergence behavior of the Jacobi, GS, and SOR based CMF-PALI methods for both complete frequency redistribution (CFR) and PFR in line scattering.

5.1 Introduction

The problem of polarized line formation in stellar atmospheres is of high scientific interest because of the diagnostic potential offered by the polarization of spectral lines (for example, see the monographs by Stenflo 1994, Landi Degl'Innocenti and Landolfi 2004). While this problem has been studied in great detail in planar and multi-dimensional geometries (see, for example, the reviews by Nagendra 2020, Trujillo Bueno 2020), it still remains relatively unexplored in spherical geometry, particularly in the presence of velocity fields and partial frequency redistribution (PFR) in scattering. One of the early works on this problem in static spherically symmetric atmospheres was by Nagendra (1988, 1989, 1994, 1995) who clearly demonstrated the effects of extendedness and PFR on the linear polarization profiles that are formed by resonance scattering. More recently Milić and Faurobert (2012) have considered the formation of polarized profiles of molecular lines in spherical geometry, assuming complete frequency redistribution (CFR) in scattering. In this chapter we consider polarized line transfer in spherically symmetric atmospheres in the presence of velocity fields accounting also for PFR in line scattering.

The extended stellar atmospheres are known to be dynamic, with low to high speed stellar winds originating in these layers. Examples may be given of the solar and stellar coronal winds. Effects of velocity fields on intensity and flux profiles, formed in extended spherical atmospheres are well studied (see, e.g., Kunasz and Hummer 1974b; Mihalas *et al.* 1975, who considered CFR in line scattering; Mihalas *et al.* 1976b, who considered angle-averaged PFR; Hubeny and Mihalas 2014 for a historical account of early works). Effects of velocity fields on linearly polarized line profiles formed due to electron scattering in spherically symmetric atmospheres are presented in Hillier (1996). In this chapter our aim is to study

the effects of velocity fields on linearly polarized line profiles including PFR, which are formed due to resonance scattering on atoms.

For spherical geometry, the numerical methods for solving the unpolarized line transfer equation in static and moving atmospheres have been developed by several workers (see, e.g., Peraiah 2002, Hubeny and Mihalas 2014). Modern iterative methods based on operator perturbation are presented, for example, in Anusha *et al.* (2009) and Hauschildt and Baron (2004, and references cited therein), for static and moving spherical atmospheres respectively. In this chapter we generalize these approximate lambda iteration (ALI) methods to include polarization with PFR in the presence of velocity fields. We present the numerical method of solution both in the observer's frame and the comoving frame (CMF) of the fluid. It is well-known that the observer's frame method becomes computationally expensive, especially when large velocity fields and PFR are considered. Thus the CMF method is the method of choice, as it is computationally faster and can handle both low- and high-velocity fields. We present the results for scattering on a two-level atom, including the effects of PFR. However, we consider only the non-relativistic regime of velocity fields, wherein mainly Doppler shift effects are significant. Thus only Doppler shift terms are considered in the CMF polarized transfer equation, and aberration and advection terms are ignored. We present the convergence properties of the CMF iterative technique developed based on Jacobi, GS, and SOR schemes for the spherically symmetric media in the presence of velocity fields.

In Section 5.2 we present the polarized PFR transfer equation in both observer's and comoving frames for the spherically symmetric media. The numerical methods of solution to solve these equations are presented in Section 5.3. The model parameters and the convergence properties of the CMF method are presented in Section 5.4. Conclusions are drawn in Section 5.5.

5.2 Polarized line transfer equation in moving spherical atmospheres

We consider an isothermal one-dimensional spherically symmetric atmosphere with velocity fields along the radius vector. A two-level atom model with an infinitely

sharp and unpolarized lower level is considered. In Section 5.2.1, the observer's frame polarized transfer equation is discussed and the relevant equation in the CMF formalism is given in Section 5.2.2.

5.2.1 Observer's frame

The polarized PFR transfer equation in the observer's frame for a spherically symmetric medium in divergence form and in the presence of radial velocity fields is given by

$$\mu\frac{\partial \boldsymbol{I}(r,\mu,x)}{\partial r}+\frac{(1-\mu^2)}{r}\frac{\partial \boldsymbol{I}(r,\mu,x)}{\partial \mu}=-\chi(r,\mu,x)[\boldsymbol{I}(r,\mu,x)-\boldsymbol{S}(r,\mu,x)]. \quad (5.1)$$

The above equation is exactly the same as Equation (4.1) but with $\chi(r,\mu,x) = \chi_l(r)\phi(r,\mu,x)+\chi_c(r)$ and the line profile function $\phi(r,\mu,x) = H(a,x-\mu V)$. Here $x-\mu V$ refers to the Doppler shifted frequency in the observer's frame, with V being a non-dimensional velocity field representing the velocity of the material relative to an external observer at rest. It is defined as $V = v_r/v_{\rm th}$, wherein v_r is the radial velocity field and $v_{\rm th}$ the mean thermal velocity (defined as $\sqrt{2kT/m}$ in standard notations). In the observer's frame both the opacity and emissivity of the material become angle (μ) dependent due to the relative motion between the source and the observer in the presence of velocity fields. All the other quantities are exactly the same as those defined in Section 4.2 of Chapter 4. An important difference is in the PFR functions, namely, in the presence of velocity fields, the redistribution matrix $\boldsymbol{R}$ continues to be given by Equation (4.6), but with $R_{\rm X,AA}(x,x')$ replaced by $R_{\rm X,AA}(x-\mu V, x'-\mu' V)$, wherein X=II, III.

We again solve the transfer equation (5.1) in the (p,z) coordinate system like in Chapter 4. Also from here onwards we represent all the vectors and matrices in the irreducible basis. In a moving atmosphere, $\mathcal{S}^K_{l,0}(z,p,x)$ for the case of CFR is independent of ϑ (and thereby p) as in the static case. However, in the case of PFR, because of the dependence of redistribution functions on μ and μ' through the Doppler shifted frequencies $x-\mu V$ and $x'-\mu' V$, $\mathcal{S}^K_{l,0}(z,p,x)$ retains the ϑ (or p) dependence. The observer's frame polarized transfer equation for the irreducible

quantities can be written in the (p, z) coordinate system as

$$\pm \frac{\partial \boldsymbol{\mathcal{I}}^{\pm}(z,p,x)}{\partial \tau(z,p,x)} = \boldsymbol{\mathcal{I}}^{\pm}(z,p,x) - \boldsymbol{\mathcal{S}}(z,p,x). \tag{5.2}$$

The monochromatic optical depth along the tangent rays in the observer's frame is given by $d\tau(z,p,x) = [\phi(z,p,x)+\beta_c]d\tau_z$, where β_c and τ_z are the same as defined in Chapter 4. $\boldsymbol{\mathcal{S}}$ now has the form similar to Equation (4.4), but with the irreducible line source vector given by

$$\boldsymbol{\mathcal{S}}_l(z,p,x) = \epsilon B_{\nu_0}\boldsymbol{\mathcal{U}} + \int_{-\infty}^{+\infty} dx' \frac{1}{2}\int_{-1}^{+1} d\mu' \frac{\boldsymbol{\mathcal{R}}(x-\mu V, x'-\mu' V)}{\phi(z,p,x)}\boldsymbol{\Psi}(\mu')\,\boldsymbol{\mathcal{I}}(\tau,\mu',x'). \tag{5.3}$$

The PFR matrix in the irreducible basis has the form

$$\begin{aligned}\boldsymbol{\mathcal{R}}(x-\mu V, x'-\mu' V) = \mathbf{W}\{&\alpha\mathbf{E}R_{\mathrm{II,AA}}(x-\mu V, x'-\mu' V)\\ &+(\boldsymbol{\mathcal{B}}-\alpha\mathbf{E})R_{\mathrm{III,AA}}(x-\mu V, x'-\mu' V)\}.\end{aligned} \tag{5.4}$$

5.2.2 Comoving frame

Following Mihalas (1978), the observer's frame transfer equation for the irreducible components of the Stokes vector (cf. Equation (5.2)) can be transformed to the co-moving frame. We consider the non-relativistic regime of the velocity field wherein mainly Doppler shift terms are significant and neglect the aberration and advection terms. For brevity, we use the same notations in both observer's and comoving frames. The non-relativistic CMF transfer equation in a spherically symmetric medium, for the irreducible intensity vector $\boldsymbol{\mathcal{I}}^{\pm}$ can be written as

$$\pm\frac{\partial \boldsymbol{\mathcal{I}}^{\pm}(z,p,x)}{\partial \tau(z,x)} = \boldsymbol{\mathcal{I}}^{\pm}(z,p,x) - \boldsymbol{\mathcal{S}}(z,x) + \frac{a(r,p)}{\chi_l(r)\phi(x)+\chi_c(r)}\frac{\partial \boldsymbol{\mathcal{I}}^{\pm}(z,p,x)}{\partial x}, \tag{5.5}$$

where

$$a(r,p) = (1-\mu^2)\frac{V}{r} + \mu^2\frac{dV}{dr}. \tag{5.6}$$

The monochromatic optical depth in the comoving frame is now given by $d\tau = [\phi(x)+\beta_c]d\tau_z$, with the absorption profile function $\phi(x) = H(a,x)$ which is now angle-independent. Unlike in the observer's frame, the PFR matrix $\boldsymbol{\mathcal{R}}$ in CMF

depends only on (x, x'). Therefore $\boldsymbol{\mathcal{S}}$ and $\boldsymbol{\mathcal{S}}_l$ depend only on frequency like their static counterparts discussed in Chapter 4.

5.3 Numerical methods

In this section we first briefly discuss the observer's frame method and then present the comoving frame method in detail.

5.3.1 Observer's frame method

In the observer's frame method, the relative velocities are treated through the Doppler shift formula, which involves changing the frequencies x and x' to their corresponding Doppler shifted frequencies, and computing the solution on the original frequency grid. The PALI techniques to solve the polarized line transfer equation in planar medium have been developed for a variety of problems (see, e.g., the reviews by Nagendra 2003, Nagendra 2014, Nagendra 2020). This PALI method can be generalized to handle spherical geometry as discussed in Chapter 4 for a static medium. In particular, we have generalized the Jacobi based scalar ALI method presented in Anusha *et al.* (2009) for spherical geometry to include polarization, PFR, and the effects of the velocity fields. The relevant PALI steps are identical to those presented in Section 3.1 of Sampoorna and Nagendra (2015b) for the case of planar moving atmosphere, but with the magnetic field being now set to zero. As discussed in the above cited paper, in the presence of velocity fields the computation of the line source vector corrections by a frequency-angle-by-frequency-angle method becomes computationally expensive. For the spherical geometry, due to the coupling of p-grid (and thereby the μ-grid) with r-grid, this method quickly becomes prohibitive, demanding huge main memory and CPU times. Thus the observer's frame method is used only for the purpose of benchmarking the comoving frame method by considering optically thin spherical shells (with the total optical thickness of $T \sim 1$).

5.3.2 Comoving frame method

In this method the transfer equation is first solved in a frame fixed to the fluid, which is also called as the Lagrangian frame and then the solution is transformed to the observer's frame. Hence solving the transfer equation in the comoving frame is a two step process. In the first step, the comoving frame transfer equation is solved iteratively using a PALI method to obtain the converged comoving frame source and Stokes vectors in the irreducible basis. In the second step, the comoving frame solution obtained on the comoving frame frequency grid is transformed to the observer's frame frequency grid. This is done by interpolating the CMF irreducible source vector $\boldsymbol{\mathcal{S}}(z, x)$ onto the observer's frame frequency grid $x - \mu V$, where x is the comoving frame frequency grid. The resulting observer's frame irreducible vector $\boldsymbol{\mathcal{S}}(z, p, x)$ is then used in a formal solver to obtain the observer's frame irreducible Stokes vector. For this purpose we need to perform a formal integration of the transfer equation in the observer's frame (see Equation (5.2)), which is done using the short-characteristic method (Olson and Kunasz 1987). Finally we transform the irreducible emergent Stokes vector, which is now in the observer's frame to the Stokes representation using the transformation formula given in Frisch (2007), namely

$$I^{\pm}(z, p, x) = \mathcal{I}_0^{0,\pm}(z, p, x) + \frac{1}{2\sqrt{2}}[3\mu^2(r, p) - 1]\mathcal{I}_0^{2,\pm}(z, p, x), \tag{5.7}$$

$$Q^{\pm}(z, p, x) = -\frac{3}{2\sqrt{2}}[1 - \mu^2(r, p)]\mathcal{I}_0^{2,\pm}(z, p, x), \tag{5.8}$$

with similar expressions relating S_I and S_Q with $\mathcal{S}_0^0$ and $\mathcal{S}_0^2$.

Comparing Equation (5.5) with Equation (4.10), it is clear that the comoving frame transfer equation differs from that of static case by an extra term called the CMF term. Hence the basic PALI steps in CMF remain the same as in the corresponding static case that are discussed in Chapter 4. The essential difference occurs in the expression for the formal solution of Equation (5.5). Consequently certain correction terms discussed in Equations (4.31)–(4.34) for the GS and SOR schemes also get modified. In the following subsections we discuss these differences in detail.

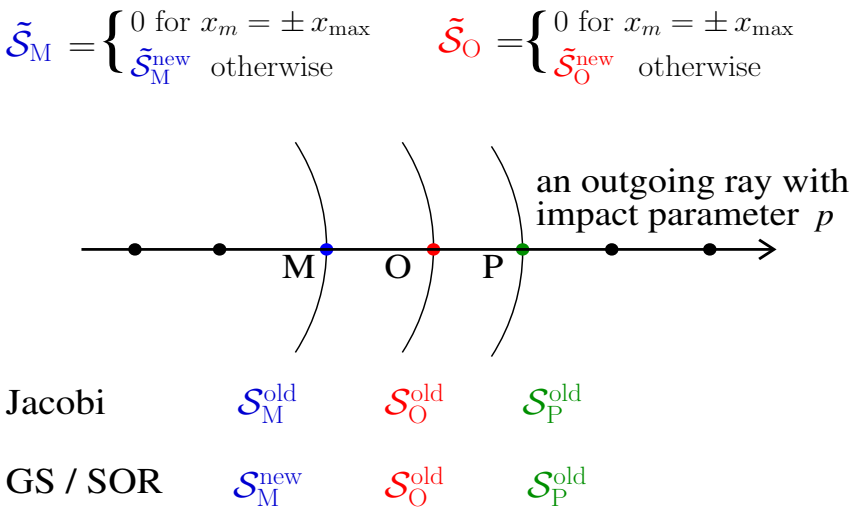

FIGURE 5.1: Schematic representation of the one-dimensional short-characteristic formal solution on an MOP stencil along a given characteristic ray with impact parameter p in the spherical atmosphere (see also Figures 4.1 and 4.2). The superscript "old" stands for the previous iterate values and "new" for the values of $\tilde{\boldsymbol{\mathcal{S}}}$ that are calculated using the intensity for the previous frequency point (see Equations (5.14)-(5.16)) that has been computed in the current iterate formal solution. A similar formal solution method is also applied to the incoming ray, wherein $\boldsymbol{\mathcal{S}}_{\rm M}^{\rm old}$ is used for GS and SOR schemes as well.

5.3.2.1 Formal solution

Following Hauschildt and Baron (2004), the CMF term in Equation (5.5) can be defined as

$$\tilde{\boldsymbol{\mathcal{S}}}(z,p,x) = -\frac{a(r,p)}{\chi(r,x)}\frac{\partial \boldsymbol{\mathcal{I}}^{\pm}(z,p,x)}{\partial x}, \tag{5.9}$$

where $\chi(r,x) = \chi_l(r)\phi(x) + \chi_c(r)$. Thus we rewrite Equation (5.5) as

$$\pm \frac{\partial \boldsymbol{\mathcal{I}}^{\pm}(z,p,x)}{\partial \tau(z,p,x)} = \boldsymbol{\mathcal{I}}^{\pm}(z,p,x) - \boldsymbol{\mathcal{S}}(z,x) - \tilde{\boldsymbol{\mathcal{S}}}(z,p,x). \tag{5.10}$$

Following the short-characteristic integration technique of Olson and Kunasz (1987), the expression for the formal solution of the spherically symmetric transfer equation (5.10) at a given point "O" on a stencil of short-characteristic (MOP with M and P being the upwind and the downwind points, respectively, see Figure 5.1) along a given ray of impact parameter p and frequency point x_m can be written

as

$$\boldsymbol{\mathcal{I}}^{\pm}_{\mathrm{O}}(p,x_m) \;=\; e^{-\Delta\tau_{\mathrm{MO}}}\boldsymbol{\mathcal{I}}^{\pm}_{\mathrm{M}}(p,x_m)+\delta\boldsymbol{\mathcal{I}}^{\pm}_{\mathrm{O}}(p,x_m)+\delta\tilde{\boldsymbol{\mathcal{I}}}^{\pm}_{\mathrm{O}}(p,x_m). \tag{5.11}$$

As in Hauschildt and Baron (2004), along an MOP stencil, we use parabolic and linear interpolation for the irreducible source vectors $\boldsymbol{\mathcal{S}}$ and $\tilde{\boldsymbol{\mathcal{S}}}$ respectively. With these choices for interpolation, the last two terms on the right-hand side of Equation (5.11) take the form

$$\delta\boldsymbol{\mathcal{I}}^{\pm}_{\mathrm{O}}(p,x_m)=\Psi^{\pm}_{\mathrm{M}}(p,x_m)\boldsymbol{\mathcal{S}}_{\mathrm{M}}(x_m)+\Psi^{\pm}_{\mathrm{O}}(p,x_m)\boldsymbol{\mathcal{S}}_{\mathrm{O}}(x_m)+\Psi^{\pm}_{\mathrm{P}}(p,x_m)\boldsymbol{\mathcal{S}}_{\mathrm{P}}(x_m), \tag{5.12}$$

and

$$\delta\tilde{\boldsymbol{\mathcal{I}}}^{\pm}_{\mathrm{O}}(p,x_m)=\Psi'^{,\pm}_{\mathrm{M}}(p,x_m)\tilde{\boldsymbol{\mathcal{S}}}_{\mathrm{M}}(p,x_m)+\Psi'^{,\pm}_{\mathrm{O}}(p,x_m)\tilde{\boldsymbol{\mathcal{S}}}_{\mathrm{O}}(p,x_m), \tag{5.13}$$

where $\Psi^{\pm}_{\mathrm{M}}$, $\Psi^{\pm}_{\mathrm{O}}$, and $\Psi^{\pm}_{\mathrm{P}}$ are the parabolic interpolation coefficients and $\Psi'^{,\pm}_{\mathrm{M}}$, $\Psi'^{,\pm}_{\mathrm{O}}$ are the linear interpolation coefficients. $\boldsymbol{\mathcal{S}}_{\mathrm{M}}$, $\boldsymbol{\mathcal{S}}_{\mathrm{O}}$, and $\boldsymbol{\mathcal{S}}_{\mathrm{P}}$ are the previous iterate irreducible source vectors at points M, O, and P, respectively for both incoming and outgoing rays in the case of Jacobi scheme and for only incoming ray in the case of GS and SOR schemes. As explained in Chapter 4, for the outgoing ray $\boldsymbol{\mathcal{S}}_{\mathrm{M}}$ takes the current iterate value in the case of GS and SOR schemes. $\tilde{\boldsymbol{\mathcal{S}}}_{\mathrm{M}}$ and $\tilde{\boldsymbol{\mathcal{S}}}_{\mathrm{O}}$ which contain the effects of the velocity field on the formal solution, are given by

$$\tilde{\boldsymbol{\mathcal{S}}}_{\mathrm{M}}(p,x_m)=-\left[\frac{a(r,p)}{\chi(r,x_m)}\right]_{\mathrm{M}}\left[\frac{\partial\boldsymbol{\mathcal{I}}^{\pm}}{\partial x}\right]_{\mathrm{M},x_m}, \tag{5.14}$$

$$\tilde{\boldsymbol{\mathcal{S}}}_{\mathrm{O}}(p,x_m)=-\left[\frac{a(r,p)}{\chi(r,x_m)}\right]_{\mathrm{O}}\left[\frac{\partial\boldsymbol{\mathcal{I}}^{\pm}}{\partial x}\right]_{\mathrm{O},x_m}. \tag{5.15}$$

We remark that, while the irreducible source vector $\boldsymbol{\mathcal{S}}$ is available from the previous iterate, the CMF term $\tilde{\boldsymbol{\mathcal{S}}}$ is calculated within the formal solver using Equations (5.14)-(5.16). Clearly the choice of parabolic interpolation for $\tilde{\boldsymbol{\mathcal{S}}}$ would require the intensity at the downwind point P which is not available beforehand. Thus integration of $\tilde{\boldsymbol{\mathcal{S}}}$ is performed using linear interpolation, which then allows for a recursive formal solution (see Equation (5.17) below). Following Hauschildt and

Baron (2004), at any point O, the frequency derivative can be discretized as

$$\left[\frac{\partial \boldsymbol{\mathcal{I}}^{\pm}}{\partial x}\right]_{\mathrm{O},x_m} = \frac{\boldsymbol{\mathcal{I}}^{\pm}_{\mathrm{O}}(p,x_m) - \boldsymbol{\mathcal{I}}^{\pm}_{\mathrm{O}}(p,x_{m\mp1})}{x_m - x_{m\mp1}}, \tag{5.16}$$

where x_{m-1} applies when $[a(r,p)]_{\mathrm{O}} \geqslant 0$ and x_{m+1} applies when $[a(r,p)]_{\mathrm{O}} < 0$. Substituting Equations (5.12)–(5.16) in Equation (5.11), we obtain the short-characteristic formal solution in the comoving frame as

$$\left\{1 + \Psi^{\prime,\pm}_{\mathrm{O}}(p,x_m)\left[\frac{a(r,p)}{\chi(r,x_m)}\right]_{\mathrm{O}}\frac{1}{(x_m - x_{m\mp1})}\right\}\boldsymbol{\mathcal{I}}^{\pm}_{\mathrm{O}}(p,x_m) = e^{-\Delta\tau_{\mathrm{MO}}}\boldsymbol{\mathcal{I}}^{\pm}_{\mathrm{M}}(p,x_m)$$
$$+\delta\boldsymbol{\mathcal{I}}^{\pm}_{\mathrm{O}}(p,x_m) + \Psi^{\prime,\pm}_{\mathrm{M}}(p,x_m)\tilde{\boldsymbol{\mathcal{S}}}_{\mathrm{M}}(p,x_m) + \Psi^{\prime,\pm}_{\mathrm{O}}(p,x_m)\left[\frac{a(r,p)}{\chi(r,x_m)}\right]_{\mathrm{O}}\frac{\boldsymbol{\mathcal{I}}^{\pm}_{\mathrm{O}}(p,x_{m\mp1})}{(x_m - x_{m\mp1})}. \tag{5.17}$$

It can be noted that when $a(r,p) = 0$, i.e., for static atmospheres, Equation (5.17) reduces to the usual static case short-characteristic formal solution expression given in Equation (4.18).

For monotonically decreasing or increasing velocity fields, Equation (5.5) represents an initio-boundary value problem. In the case of spherical geometry, the initial condition in frequency is determined by the sign of the coefficient $a(r,p)$ (see Mihalas *et al.* 1975). Following Mihalas *et al.* (1975), we set the initial condition to be $\frac{\partial \boldsymbol{\mathcal{I}}^{\pm}}{\partial x}$=0 either at $x = -x_{\max}$ or at $x = +x_{\max}$ depending on the sign of $a(r,p)$. When $a(r,p) \geqslant 0$ the initial condition is given at $x = -x_{\max}$ and for $a(r,p) < 0$ it is given at $x = +x_{\max}$. Clearly, x runs from $-x_{\max}$ to $+x_{\max}$ when $a(r,p) \geq 0$ and vice-versa for $a(r,p) < 0$.

The Jacobi, GS, and SOR iterative schemes discussed in Section 4.3 for the static case continue to remain valid in the CMF, but now the formal solution is given by Equation (5.17). Consequently some of the corrections discussed in Section 4.3.3 for the static GS and SOR schemes need to be modified in the case of CMF. They are discussed in the following subsection.

5.3.2.2 Modified corrections for the GS and SOR schemes in the CMF

The algorithm for the implementation of GS and SOR schemes for a static spherical atmosphere is presented in detail in Section 4.3.3. We recall that because old values

of irreducible source vector components are used in the incoming part, while new values for the upwind point are used in the outgoing part, PFR mean intensity vector and the intensity of the outgoing ray had to be corrected to get their actual values. These corrections for a static atmosphere are given by Equations (4.31)–(4.34). In the CMF, since the expression for the formal solution (Equation (5.17)) is different from that for static case, these corrections get modified. To calculate these modified corrections in the CMF, we consider Equation (5.17). Since at $x = -x_{\max}$ (for $a(r,p) \geq 0$) or at $x = +x_{\max}$ (for $a(r,p) < 0$), initial conditions are applied, the Equation (5.17) reduces to Equation (4.18). Thus, the corrections $\Delta\overline{\boldsymbol{\mathcal{J}}}^{-}_{x,N-1}$ and $\Delta\boldsymbol{\mathcal{I}}^{+}_{x,N-1}$ are calculated as in Equations (4.31) and (4.34) respectively. When $x \neq \pm x_{\max}$ Equation (4.33) needs to be modified as follows:

$$\begin{aligned}\Delta\boldsymbol{\mathcal{I}}^{-}_{x_m,N-1} = &\Bigg\{\Psi^{-}_{\mathrm{N}}(p,x_m)\delta\boldsymbol{\mathcal{S}}_{x_m,N} \\ &+\Psi^{\prime,-}_{\mathrm{N}-1}(p,x_m)\left[\frac{a(r,p)}{\chi(r,x_m)}\right]_{N-1}\frac{\Delta\boldsymbol{\mathcal{I}}^{-}_{x_{m\mp1},N-1}}{(x_m - x_{m\mp1})}\Bigg\}\Bigg/ \\ &\left\{1+\Psi^{\prime,-}_{\mathrm{N}-1}(p,x_m)\left[\frac{a(r,p)}{\chi(r,x_m)}\right]_{N-1}\frac{1}{(x_m - x_{m\mp1})}\right\}. \end{aligned} \tag{5.18}$$

Also, when $x \neq \pm x_{\max}$, Equation (4.34) is modified as follows:

$$\begin{aligned}\Delta\boldsymbol{\mathcal{I}}^{+}_{x_m,N-1} = \quad &\Psi^{+}_{\mathrm{N}-1}(p,x_m)\delta\boldsymbol{\mathcal{S}}_{x_m,N-1} + \Psi^{\prime,+}_{\mathrm{N}-1}(p,x_m) \\ &\times\left[\frac{a(r,p)}{\chi(r,x_m)}\right]_{N-1}\frac{\Delta\boldsymbol{\mathcal{I}}^{+}_{x_{m\mp1},N-1}}{(x_m - x_{m\mp1})}. \end{aligned} \tag{5.19}$$

5.4 Convergence properties of CMF-PALI methods

Here we present the convergence behavior of CMF-PALI methods based on Jacobi, GS, and SOR schemes using maximum relative change (MRC) and surface true error (as in Section 4.5 for the static case). The model parameters are the same as those discussed in Section 4.4. The problem at hand requires high spatial resolution particularly when transforming the CMF solution to the observer's frame. This involves performing a formal solution of the observer's frame transfer equation (see

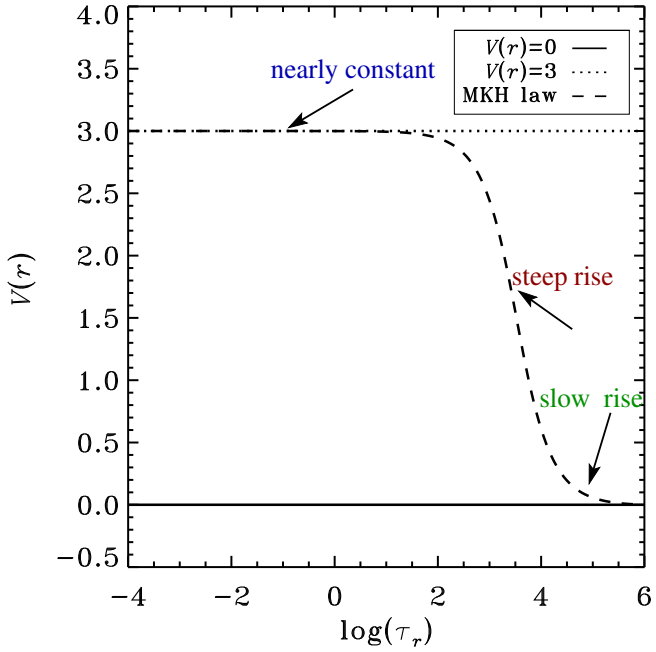

FIGURE 5.2: Non-dimensional radial velocity field $V(r)$ as a function of radial optical depth τ_r. The solid line corresponds to the static case, the dotted line to $V(r)$=3 mean thermal units, and the dashed line to MKH law with V_0=3, $a = 2(R-1)$, and $b = -(R+1)/(R-1)$.

Section 5.3.2), wherein the Doppler shift effects on $\Delta\tau(z, p, x)$ computation need to be accurately determined (see, e.g., Mihalas 1978). Thus we use a logarithmically spaced τ_r-grid with 20 points per decade.

5.4.1 Empirical velocity laws

The empirical velocity laws used for our studies are shown in Figure 5.2. The static atmosphere with $V(r)$=0 is shown for reference. We consider two types of velocity laws: (1) a spherical atmosphere moving with constant radial velocity toward the observer; and (2) a tangent velocity law given in Mihalas *et al.* (1975), hereafter referred to as MKH law. This velocity law simulates a real stellar wind, with a slow rise at the bottom of the atmosphere, followed by a steep rise in velocity, finally reaching a nearly constant velocity in the outer layers. This velocity law is given by

$$V(r) = V_0[\tan^{-1}(ar + b) - \tan^{-1}(a + b)], \tag{5.20}$$

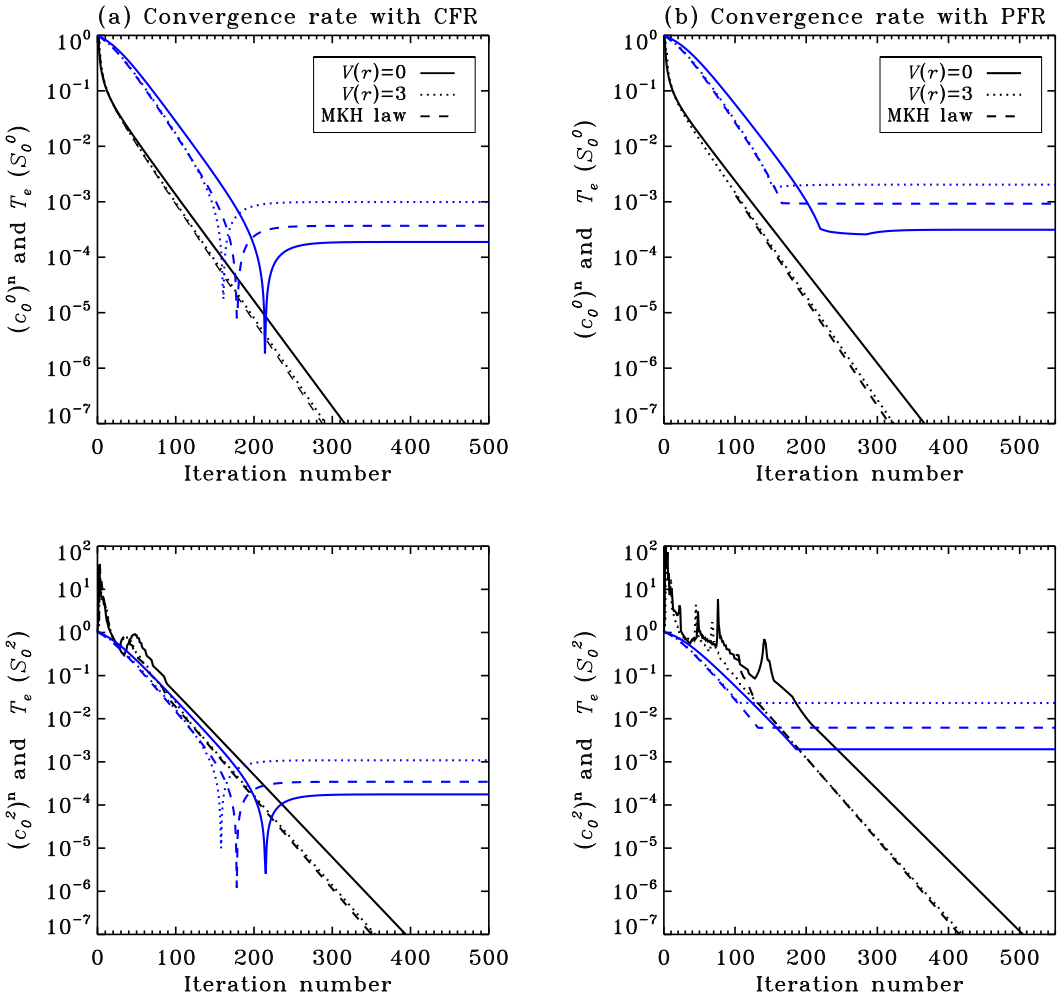

FIGURE 5.3: Maximum relative change of CMF irreducible source vector components $(c_0^0)^n$ (top panels) and $(c_0^2)^n$ (bottom panels) as a function of iteration number (black lines) calculated using Jacobi scheme. Blue lines show the surface true error on $\mathcal{S}_0^0$ (top panels) and $\mathcal{S}_0^2$ (bottom panels). Panel (a) corresponds to the case of CFR and panel (b) to the case of PFR. Model parameters are given in Section 4.4.

where V_0 is the maximum expansion velocity. Parameters a and b are chosen such that the maximum velocity gradient dV/dr occurs at the specified radius denoted by $r_v(= -b/a)$; and we have one characteristic width of the velocity function (namely, $c = a(r_v - 1)=1$) between $r = r_v$ and $r = 1$. Following Mihalas *et al.* (1975), we have chosen $r_v = (R + 1)/2$.

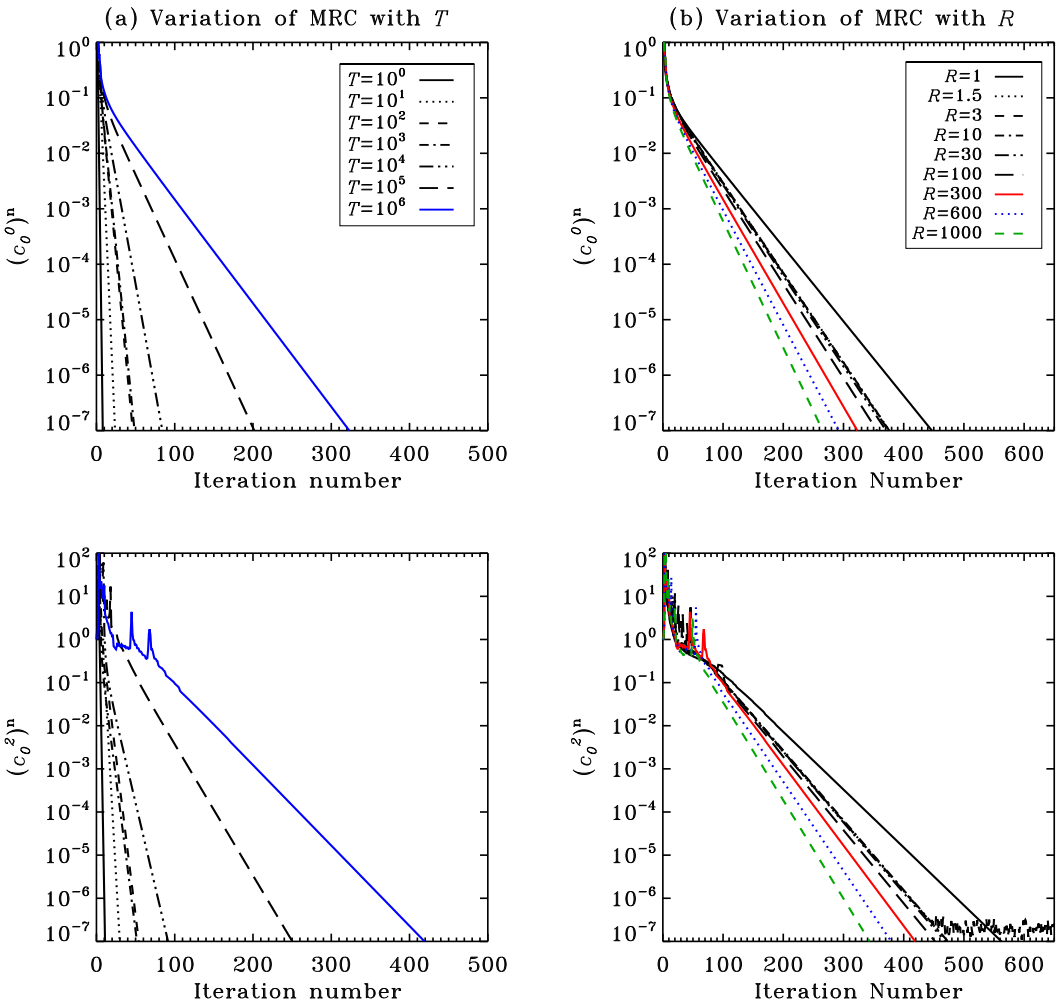

FIGURE 5.4: Maximum relative change of CMF irreducible source vector components $(c_0^0)^n$ and $(c_0^2)^n$ as a function of iteration number for the case of PFR and for a constant velocity field of $V(r) = 3$ calculated using Jacobi scheme. Model parameters are given in Section 4.4. Panel (a) shows the effect of varying T with fixed outer radius R=300 and panel (b) shows the effect of varying R with fixed $T = 10^6$, values of which are given in the inset box.

5.4.2 Convergence behavior of the CMF Jacobi scheme

In this section we study the convergence properties of the CMF-PALI method, based on Jacobi scheme, by following the MRC of the CMF irreducible source vector components with iteration. The MRC of the CMF source vector components at the n^{th} iterate is defined in Equation (4.36) of Section 4.5 of Chapter 4. The iterations are stopped when $\max[(c_0^0)^n, (c_0^2)^n] < 10^{-8}$. Figure 5.3 shows a plot of $(c_0^0)^n$ and $(c_0^2)^n$ versus iteration number for the case of CFR (panel (a)) and PFR

(panel (b)) both in the presence and absence of velocity fields. As expected the convergence is somewhat slower in the case of PFR than in the case of CFR (due to photon-trapping in the wings). Also the rate of convergence is slightly larger in the presence of a velocity field than in the static case (compare black solid and dotted or dashed lines). This is because the photons escape more easily from a moving atmosphere than the static one (see Kunasz and Hummer 1974b). Thus the CMF term (see Equation (5.9)) appears to smoothen the transfer problem. For both the velocity laws chosen by us, the rate of convergence is nearly identical (dotted black and dashed lines nearly coincide).

To illustrate the numerical accuracy of the converged numerical solution obtained from CMF-PALI method, based on Jacobi scheme, we also plot in Figure 5.3 the surface true error (see Equation (4.37) for definition) of CMF irreducible source vector components $\mathcal{S}_0^0$ and $\mathcal{S}_0^2$ (shown as blue lines). The true solution required to calculate the relative surface true error, is obtained on a spatial grid of 40 points per decade. As expected the true error is slightly larger for the case of PFR than for CFR. Also the true error is larger in the presence of velocity fields than the corresponding static case. This may be due to the use of local upwind scheme for the frequency derivative in the CMF term and also due to the use of linear interpolation for the CMF source term. In the case of CFR, surface true error on $\mathcal{S}_0^0$ and $\mathcal{S}_0^2$ are of the nearly similar magnitude (see also Trujillo Bueno 1999). Whereas in the case of PFR, true error on $\mathcal{S}_0^2$ is slightly larger than that on $\mathcal{S}_0^0$ (see also Sampoorna and Nagendra 2016).

In Figure 5.4, $(c_0^0)^n$ and $(c_0^2)^n$ are plotted as a function of iteration number for varying T (panel (a)) and varying R (panel (b)) for the case of PFR and for a constantly moving spherical atmosphere. As T increases the rate of convergence decreases. In other words, larger the optical thickness of the sphere, slower is the convergence. This is because as T increases number of scatterings also increases. From panel (b) we see that the rate of convergence increases with an increase in R. This is because the mean number of scatterings decrease as R increases (see Table VII of Kunasz and Hummer 1974a). For the same reason the convergence is faster in the case of spherical geometry than in planar case ($R = 1$). From Figures 5.3 and 5.4, it is clear that the iterations can be stopped when the MRC is less than 10^{-4}, as we are already in the asymptotic region of the MRC curve. We have also computed the surface true error for all the cases shown in Figure 5.4. For

varying optical thickness T (Figure 5.4(a)), the surface true error is on the order of 0.23 $\times 10^{-5}$ to 0.03% on $\mathcal{S}_0^0$ and 0.19% on $\mathcal{S}_0^2$. For varying R (Figure 5.4(b)), it is on the order of 0.029% to 0.045% on $\mathcal{S}_0^0$ and 0.03% to 0.19% on $\mathcal{S}_0^2$.

We remark that the rates of convergence of $\mathcal{S}_0^0$ and $\mathcal{S}_0^2$ shown in Figures 5.3 and 5.4 are somewhat slow. This is because we have chosen a depth grid with 20 points per decade. It is well-known that the ALI (or PALI) methods based on Jacobi iterative scheme exhibit slower convergence rate as the number of points per decade is increased (see, e.g., Figure 2 of Anusha *et al.* 2009). The rate of convergence can be accelerated using either Ng acceleration or by using iterative techniques based on GS and SOR schemes which we discuss in the next section. We also note that rate of convergence mainly depends on number of depth points per decade and is not much affected by refining the frequency grid. Although the rate of convergence as shown in Figures 5.3 and 5.4 is somewhat slow, we have verified that the converged numerical solution that we obtained is stable (with respect to depth, angle, and frequency grids). Indeed, we have reproduced the scalar solution with and without velocity fields presented in Kunasz and Hummer (1974b), Mihalas *et al.* (1975, 1976b).

5.4.3 Convergence behavior of the CMF GS and SOR schemes

Figure 5.5 shows a plot of $(c_0^0)^n$ (top panels) and $(c_0^2)^n$ (bottom panels) as a function of iteration number for the case of CFR (panel (a)) and PFR (panel (b)) both in static (black lines) and constantly moving atmosphere with $V(r) = 3$ (blue lines) for Jacobi (solid lines), GS (dotted lines), and SOR (dashed lines) schemes. For a static spherical atmosphere the convergence behavior of all the three iterative schemes is identical to that discussed in Section 4.5. This continues to remain valid also in the presence of velocity fields demonstrating the correctness of our generalization of these schemes in the CMF.

Figure 5.6 shows a plot of the surface true error on $\mathcal{S}_0^0$ (top panels) and $\mathcal{S}_0^2$ (bottom panels) as a function of iteration number for the case of CFR (panel (a)) and PFR (panel (b)) both in static (black lines) and constantly moving atmosphere with $V(r) = 3$ (blue lines) for Jacobi (solid lines), GS (dotted lines), and SOR

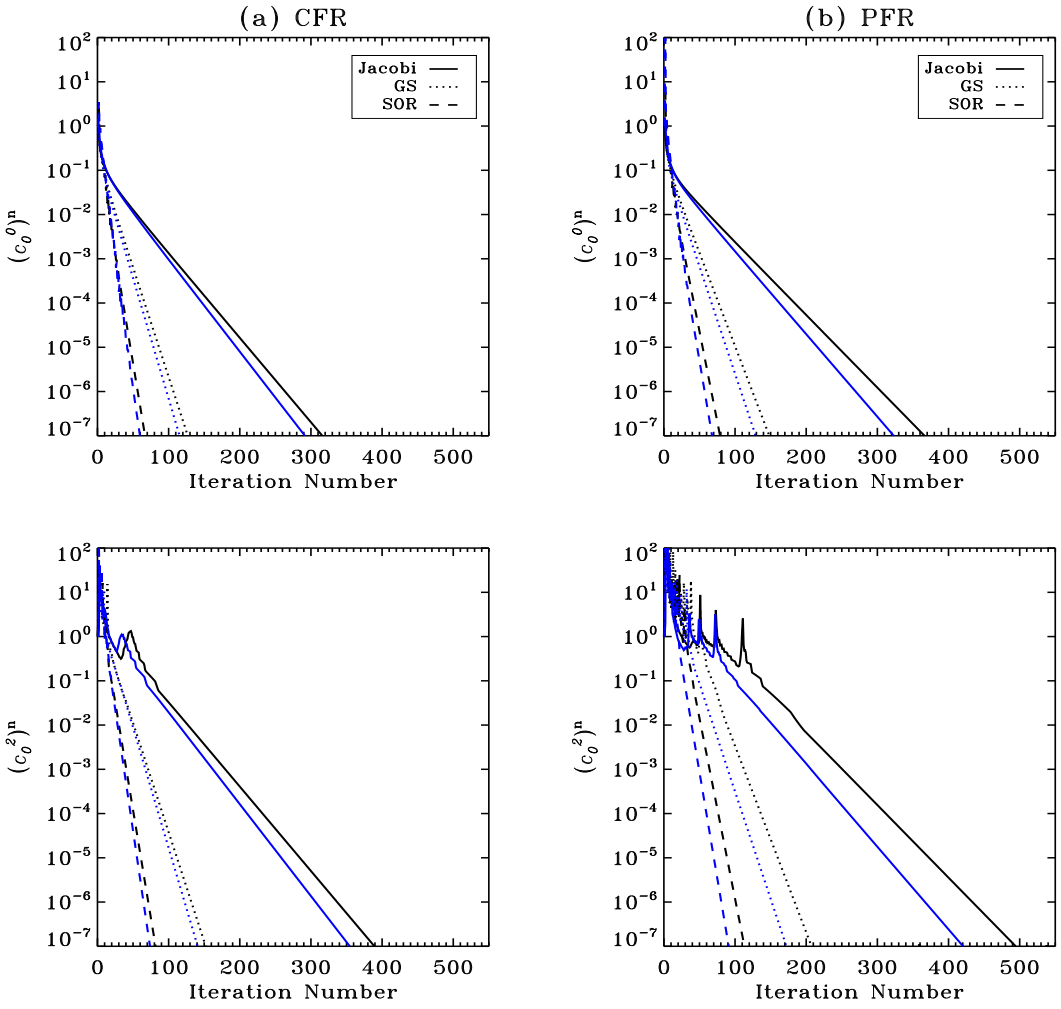

FIGURE 5.5: Maximum relative change of CMF irreducible source vector components $(c_0^0)^n$ (top panels) and $(c_0^2)^n$ (bottom panels) as a function of iteration number for the static (black lines) and constantly moving atmosphere with $V(r) = 3$ (blue lines). Panel (a) corresponds to the case of CFR and panel (b) to the case of PFR. Model parameters are given in Section 4.4. Different line types are for the Jacobi (solid lines), GS (dotted lines) and SOR (dashed lines) schemes as given in the inset box. The SOR parameter $\omega = 1.22$.

(dashed lines) schemes. The true solution required to calculate the surface true error is obtained by using a grid whose resolution is twice finer (40 points/decade) than the one on which we determine the true error (20 points/decade). Clearly, the surface true error for the case of PFR is larger than that for CFR. The surface true error is also larger in the presence of velocity fields (see Section 5.4.2). For the case of CFR, the surface true error on $\mathcal{S}_0^0$ is 0.018 % and 0.098 % for the static and velocity cases respectively, while on $\mathcal{S}_0^2$ it is 0.017 % and 0.108 % for the static and velocity cases respectively. On the other hand for PFR, corresponding surface

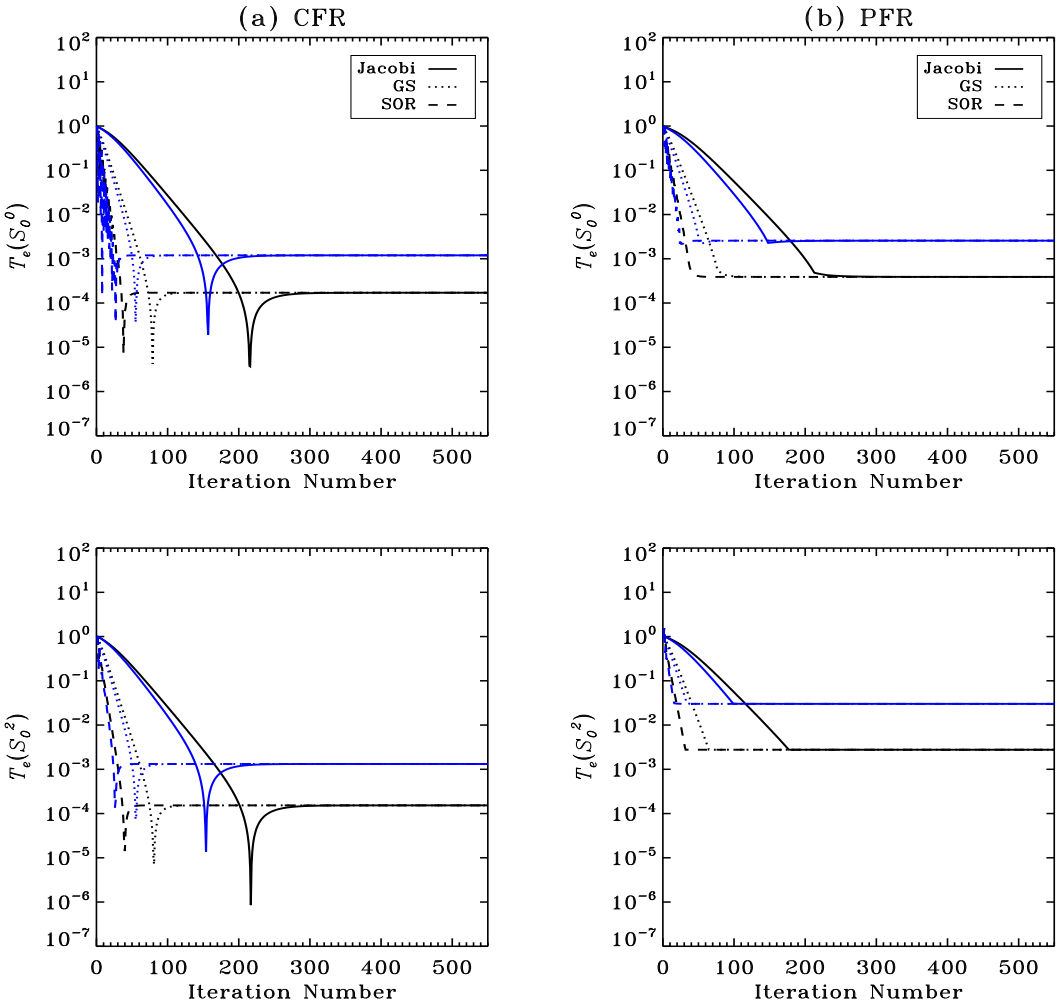

FIGURE 5.6: The surface true error on $\mathcal{S}_0^0$ (top panels) and $\mathcal{S}_0^2$ (bottom panels) as a function of iteration number for the static (black lines) and constantly moving atmosphere with $V(r) = 3$ (blue lines). Panel (a) corresponds to the case of CFR and panel (b) to the case of PFR. Model parameters are given in Section 4.4. Different line types are for the Jacobi (solid lines), GS (dotted lines) and SOR (dashed lines) schemes as given in the inset box. The SOR parameter $\omega = 1.22$.

true error are 0.031 % and 0.20% on $\mathcal{S}_0^0$ and 0.19 % and 2.31% on $\mathcal{S}_0^2$. The surface true errors on $\mathcal{S}_0^0$ and $\mathcal{S}_0^2$ are somewhat of similar magnitudes in the case of CFR. Whereas in the case of PFR, the surface true error on $\mathcal{S}_0^2$ is larger than that on $\mathcal{S}_0^0$ by about 10 % as already noted in Section 4.5. Like the MRC plots, the surface true error plots also clearly demonstrate that the GS and SOR schemes converge much faster than the Jacobi scheme not only in static case but also in the presence of velocity fields.

5.5 Concluding remarks

It is well-known that when photon mean free path is a non-vanishing fraction of the radius of curvature of the atmosphere, then the plane-parallel approximation breaks down. This is particularly true for extended stellar atmospheres, like in the solar corona, giant and super giant stars, Wolf–Rayet stars etc. In this chapter we have considered the problem of polarized line formation in spherically symmetric extended atmospheres with velocity fields. We have developed both observer's frame and comoving frame methods to solve this problem. In particular, we applied the polarized accelerated lambda iteration method (see reviews by Nagendra 2003 and Nagendra and Sampoorna 2009), with appropriate modifications to handle the velocity fields. We used the second frequency discritization of Hauschildt and Baron (2004) to handle the comoving frame term. We also discussed the necessary modifications to be considered for applying the GS and SOR schemes to the problem of radiative transfer in expanding spherical atmospheres.

Unlike the planar atmospheres, in the extended spherical atmospheres, the observer's frame method quickly becomes computationally prohibitive. This clearly demonstrates the need for the comoving frame method. For our numerical studies, we considered isothermal atmospheres with inverse square law opacity and radial velocity fields. Also, resonance scattering on a two level atom with unpolarized ground level is considered with both CFR and angle-averaged PFR mechanisms. We have studied the convergence behavior and the surface true error of the newly developed CMF-PALI method based on the Jacobi, GS, and SOR schemes for both CFR and PFR cases. We have also studied the convergence behavior for varying optical thickness T and the extendedness R for the spherically symmetric constantly moving atmosphere with PFR.

Chapter 6

Polarized Line Formation in Spherically Symmetric Moving Atmospheres: *Numerical Studies*[1]

An overview

Iterative techniques based on the Jacobi, Gauss-Seidel (GS), and successive overrelaxation (SOR) schemes to solve the problem of resonance line polarization formed in spherically symmetric static and expanding atmospheres are developed in Chapters 4 and 5 respectively. For the latter a comoving frame (CMF) formulation has been developed. In this chapter we present and discuss the numerical solutions obtained in spherically symmetric static and moving atmospheres. For our studies, we consider scattering on a two-level atom, including the effects of partial frequency redistribution (PFR). We study the effects of velocity fields, extendedness, and frequency redistribution on the polarized line profiles formed in highly extended atmospheres. We also present the center-to-limb variation (CLV) of the polarized profiles including both complete frequency redistribution (CFR) and PFR.

[1]This chapter is based on the publication: Megha *et al.* (2019b)

6.1 Introduction

Solar and Stellar atmospheres are known to be dynamic in nature. These systematic velocity fields in spectral line forming regions strongly affect the shapes and amplitudes of the polarized spectral lines. For example, P-Cygni profiles with a blue absorption and a red emission are known to be formed in an extended and expanding stellar atmosphere. Effects of macroscopic velocity fields on the intensity and flux profiles have been studied in great details (Hubeny and Mihalas 2014). However, similar studies in the case of polarized spectral lines are sparse, particularly in extended spherically symmetric atmospheres with PFR as the scattering mechanism.

Effects of velocity fields on linearly polarized line profiles formed in a planar atmosphere are presented in Sengupta (1993), Rangarajan (1997), Carlin *et al.* (2012, 2013), for CFR in scattering, and in Nagendra (1996), Sampoorna and Nagendra (2015a,b, 2016) for PFR in scattering. In the case of spherically symmetric atmospheres such studies are presented in Hillier (1996) for electron scattering. In this chapter we present effects of velocity fields on linearly polarized line profiles formed in spherically symmetric expanding atmospheres for PFR in scattering.

The fundamental properties of the spherically symmetric atmosphere when compared to the plane-parallel case are: bias in scattering to the larger radii, dilution of the diffuse radiation field, and peaking of radiation in the radial direction. These peculiarities of the spherical radiative transfer are discussed in detail in Kunasz and Hummer (1974a,b). These properties of the spherical atmosphere, in particular the outward peaking of the radiation, induces a high degree of polarization as we move from center-to-limb (Cassinelli and Hummer 1971; Chapman 1966, see also Section 6.3).

In Chapters 4 and 5, we respectively developed the iterative techniques to solve the polarized line transfer equation in spherically symmetric static and expanding atmospheres. In particular, we extended the CMF-ALI method of Hauschildt and Baron (2004) to include polarization and PFR. For our studies we considered the CMF transfer equation in the non-relativistic limit. The atmospheric and atomic parameters used for the solutions presented in this chapter are the same as those detailed in Section 4.4, while the empirical velocity laws used are the same as those

given in Section 5.4.1. Here we use the CMF-PALI method presented in Chapter 5 and discuss the effects of velocity fields on the polarized line profiles making use of contribution functions (cf. Section 6.2). We also discuss the center-to-limb variation (CLV) of the polarized line profiles (cf. Section 6.3), and interesting effects of extendedness on the linearly polarized profiles formed under both CFR and PFR (cf. Section 6.4). Finally Section 6.5 gives the concluding remarks.

6.2 Effect of velocity field in spherical atmospheres

Figure 6.1 shows the emergent polarization profiles, computed with different radial velocity laws discussed in Section 5.4.1, for the case of CFR (panel (a)) as well as PFR (panel (b)). The intensity exhibits a self-reversed emission profile. The central absorption is due to the contribution from the optically thick stellar core, while the two emission peaks are due to the optically thin emission lobes. In particular the red emission peak comes from the far side of the hemisphere, while the blue emission peak gets its contribution from the near side of the hemisphere (Hubeny and Mihalas 2014). In the absence of the velocity field both the hemispheres are symmetric, thereby giving rise to symmetric emission peaks. The emission peaks in the case of PFR have higher amplitude than in the CFR case, due to increased transfer effects in the wings for the case of PFR. In the presence of velocity field the far side of the hemisphere moves away from the observer, while the near side approaches the observer. Furthermore, the opacity toward the blue side increases while that on the red side decreases (van Blerkom and Hummer 1968). As a result the red emission peak formed in the far side escapes easily from the near side, while the blue emission peak encounters increased absorption and scattering in the near side before escaping the atmosphere. This difference gives rise to asymmetric emission peaks with the blue emission peak smaller in height than the red emission peak. Also the line center and the blue emission peak are slightly blueshifted due to the velocity field.

The static Q/I profile, with a central peak followed by a core minima and wing peaks, exhibits a typical triple peak structure due to PFR (see the solid line in the Q/I panel of Figure 6.1(b)). However, the wing PFR peaks are enhanced

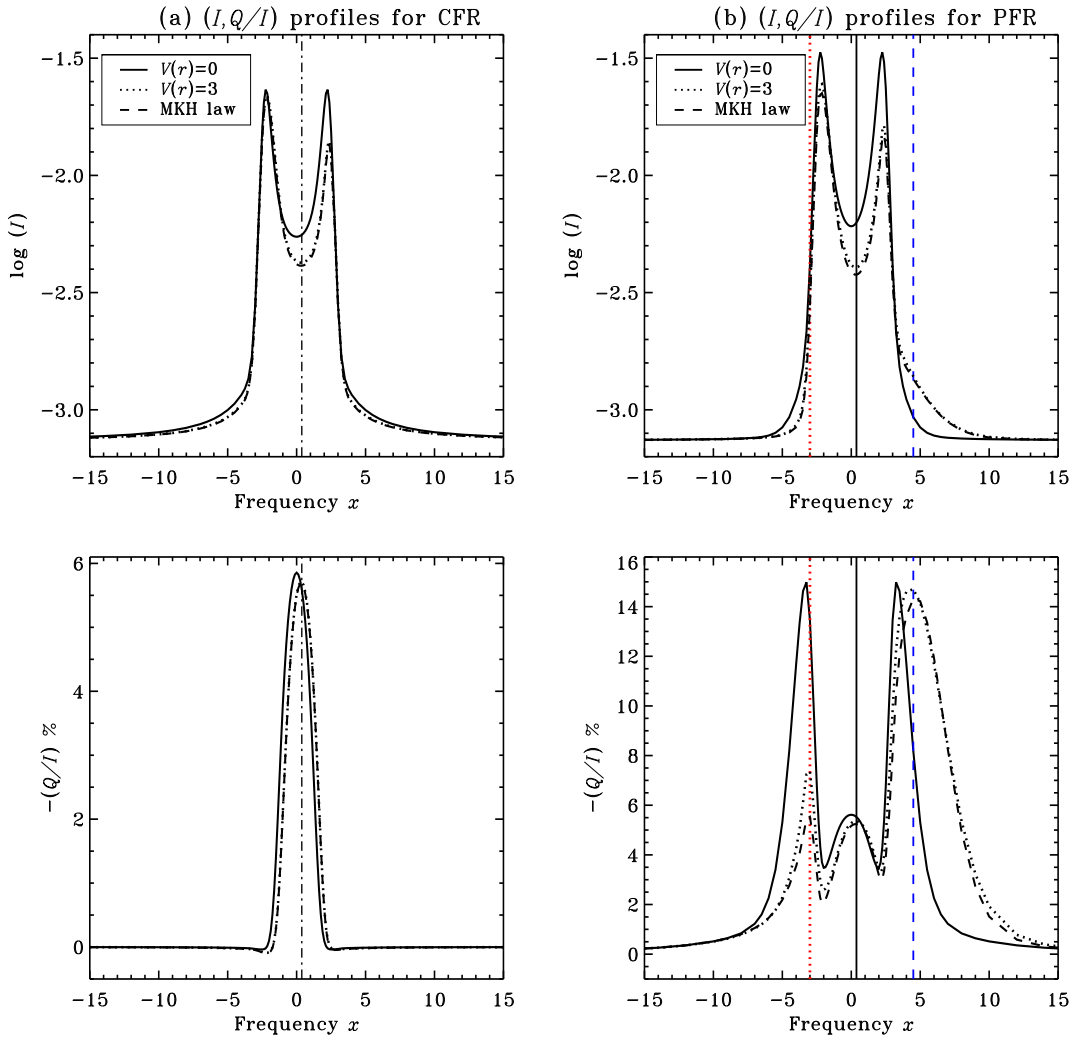

FIGURE 6.1: Emergent $(I, Q/I)$ profiles from spherically symmetric atmospheres with different velocity laws. Panel (a) corresponds to the case of CFR and panel (b) to the case of PFR. The model parameters are given in Sections 4.4 and 5.4.1. The line-of-sight is at μ=0.11. Different line types represent different velocity laws as shown in Figure 5.2. Vertical lines mark the frequency positions of line core peak and wing PFR peaks corresponding to the dotted line in the Q/I panels.

in magnitude compared to the line center peak. This is due to the scattering contribution from the optically thin emission lobes at large distances from the stellar core having a larger degree of anisotropy due to outward peaking of the radiation field. The corresponding CFR Q/I profile is confined to the line core (see the solid line in the Q/I panel of Figure 6.1(a)). In the presence of velocity fields, line center CFR as well as PFR peaks and the wing PFR peaks are slightly blueshifted. Also the blue wing PFR peak is broadened. On the other hand, the red wing PFR peak is considerably diminished in magnitude. These interesting

effects of velocity fields on the wing PFR peaks in Q/I can be understood using the depth dependence of the contribution function and the source vector along a given impact parameter ray (see Section 6.2.1.) The (I, Q/I) profiles computed with a constant velocity field and MKH velocity law do not differ greatly (compare dotted and dashed lines in Figure 6.1). This is due to the fact that the MKH velocity law is nearly constant over large regions of the atmosphere (see Figure 5.2). It is useful to note that the frequency positions of the wing PFR peaks in Q/I profiles do not correspond to the frequency positions of emission peaks in I profiles (see the vertical line in Figure 6.1(b)). This is because the wing PFR peaks in Q/I arise due to the scattering mechanism of $R_{\rm II,AA}$ function, whereas emission peaks in I arise due to the radiative transfer effects in a spherical atmosphere.

6.2.1 Contribution functions and source vectors

Following Magain (1986), the contribution functions for I and Q along a given impact parameter ray in a spherically symmetric moving atmosphere may be defined as

$$C_i(z,p,x) = \ln(10)\frac{\chi_l(r)\phi(r,\mu,x)+\chi_c(r)}{\chi_l(r)\phi(r,\mu,x=0)+\chi_c(r)}\tau(z,p,x=0)e^{-\tau(z,p,x)}S_i(z,p,x), \quad (6.1)$$

where i =0, 1 for I and Q. It is well-known that C_I and C_Q for a given x and p give the relative contribution of different spherical shells along the considered impact parameter ray to that frequency in the emergent $(I, Q/I)$ profiles.

Figures 6.2(a) and 6.2(b), show a plot of C_I and C_Q versus the line integrated tangential optical depth τ_z for a ray of impact parameter p=298 (which emerges at μ=0.11) for x=0.375 corresponding to a Q/I line core peak for $V(r)$=3 (see solid vertical line in Figure 6.1(b)) and for x corresponding to wing PFR peaks in Q/I profile for $V(r)$=3 (see red dotted and blue dashed vertical lines in Figure 6.1(b)), respectively. Although the total optical thickness is 10^6, for the chosen lobe ray, the maximum line integrated tangential optical depth reached is 3.88×10^2. This is because of the inverse square law variation of the opacity along the radius. Thus the total optical thickness of 10^6 is attained only for core rays, which then progressively decreases for lobe rays. From Figure 6.2(a), we see that the peak contribution to the line core peak in Q/I comes from $\tau_z \approx 2.5$, with the velocity

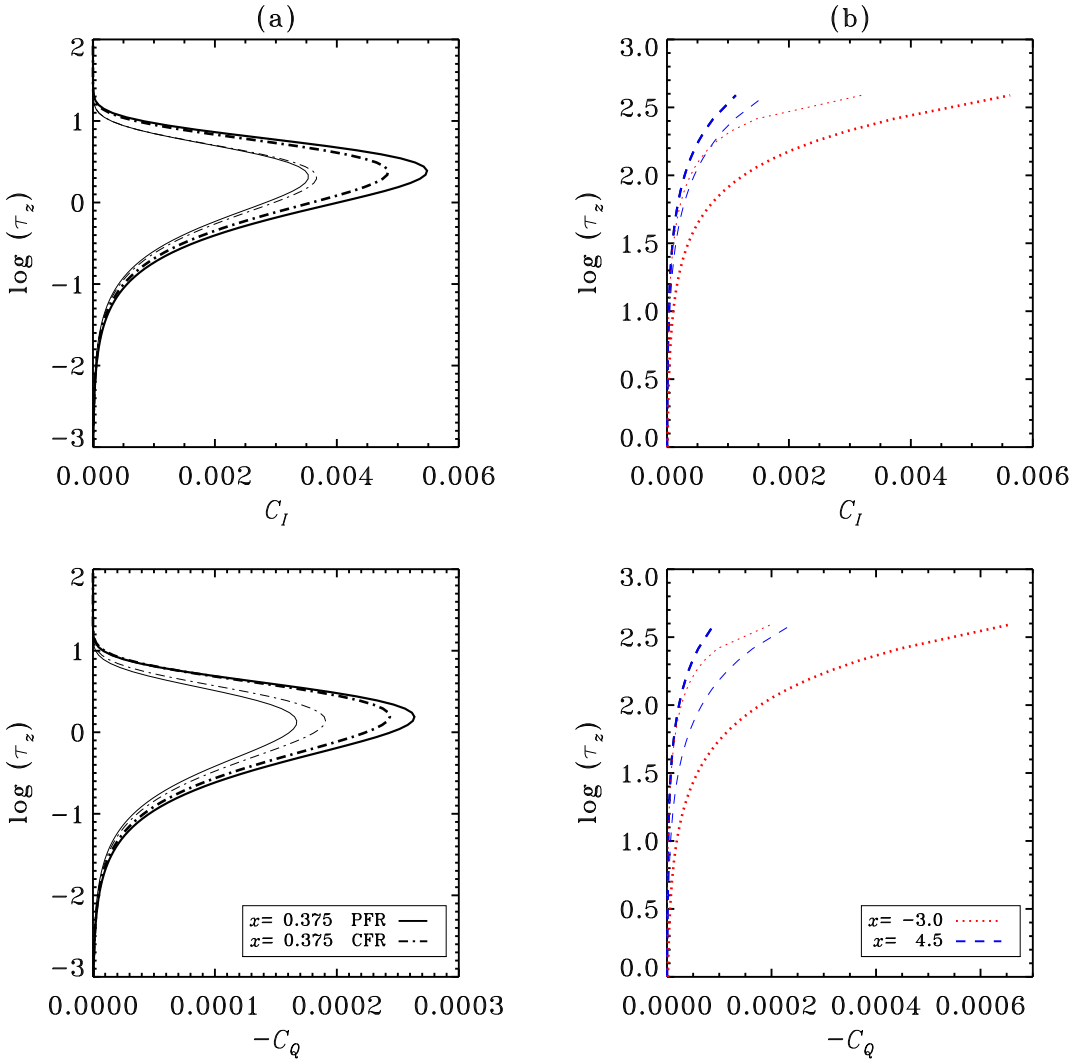

FIGURE 6.2: Panels (a) and (b) show a plot of C_I and C_Q, versus line integrated tangential optical depth τ_z for a ray with impact parameter p=298, and for different values of frequency x (indicated in the inset box). All the frequency points are chosen keeping the Q/I profile of a constantly moving atmosphere with $V(r)$=3 as the reference (see the vertical lines in Figure 6.1). Thin lines correspond to the case of a constantly moving spherical atmosphere with $V(r) = 3$, while thick lines to the case of static spherical atmosphere. Excepting the dotted-dashed lines all the other line types correspond to the case of PFR. Model parameters are given in Sections 4.4 and 5.4.1. Although log τ_z varies from -6 to 2.58, a shorter y-axis range has been chosen in panels (a) and (b) in order to show the variation of C_I and C_Q more clearly (as outside this range C_I and C_Q tend to zero).

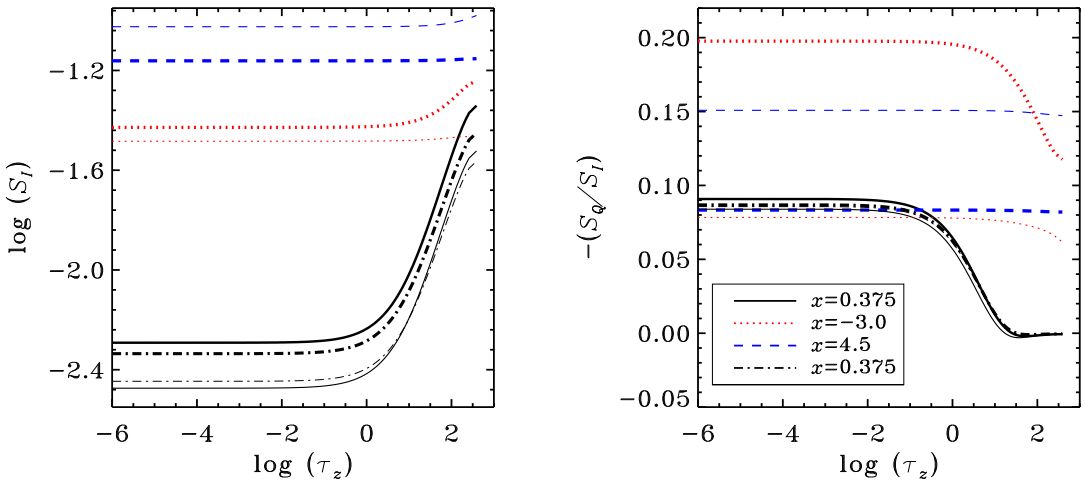

FIGURE 6.3: Plot of S_I and S_Q/S_I versus line integrated tangential optical depth τ_z for a ray with impact parameter p=298, and for different values of frequency x (indicated in the inset box). All the other descriptions are as indicated in caption of Figure 6.2. The thin dotted-dashed line in the S_Q/S_I panel is right below the thick dotted-dashed line and it is indistinguishable in the adopted scale.

field case formed slightly higher in the atmosphere than the corresponding static case for both CFR (compare thick and thin dotted-dashed lines in Figure 6.2(a)) and PFR (compare thick and thin solid lines in Figure 6.2(a)). This is because the maxima of the line opacity now shifts toward the blue side of the line profile in the presence of velocity field. For the same reason the peak values of C_I and C_Q also drop to a smaller value. In the case of wing PFR peaks, C_I and C_Q do not exhibit a closed curve as seen in Figure 6.2(a). Instead C_I and C_Q show an open curve, with the peak contribution coming from the mid-line of the spherical atmosphere. This is because the monochromatic total optical thickness at the wing PFR peaks of Q/I is much smaller than that at line core peak by about 4 orders of magnitude. For the blue wing PFR peak larger portions of the atmosphere contribute to the line formation in moving media compared to the corresponding static case (compare thick and thin blue dashed lines in Figure 6.2(b)). An inverse of this behavior is seen for the red wing PFR peak (compare thick and thin red dotted lines in Figure 6.2(b)). For a given LOS the projected velocity varies over a larger range (from 0 to $\mu_{\rm max}V$ as μ varies from 0 to $\mu_{\rm max}$, with $\mu_{\rm max} = \sqrt{1-(p/R)^2}$) along the ray. Since the blue wing gets contribution from a larger portion of the atmosphere, the blue wing PFR component is broadened more than the red wing component. This

can be seen not only in Q/I profile but also in I profile for $3.5 \leq x \leq 10$ (see Figure 6.1(b)).

To understand the modification in the amplitudes of the line core peak, red and blue wing PFR peaks brought about by the velocity field compared to the corresponding static case, we show in Figure 6.3 a plot of S_I (which is proportional to mean intensity of the radiation field) and the ratio S_Q/S_I (which is a measure of radiation anisotropy) versus the line integrated tangential optical depth τ_z for a ray of impact parameter p=298 (which emerges at μ=0.11). From Equation (5.3) it is clear that $\mathcal{S}^0_{l,0}$ is directly proportional to $\bar{\mathcal{J}}^0_0$ (the mean intensity that is given by scattering integral in Equation (5.3)) and $\mathcal{S}^2_{l,0}$ to $\bar{\mathcal{J}}^2_0$. Unlike the planar atmosphere in a spherical atmosphere, for a given LOS the μ varies from 0 at the mid line to $\mu_{\rm max} = \sqrt{1-(p/R)^2}$. Thus S_I and S_Q along a given p exhibit a more stronger μ dependence than $\mathcal{S}^0_0$ and $\mathcal{S}^2_0$ themselves (see Equations (5.7) and (5.8) with S_I and S_Q in place of I and Q; and $\mathcal{S}^0_0$ and $\mathcal{S}^2_0$ in place of $\mathcal{I}^0_0$ and $\mathcal{I}^2_0$). Therefore, in a spherical atmosphere, S_I and S_Q/S_I provide a better representation of the mean intensity and local radiation anisotropy than the $\bar{\mathcal{J}}^0_0$ and $\bar{\mathcal{J}}^2_0/\bar{\mathcal{J}}^0_0$. For this reason we have plotted S_I and S_Q/S_I in Figure 6.3.

Apart from producing a Doppler shift of photons, the velocity field modifies the scattering integral and thereby the source vector. This modification leads to the so-called Doppler brightening or dimming effect depending on whether the spectral line is in absorption or emission (see Section 12.4 of Landi Degl'Innocenti and Landolfi 2004, also Carlin *et al.* 2012). We note that Doppler brightening or dimming referred to here is largely based on increase or decrease of the mean intensity with respect to the corresponding static case more than the specific intensity itself. The atoms in the higher layers that are moving with larger velocity intercept more effectively the radiation from the blue wing photons emerging from the deeper layers. If the underlying spectral line is in absorption, then the wings have higher intensity than the core thereby leading to an increase in mean intensity. On the other hand if the spectral line is in emission, then the wings have smaller intensity than the core, leading to a decrease in mean intensity. The Doppler brightening or dimming is relatively more pronounced for $\mu = 1$, because the corresponding projected velocity (μV) is larger. This introduces an additional limb darkening and thereby causing an increase or decrease in anisotropy of the radiation, depending

on whether Doppler brightening or dimming is involved. From the above discussion, it is clear that Doppler brightening or dimming comes into play only when velocity gradients are present along an LOS. In a planar atmosphere a constant velocity field would therefore produce only Doppler shift of $(I, Q/I)$ profiles (see, e.g., Carlin *et al.* 2012, Sampoorna and Nagendra 2015b). However, in a spherical atmosphere with constant radial velocity, Doppler brightening and dimming are at play, because the projected velocity μV varies all along a given LOS, due to the variation of μ. Another important difference with respect to the planar case is the following. An absorption or emission line formed in an isothermal planar atmosphere continues to be in absorption or emission when the LOS changes from center to limb (see Figures 6.4(a) and (b)). However, in a spherical atmosphere the spectral line can change from being in absorption for core rays to nearly an emission line for extreme lobe rays with self-reversed emission line for intermediate positions (see, e.g., Figures 6.5(a) and 6.6(a)). As a result Doppler brightening and dimming are simultaneously present.

Compared to the static case, the S_I at $x = 0.375$ for the constantly moving case has reduced in magnitude for both CFR (compare thick and thin dotted-dashed lines in Figure 6.3) and PFR (compare thick and thin solid lines in Figure 6.3). This continues to be the case for the red wing PFR peak (compare thick and thin red dotted lines in Figure 6.3). Correspondingly the S_Q/S_I has also decreased for the case of moving media compared to the static case, the decrease being significantly larger for the red wing PFR peak than the line center peak. This is due to Doppler dimming (see Landi Degl'Innocenti and Landolfi 2004). Doppler dimming effects can be clearly seen in both $(I, Q/I)$ profiles for -6$\leq x \leq$3 (compare, e.g., solid and dotted lines in Figure 6.1(b)). The blue wing PFR peak on the other hand exhibits Doppler brightening in S_I (compare thick and thin blue dashed lines in Figure 6.3), namely larger values of S_I for nonzero velocity fields than the static case. The corresponding S_Q/S_I is larger for the case of moving media than the static case. Doppler brightening effects can be clearly seen in both $(I, Q/I)$ profiles for $3 < x \leq 10$ (compare, e.g., solid and dotted lines in Figure 6.1(b)). These differences in S_Q/S_I between different frequency points discussed above are clearly reflected in the Q/I profile.

From Figures 6.2(a) and 6.2(b) we can see that line core peak and the wing PFR peaks get their peak contribution from a spherical shell with $\tau_z \approx$2.5 and

from the mid line respectively. It is easy to verify that S_Q/S_I values around $\tau_z \approx 2.5$ (see black solid and dotted-dashed lines in Figure 6.3) and the mid line (see, e.g., red dotted and blue dashed lines in Figure 6.3) nearly match with the corresponding emergent Q/I values (see Figure 6.1). Thus in the same way as the Eddington–Barbier relation for polarization (Faurobert 1988, Frisch *et al.* 2009), which relates S_Q/S_I and emergent Q/I values at $\tau_{x\mu} = 1$, the contribution function, which provides the value of τ_z corresponding to the peak contribution to a given frequency, seems to represent a similar relation between the emergent Q/I and S_Q/S_I at that τ_z. However, unlike the Eddington–Barbier relation which applies only to semi-infinite atmosphere, the relation provided by contribution function, appears to be valid for any T. These statements regarding usefulness of the contribution function however, need to be further substantiated using detailed parametric studies, which is beyond the scope of the present Chapter.

6.3 Center-to-limb variation (CLV) of linearly polarized profiles

In Figure 6.4, we present CLV of intensity and linear polarization Q/I profiles for planar static atmosphere (CFR in panel (a) and PFR in panel (b)). Figures 6.5 and 6.6 show similar variation in spherical static atmosphere (panel (a)) and spherical constantly moving atmosphere (panel (b)) with CFR and PFR respectively. The planar static profiles are shown for comparison. They are computed with the same model parameters as given in Section 5.4.1, but with R=1.

We first discuss the CLV of $(I, Q/I)$ profiles computed using CFR. In the case of planar static atmosphere, we obtain an absorption line in intensity that exhibits limb darkening, while the corresponding Q/I profiles, which are confined to the line core, exhibit limb brightening as expected (see Figure 6.4(a)). In the case of spherical static atmosphere, disk center intensity again exhibits an absorption profile because the main contribution comes from the central stellar core (see the black solid line in Figure 6.5(a)). As soon as we move away from the disk center the optically thin extended lobe starts to contribute, giving rise to a self-reversed emission line. The contribution of central stellar core to absorption progressively decreases as we move toward the limb, finally resulting in an emission line for μ=0.02 (see

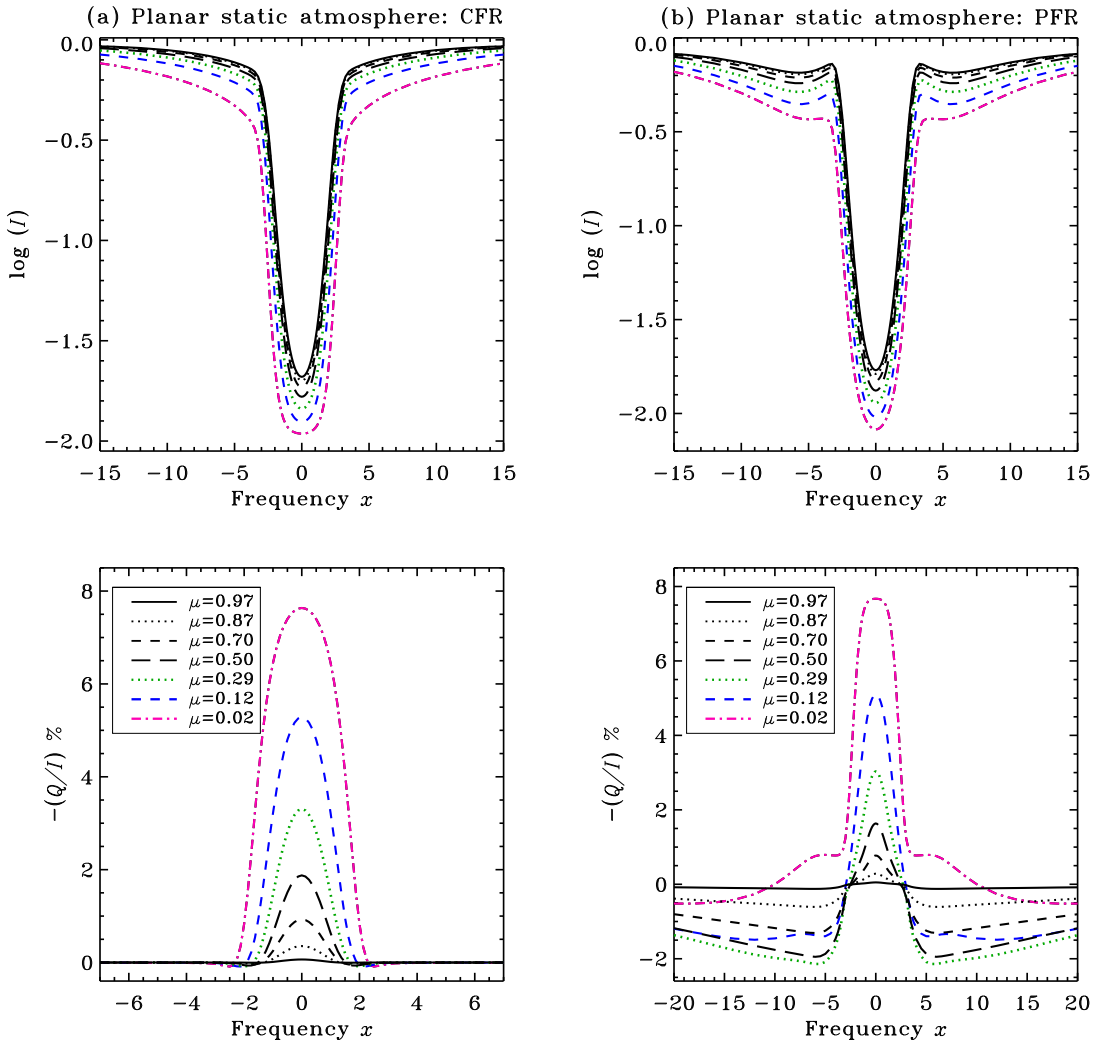

FIGURE 6.4: Center-to-limb variation of the emergent intensity and Q/I profiles for the case of planar atmosphere. The model parameters are given in Sections 4.4 and 5.4.1. Panel (a) corresponds to the case of CFR and panel (b) to the case of PFR. Different values of chosen μ are given in inset box.

the pink dotted-dashed line in Figure 6.5(a)). The corresponding Q/I profiles exhibit limb brightening as in the planar case. However, due to outward peaking of the radiation, Q/I profiles for smaller μ are somewhat broader with slightly larger amplitudes than the corresponding planar case. In the presence of a constant velocity field, I and Q/I profiles both exhibit a blueshift that progressively decreases as we move from disk center to limb as expected (see Figure 6.5(b)). In the intensity profiles, the emission peaks on the blue side are reduced, while those on the red side more or less retain this amplitude as in the corresponding static case for the same reason discussed in Section 6.2. However, the emission peak on

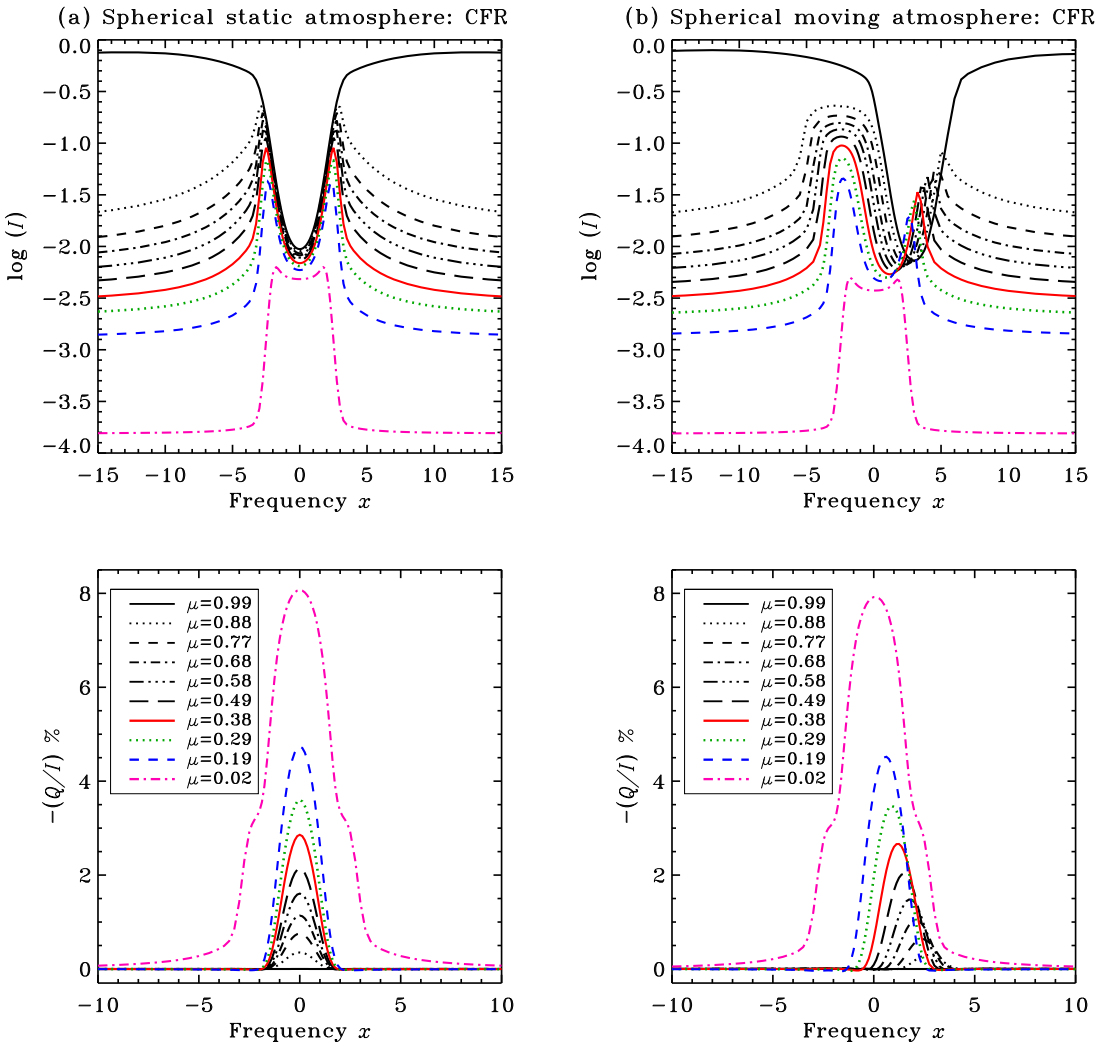

FIGURE 6.5: Center-to-limb variation of the emergent intensity and Q/I profiles for the case of spherical atmosphere with CFR. The model parameters are given in Sections 4.4 and 5.4.1. Panel (a) corresponds to the static atmosphere and panel (b) to the case of constantly moving atmosphere with $V(r) = 3$.

the red side is slightly redshifted, as the contribution to this peak comes from the far side of the hemisphere, which is moving away from the observer.

When angle-averaged PFR is taken into account the CLV of I and Q/I profiles is essentially similar to the CFR case discussed above. However, the PFR I profiles for the planar case exhibit a self-reversed absorption line with broad damping wings, which is typical of PFR (see Figure 6.4(b)). The effect of PFR can be clearly seen in the corresponding Q/I profiles, which show a central peak and PFR wing peaks, with Q/I reaching zero far in the wings unlike the corresponding CFR case. In the case of spherical static atmosphere the disk center I profile

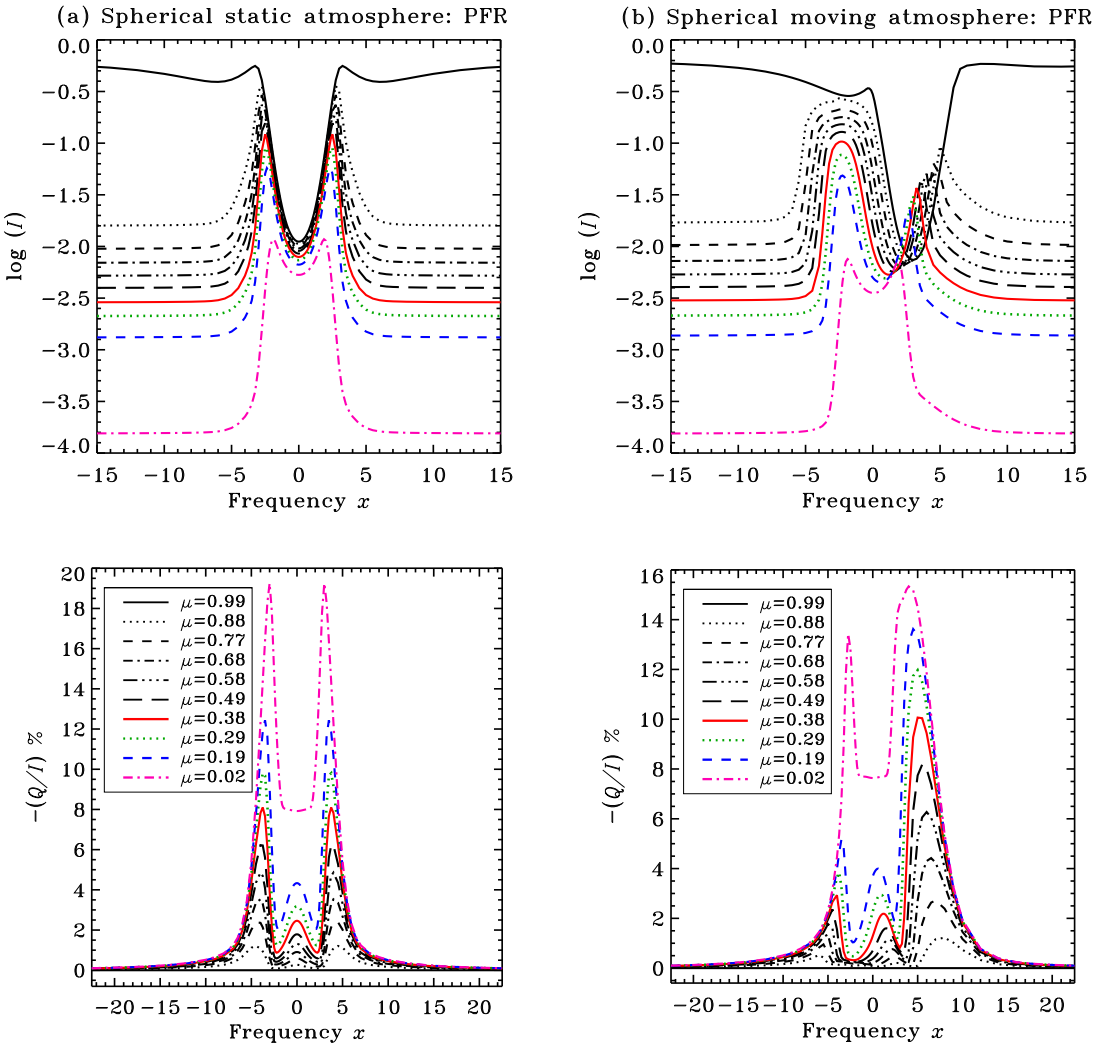

FIGURE 6.6: Same as Figure 6.5, but for the case of PFR.

essentially has a similar shape as the corresponding planar case (compare black solid lines in I panels of Figures 6.4(b) and 6.6(a)). However, as we move towards the limb, the differences between CFR I profiles and the corresponding PFR I profiles decreases relatively as the contribution from optically thin extended lobe dominates (compare I panels in Figures 6.5(a) and 6.6(a)). On the other hand the PFR Q/I profiles for the spherical static case, exhibit completely different shape than the corresponding planar case (compare Q/I panels in Figures 6.4(b) and 6.6(a)). Essentially we see a triple peak structure for $0.19 \leqslant \mu \leqslant 0.88$, while a double peak is seen for $\mu = 0.02$. The effect of outward peaking of the radiation field is more pronounced in the case of PFR due to increased trapping of photons in the line wings. For example, the wing PFR peaks show larger amplitude ($\sim 20\%$) as

we go toward the limb (see pink dotted-dashed lines in Figure 6.6(a)). We believe that the peculiarities of spherical geometry and the nature of PFR functions couple in an intricate way to produce the Q/I profiles presented in Figure 6.6(a).

The effect of a constant velocity field on the PFR I and Q/I profiles (see Figure 6.6(b)) is similar to the corresponding CFR profiles (see Figure 6.5(b)). However, the PFR Q/I profiles show a notable decrease in amplitude in the wings when compared to the corresponding spherical static case (compare Q/I panels in Figures 6.6(a) and 6.6(b)). Also the blue wing PFR peak is higher than the red wing PFR peak (see Q/I panel in Figure 6.6(b)), the differences being larger for $\mu \rightarrow 1$. As already discussed in Section 6.2.1, this can be understood as follows. The velocity fields are known to produce a Doppler brightening in the case of absorption lines and Doppler dimming in the case of emission lines (see Landi Degl'Innocenti and Landolfi 2004). Consequently, anisotropy increases or decreases respectively. The I profiles in a spherical medium change from an absorption line to self-reversed emission line as we go from center to limb. Thus both Doppler brightening and dimming are simultaneously at play in the presence of velocity fields. This is then reflected in the corresponding Q/I profile as noted in Section 6.2.1.

6.4 Effect of extendedness (R) of spherical atmosphere

In Figures 6.7, 6.9, and 6.10 we show the effect of extendedness R of the spherical atmosphere on the I and Q/I profiles both for the static (panel (a)) and constantly moving (panel (b)) atmospheres. The outer radius R of the spherically symmetric atmosphere is varied from 1.5 to 1000. The profiles computed with CFR are shown in Figure 6.7, while those computed with angle-averaged PFR are shown in Figures 6.9 and 6.10. The corresponding planar solution (R=1) is shown for reference. When R=1.5, the contribution from the central stellar core dominates over the emission lobes, resulting in an absorption line even for μ=0.11 (see dotted lines in I panels of Figures 6.7 and 6.9). As R increases the contribution from the emission lobes increases resulting in a self-reversed emission profile for both static and moving atmospheres and also for both CFR and PFR cases (see I panels of Figures 6.7, 6.9, and 6.10).

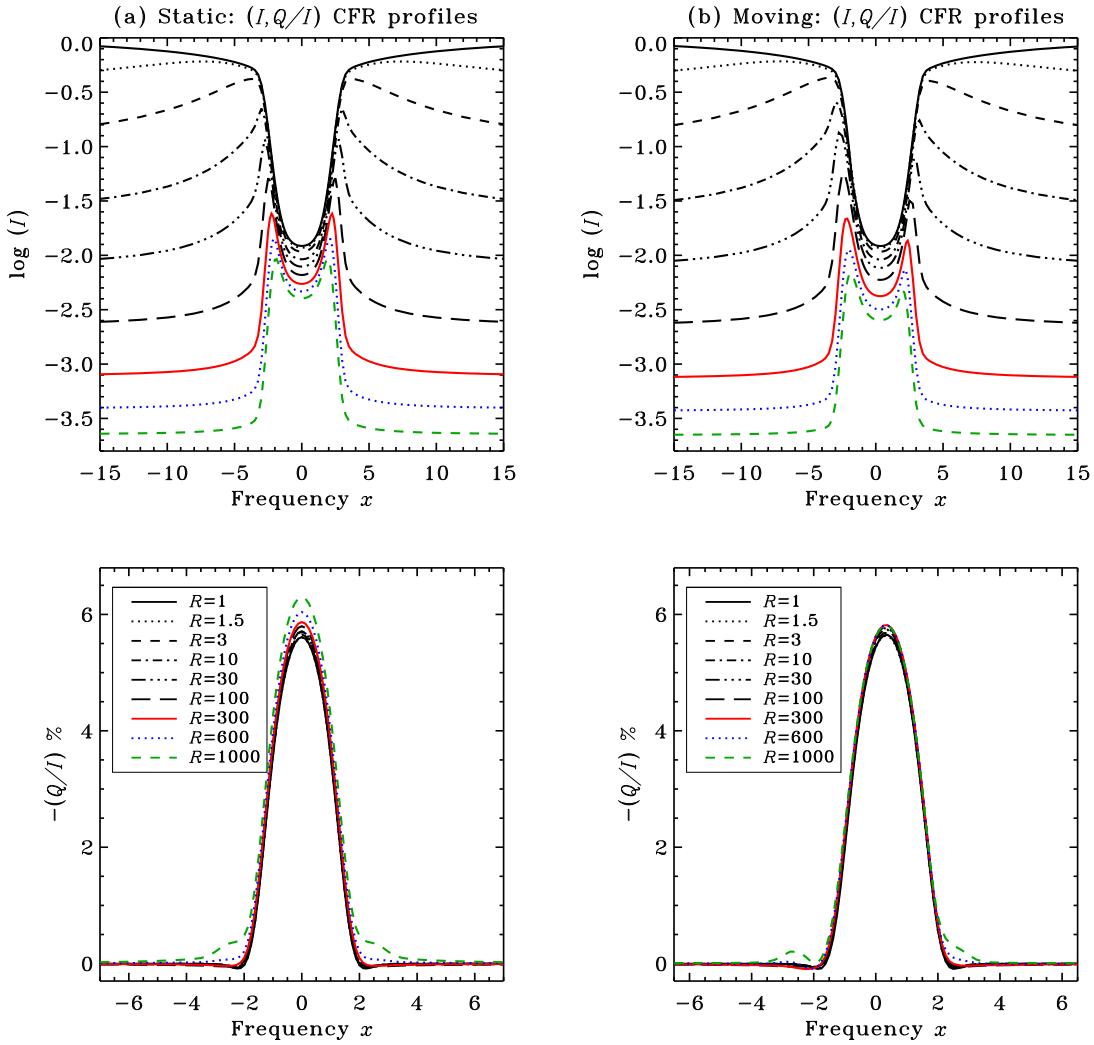

FIGURE 6.7: Emergent intensity and Q/I profiles for varying outer radius R of the spherical atmosphere in the case of CFR. The line-of-sight is at $\mu = 0.11$. Other model parameters are given in Sections 4.4 and 5.4.1. Panel (a) shows the profiles for a static atmosphere, while panel (b) for a constantly moving atmosphere with $V(r) = 3$.

The Q/I profiles computed with CFR are confined to the line core and are somewhat less sensitive to the extendedness R (see Q/I panels in Figure 6.7). The sensitivity is smaller in the presence of velocity fields than in the static case. This can also be seen in the depth dependence of S_Q/S_I for different R (see Figure 6.8). This may be due to the reason that line core polarization gets dominant contribution from the central stellar core. In order to understand the effect of extendedness R on the line profiles in greater detail we plot in Figure 6.8, S_I and S_Q/S_I as a function of line integrated tangential optical depth τ_z for the case

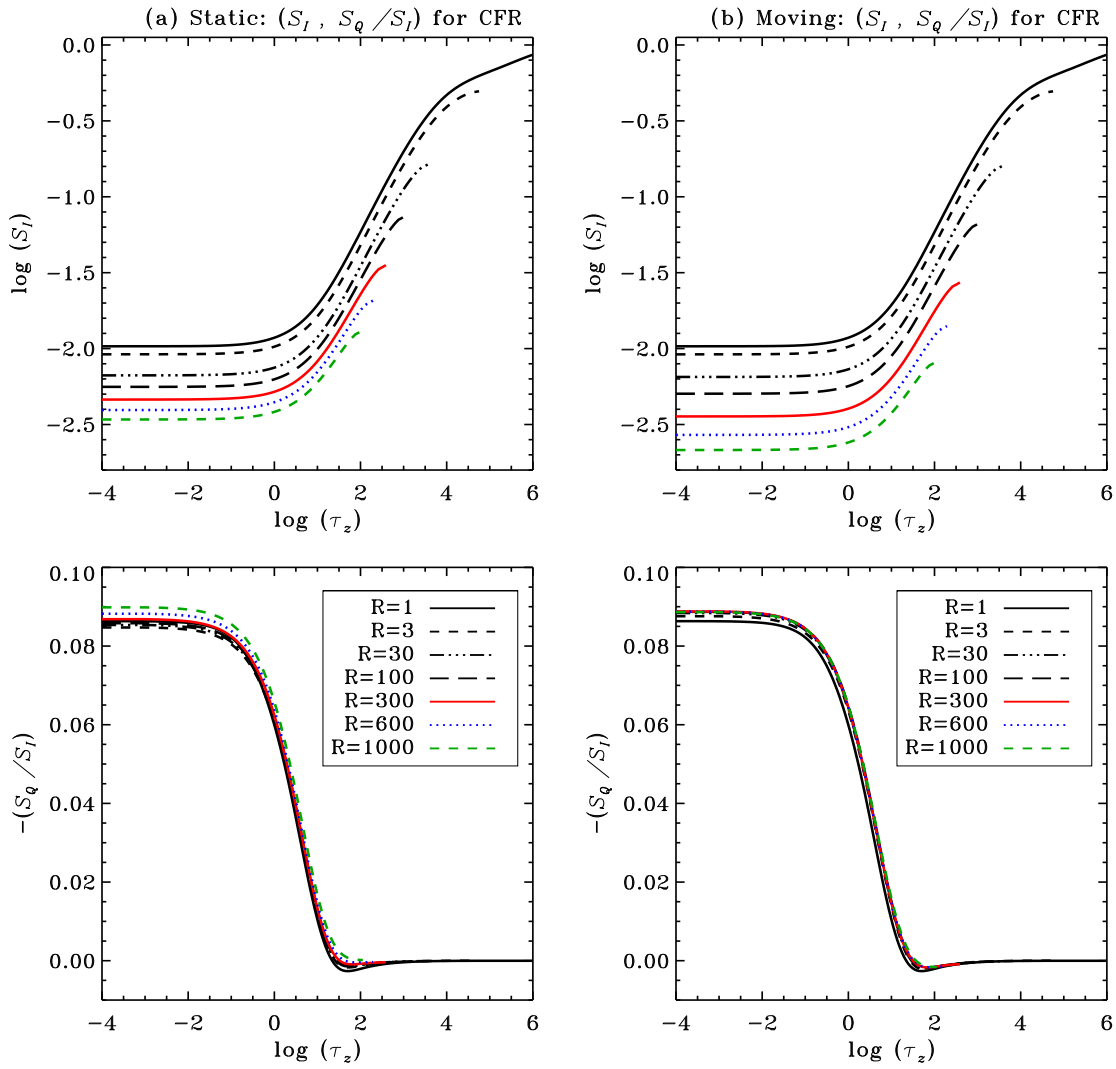

FIGURE 6.8: Intensity source function (S_I, top panels) and polarized source function (S_Q/S_I, bottom panels) versus line integrated optical depth τ_z for a tangent ray that emerges with $\mu = 0.11$, for CFR at $x = 0.375$, and for different values of R (indicated in the inset box). Panel (a) corresponds to the static atmosphere and panel (b) to the constantly moving atmosphere with $V(r)$=3. Other model parameters are given in Sections 4.4 and 5.4.1.

of CFR. For a static spherical atmosphere, S_I decreases with an increase in R, which is due to the dilution of the radiation field. However, due to the outward peaking of the radiation field, the corresponding S_Q/S_I (which is a measure of radiation anisotropy) increases with increasing R particularly in the outer layers. In the presence of velocity fields, Doppler dimming (i.e, decrease in S_I compared to the corresponding static case), which is larger for larger R, causes a decrease in S_Q/S_I compared to the corresponding static case (see Figure 6.8(b)). This results in reduced sensitivity of CFR Q/I profiles to extendedness R, for moving

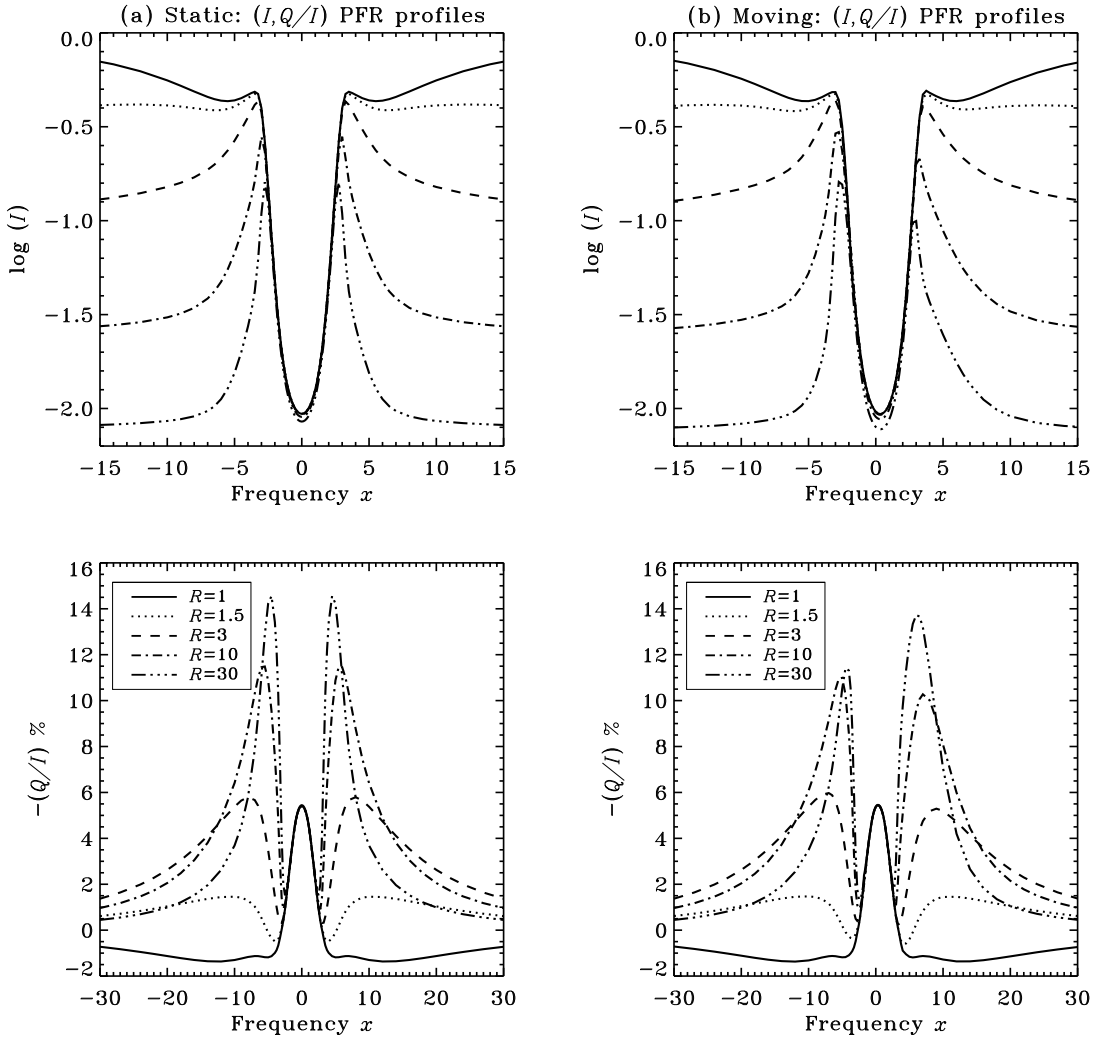

FIGURE 6.9: Same as Figure 6.7, but for the case of angle-averaged PFR and for $1 \leq R \leq 30$.

spherical atmospheres. Also from the contribution function (not shown here) the peak contribution to $x = 0.375$ comes from the spherical shell with $\tau_z \approx 2.5$ irrespective of the outer radius R. Again it is easy to verify that S_Q/S_I values at $\tau_z \approx 2.5$ and $x = 0.375$ nearly map the corresponding emergent Q/I values shown in Figure 6.7.

Now we discuss the effect of extendedness R on Q/I profiles computed with PFR (see Figures 6.9 and 6.10). As already discussed in Section 6.3, Q/I profiles that formed in a spherical atmosphere differ from those formed in a planar atmosphere, particularly in the wings due to the contribution from optically thin extended lobes. This is clearly visible for $R = 1.5$ itself (compare solid and dotted

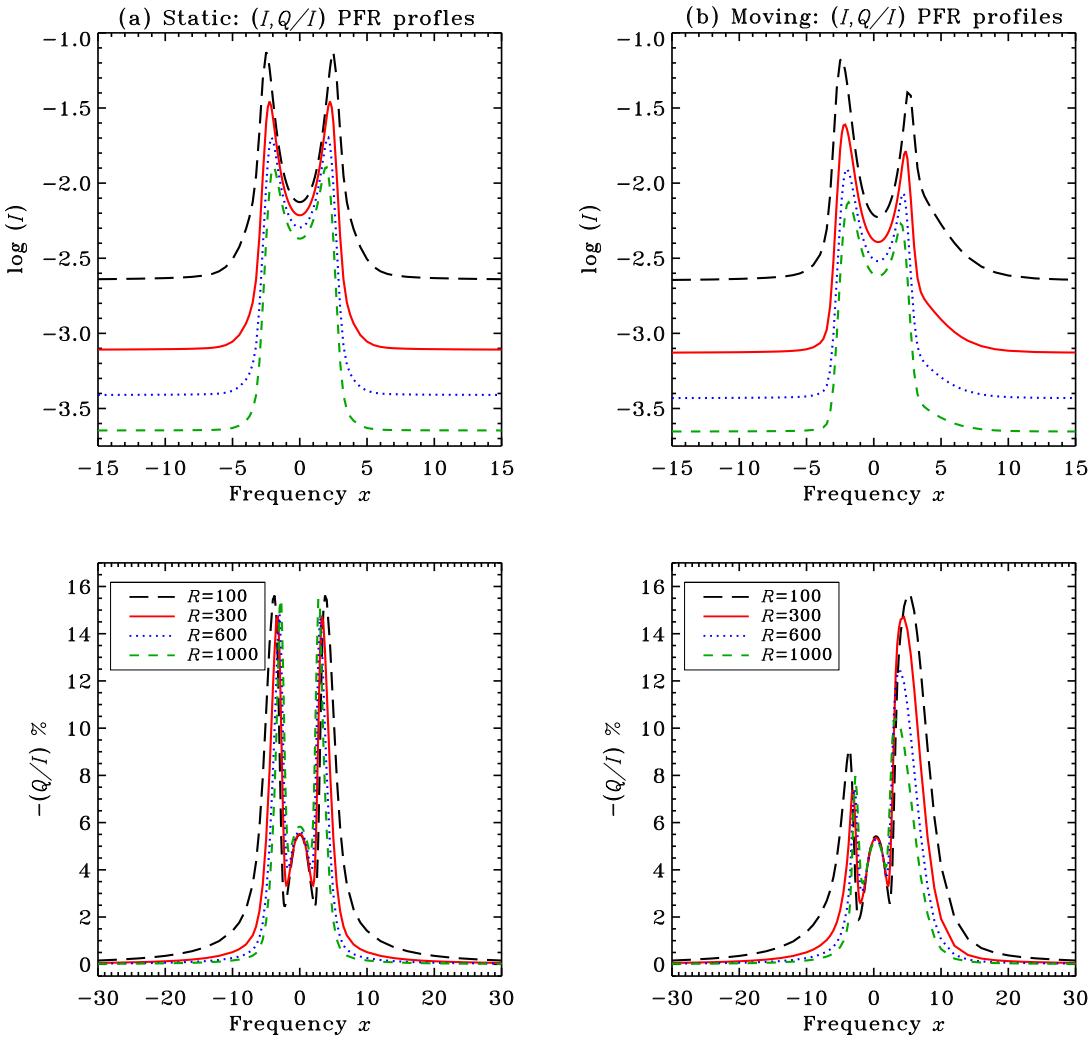

FIGURE 6.10: Same as Figure 6.7, but for the case of angle-averaged PFR and for $100 \leq R \leq 1000$.

lines in Q/I panels of Figure 6.9). In particular, the Q/I profile computed in a static spherical atmosphere with PFR and for $R = 1.5$ exhibits a central peak, core minima around $|x| = 3$, and wing PFR peaks around $|x| = 10$ (see the dotted line in Figure 6.9(a)). The line core of the PFR Q/I profiles nearly coincide for $1 \leqslant R \leqslant 100$. This can also be clearly seen from Figure 6.11(a), wherein the S_Q/S_I at line center nearly coincides for $1.5 \leqslant R \leqslant 100$, which in tern nearly coincides with $R = 1$. We remark that for clarity of presentation, in Figures 6.8 and 6.11 we have shown the S_I and S_Q/S_I only for selected values of R. For $R > 100$, we see slight increase in Q/I and S_Q/S_I at line center (see Figures 6.10(a) and 6.11(a)). In the presence of velocity fields, the S_Q/S_I at the line core peak nearly coincide for $1.5 \leqslant R \leqslant 1000$ (see Figure 6.11(c)), however, it slightly decreases for $R \geqslant$

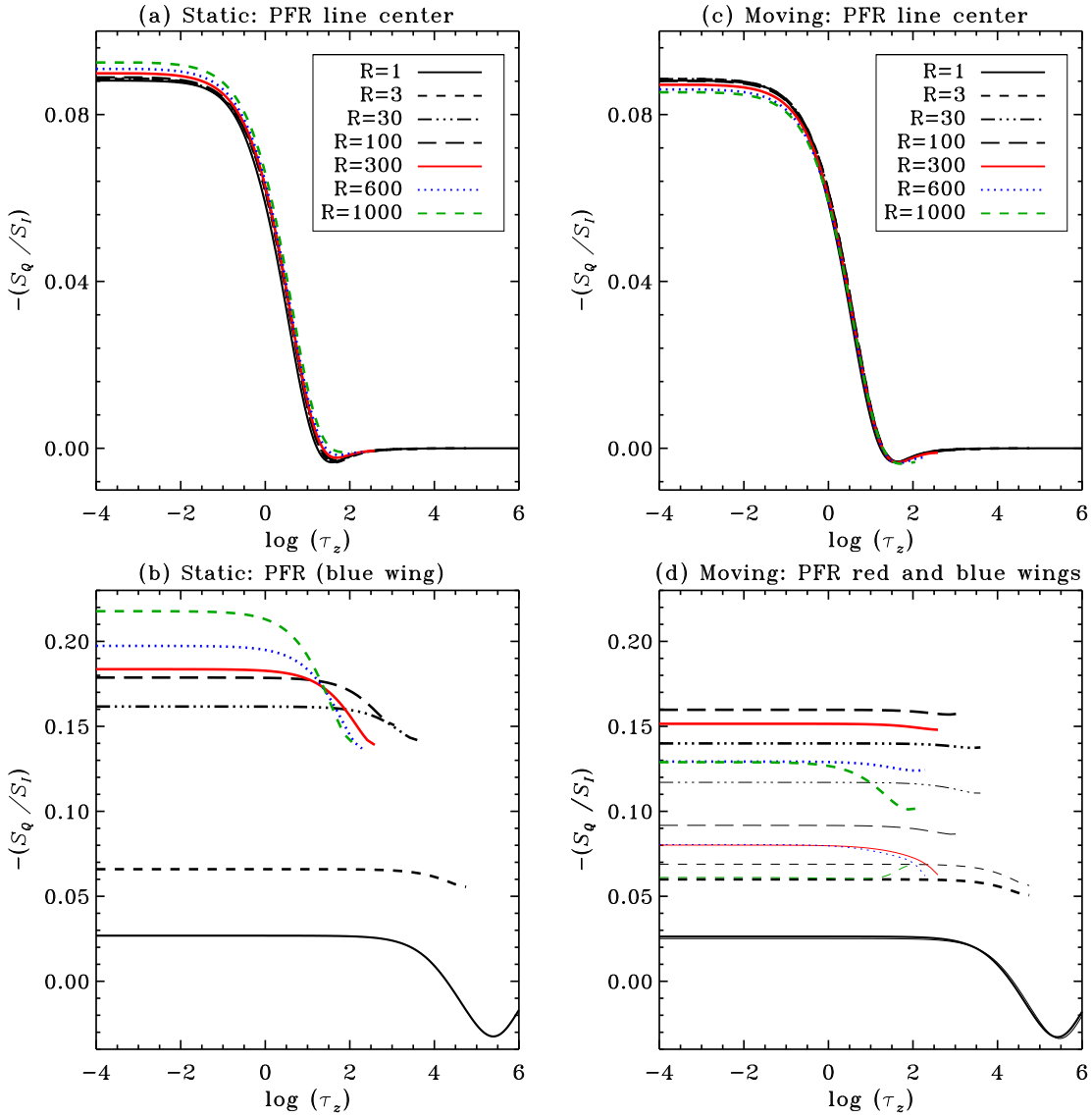

FIGURE 6.11: Polarized source function S_Q/S_I versus line integrated optical depth τ_z for a tangent ray that emerges with $\mu = 0.11$, and for different values of R (indicated in the inset box) with PFR. Other model parameters are given in Sections 4.4 and 5.4.1. Left panels correspond to the static case, while the right panels to a constantly moving atmosphere with $V(r) = 3$. Panels (a) and (c) show the source function at the line center frequency. Panel (b) shows the source function at the blue wing PFR peak frequencies. For the static case blue and red wing PFR peaks are symmetric and hence the S_Q/S_I corresponding to red wing PFR peak is not shown. Panel (d) shows the S_Q/S_I at the red wing (thin lines) and blue wing (thick lines) PFR peaks.

300 in the outermost layers due to Doppler dimming. Correspondingly, the Q/I line center peak exhibits only a marginal dependence on R. This is because the line core peak gets its peak contribution from $\tau_z \approx 2.5$ layer wherein S_Q/S_I for different R nearly coincide (see Figures 6.11(a) and 6.11(c)).

On the other hand the wing PFR peaks are highly sensitive to extendedness R, due to the enhanced contribution from emission lobes. As R increases the Q/I at wing PFR peaks increase in magnitude and saturate to around 16% in the static case for $R \geqslant 100$. This is expected because as R increases, the outward peaking of the radiation also increases. As a result S_Q/S_I at wing PFR peaks also increases with an increase in R (see Figure 6.11(b)). Indeed, the S_Q/S_I values at the mid line (from where the maximum contribution comes to the wing PFR peaks according to the contribution function) nearly correspond to the Q/I wing PFR peak values. Apart from an increase in amplitude, the position of the wing PFR peak also shifts progressively toward the line center thereby making the Q/I profile narrower for larger R. The core minima in Q/I also shifts toward line center with increasing R, slowly reducing the existence of the central peak. This may be attributed to the increased contribution from the emission lobes that increases as R increases. In the presence of a constant velocity field a similar effect can be seen. However, for $3 \leq R < 30$, the red wing PFR peak is slightly higher in amplitude than the blue wing PFR peak, and for $30 \leq R \leq 1000$ the blue wing PFR peak has higher amplitude than the red wing PFR peak. This can also be seen clearly in the corresponding S_Q/S_I plot (compare thin and thick lines in Figure 6.11(d)). Also unlike the static case, the S_Q/S_I at the red wing PFR peak increases with R up to $R = 30$ and then starts to decrease (see thin lines in Figure 6.11(d)). In the case of the blue wing PFR peak, the S_Q/S_I increases until $R = 100$, and then decreases with further increase in R (see thick lines in Figure 6.11(d)). These are clearly reflected in the Q/I profiles (see Figures 6.9 and 6.10). The reason for such a behavior is the following. From Figure 6.9, we see that although the I profile for $3 \leq R < 30$ is a self-reversed emission profile, the wings have higher amplitudes than the line core. Indeed, for $R = 3$ this continues to be the case for $0.008 \leq \mu \leq 0.99$ and it reverses for $\mu < 0.008$. Thus Doppler brightening tends to dominate over Doppler dimming. This can be seen in the Q/I red wing PFR peak, which is slightly higher than the corresponding static case (compare dashed lines in Q/I panels of Figures 6.9(a) and 6.9(b)). However, the blue wing PFR

peak has slightly diminished compared to the corresponding static case. This may be the effect of multiple scattering, which is relatively larger toward the blue side. For $R = 10$, $I_{\rm wing} > I_{\rm core}$ occurs for $0.04 \leq \mu \leq 0.99$ and it reverses for $\mu < 0.04$. As a result Doppler dimming slowly tends to equalize the Doppler brightening effect, giving rise to an overall decrease of Q/I both at the red and blue wing PFR peaks, the decrease being slightly more at the blue wing than at the red wing (for the same reason noted for $R = 3$). For $R \geq 30$, $I_{\rm wing} < I_{\rm core}$ is satisfied for larger ranges of μ (see, e.g., I panels in Figures 6.6(a) and 6.6(b) for $R = 300$) thereby allowing Doppler dimming to dominate. However, because the blue side suffers a larger number of scatterings, it has a larger probability of getting affected by outward peaking of the radiation field (which increases with increasing R). This leads to higher blue wing PFR peak than the red wing PFR peak. On the other hand red wing photons easily escape due to decreased opacity on the red side, not lending themselves to be affected by the outward peaking of the radiation field.

6.5 Concluding remarks

Here we have used the CMF-PALI method developed in Chapter 5 for the case of polarized spherically symmetric moving atmospheres, to study the effects of (1) frequency redistribution, (2) velocity fields, and (3) extendedness of the atmosphere. We also presented the center-to-limb variation of the polarized profiles, which clearly showed the effect of outward peaking of the radiation field. We showed that the Q/I profiles computed with CFR are somewhat less sensitive to the extendedness R of the atmosphere, while those computed with PFR are highly sensitive, particularly in the wings. Indeed, the positions of the wing PFR peaks shift toward the line center and also their amplitudes initially increase, and then saturate as R increases.

We showed that the velocity fields modify both the amplitude and shape of the Q/I profiles. The contribution from the emission lobes of the static extended atmosphere significantly enhances the wing PFR peaks in Q/I profiles. The presence of velocity fields further produces highly asymmetric wing PFR peaks. Thus, together with intensity, the linear polarization provides a sensitive diagnostic of velocity fields in extended atmospheres.

Chapter 7

Resonance Line Polarization in Spherically Symmetric Moving Media: *a Parametric Study* [1]

An overview

Here we apply the CMF-PALI method developed in Chapter 5 to make a detailed parametric study of the resonance line polarization formed in spherically symmetric moving atmosphere. We discuss the dependence of linearly polarized profiles on different atmospheric and atomic parameters, considering the effects of partial frequency redistribution (PFR). We present the polarized line profiles for both static and constantly moving atmospheres by varying the model parameters one at a time.

7.1 Introduction

The spectroscopic observations of different classes of astrophysical objects like supergiants, Wolf-Rayet stars, novae, and supernovae indicate the existence of high-velocity outward gas flows. The spectral line profiles of these objects are of P Cygni type (Beals 1931) with redshifted emission and blueshifted absorption

[1] This chapter is based on the publications: Megha *et al.* (2019b,a)

indicating the rapid outflow of matter in the outer layers of their atmospheres. These outward gas flows lead to extended atmospheres. Even small extensions present in solar type stars are highly structured which give rise to significant observable effects. Therefore, a precise treatment of such problems require going beyond the plane-parallel model.

Nagendra (1988, 1989) discuss the comparison between plane-parallel and spherically symmetric atmospheres in presence of resonance line polarization. In these papers, the author also presents the linear polarization profiles for complete frequency redistribution (CFR), PFR, and coherent scattering mechanisms and their dependence on physical parameters such as extendedness R, thermalization parameter ϵ, optical thickness T for the case of a two-level atom model. Nagendra (1994) used the Domke-Hubeny (DH) redistribution matrix (Domke and Hubeny 1988) to understand the effects of elastic and inelastic collisions on scattering in spherical atmosphere. Nagendra (1995) present a study of the linear polarization of both resonance and subordinate lines that are formed in spherical atmospheres. In particular, he presents a detailed study on ϵ, T, R, damping parameter a, power law index $\tilde{n}$ considering the DH redistribution matrix. In all the above-mentioned papers, the author considers only the static atmosphere. In this chapter, we present a similar parametric study for the case of spherically symmetric moving atmospheres. For this purpose, we apply the CMF-PALI method presented in Chapter 5 to understand the quantitative behavior of the linear polarization when the basic model parameters are varied systematically one at a time keeping the other parameters as constants.

7.2 Model parameterization

For our studies we consider the following set of 'standard model parameters'. An isothermal, spherically symmetric atmosphere with inverse square law opacity distribution (i.e., $\chi_{l,c} \propto r^{-\tilde{n}}$, here the power law opacity index $\tilde{n}$=2), a frequency averaged total radial line optical thickness of T, and an outer radius R is considered. We use reflecting boundary condition, namely $\boldsymbol{\mathcal{I}}^{+}(\tau = T, p, x) = \boldsymbol{\mathcal{I}}^{-}(\tau = T, p, x)$ at the lower boundary and $\boldsymbol{\mathcal{I}}^{-}(\tau = 0, p, x) = 0$ at the outer boundary. For discretization of radius r, the impact parameter p, angle μ, frequency x, and depth

grid τ_r we have followed Anusha *et al.* (2009, see also Section 4.4). The 'standard model parameters' are: $T = 10^6$, $R = 30$, $\beta_c = 10^{-6}$, $\epsilon = 10^{-4}$, $a = 10^{-3}$, $B_{\nu_0} = 1$, and no elastic collisions. For our studies we consider both static ($V(r)$=0) and a constantly moving atmosphere with $V(r)$=3 mean thermal units (in Sections 7.3–7.8). We show all the results for a fixed line-of-sight (LOS) of μ=0.11. The effect of extendedness R on the linearly polarized line profiles formed in static and moving media is presented in Chapter 6. Following Nagendra (1988, 1994, 1995) here we present the dependence of linearly polarized profiles on ϵ (cf. Section 7.3), β_c (cf. Section 7.4), T (cf. Section 7.5), a (cf. Section 7.6), the power law opacity index $\tilde{n}$ (cf. Section 7.7), the elastic collision rate $\Gamma_{\rm E}/\Gamma_{\rm R}$ (cf. Section 7.8), and $V(r)$ (cf. Section 7.9), when they are varied one at a time around the standard model parameters, while keeping the other parameters as constants.

7.3 Dependence on thermalization parameter ϵ

Figure 7.1 shows the emergent PFR $(I, Q/I)$ profiles from a spherically symmetric static (panel (a)) and a constantly moving atmosphere with $V(r)$=3 (panel (b)) for varying values of thermalization parameter ϵ in the range $[10^{-8}, 1]$. ϵ gives the probability that a photon is destroyed during scattering process due to collisional de-excitation. Here ϵ=1 refers to the pure LTE case and other values refer to the NLTE case. As the value of ϵ increases from 10^{-8} to 1, the thermal coupling of photons with the continuum also increases due to increase in the number of collisions in the medium. For $\epsilon = 10^{-8}$, the intensity shows a self-absorbed symmetric emission profile for the static case (see Figure 7.1a). As the ϵ value increases from 10^{-8} to 1, the intensity around the line core region increases. Also self-absorbed part of the profile becomes shallower and finally disappears for $\epsilon = 1$. Furthermore, for $\epsilon = 1$, the symmetric emission peaks around $x = \pm 2.25$ disappear as there is no scattering contribution from the extended lobes. The linear polarization Q/I profile (Figure 7.1a, lower panel) for $\epsilon = 10^{-8}$ shows a triple peak structure due to PFR. As ϵ value increases, the magnitude of linear polarization in the line core region decreases due to a decrease in the number of scatterings and the profile becomes completely flat with zero polarization for $\epsilon = 1$. However at the PFR wing peaks, we see that Q/I is nearly the same for ϵ between 10^{-8} and 10^{-6}, then increases for $10^{-5} \leq \epsilon \leq 10^{-4}$, and then decreases for $\epsilon \geq 10^{-3}$. To understand

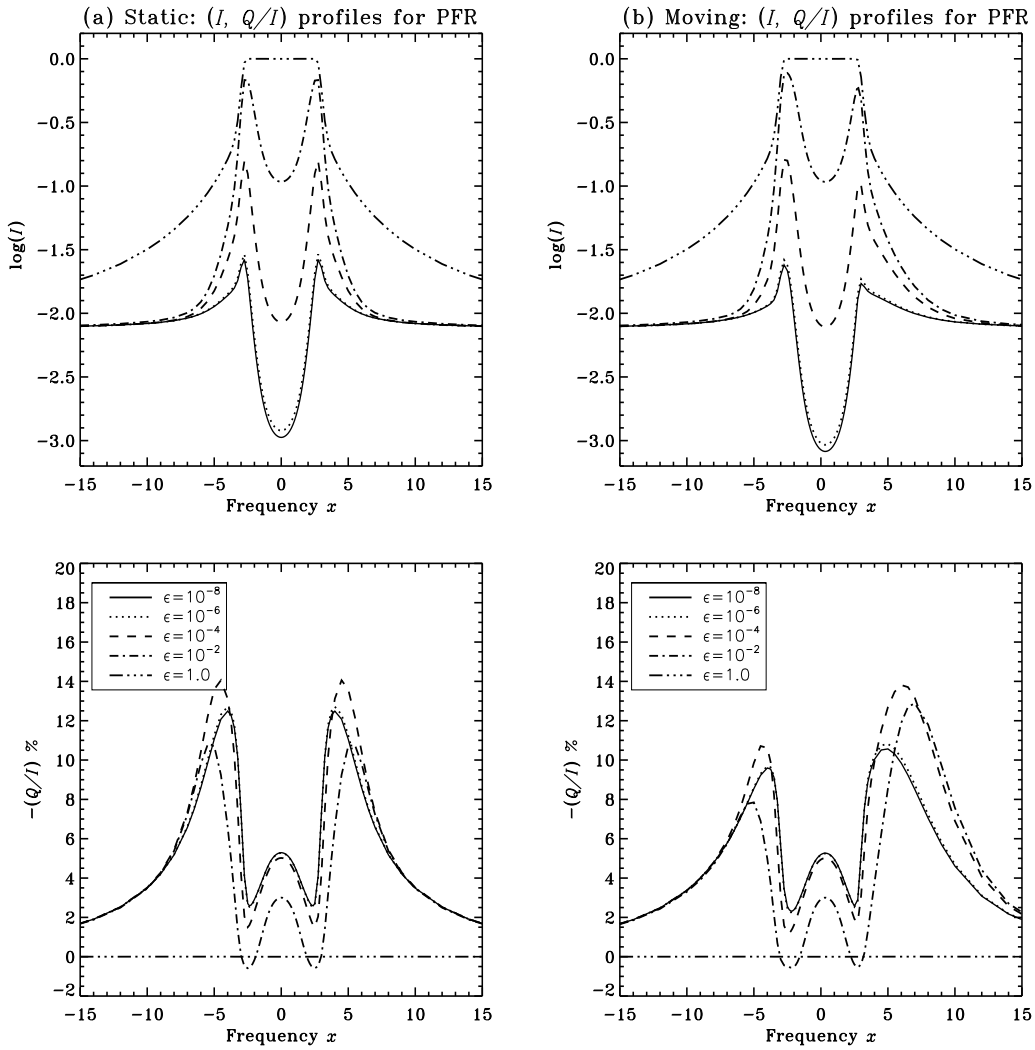

FIGURE 7.1: Emergent PFR $(I, Q/I)$ profiles from a spherically symmetric static (panel (a)) and a constantly moving atmosphere with $V(r)$=3 (panel (b)) for varying values of thermalization parameter ϵ (which are given in the inset box). Other model parameters are given in Section 7.2. The line-of-sight is at $\mu = 0.11$.

this we recall that in a spherical atmosphere with $B_{\nu_0} = 1$, photons are created substantially closer to the surface (see Kunasz and Hummer 1974a), from where they escape much more readily. With increase in ϵ the photon creation rate increases, while mean number of scatterings decrease. For $\epsilon \leq 10^{-6}$, mean number of scatterings are nearly the same (see Table IV of Kunasz and Hummer 1974a which corresponds to the case of $\tilde{n} = 0$) so that I and Q/I are nearly the same for ϵ between 10^{-8} and 10^{-6}. For $10^{-5} \leq \epsilon \leq 10^{-4}$, although the mean number of scatterings decrease relatively, since the photons are created near the surface

a moderate number of scatterings would result in larger values of Q/I. This is particularly the case for highly extended atmosphere ($R = 30$) considered in this Chapter. For $\epsilon > 10^{-4}$ mean number of scatterings decrease considerably resulting in decreasing values of Q/I as in planar atmospheres. Our numerical studies show that, such a dependence of Q/I on ϵ is seen for $R > 10$, while for $R \leq 10$ the Q/I monotonically decreases with increasing ϵ not only in the line core but also in the PFR wings.

In the presence of velocity fields the line profiles are asymmetric about the line center (see Figure 7.1b). In particular the red and blue wing PFR peaks in Q/I get highly affected in the presence of velocity gradients. We recall that although we have considered a constant velocity field, the Doppler shift $\mu(r, p)V(r)$ along a given impact parameter ray changes (as μ varies due to sphericity effects) thereby producing a velocity gradient in the z-direction. The dependence of I and Q/I profiles on ϵ for non-zero velocity field is similar to the corresponding static case. Apart from producing Doppler shift, the velocity fields modify the source function gradient thereby either enhancing or reducing the anisotropy of the radiation field. In a spherical atmosphere this modification is different for red and blue wing PFR peaks of the Q/I profile (due to sphericity effects and as the intensity is a self-absorbed emission profile), which results in the high asymmetry noted above. A more detailed discussion can be found in Chapter 6.

7.4 Dependence on continuous absorption parameter β_c

Figure 7.2 shows the emergent PFR $(I, Q/I)$ profiles from a spherically symmetric static (panel (a)) and a constantly moving atmosphere with $V(r)$=3 (panel (b)) for varying values of continuous absorption parameter β_c in the range [0, 1]. β_c is the ratio of continuum opacity to frequency averaged line opacity both of which are taken to follow the inverse square law. Hence β_c remains constant throughout the spherical atmosphere. Here the continuum optical depth which is $\beta_c T$ is different for different models. $\beta_c = 0$ corresponds to a pure line case. Here the intensity shows self-absorbed emission profile, with the wings falling sharply towards zero due to the absence of continuous absorption. With the increase of β_c from 0 to 10^{-6}

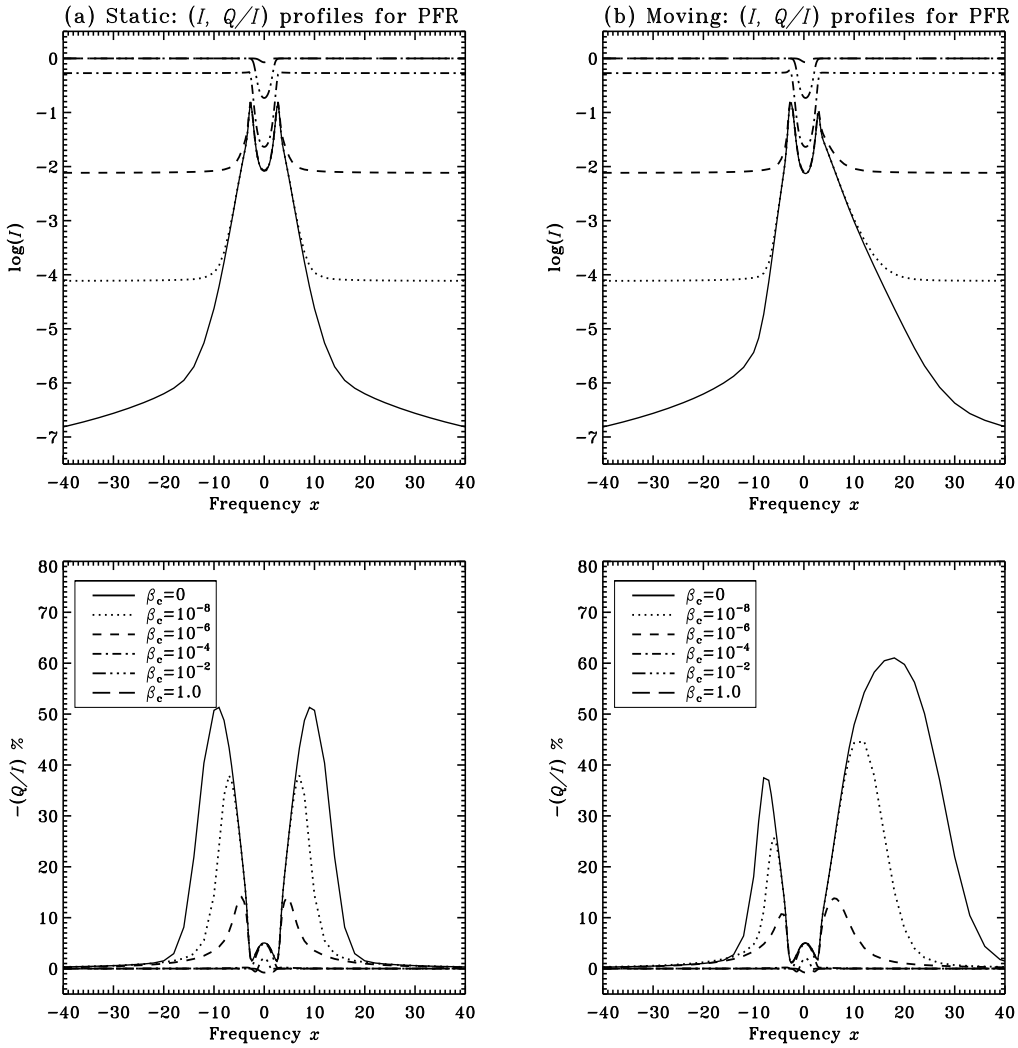

FIGURE 7.2: Emergent PFR $(I, Q/I)$ profiles from a spherically symmetric static (panel (a)) and a constantly moving atmosphere with $V(r)$=3 (panel (b)) for varying values of continuous absorption parameter β_c (which are given in the inset box). Other model parameters are given in Section 7.2. The line-of-sight is at $\mu = 0.11$.

the intensity does not change much in the line core region but the increase in the value of β_c contributes to the continuum leading to larger values of intensity in the wings. Consequently, the emission peaks slowly decrease in their height relative to the continuum and finally cease to exist for $\beta_c = 10^{-4}$, for which the intensity now exhibits an absorption profile. For $\beta_c = 0$, the linear polarization shows triple peaks due to PFR with highly enhanced wing peaks (see the solid line in Q/I panel of Figure 7.2(a)). The Q/I at the wing PFR peaks is on the order of 50 %. This is because of the strong outward peaking of the radiation field in a spherically

symmetric atmosphere, which makes the radiation field highly anisotropic. With the increase in the value of β_c, the magnitude of linear polarization reduces as the contribution from the unpolarized continuum photons dilute the polarized radiation field. Especially the wing PFR peaks sharply fall down and they disappear for $\beta_c = 10^{-4}$ and with a sign reversal for $\beta_c = 10^{-2}$. This is because the unpolarized continuum source function becomes equal to or larger than the line source function at progressively smaller frequencies (Faurobert 1988, see also Nagendra 1995). For $\beta_c = 1$, the linear polarization nearly becomes zero with weak negative polarization in the line core. In the presence of velocity field, the intensity for $\beta_c < 10^{-4}$ is strongly affected in the blue region. The effect of velocity field exists only in the line core region of intensity profile with further increase in β_c as the continuum absorption dominates over that of line. The presence of velocity field has similar effects on the linear polarization profiles with strong enhancement in the magnitude of blue wing PFR peak for $\beta_c < 10^{-4}$.

7.5 Dependence on line averaged radial optical thickness T

Figure 7.3 shows the emergent PFR $(I, Q/I)$ profiles from a spherically symmetric static (panel (a)) and a constantly moving atmosphere with $V(r)$=3 (panel (b)) for varying values of optical thickness T from 1 to 10^7. Such a wide variation in T allows us to sample effectively thin ($\epsilon T = 10^{-4}$) to thick ($\epsilon T = 10^3$) atmospheres. The intensity is in emission up to $T = 10^3$ with increasing magnitude and line width. This is clearly an NLTE effect, as number of scatterings increase as T increases. For $T > 10^4$, the medium starts to become effectively thick particularly in the stellar core, thereby giving rise to self absorption in the line core. Thus, for T in the range 10^4 to 10^7, the intensity shows self-absorbed emission profile with increased broadening. The linear polarization Q/I profiles show a clear sensitivity to variations in T. For T from 1 to 10, the polarization is confined to the line core. This is because the medium is effectively thin ($\epsilon T \ll 1$). With further increase in T from 10^2 to 10^5, PFR wing peaks start to appear with wing peaks shifting towards higher frequency points. Furthermore, for $T > 10^3$ the wing PFR peaks exhibit a progressive decrease in magnitude. This outward shift and decrease in

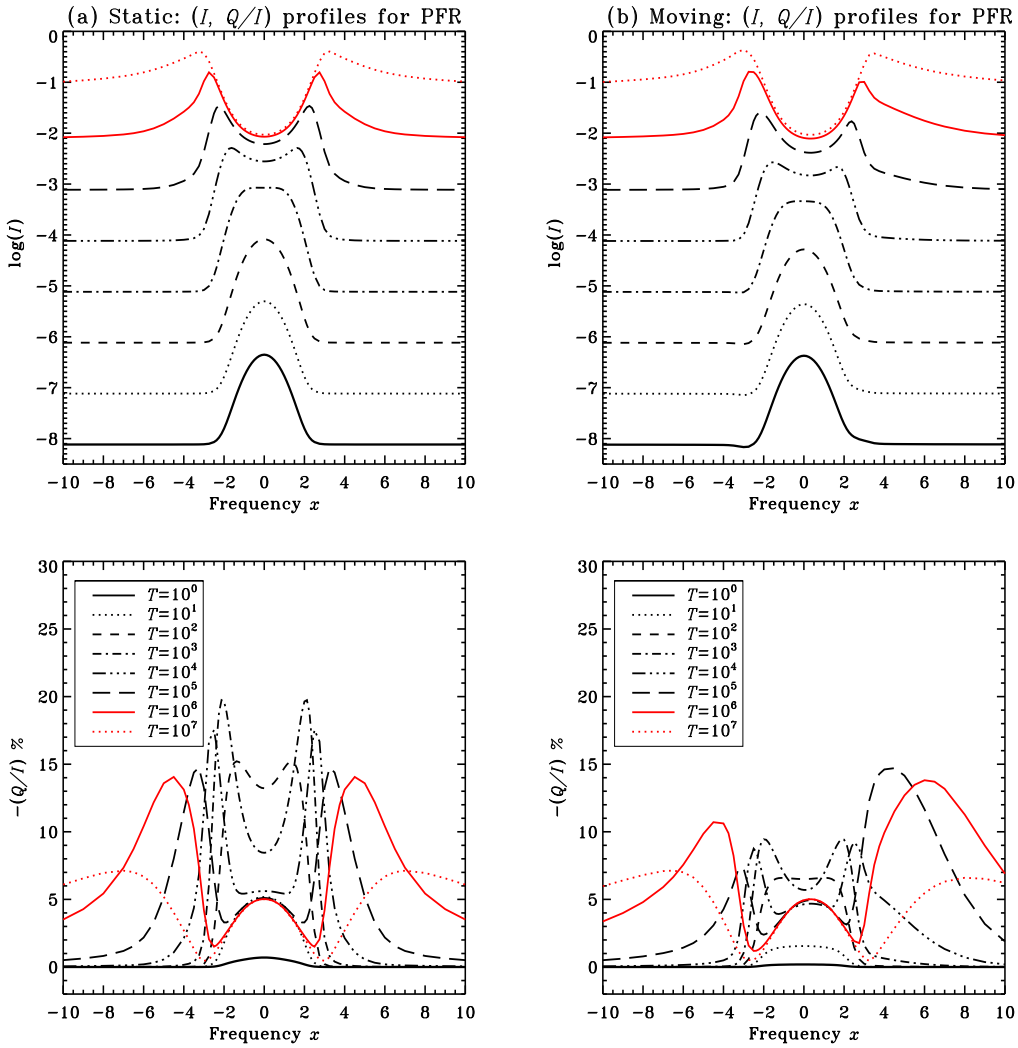

FIGURE 7.3: Emergent PFR $(I, Q/I)$ profiles from a spherically symmetric static (panel (a)) and a constantly moving atmosphere with $V(r)$=3 (panel (b)) for varying values of line averaged radial optical thickness T (which are given in the inset box). Other model parameters are given in Section 7.2. The line-of-sight is at $\mu = 0.11$.

magnitude are due to the larger optical depths in the outer layers as the medium becomes more and more effectively thick with increasing T. For the same reason for $T \geq 10^5$, the central peak is also formed in Q/I. The velocity fields give rise to a Doppler blue shift and also an asymmetry about the line center in the $(I, Q/I)$ profiles. The dependence of I profiles on T for non-zero velocity field is similar to the corresponding static case. For $T \leq 10^4$, the Q/I profiles with velocity fields exhibit a strong Doppler dimming throughout the profile. This is because the corresponding intensity profiles are in emission except for $T = 10^4$.

For the same reason the $(I, Q/I)$ profiles are weakly asymmetric about the line center. For $T = 10^4$ a shallow self-absorption in the line core region is seen in I profile. Consequently a slight asymmetry between the red and blue wing PFR peaks in Q/I is seen accompanied with slightly broadened blue wing PFR peak. This asymmetry and broadening of blue wing PFR peak in Q/I are enhanced for $T > 10^4$, as for these cases intensity exhibits a more stronger self-absorption in the line core.

7.6 Dependence on damping parameter a

Figure 7.4 shows the emergent PFR $(I, Q/I)$ profiles from a spherically symmetric static (panel (a)) and a constantly moving atmosphere with $V(r)$=3 (panel (b)) for varying values of damping parameter a in the range 10^{-9} to 10^{-1}. Since we neglect the effects of elastic collisions, the damping parameter is given by $a = \Gamma_R/4\pi\Delta\nu_D$. Thus, the variation of a is equivalent to the variation in radiative damping width Γ_R. As the value of a increases intensity profiles become more broader leading to a strong damping wings. The linear polarization profiles also exhibit a broadening with increasing a. In particular the wing PFR peaks are much broader and also shift to larger frequency away from the line center. Moreover, amplitude of wing PFR peaks initially increases with increasing values of a and then decreases for $a = 0.1$ which is perhaps due to excessive line broadening. We recall that with increasing values of a the PFR becomes more and more important resulting in $(I, Q/I)$ profiles shown in Figure 7.4. This dependence of $(I, Q/I)$ profiles on damping parameter a is similar to the planar case (see, e.g., Figure 8 of Sampoorna *et al.* 2010). In the presence of velocity field the asymmetries are present in $(I, Q/I)$ profiles, while the dependence on variation of a is similar to the corresponding static case.

7.7 Dependence on power law opacity index $\tilde{n}$

Figure 7.5 shows the emergent PFR $(I, Q/I)$ profiles from a spherically symmetric static (panel (a)) and a constantly moving atmosphere with $V(r)$=3 (panel (b))

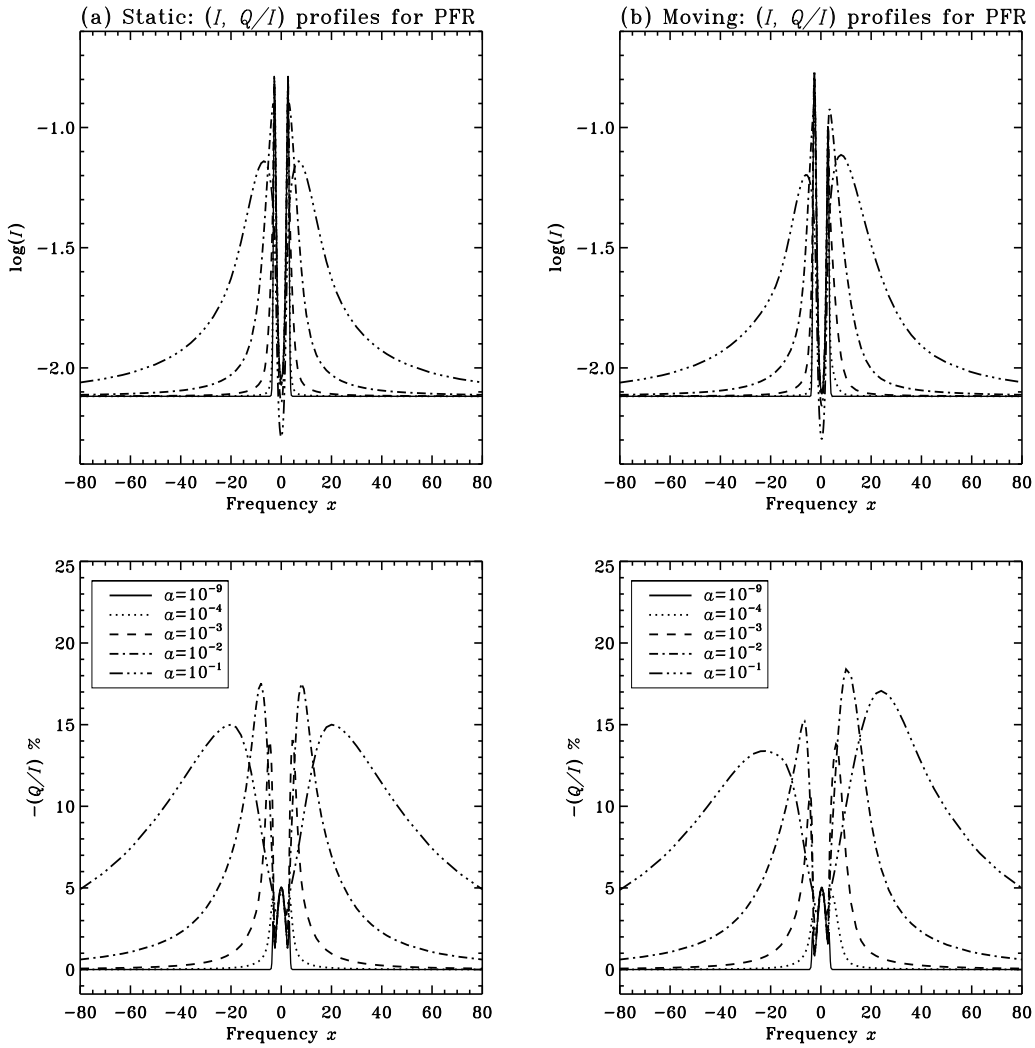

FIGURE 7.4: Emergent PFR $(I, Q/I)$ profiles from a spherically symmetric static (panel (a)) and a constantly moving atmosphere with $V(r)$=3 (panel (b)) for varying values of damping parameter a (which are given in the inset box). Other model parameters are given in Section 7.2. The line-of-sight is at $\mu = 0.11$.

for varying values of power law opacity index $\tilde{n}$. The density distribution in a spherical atmosphere generally obeys a power law type of opacity distribution namely $\chi_{l,c}(r) \propto r^{-\tilde{n}}$. Here we vary $\tilde{n}$ in the range 0 to 4. For $\tilde{n} = 0$, we have a homogeneous sphere. It is well-known that sphericity effects do not develop fully in a homogeneous sphere and are seen only for $\tilde{n} > 1$ (see Kunasz and Hummer 1974a). Consequently the emission contributions from the extended lobes are uniformly large for $\tilde{n} = 0$ giving rise to an absorption profile in intensity. As $\tilde{n}$ increases the scattering contribution from the extended lobes increases significantly

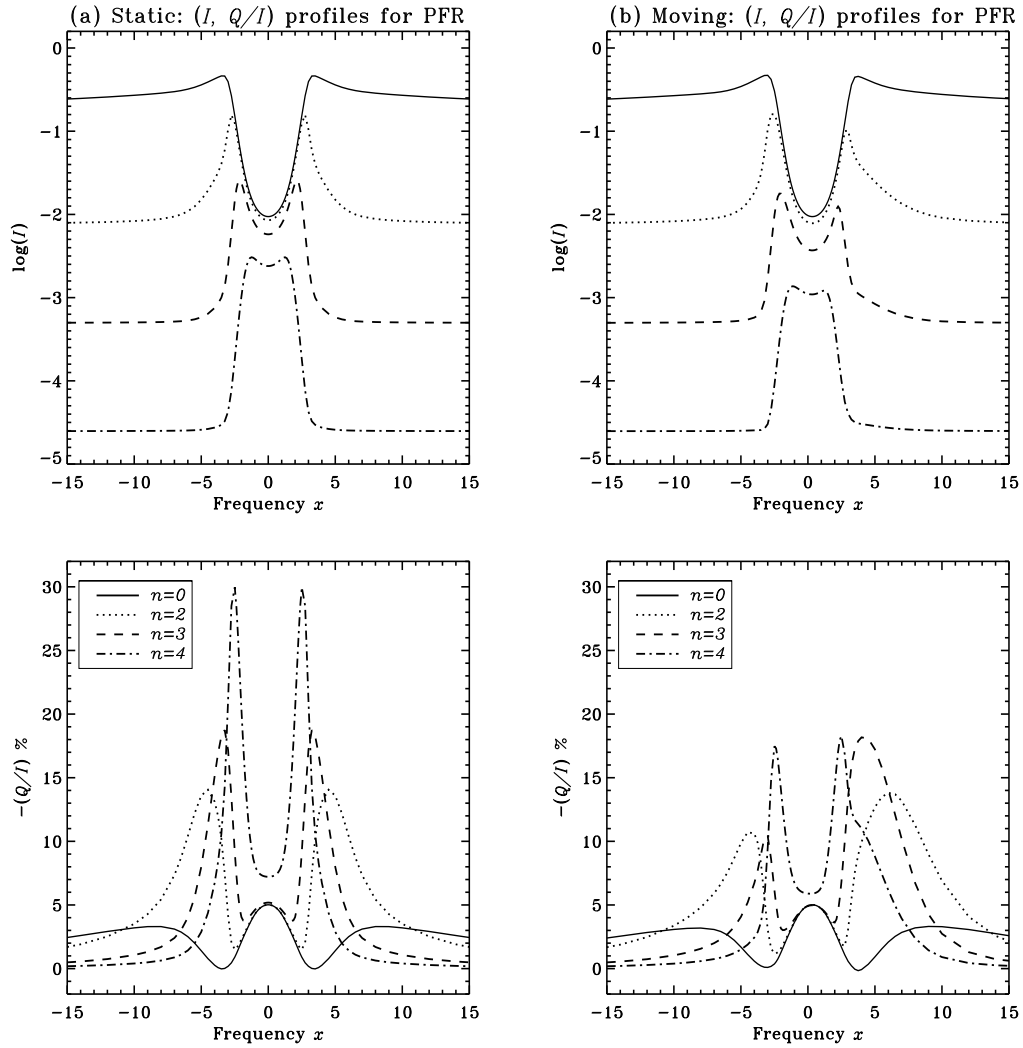

FIGURE 7.5: Emergent PFR $(I, Q/I)$ profiles from a spherically symmetric static (panel (a)) and a constantly moving atmosphere with $V(r)$=3 (panel (b)) for varying values of power law opacity index $\tilde{n}$ (which for brevity of notations is referred to as n in the figure legend and its values are in the inset box). Other model parameters are given in Section 7.2. The line-of-sight is at $\mu = 0.11$.

giving rise to self-absorbed emission profile for $\tilde{n} = 2$, 3 and an emission profile with extremely shallow line core absorption for $\tilde{n} = 4$. Since with increasing $\tilde{n}$, the total opacity rapidly decreases as we move outward, the intensity also drops as $\tilde{n}$ increases. For $\tilde{n} = 0$, 2, and 3 the Q/I profile exhibits a typical triple peak structure. As $\tilde{n}$ increases, the wing PFR peaks become more narrower and shift towards the line core region due to the decrease in optical thickness of extended lobes. Due to the dominant contributions from photons that are scattered small number of times, the amplitude of wing PFR peaks also increases with $\tilde{n}$. For

$\tilde{n} \geq 3$ the line core peak disappears as the medium becomes optically thin also at the stellar core. In the presence of velocity field intensity exhibits an asymmetric profile about the line center for $\tilde{n} = 2$, 3, and 4, while the intensity for $\tilde{n} = 0$ exhibits only a blue shift. Even the linear polarization profiles show asymmetry for $\tilde{n} = 2$, 3, and 4. For $\tilde{n} = 4$ the Q/I exhibits a strong Doppler dimming throughout the profile as the corresponding I profile is nearly in emission.

7.8 Dependence on elastic collisions $\Gamma_{\rm E}$

Figure 7.6 shows the effect of elastic ($\Gamma_{\rm E}$) and depolarizing ($D^{(2)}$) collisions on the emergent PFR $(I, Q/I)$ profiles formed in a spherical static (panel (a)) and a constantly moving (panel (b)) atmosphere. The depolarizing elastic collision rate $D^{(2)} = 0.5\Gamma_{\rm E}$ (see, e.g., Stenflo 1994). The ratio $\Gamma_{\rm E}/\Gamma_{\rm R}$ is varied from 0.1 to 100 in steps of 10. Now the redistribution matrix contains the contributions from both $R_{\rm II,AA}$ and $R_{\rm III,AA}$ type scattering. Like in the planar atmosphere the intensity profiles become slightly broader when the elastic collision rate is increased. As for the Q/I, elastic collisions have a depolarizing effect, with $D^{(2)}$ operating in the line core, and $\Gamma_{\rm E}$ in the line wings. These effects are common to both static and constantly moving atmospheres.

7.9 Dependence on $V(r)$

Figure 7.7 shows the effect of the non-dimensional radial velocity field $V(r)$ on the emergent $(I, Q/I)$ profiles formed in a spherical atmosphere with CFR (panel (a)) and PFR (panel (b)). The intensity exhibits a self-reversed symmetric emission profile for both CFR and PFR when $V(r) = 0$. As the value of $V(r)$ increases from 0 to 9 mean thermal units, the line core and emission peaks, for both CFR and PFR, show increased blueshift along with increased asymmetry in the red and blue emission peaks compared to the corresponding static values. The static PFR Q/I profile exhibits a typical triple peak structure, whereas the corresponding CFR Q/I profile is confined to the line core. As the value of $V(r)$ increases, the Q/I line core for both CFR and PFR cases and the blue wing PFR peak, are

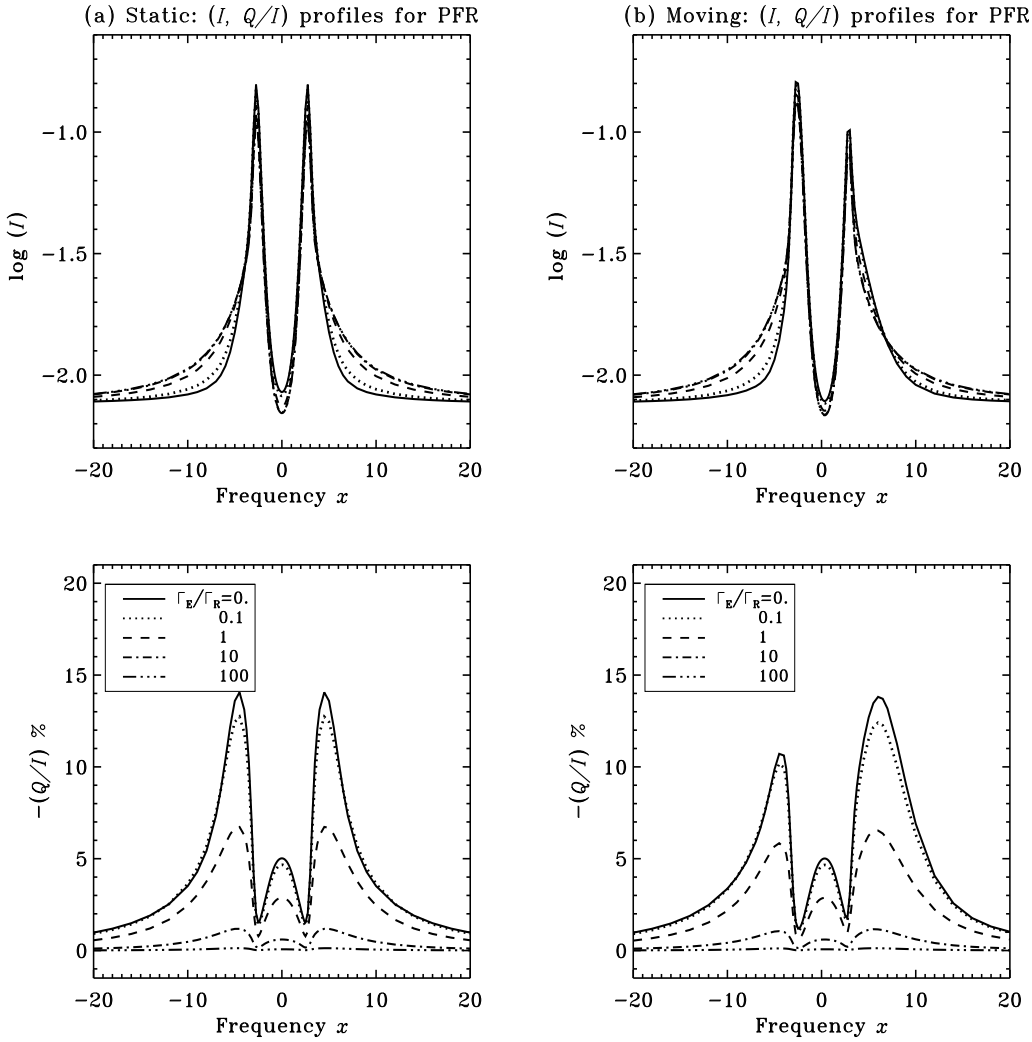

FIGURE 7.6: Emergent PFR $(I, Q/I)$ profiles from a spherically symmetric static (panel (a)) and constantly moving atmosphere with $V(r)$=3 (panel (b)) for varying values of $\Gamma_{\rm E}/\Gamma_{\rm R}$ (which are given in the inset box). Other model parameters are given in Section 7.2. The line-of-sight is at $\mu = 0.11$.

progressively blueshifted. As already noted in Section 6.2, wing PFR peaks are asymmetric in the presence of velocity fields. The magnitude of the Q/I red wing PFR peak decreases with increasing $V(r)$ due to Doppler dimming. However, the blue wing PFR peak exhibits Doppler brightening for $V(r) = 1$. With further increase in $V(r)$, it however exhibits Doppler dimming. Indeed Doppler dimming is seen in I profiles for $-8 < x < 4$, and in Q/I profiles for $-8 < x < x_1$, wherein the value of x_1 depends on the value of $V(r)$. For example $x_1 = 4$ for $V(r) = 1$, while it is 7 for $V(r) = 9$. For $4 < x < 17$ and $x_1 < x < 20$, the I and Q/I profiles respectively exhibit Doppler brightening. Also, we note that the blue wing PFR

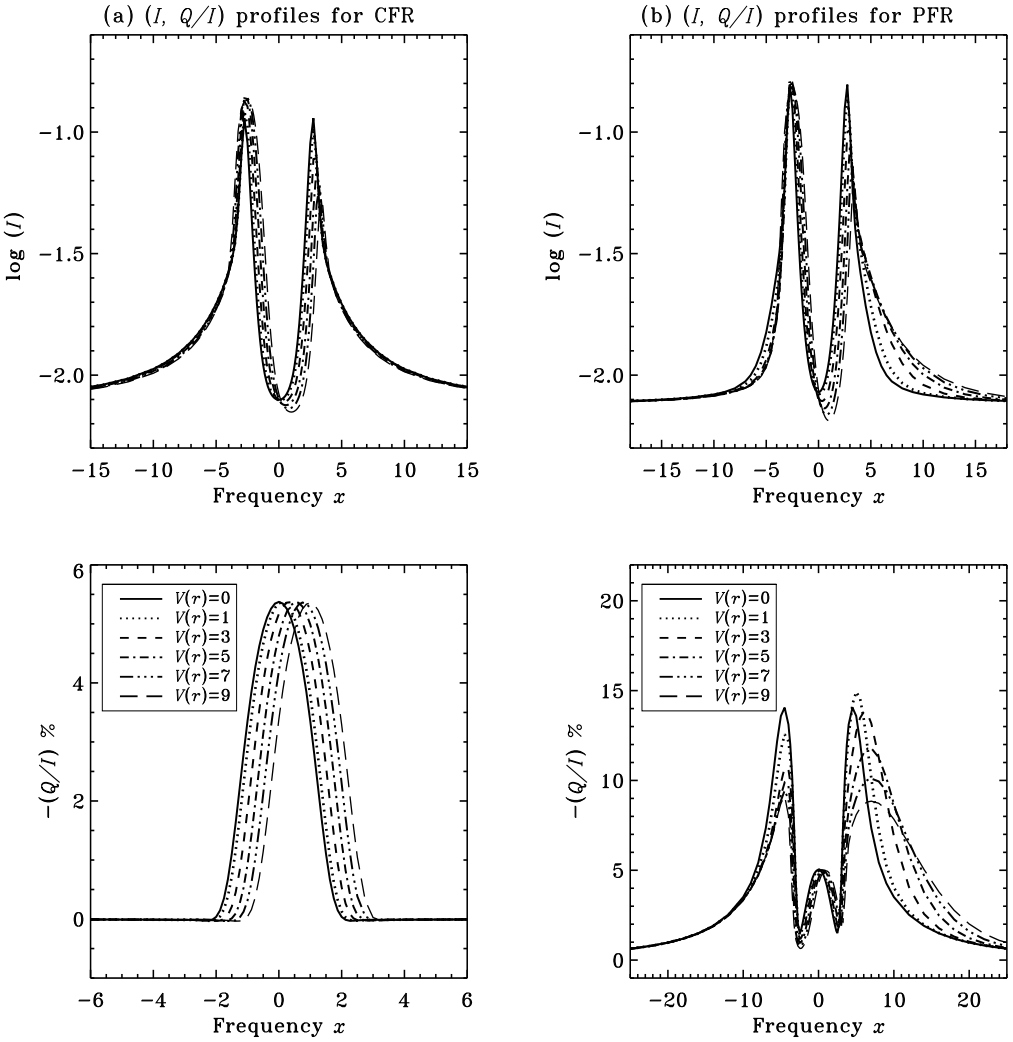

FIGURE 7.7: Emergent $(I, Q/I)$ profiles from a spherically symmetric atmosphere with CFR (panel (a)) and PFR (panel (b)) for varying values of $V(r)$ (which are given in the inset box). Other model parameters are given in Section 7.2. The line-of-sight is at $\mu = 0.11$.

peak becomes progressively broader with the increasing values of $V(r)$. As in Section 6.2, this dependence of I and Q/I profiles on $V(r)$ can be understood using the contribution functions and source vector plots.

7.10 Concluding remarks

The comoving frame method to solve the problem of polarized PFR line formation in spherically symmetric atmospheres with velocity fields is developed in Chapter

5. Here we use this method to study the effects of different model parameters on the linearly polarized line profiles formed in spherically symmetric static and moving atmospheres. We have varied the model parameters in a wide range, one at a time, to study their effects on the line profile. We showed that the line profiles exhibit a strong dependence on each of the parameters selected for our study and thus help in understanding the polarized lines formed in extended and expanding atmospheres. We showed that the velocity fields modify both the amplitude and shape of the Q/I profiles. Such a modification is significant when the corresponding intensity profiles exhibit a self-absorbed emission profile. This is because, in this case both Doppler brightening and dimming are simultaneously at play (as discussed in Chapter 6). In those cases where the intensity profiles are in emission, the corresponding Q/I profiles exhibit a strong Doppler dimming apart from a Doppler blue shift, when non-zero velocity fields are present in the line forming regions. It is important to note that strong asymmetry between the blue and red wing PFR peaks do not exist if the intensity profiles are only in emission or in pure absorption.

Chapter 8

Polarized Line Formation in Spherically Symmetric Expanding Atmospheres with Weak Field Hanle Effect[1]

An overview

Magnetic fields are all pervading in the astrophysical plasmas. They play an important role in the formation and evolution of stars. Magnetic fields leave their fingerprints in the polarized line profiles. Thus, studying the polarized line profiles helps us to understand the underlying fields, their evolution, and in predicting the physical phenomena that are at play in the stellar atmospheres. In Chapters 5, 6, and 7 we have studied the problem of polarized line formation in spherically symmetric moving atmospheres without magnetic fields. In the current chapter, we study the mentioned problem in the presence of weak magnetic fields using the Hanle effect. We generalize the Jacobi based CMF-PALI method developed in the Chapter 5, to include the weak field Hanle effect with angle-averaged (AA) partial frequency redistribution (PFR) given by approximation-III of Bommier (1997b). We present the preliminary results showing the effect of a weak magnetic field on

[1]This chapter is based on the publication: Megha *et al.* (2020b)

the polarized line profiles formed in spherically symmetric moving atmospheres with both complete frequency redistribution (CFR) and PFR.

8.1 Introduction

Magnetic field is the major driver of most of the physical phenomena occurring in the solar atmosphere. In spite of its key role in controlling the dynamics of the upper solar atmosphere, magnetic field still remains as a quantity not well determined. Though there are many techniques for determining the magnetic field in the corona using the mechanisms like bremsstrahlung and radio gyroresonance, they provide field strengths in different regions of the outer atmosphere (transition region and above) without altitude information (e.g., Gibson *et al.* 2016). Also these techniques are effective mainly in active regions. Coronal magnetic fields can also be approximated through MHD modeling by extrapolating photospheric measurements (e.g., Wiegelmann *et al.* 2014). However, these approaches have limitations since they are based on certain assumptions. In principle, determination of magnetic field in the solar atmosphere is possible via linear polarization measurement of spectral lines with suitable sensitivity to Hanle effect (Stenflo 1994). Several UV/EUV lines like H I Ly α and β are the most intense lines in the off-limb coronal spectrum which are sensitive to Hanle effect (Raouafi *et al.* 2016).

Hanle effect is the result of quantum interferences between different magnetic sub-levels of a given atomic level involved in the transition. Hanle effect is the modification (depolarization or repolarization and rotation of plane of linear polarization) of resonance scattering in the presence of weak magnetic fields (see Stenflo 1994, Trujillo Bueno 2001, and Landi Degl'Innocenti and Landolfi 2004 for details). It occurs when the magnetic (or Zeeman) splitting ($g_J\omega_B$) and the radiative width ($\Gamma_{\rm R}$) of the upper or lower level of the transition fulfill the following condition:

$$\Gamma_B = \frac{g_J\omega_B}{\Gamma_{\rm R}} \sim 1, \tag{8.1}$$

where g_J is the Landé g-factor of the upper or lower level, ω_B is the Larmor frequency, and $\Gamma_{\rm R}$ is the radiative width of the upper or lower atomic level. Hanle effect in selected spectral lines yields a powerful diagnostic tool for measuring

magnetic fields typically ranging from a few milli-Gauss to several hundred Gauss. Unlike the Zeeman effect, the Hanle effect in spectral lines by turbulent magnetic fields can be detected in the weak field regime allowing the determination of the strength of the field in mixed-polarity regions. In recent years the Hanle effect is also used as a diagnostic tool in stellar astrophysics (see, e.g., Ignace 2001, Bommier 2012).

The polarized line transfer equation including the Hanle effect and angle-averaged (AA) PFR in a plane-parallel atmosphere was first solved by Faurobert-Scholl (1991) using a Feautrier method. A PALI method based on operator splitting was developed in Nagendra *et al.* (1998, 1999, 2000) to solve the same problem for both CFR and AA-PFR. The PALI method is efficient and much faster than the Feautrier method. The above cited papers used a Hanle redistribution matrix, which was basically a product of AA-PFR function (see Hummer 1962) and a Hanle phase matrix (Stenflo 1994). Furthermore, a 1D frequency cut-off (cf. Equation (1.34)) was used to account for the fact that Hanle effect operates only in the line core. Bommier (1997b) derived self-consistent polarized redistribution matrices for the Hanle effect in a two-level atom including the effect of collisions. Fluri *et al.* (2003) developed a generalized PALI method to solve the polarized line transfer equation in planar atmospheres, including the angle-averaged Hanle PFR matrix of Bommier (1997b), given by the so-called approximation-III.

Here we consider the problem of polarized line formation in the spherically symmetric atmospheres, including the effect of weak oriented magnetic fields through the Hanle effect. We include the angle-averaged Hanle PFR matrix following approximation-III of Bommier (1997b). We also take into account the effects of a non-relativistic radial velocity field. We develop the numerical method of solution for the concerned radiative transfer problem using a decomposition of the Stokes parameters into a set of six irreducible components (Frisch 2007). In particular, we generalize the Jacobi based CMF-PALI method presented in Chapter 5 to include the weak field Hanle effect.

This chapter is organized as follows. In Section 8.2 we present the spherically symmetric polarized transfer equation in the observer's frame, including the Hanle effect. In Section 8.3 we present the corresponding equation in the comoving frame and in the irreducible spherical tensor basis. The numerical method of solution is

discussed in Section 8.4. Results and discussions are presented in Section 8.5, and concluding remarks in Section 8.6.

8.2 Polarized radiative transfer with the Hanle effect

Here we assume that the magnetic fields are weak (the Hanle regime) and work with angle-averaged frequency redistribution functions. The corresponding Hanle PFR matrix is given by approximation-III of Bommier (1997b). We consider an isothermal one-dimensional spherically symmetric atmosphere with velocity fields along the radius vector and permeated by weak magnetic fields. The observer's frame polarized PFR transfer equation for a spherically symmetric medium in divergence form, and in the presence of weak magnetic field $\boldsymbol{B}$ is given by

$$\mu\frac{\partial \boldsymbol{I}(r,\boldsymbol{n},x)}{\partial r}+\frac{(1-\mu^2)}{r}\frac{\partial \boldsymbol{I}(r,\boldsymbol{n},x)}{\partial \mu}=-\chi(r,\mu,x)[\boldsymbol{I}(r,\boldsymbol{n},x)-\boldsymbol{S}(r,\boldsymbol{n},x)], \quad (8.2)$$

where $\boldsymbol{I}=(I,Q,U)^{\mathrm{T}}$ is the polarized intensity vector, $\boldsymbol{S}$ is the total source vector, which are now three-component vectors in the presence of a weak magnetic field. We recall that in a weak magnetic field, the circular polarization represented by Stokes V gets decoupled from the other three Stokes parameters. Also, since we are in the Hanle regime, the absorption coefficient continues to be a scalar (see, e.g., Stenflo 1994; Landi Degl'Innocenti and Landolfi 2004). In the above equation, $\boldsymbol{n}=(\vartheta,\varphi)$ defines the ray direction with ϑ and φ being the inclination and azimuth of the ray about the local radius vector and $\mu=\cos\vartheta$. The above equation is exactly in the same form as in Equation (5.1) but now $\boldsymbol{I}$ and $\boldsymbol{S}$ depend on φ due to the breaking of the axi-symmetry of the problem by the presence of weak magnetic field. All the other quantities are the same as those defined in Sections 4.2 and 5.2.1 of Chapters 4 and 5, respectively.

We solve Equation (8.2) in the (p,z) coordinate system as in Chapters 4 and 5. The polarized transfer equation in the (p,z) coordinate system is written as

$$\pm\frac{\partial \boldsymbol{I}^{\pm}(z,p,\varphi,x)}{\partial\tau(z,p,x)}=\boldsymbol{I}^{\pm}(z,p,\varphi,x)-\boldsymbol{S}(z,p,\varphi,x), \quad (8.3)$$

for outgoing (+) and incoming (−) rays, respectively. The total source vector is given by

$$\boldsymbol{S}(z,p,\varphi,x) = \frac{\phi(z,p,x)\boldsymbol{S}_l(z,p,\varphi,x) + \beta_c \boldsymbol{S}_c}{\phi(z,p,x)+\beta_c}, \tag{8.4}$$

where $\boldsymbol{S}_c = B_{\nu_0}\boldsymbol{U}$ is the unpolarized continuum source vector, with B_{ν_0} the Planck function at the line center, and $\boldsymbol{U} = (1,0,0)^{\mathrm{T}}$. For a two-level atom with infinitely sharp and unpolarized lower-level, the line source vector has the form

$$\boldsymbol{S}_l(z,p,\varphi,x) = \epsilon B_{\nu_0}\boldsymbol{U} + \int_{-\infty}^{+\infty} dx' \frac{1}{2}\oint \frac{d\boldsymbol{n}'}{4\pi} \frac{\mathbf{R}(x-\mu V,\boldsymbol{n},x'-\mu' V,\boldsymbol{n}',\boldsymbol{B})}{\phi(z,p,x)} \boldsymbol{I}(\tau,\boldsymbol{n}',x'). \tag{8.5}$$

Here the primed symbols $x', \boldsymbol{n}'$ refer to the incoming photons and the unprimed ones to scattered photons. $\mathbf{R}$ is the Hanle redistribution matrix (Bommier 1997b) and $\boldsymbol{B}$ is the magnetic field vector. In the presence of velocity fields, the $\mathbf{R}$ matrix continues to be given by approximation-III of Bommier (1997b), but with x and x' replaced by $x-\mu V$ and $x'-\mu' V$. As we have already discussed about the limitations of observer's frame in Chapter 5, we consider the CMF for further discussions.

8.3 Irreducible spherical tensor decomposition in the CMF

Source vector $\boldsymbol{S}$ and the Stokes vector $\boldsymbol{I}^{\pm}$ in Equation (8.3) depend on impact parameter p (thereby ϑ) and azimuth φ of the radiation field. Following Frisch (2007), the vectors $\boldsymbol{S}$ and $\boldsymbol{I}^{\pm}$ can be decomposed into six cylindrically symmetric components, $\mathcal{S}^K_Q$ and $\mathcal{I}^{K,\pm}_Q$, with K =0, 2 and $Q \in [-K,+K]$, if one represents the former in terms of the spherical irreducible tensors for polarimetry defined in Landi Degl'Innocenti and Landolfi (2004). With these components one can construct an irreducible source vector $\boldsymbol{\mathcal{S}}$ and an irreducible Stokes vector $\boldsymbol{\mathcal{I}}^{\pm}$. This decomposition is useful because $\boldsymbol{\mathcal{S}}$ becomes independent of both p and φ and $\boldsymbol{\mathcal{I}}^{\pm}$ becomes independent of the azimuthal angle φ for the static and moving atmospheres in the CMF frame (see, e.g., Sampoorna and Nagendra 2015b, also Chapter 5). The CMF transfer equation in the irreducible basis for the weak field Hanle effect and for the non-relativistic velocity fields has the form as in Equation

(5.10). However, unlike the non-magnetic case, the irreducible vector $\boldsymbol{\mathcal{I}}^{\pm}$ is now a six-component vector of the form $\boldsymbol{\mathcal{I}}^{\pm}$= $[\mathcal{I}_0^{0,\pm}, \mathcal{I}_0^{2,\pm}, \mathcal{I}_1^{2x,\pm}, \mathcal{I}_1^{2y,\pm}, \mathcal{I}_2^{2x,\pm}, \mathcal{I}_2^{2y,\pm}]^{\mathrm{T}}$. The six-component irreducible source vector $\boldsymbol{\mathcal{S}}$ now has a form similar to Equation (8.4), but with $\phi(z, p, x)$ replaced by $\phi(x)$ in the CMF and the irreducible line source vector is given by

$$\boldsymbol{\mathcal{S}}_l(z, x) = \epsilon B_{\nu_0} \boldsymbol{\mathcal{U}} + \int_{-\infty}^{+\infty} dx' \frac{\boldsymbol{\mathcal{R}}(x, x', \boldsymbol{B})}{\phi(x)} \boldsymbol{\mathcal{J}}_{x'}, \tag{8.6}$$

where $\boldsymbol{\mathcal{U}} = [1, 0, 0, 0, 0, 0]^{\mathrm{T}}$ and $\phi(x) = H(a, x)$ is the line profile function in the CMF. The mean intensity vector $\boldsymbol{\mathcal{J}}_{x'}$ is given by

$$\boldsymbol{\mathcal{J}}_{x'} = \frac{1}{2} \int_{-1}^{+1} \boldsymbol{\Psi}(\mu') \boldsymbol{\mathcal{I}}(\tau, \mu', x') d\mu', \tag{8.7}$$

where $\boldsymbol{\Psi}(\mu)$ is the 6×6 matrix whose explicit form is given in Frisch (2007). $\boldsymbol{\mathcal{R}}(x, x', \boldsymbol{B})$ is the angle-averaged Hanle redistribution matrix in the irreducible basis. We recall that it is given by the approximation-III of Bommier (1997b). Following Anusha *et al.* (2011a), we write this matrix in the irreducible basis as

$$\boldsymbol{\mathcal{R}}(x, x', \boldsymbol{B}) = \mathbf{M}_{\mathrm{II}}^{(i)}(\boldsymbol{B}) R_{\mathrm{II,\,AA}}(x, x') + \mathbf{M}_{\mathrm{III}}^{(i)}(\boldsymbol{B}) R_{\mathrm{III,\,AA}}(x, x'). \tag{8.8}$$

$R_{\mathrm{II,\,AA}}(x, x')$ and $R_{\mathrm{III,\,AA}}(x, x')$ are the type-II and type-III angle-averaged redistribution functions of Hummer (1962). Here i=1, 2, 3, 4, 5 label the different frequency domains as in Bommier (1997b). Indices 1–3 refer to the domains corresponding to $R_{\mathrm{III,AA}}$, and indices 4 and 5 to the domains corresponding to $R_{\mathrm{II,AA}}$.

The 6×6 matrices $\mathbf{M}_{\mathrm{II,\,III}}^{(i)}(\boldsymbol{B})$ are given below. Let $\mathbf{M}(\boldsymbol{B}, \Gamma_B)$ denote the Hanle phase matrix as defined in Landi Degl'Innocenti and Landolfi (2004), where Γ_B is defined in Equation (8.1). This matrix depends on field strength parameter Γ_B, field inclination ϑ_B, and azimuth φ_B defined about the local radius vector. As in Anusha *et al.* (2011a), we define 6×6 diagonal matrices, namely $\mathbf{W}$, $\boldsymbol{\alpha}$, $\boldsymbol{\beta}$, and $\mathbf{F}$. The diagonal elements of these matrices are given by

$$\mathrm{W}_{11} = W_0; \quad \mathrm{W}_{jj} = W_2; \quad \text{for} \quad j = 2, ..., 6, \tag{8.9}$$

where $W_0 = 1$ and W_2 is the polarizability factor;

$$\alpha_{jj} = \alpha; \quad \text{for} \quad j = 1, ..., 6, \tag{8.10}$$

and

$$\beta_{11} = \beta^{(0)}; \quad \beta_{jj} = \beta^{(2)} \quad \text{for} \quad j = 2, ..., 6, \tag{8.11}$$

$$\mathrm{F}_{11} = 1 - \frac{\alpha}{\beta^{(0)}}; \quad \mathrm{F}_{jj} = 1 - \frac{\alpha}{\beta^{(2)}}, \quad \text{for} \quad j = 2, ..., 6. \tag{8.12}$$

In the above equations α and $\beta^{(K)}$ denote the branching ratios and are defined respectively, in Equations (4.7) and (4.8). As in Bommier (1997b), we define the coefficients

$$\Gamma'_K = \beta^{(K)}\Gamma_B; \qquad \Gamma'' = \alpha\Gamma_B. \tag{8.13}$$

$\mathbf{M}^{(i)}_{\mathrm{II,III}}(\boldsymbol{B})$ for different frequency domains can be obtained using the following algorithmic form, which involves a cut-off frequency $v_c(a)$ defined in Bommier (1997b) and a constant $z = 2\sqrt{2} + 2$. This algorithmic form is as follows:
If

$$\begin{aligned}\big\{[zv_c(a) \mid x' \mid -(x^2 + x'^2)] < [(z-1)v_c^2(a)] \quad \text{and} \quad [zv_c(a) \mid x \mid -(x^2 + x'^2)] \\ < [(z-1)v_c^2(a)] \quad \text{and} \quad \mid x' \mid < \sqrt{2}v_c(a) \quad \text{and} \quad \mid x \mid < \sqrt{2}v_c(a)\big\},\end{aligned} \tag{8.14}$$

then domain 1:

$$\mathbf{M}^{(1)}_{\mathrm{III}}(\boldsymbol{B}) = \mathbf{W}\{\boldsymbol{\beta}\mathbf{M}(\boldsymbol{B}, \Gamma'_2) - \boldsymbol{\alpha}\mathbf{M}(\boldsymbol{B}, \Gamma'')\}, \tag{8.15}$$

elseif

$$\{\mid x' \mid < v_c(a) \quad \text{or} \quad \mid x \mid < v_c(a)\}, \tag{8.16}$$

then domain 2:

$$\mathbf{M}^{(2)}_{\mathrm{III}}(\boldsymbol{B}) = \mathbf{W}\{[\boldsymbol{\beta} - \boldsymbol{\alpha}]\mathbf{M}(\boldsymbol{B}, \Gamma'_2)\}, \tag{8.17}$$

else domain 3:

$$\mathbf{M}^{(3)}_{\mathrm{III}}(\boldsymbol{B}) = \mathbf{WF}\{[\boldsymbol{\beta} - \boldsymbol{\alpha}]\mathbf{M}(\boldsymbol{B}, \Gamma'_2) + \boldsymbol{\alpha}\}, \tag{8.18}$$

endif.

If

$$\{[x(x+x')] < 2v_c^2(a) \text{ and } [x'(x+x')] < 2v_c^2(a)\}, \tag{8.19}$$

then domain 4:

$$\mathbf{M}_{\rm II}^{(4)}(\boldsymbol{B}) = \alpha \mathbf{WM}(\boldsymbol{B}, \Gamma''), \tag{8.20}$$

else domain 5:

$$\mathbf{M}_{\rm II}^{(5)}(\boldsymbol{B}) = \alpha \mathbf{W}, \tag{8.21}$$

endif.

8.4 The numerical method of solution

Here we discuss the basic equations of the Jacobi based CMF-PALI method used in solving the radiative transfer equation with Hanle effect. It is based on the core-wing method of Fluri *et al.* (2003). The formal solution of the Hanle transfer equation may be stated in terms of the Lambda operator as

$$\boldsymbol{\mathcal{J}}_x = \boldsymbol{\Lambda}_x[\boldsymbol{\mathcal{S}}_x] + \boldsymbol{T}_x, \tag{8.22}$$

where $\boldsymbol{\Lambda}_x$ and $\boldsymbol{T}_x$ are given by Equations (4.20) and (4.21) respectively. Unlike the non-magnetic case, here $\boldsymbol{\mathcal{J}}_x$, $\boldsymbol{\mathcal{S}}_x$, and $\boldsymbol{T}_x$ are 6-component vectors, while $\boldsymbol{\Lambda}_x$ and $\boldsymbol{\Psi}(\mu)$ are 6×6 matrices. Now we define the local, monochromatic approximate Lambda operator $\boldsymbol{\Lambda}_x^*$ as

$$\boldsymbol{\Lambda}_x = \boldsymbol{\Lambda}_x^* + \delta\boldsymbol{\Lambda}_x = \boldsymbol{\Lambda}_x^* + (\boldsymbol{\Lambda}_x - \boldsymbol{\Lambda}_x^*). \tag{8.23}$$

With this we set up a Jacobi iterative scheme to compute the source vectors as

$$\boldsymbol{\mathcal{S}}_x^{(n+1)} = \boldsymbol{\mathcal{S}}_x^{(n)} + \delta\boldsymbol{\mathcal{S}}_x^{(n)}; \quad \boldsymbol{\mathcal{S}}_{l,x}^{(n+1)} = \boldsymbol{\mathcal{S}}_{l,x}^{(n)} + \delta\boldsymbol{\mathcal{S}}_{l,x}^{(n)}, \tag{8.24}$$

where the superscript n refers to the nth iteration. From the CMF equivalent of Equation (8.4) in the irreducible basis it follows that

$$\delta\boldsymbol{\mathcal{S}}_x^{(n)} = p_x \delta\boldsymbol{\mathcal{S}}_{l,x}^{(n)}; \quad \text{with } p_x = \frac{\phi_x}{\phi_x + \beta_c}. \tag{8.25}$$

Using this we can write

$$\boldsymbol{\mathcal{J}}_x^{(n+1)} \approx \boldsymbol{\mathcal{J}}_x^{(n)} + p_x \boldsymbol{\Lambda}_x^* [\delta \boldsymbol{\mathcal{S}}_{l,x}^{(n)}]. \tag{8.26}$$

With this the line source vector corrections can be written as

$$\delta \boldsymbol{\mathcal{S}}_{l,x}^{(n)} - \frac{1}{\phi_x} \int_{-\infty}^{+\infty} dx' p_{x'} \boldsymbol{\mathcal{R}}(x, x', \boldsymbol{B}) \boldsymbol{\Lambda}_{x'}^* [\delta \boldsymbol{\mathcal{S}}_{l,x'}^{(n)}] = \boldsymbol{r}_x^{(n)}, \tag{8.27}$$

where

$$\boldsymbol{r}_x^{(n)} = \boldsymbol{\mathcal{S}}_{\mathrm{FS},l,x}^{(n)} - \boldsymbol{\mathcal{S}}_{l,x}^{(n)}, \tag{8.28}$$

with the formal line source vector $\boldsymbol{\mathcal{S}}_{\mathrm{FS},l,x}^{(n)}$ given by

$$\boldsymbol{\mathcal{S}}_{\mathrm{FS},l,x}^{(n)} = \epsilon B_{\nu_0} \boldsymbol{\mathcal{U}} + \frac{1}{\phi_x} \int_{-\infty}^{+\infty} dx' \boldsymbol{\mathcal{R}}(x, x', \boldsymbol{B}) \boldsymbol{\mathcal{J}}_{x'}^{(n)}, \tag{8.29}$$

where the mean intensity $\boldsymbol{\mathcal{J}}_x^{(n)}$ is computed using the short characteristic formal solver in the CMF (see Section 5.3.2.1).

8.4.1 Estimation of source vector corrections using approximated domains

Following Fluri *et al.* (2003), the core-wing separation scheme is applied to compute $\delta \boldsymbol{\mathcal{S}}_{l,x}^{(n)}$ by redefining the frequency domains (see Figure 2 of Fluri *et al.* 2003). These approximated domains are used only for the computation of the source vector corrections in the CMF-PALI iterations. In the core-wing scheme, the type-III redistribution function R_{III} is approximated by complete frequency redistribution (CFR) in the line core (defined by $|x| \leq v_c(a)$) and it is neglected in the line wings (as ϕ_x is sufficiently small in the wings). The type-II redistribution function R_{II} is treated as CFR in the line core and coherent scattering (CS) in the line wings. By doing this the line core and the line wings decouple from each other.

Thus, R_{III} part in the integral of Equation (8.27) now simplifies to the following

$$\frac{1}{\phi_x} \int_{-\infty}^{+\infty} dx' p_{x'} \mathbf{M}_{\mathrm{III}}^{(i)} R_{\mathrm{III}}^{xx'} \boldsymbol{\Lambda}_{x'}^* [\delta \boldsymbol{\mathcal{S}}_{l,x'}^{(n)}] \approx \begin{cases} \mathbf{M}_{\mathrm{III}}^{(1)} \Delta T_{\mathrm{core}}^{(n)}, & \text{for } \mid x \mid \leq v_c(a) \\ \mathbf{M}_{\mathrm{III}}^{(2)} \Delta T_{\mathrm{core}}^{(n)}, & \text{for } \mid x \mid > v_c(a) \end{cases} . \tag{8.30}$$

The matrix corresponding to domain 3, namely $\mathbf{M}_{\rm III}^{(3)}$ is not used because the line wing part is neglected.

Following Nagendra *et al.* (1999), the $R_{\rm II}$ part in the integral of Equation (8.27) with core-wing scheme now simplifies to the following

$$\frac{1}{\phi_x}\int_{-\infty}^{+\infty} dx' p_{x'} \mathbf{M}_{\rm II}^{(i)} R_{\rm II}^{xx'} \mathbf{\Lambda}_{x'}^{*}[\delta \boldsymbol{\mathcal{S}}_{l,x'}^{(n)}] \approx \begin{cases} \mathbf{M}_{\rm II}^{(4)} \Delta T_{\rm core}^{(n)}, & \text{for } \mid x \mid \leq v_c(a) \\ (1-\alpha_x)\mathbf{M}_{\rm II}^{(5)} \Delta T_{\rm core}^{(n)} + \alpha_x \mathbf{M}_{\rm II}^{(5)} p_x \mathbf{\Lambda}_x^{*}[\delta \boldsymbol{\mathcal{S}}_{l,x}^{(n)}], & \text{for } \mid x \mid > v_c(a) \end{cases} \tag{8.31}$$

where the core-wing separation coefficient is given by

$$\alpha_x = \begin{cases} 0, & \text{for } \mid x \mid \leq v_c(a) \\ \frac{R_{\rm II}(x,x')}{\phi_x}, & \text{for } \mid x \mid > v_c(a) \end{cases} . \tag{8.32}$$

Using Equations (8.30) and (8.31), the source vector correction in the line core ($\mid x \mid \leq v_c(a)$) can be obtained as

$$\delta \boldsymbol{\mathcal{S}}_{l,x}^{(n)} = [\mathbf{M}_{\rm III}^{(1)} + \mathbf{M}_{\rm II}^{(4)}] \Delta T_{\rm core}^{(n)} + \boldsymbol{r}_x^{(n)}. \tag{8.33}$$

By applying the following integral operator from the left of the Equation (8.33)

$$\int_{-v_c(a)}^{+v_c(a)} \phi_x p_x \mathbf{\Lambda}_x^{*}[\ ] dx, \tag{8.34}$$

expression for $\Delta T_{\rm core}^{(n)}$ which is now frequency independent can be obtained as

$$\Delta T_{\rm core}^{(n)} = \left\{ \mathbf{E} - \int_{-v_c(a)}^{+v_c(a)} \phi_x p_x \mathbf{\Lambda}_x^{*} dx [\mathbf{M}_{\rm III}^{(1)} + \mathbf{M}_{\rm II}^{(4)}] \right\}^{-1} \bar{\boldsymbol{r}}_{\rm core}^{(n)}, \tag{8.35}$$

where

$$\bar{\boldsymbol{r}}_{\rm core}^{(n)} = \int_{-v_c(a)}^{+v_c(a)} \phi_x p_x \mathbf{\Lambda}_x^{*}[\boldsymbol{r}_x^{(n)}] dx. \tag{8.36}$$

Again using Equations (8.30) and (8.31), the source vector correction in the line wing ($\mid x \mid > v_c(a)$) can be obtained as

$$\delta\boldsymbol{\mathcal{S}}_{l,x}^{(n)} = \left[\mathbf{E} - \alpha_x p_x \mathbf{M}_{\rm II}^{(5)} \boldsymbol{\Lambda}_x^*\right]^{-1} \left\{ \left[\mathbf{M}_{\rm III}^{(2)} + (1-\alpha_x)\mathbf{M}_{\rm II}^{(5)}\right] \Delta T_{\rm core}^{(n)} + \boldsymbol{r}_x^{(n)} \right\}. \quad (8.37)$$

Further details on the formal solution of the comoving frame polarized transfer equation are discussed in Chapter 5 for the non-magnetic case. These steps remain the same in the presence of magnetic fields, except that number of irreducible components change from two for the non-magnetic case to six in the weak field Hanle case.

8.5 Results and discussions

We study the convergence properties of the Jacobi based CMF-PALI method developed for weak field Hanle effect in Section 8.4, by plotting the maximum relative change (MRC) of the irreducible source vector components $(c_Q^K)^n$, which are defined similar to Equation (4.36) but with $\mathcal{S}_Q^K$. Thus, clearly $(c_Q^K)^n$ is now a six-component vector in the presence of magnetic field. In Figure 8.1, we plot $(c_Q^K)^n$ for both CFR (panels (a), (b), (c)) and PFR (panels (d), (e), (f)) for the different velocity laws shown in Figure 5.2. Other model parameters are the same as in Sections 4.4 and 5.4.1 except that here we chose the extension as $R = 3$. We see that the rate of convergence for $(c_0^0)^n$ is similar to that of the corresponding non-magnetic case for both CFR and PFR. The other components $(c_Q^2)^n$ converge relatively slower as expected in the presence of magnetic field. In the case of CFR the convergence behavior is similar for all the velocity laws that we have considered. This is perhaps due to the choice of smaller extension. However, for PFR the convergence of irreducible components $(c_1^{2x})^n$, $(c_1^{2y})^n$, $(c_2^{2x})^n$, $(c_2^{2y})^n$ is slightly modified for different velocity law cases (compare Figures 8.1(d), 8.1(e), and 8.1(f)). In particular, several sharp peaks persist as far as 150 iterations (see, e.g., dotted-dashed line in Figure 8.1(f)). This is due to the presence of CMF term in the transfer equation. Also the number of iterations required for the convergence in the case of PFR is greater than the CFR case for the same reasons described in Chapter 5.

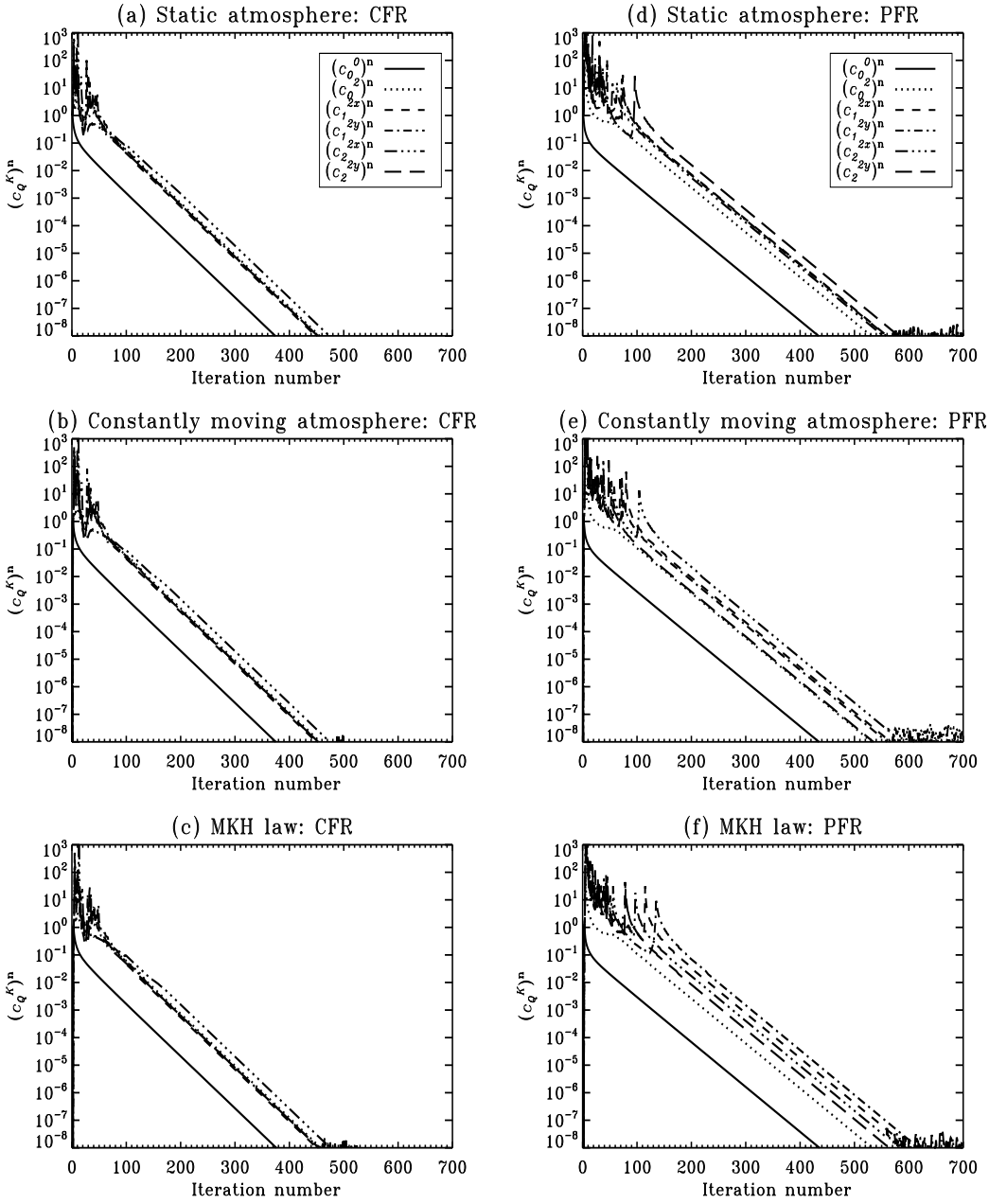

FIGURE 8.1: Maximum relative change of comoving frame irreducible source vector components $(c_Q^K)^n$ (a six component vector) as a function of iteration number for $R = 3$ for both CFR (panels (a), (b), (c)) and PFR (panels (d), (e), (f)) with different velocity laws shown in Figure 5.2. The magnetic field parameters used are $(\Gamma_B, \vartheta_B, \varphi_B)$= (1, 40°, 0°). Other model parameters are the same as in Sections 4.4 and 5.4.1.

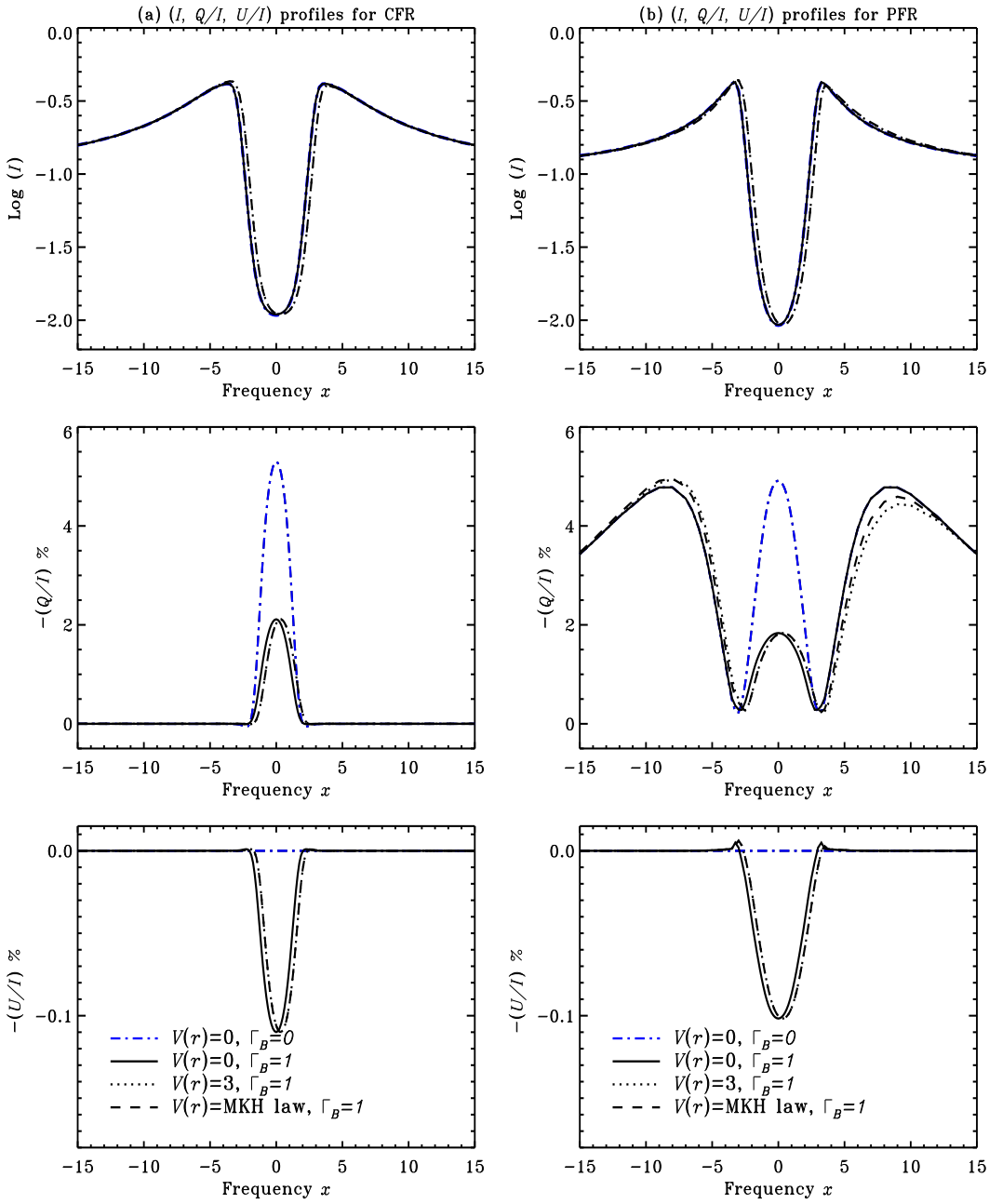

FIGURE 8.2: Emergent polarized $(I, Q/I, U/I)$ profiles from a spherically symmetric atmosphere with $R = 3$ and for different velocity laws shown in Figure 5.2 in the presence of a weak magnetic field. The static non-magnetic solution is shown as dotted-dashed line for reference. Other line types are indicated in the figure legend. The line-of-sight is at μ=0.11 and $\varphi = 0°$. The magnetic field parameters are $(\Gamma_B, \vartheta_B, \varphi_B)$= (1, 40°, 0°). Other model parameters are the same as in Sections 4.4 and 5.4.1. Solid and dotted-dashed lines, and dotted and dashed lines coincide in the I panels.

Figure 8.2 shows the emergent $(I, Q/I, U/I)$ profiles for different velocity laws and for a non-zero magnetic field. The model parameters are the same as those listed in Sections 4.4 and 5.4.1 except that here we chose the extension as $R = 3$. The static non-magnetic polarized profile is shown for reference (see, dotted-dashed line). From Figure 8.2 we clearly see that Stokes I profiles are nearly insensitive to the weak field (compare dotted-dashed and solid lines in Figure 8.2). The shapes of the Q/I profiles for both magnetic and non-magnetic cases are nearly the same, except for the Hanle depolarization in the line core (compare solid and dotted-dashed lines). The Stokes U/I profiles are generated due to Hanle rotation. We see that the dependence of magnetic Q/I profiles on the velocity fields in the case of both constantly moving atmosphere and with MKH law is similar to those shown by the corresponding non-magnetic Q/I profiles (see, e.g., dashed lines in Figures 6.7 and 6.9 for CFR and PFR respectively). In a moving atmosphere, the Hanle effect continues to operate in the Doppler shifted line core. Further, in the presence of velocity fields, due to Doppler shifts of the line profiles, entire U/I profiles shift toward the blue side.

8.6 Concluding remarks

Here we extended the problem of polarized line formation with weak field Hanle effect and PFR to the spherically symmetric expanding atmospheres. We used approximation-III of Bommier (1997b) to handle the Hanle effect with PFR. We apply the appropriately modified Jacobi based CMF-PALI method developed in Chapter 5 to include the effects of a weak magnetic field and radial velocity fields. We studied the MRC of all the six irreducible source vector components obtained using the Jacobi scheme. We presented preliminary results for the problem at hand. We showed the polarized line profiles for a fixed magnetic field orientation and in the presence of radial velocity fields. We observed that, in the presence of velocity fields Hanle effect operates in the Doppler shifted line core. Thus, the linear polarization computed with weak field Hanle effect and PFR provides a sensitive diagnostic of velocity fields and magnetic fields in extended spherical atmospheres.

We remark that the assumption of a fixed orientation for the magnetic field throughout the spherical atmosphere is only of academic interest and is not physical. For this reason, in this chapter we do not attempt to make a very detailed study of the polarized line profiles as in Chapters 6 and 7 for the non-magnetic case. A physically more realistic magnetic field configuration would be either a radial field or a dipolar field (as considered in Chapters 2 and 3). In the weak field regime considered in this chapter, the radial field does not produce any Hanle effect as the axial symmetry of the problem is not broken. As shown in Chapters 2 and 3, the dipolar field does produce the Hanle effect not only in the disk resolved case, but also when integrated over the visible stellar disk (see, e.g., López Ariste *et al.* 2011; Bommier 2012; Manso Sainz and Martínez González 2012). In the above-cited works only single scattering or last scattering approximation were considered to study the dependence of linear polarization due to the Hanle effect on dipolar field strength, and on the inclination of dipole axis with the stellar rotation axis. The extension of these works to include multiple scattering in spherically symmetric static and expanding atmospheres is under progress and hence beyond the scope of this thesis.

Chapter 9

Summary and Future Prospects

9.1 Summary

Understanding the nature of solar magnetic fields is the first step towards perceiving the global magnetic fields in the astrophysical plasmas. Studying the polarized line profiles formed in such media is one of the best ways to achieve this goal. Therefore in this thesis we aim at developing the necessary theoretical tools to determine the solar and stellar magnetic fields. For this, we harness the sensitivity of both forbidden (magnetic dipole, M1 allowed) and permitted (electric dipole, E1 allowed) lines which form under different physical conditions, to the magnetic field. In the first part of this thesis, we develop the necessary scattering theory for M1 transitions. Since the forbidden lines are optically thin, it is not necessary to solve the transfer equation. However, due to variations in the density of scattering atoms, it is required to account for integration along the line-of-sight (LOS). On the other hand, the permitted lines are generally optically thick, requiring the inclusion of the transfer effects when modeling them. Also the extended solar or stellar atmospheres are known to be dynamic with macroscopic velocity fields being present in the line forming regions. Thus the second part of this thesis is devoted to develop the numerical technique to solve the polarized line radiative transfer equation in a spherically symmetric expanding atmospheres. We also account for the effects of weak magnetic fields via the Hanle effect in the permitted lines.

In Chapter 2 we derived the Hanle-Zeeman scattering matrix for M1 transitions using the scattering theory of Stenflo (1998) and classical M1 damped oscillator model of Casini and Lin (2002). Unlike the previous works, who considered the forbidden line formation theory in only saturated Hanle regime for applications in the solar corona, we developed a more general scattering theory that is applicable to any forbidden lines undergoing $J = 0 \rightarrow 1 \rightarrow 0$ M1 transitions in arbitrary strength magnetic fields covering Hanle, saturated Hanle, Hanle-Zeeman, and Zeeman regimes in a continuous way. In Chapter 3 we applied this theory to study the polarized profile of [Fe XIII] 10747 Å coronal forbidden emission line. Measurement of full Stokes vector of the forbidden lines can constrain both LOS field strength through longitudinal Zeeman effect (Stokes V) and orientation of projected magnetic field on the plane-of-sky (POS) through saturated Hanle effect (Stokes Q and U). We also studied the effect of different types of density distributions, magnetic field configurations, and radial velocity fields on the polarized line profile, thereby demonstrating the importance of spectropolarimetry in forbidden emission lines as a sensitive diagnostic tool in the solar corona.

Considering the fact that the plane-parallel approximation breaks down when the photon mean free path is a non-vanishing fraction of the radius of curvature of the stellar atmosphere, in part-II of this thesis, we developed the numerical techniques to solve the polarized line formation in spherically symmetric atmospheres. Also, the highly structured extended atmospheres are known to be dynamic, with low to high speed stellar winds originating in these layers. Solving the polarized transfer equation in the extended and expanding atmospheres in the observer's or lab frame is numerically very expensive due to the intricate coupling between the frequency, angle, and spatial variables, requiring relatively large memory and CPU time. Therefore, we developed computationally superior method called the comoving frame (CMF) method to solve the polarized transfer equation in the fluid frame in which the frequency, angle, and spatial couplings can be treated in the same way as in static atmospheres. For our studies we considered non-relativistic radial velocity fields, thereby accounting only for Doppler shift effects and neglecting advection and aberration of photons. For numerical simplicity, we solved the polarized transfer equation in the irreducible basis and in the (p, z) coordinate system, which involves solving the transfer equation along each characteristic ray

with impact parameter p and distance along the ray as z. The CMF transfer equation takes a similar form as that of the static case, except containing an extra term called the CMF-term that contains the effects of radial velocity fields. We used polarized accelerated lambda iteration (PALI) technique to solve the polarized transfer equation in the CMF. We presented the highly convergent fast iterative techniques like Gauss-Seidel (GS) and successive overrelaxation (SOR) beside the Jacobi iterative scheme in both static and expanding spherical atmospheres. We showed the superior convergence behavior of GS and SOR schemes over that of Jacobi scheme using the maximum relative change (MRC) and surface true error calculations.

Using the CMF-PALI method developed in Chapters 4 and 5, we studied the numerical solutions by plotting the linearly polarized line profiles in the presence of both complete frequency redistribution (CFR) and partial frequency redistribution (PFR) in scattering and interpreted the results with the help of contribution functions and Stokes source vector (Chapter 6). We showed that the velocity fields modify both the amplitude and shape of the Q/I profiles. We observed that such a modification is significant when the corresponding intensity profiles exhibit a self-absorbed emission profile in which both Doppler brightening and dimming effects are simultaneously at play. We also studied the center-to-limb variation (CLV) of the Stokes profiles and the nature of linearly polarized profiles with the variation of the extension R of the atmosphere. We demonstrated that the linear polarization in the wings produced due to PFR is highly sensitive to variations in the extension R. In Chapter 7 we studied the behavior of the linearly polarized profiles when the model parameters are varied one at a time and by keeping the other values as constants, for both static and moving atmospheres.

In Chapter 8 we described the inclusion of weak magnetic fields in the problem discussed in Chapter 5. To numerically solve this problem, we used the Jacobi-based CMF-PALI method with appropriate modifications. For the Hanle redistribution matrix, we considered approximation-III of Bommier (1997b) which represents the angle-averaged PFR in the presence of a weak magnetic field. We presented the polarized line profiles computed for a weak magnetic field of fixed orientation, with and without velocity fields, and for the case of CFR and PFR. Our studies show that in the presence of velocity fields the Hanle effect is operative in the Doppler shifted line core. Finally, we conclude that the linear polarization

computed with weak field Hanle effect and PFR is expected to provide a sensitive diagnostic of velocity fields, magnetic fields, and extension of the spherical atmospheres.

9.2 Future prospects

In this section, we briefly discuss the future prospects of the work carried out in the present thesis.

In Chapter 3, we presented the linear polarization maps that one would obtain if the coronal magnetic field is approximated by either radial or dipolar field configurations. However, in reality the coronal magnetic fields are more complex than these simpler field configurations. A better representation of the coronal magnetic fields are those obtained by potential or nonlinear force-free field extrapolation of the photospheric input magnetic fields generated through MHD simulations or through direct measurements using coronal emission lines (Lin *et al.* 2000, 2004; Liu and Lin 2008; Inoue 2016). As a natural next step, we propose to include such coronal magnetic fields to produce linear polarization maps that may be more closer to the observations (which may become available in the future). The theory developed in Chapter 2, can also be applied to other forbidden lines, in order to explore their diagnostic potential.

Part-II of this thesis dealt with solving the polarized radiative transfer problem in a spherically symmetric atmosphere with non-relativistic velocity fields, thereby neglected the advection and aberration effects. Mihalas *et al.* (1976a) solved the fully relativistic transfer equation in the CMF using modified Feautrier method (involves matrix inversion). In the presence of relativistic velocity fields the characteristic rays are no longer straight lines but are curved. Mihalas *et al.* (1976a) found the trajectories of these characteristic rays by numerically solving the corresponding ray equations and then integrating the transfer equation on the so obtained characteristics. Hauschildt and Wehrse (1991) also provided the solution to the special relativistic transfer equation using discrete ordinate matrix exponential (DOME) method which involves matrix diagonalization. These two methods require considerably large CPU time. To overcome this, Hauschildt and Baron (2004); Baron and Hauschildt (2004) solved the fully relativistic transfer equation

respectively for both monotonic and non-monotonic velocity fields using CMF-ALI method (see also Hauschildt 1992). It is important to include special relativistic effects in the transfer equation to study the high velocity flows which can occur in the expanding shells of novae, supernovae, galactic winds etc. (Hauschildt *et al.* 1991). The above cited papers considered transfer of unpolarized radiation with CFR in line scattering. In the near future we plan to extend these works to include the scattering polarization together with PFR effects.

In part-II of this thesis we adopted only the angle-averaged version of the PFR matrix for studying the linearly polarized line profiles formed in expanding spherical atmosphere. In an extended spherical atmosphere, the radiation field strongly peaks in the radial direction, which is especially more enhanced in the outer layers. Furthermore, in expanding atmospheres, the photons escape even more readily (Kunasz and Hummer 1974b). Therefore, we may expect that the use of angle-averaged PFR may not be sufficient to accurately compute the $(I, Q/I)$ profiles unlike the planar case. We recall that in a planar atmosphere angle-averaged PFR suffices to compute the non-magnetic $(I, Q/I)$ profiles for both with and without velocity fields (see, e.g., Faurobert 1988; Sampoorna *et al.* 2011; Sampoorna and Nagendra 2015b). In other words, there is a need to evaluate the importance of including angle-dependent PFR effects for the case of extended and expanding spherical atmospheres. Peraiah (1978) included angle-dependent PFR effects in the solution of unpolarized line transfer in an expanding spherical atmosphere but in the observer's frame, thereby limited to low velocity fields. Mihalas (1980) considered the same problem but in the CMF and hence suitable to handle both low and high-velocity fields. Clearly, our next step would be to include the angle-dependent PFR effects in the polarized transfer problem in expanding spherical atmospheres. Such studies are useful to understand the formation of optical and IR lines in stellar winds, nebulae, protostellar envelopes etc. wherein velocity gradients are present.

For the results presented in Chapters 6 and 7, we have used isothermal model atmospheres. Since the real stellar atmosphere is not isothermal, we would like to extend this work to include realistic model atmospheres and study the effects of extendedness on the emergent polarized line profiles. In Chapter 8, we have assumed a fixed orientation for the magnetic field throughout the spherical atmosphere. Such an assumption is however not physical. As shown in López Ariste

et al. (2011); Bommier (2012); Manso Sainz and Martínez González (2012), the Hanle effect can be used for magnetic field determination even in the case of stars. However, these works consider only single scattering or last scattering approximation to study the dependence of linear polarization due to Hanle effect on dipolar field strength, and orientation with respect to the stellar rotation axis. We plan to extend these works to include multiple scattering, which requires solving the polarized radiative transfer equation. In other words, we propose to extend the work presented in Chapter 8, to include a dipolar magnetic field in the future.

It was shown in earlier works that if a cylindrical structure is approximated by a plane-parallel slab, the emergent intensities can have errors up to 30 % (e.g., Gouttebroze *et al.* 1986). Radiative transfer in cylindrical media is important for studying the line formation in solar prominences, coronal loops, etc. which exhibit cylindrical thread-like structure. Gouttebroze (1990) generalized the discrete ordinate method (DOM), as a semi-analytical method to solve the unpolarized transfer equation in a 1D cylindrical geometry. He showed that this method can also handle PFR in scattering. This work was generalized to solve the cylindrical transfer with multilevel atom using ALI method by Gouttebroze (2004). This work was further extended to 2D by Gouttebroze (2005) and to 3D by Hauschildt and Baron (2009). Independently, van Noort *et al.* (2002) have developed an ALI method to solve the 2D unpolarized radiative transfer problem in Cartesian, cylindrical, and spherical coordinates. Milić (2013) extended the 2D cylindrical radiative transfer method of van Noort *et al.* (2002) to include scattering polarization with CFR. In this thesis we have focused our attention on 1D spherical geometry. As a next step it would be interesting to extend our 1D spherical polarized PFR code to solve the polarized transfer equation with PFR in cylindrical geometry. Such an effort will be useful to study the polarized lines formed in cylindrical structures in the solar atmosphere, such as spicules, prominences, and coronal loops.

Bibliography

Akhmedov, S. B., Gelfreikh, G. B., Bogod, V. M. and Korzhavin, A. N., 1982, "The Measurement of Magnetic Fields in the Solar Atmosphere above Sunspots Using Gyro-Resonance Emission", *Solar Phys.*, **79**, 41–58. [DOI], [URL]

Alfvén, H., 1943, "On Sunspots and the Solar Cycle", *Arkiv for Matematik, Astronomi och Fysik*, **29A**, 1–17. [URL]

Anusha, L. S. and Nagendra, K. N., 2011, "Polarized Line Formation in Multidimensional Media. I. Decomposition of Stokes Parameters in Arbitrary Geometries", *Astrophys. J.*, **726**, 6 (13 pages). [DOI], [URL]

Anusha, L. S., Nagendra, K. N., Paletou, F. and Léger, L., 2009, "Preconditioned Bi-conjugate Gradient Method for Radiative Transfer in Spherical Media", *Astrophys. J.*, **704**, 661–671. [DOI], [URL], [arXiv:0906.2926 [astro-ph.SR]]

Anusha, L. S., Nagendra, K. N., Bianda, M., Stenflo, J. O., Holzreuter, R., Sampoorna, M., Frisch, H., Ramelli, R. and Smitha, H. N., 2011a, "Analysis of the Forward-scattering Hanle Effect in the Ca I 4227 Å Line", *Astrophys. J.*, **737**, 95 (17 pages). [DOI], [URL]

Anusha, L. S., Nagendra, K. N. and Paletou, F., 2011b, "Polarized Line Formation in Multi-dimensional Media. II. A Fast Method to Solve Problems with Partial Frequency Redistribution", *Astrophys. J.*, **726**, 96 (13 pages). [DOI], [URL]

Arnaud, J. and Newkirk, G., Jr., 1987, "Mean properties of the polarization of the Fe XIII 10747 A coronal emission line", *Astron. Astrophys.*, **178**, 263–268. [URL]

Asensio Ramos, A. and Trujillo Bueno, J., 2006, "Very Efficient Methods for Multilevel Radiative Transfer in Atomic and Molecular Lines", in *Radiative transfer*

and applications to very large telescopes, (Ed.) Stee, Ph., EAS Publications Series, **18**, 25-48, EDP Sciences, Les Ulis. [DOI], [URL], [arXiv:astro-ph/0512248 [astro-ph]]

Athay, R. G., Querfeld, C. W., Smartt, R. N., Landi Degl'Innocenti, E. and Bommier, V., 1983, "Vector Magnetic Fields in Prominences - Part Three - He I D3 Stokes Profile Analysis for Quiescent and Eruptive Prominences", *Solar Phys.*, **89**, 3–30. [DOI], [URL]

Auer, L., Fabiani Bendicho, P. and Trujillo Bueno, J., 1994, "Multidimensional radiative transfer with multilevel atoms. I. ALI method with preconditioning of the rate equations.", *Astron. Astrophys.*, **292**, 599–615. [URL]

Baron, E. and Hauschildt, P. H., 2004, "Co-moving frame radiative transfer in spherical media with arbitrary velocity fields", *Astron. Astrophys.*, **427**, 987–994. [DOI], [URL], [arXiv:astro-ph/0408212 [astro-ph]]

Baschek, B., Efimov, G. V., von Waldenfels, W. and Wehrse, R., 1997, "Radiative transfer in moving spherical atmospheres. II. Analytical solution for fully relativistic radial motions.", *Astron. Astrophys.*, **317**, 630–635. [URL]

Beals, C. S., 1931, "The contours of emission bands in novae and Wolf-Rayet stars", *Mon. Not. Roy. Astron. Soc.*, **91**, 966–977. [DOI], [URL]

Belluzzi, L. and Trujillo Bueno, J., 2014, "The transfer of resonance line polarization with partial frequency redistribution and J-state interference. Theoretical approach and numerical methods", *Astron. Astrophys.*, **564**, A16 (18 pages). [DOI], [URL], [arXiv:1403.1701 [astro-ph.SR]]

Bianda, M., Solanki, S. K. and Stenflo, J. O., 1998a, "Hanle depolarisation in the solar chromosphere", *Astron. Astrophys.*, **331**, 760–770. [URL]

Bianda, M., Stenflo, J. O. and Solanki, S. K., 1998b, "Hanle diagnostics of solar magnetic fields: the SR II 4078 Angstrom line", *Astron. Astrophys.*, **337**, 565–578. [URL]

Bird, M. K. and Edenhofer, P., 1990, "Remote Sensing Observations of the Solar Corona", in *Physics of the Inner Heliosphere I*, (Eds.) Schwenn, R., Marsch, E., pp. 13–97, Springer-Verlag, Berlin, Germany. [URL]

Bommier, V., 1996, "Atomic Coherences and Level-Crossings Physics", *Solar Phys.*, **164**, 29–47. [DOI], [URL]

Bommier, V., 1997a, "Master equation theory applied to the redistribution of polarized radiation, in the weak radiation field limit. I. Zero magnetic field case", *Astron. Astrophys.*, **328**, 706–725. [URL]

Bommier, V., 1997b, "Master equation theory applied to the redistribution of polarized radiation, in the weak radiation field limit. II. Arbitrary magnetic field case", *Astron. Astrophys.*, **328**, 726–751. [URL]

Bommier, V., 2012, "Hanle effect from a dipolar magnetic structure: the case of the solar corona and the case of a star", *Astron. Astrophys.*, **539**, A122 (7 pages). [DOI], [URL]

Bommier, V., 2016a, "Master equation theory applied to the redistribution of polarized radiation in the weak radiation field limit. III. Theory for the multilevel atom", *Astron. Astrophys.*, **591**, A59 (13 pages). [DOI], [URL]

Bommier, V., 2016b, "Master equation theory applied to the redistribution of polarized radiation in the weak radiation field limit. IV. Application to the second solar spectrum of the Na I D1 and D2 lines", *Astron. Astrophys.*, **591**, A60 (11 pages). [DOI], [URL]

Bommier, V., 2017, "Master equation theory applied to the redistribution of polarized radiation in the weak radiation field limit. V. The two-term atom", *Astron. Astrophys.*, **607**, A50 (15 pages). [DOI], [URL], [arXiv:1708.05579 [astro-ph.SR]]

Bommier, V. and Sahal-Bréchot, S., 1978, "Quantum theory of the Hanle effect: calculations of the Stokes parameters of the D_3 helium line for quiescent prominences.", *Astron. Astrophys.*, **69**, 57–64. [URL]

Bommier, V. and Sahal-Bréchot, S., 1982, "The Hanle Effect of the Coronal Lα Line of Hydrogen - Theoretical Investigation", *Solar Phys.*, **78**, 157–178. [DOI], [URL]

Bommier, V. and Stenflo, J. O., 1999, "Partial frequency redistribution with Hanle and Zeeman effects. Non-perturbative classical theory", *Astron. Astrophys.*, **350**, 327–333. [URL]

Bommier, V., Sahal-Bréchot, S. and Leroy, J. L., 1986, "The linear polarization of hydrogen H-beta radiation and the joint diagnostic of magnetic field vector and electron density in quiescent prominences. I - The magnetic field. II - The electron density", *Astron. Astrophys.*, **156**, 79–94. [URL]

Bommier, V., Derouich, M., Landi Degl'Innocenti, E., Molodij, G. and Sahal-Bréchot, S., 2005, "Interpretation of second solar spectrum observations of the Sr I 4607 Å line in a quiet region: Turbulent magnetic field strength determination", *Astron. Astrophys.*, **432**, 295–305. [DOI], [URL]

Campbell, W. W. and Moore, J. H., 1919, "The spectrum of the solar corona", *Lick Observatory Bulletin*, **10**, 8–14. [DOI], [URL]

Cannon, C. J., 1973, "Frequency-Quadrature Perturbations in Radiative-Transfer Theory", *Astrophys. J.*, **185**, 621–630. [DOI], [URL]

Carlin, E. S. and Asensio Ramos, A., 2015, "Chromospheric Diagnosis with Ca II Lines: Forward Modeling in Forward Scattering. I", *Astrophys. J.*, **801**, 16 (15 pages). [DOI], [URL], [arXiv:1412.5386 [astro-ph.SR]]

Carlin, E. S., Manso Sainz, R., Asensio Ramos, A. and Trujillo Bueno, J., 2012, "Scattering Polarization in the Ca II Infrared Triplet with Velocity Gradients", *Astrophys. J.*, **751**, 5 (13 pages). [DOI], [URL], [arXiv:1203.4438 [astro-ph.SR]]

Carlin, E. S., Asensio Ramos, A. and Trujillo Bueno, J., 2013, "Temporal Evolution of the Scattering Polarization of the Ca II IR Triplet in Hydrodynamical Models of the Solar Chromosphere", *Astrophys. J.*, **764**, 40 (12 pages). [DOI], [URL], [arXiv:1210.1525 [astro-ph.SR]]

Casini, R. and Judge, P. G., 1999, "Spectral Lines for Polarization Measurements of the Coronal Magnetic Field. II. Consistent Treatment of the Stokes Vector for Magnetic-Dipole Transitions", *Astrophys. J.*, **522**, 524–539. [DOI], [URL]

Casini, R. and Lin, H., 2002, "A Classical Model for the Damped, Magnetic Dipole Oscillator", *Astrophys. J.*, **571**, 540–544. [DOI], [URL]

Casini, R. and Manso Sainz, R., 2016a, "Frequency Redistribution of Polarized Light in the Λ-Type Multi-Term Polarized Atom", *Astrophys. J.*, **824**, 135 (11 pages). [DOI], [URL], [arXiv:1602.07173 [astro-ph.SR]]

Casini, R. and Manso Sainz, R., 2016b, "Laboratory Frequency Redistribution Function for the Polarized Λ -type Three-term Atom", *Astrophys. J.*, **833**, 197 (11 pages). [DOI], [URL], [arXiv:1612.04362 [astro-ph.GA]]

Casini, R., Landi Degl'Innocenti, M., Manso Sainz, R., Landi Degl'Innocenti, E. and Landolfi, M., 2014, "Frequency Redistribution Function for the Polarized Two-term Atom", *Astrophys. J.*, **791**, 94 (17 pages). [DOI], [URL], [arXiv:1406.6129 [astro-ph.SR]]

Cassinelli, J. P. and Hummer, D. G., 1971, "Radiative transfer in spherically symmetric systems-II. The non-conservative case and linearly polarized radiation", *Mon. Not. Roy. Astron. Soc.*, **154**, 9–21. [DOI], [URL]

Cernicharo, J., Goicoechea, J. R., Pardo, J. R. and Asensio-Ramos, A., 2006, "Warm Water Vapor around Sagittarius B2", *Astrophys. J.*, **642**, 940–953. [DOI], [URL], [arXiv:astro-ph/0601336 [astro-ph]]

Chandrasekhar, S., 1934, "On the hypothesis of the radial ejection of high-speed atoms for the Wolf-Rayet stars and the novae", *Mon. Not. Roy. Astron. Soc.*, **94**, 522–538. [DOI], [URL]

Chandrasekhar, S., 1945a, "The Radiative Equilibrium of an Expanding Planetary Nebula. I. Radiation Pressure in Lyman-α.", *Astrophys. J.*, **102**, 402–428. [DOI], [URL]

Chandrasekhar, S., 1945b, "The Formation of Absorption Lines in a Moving Atmosphere", *Reviews of Modern Physics*, **17**, 138–156. [DOI], [URL]

Chandrasekhar, S., 1946a, "On the Radiative Equilibrium of a Stellar Atmosphere. X.", *Astrophys. J.*, **103**, 351–370. [DOI], [URL]

Chandrasekhar, S., 1946b, "On the Radiative Equilibrium of a Stellar Atmosphere. XI.", *Astrophys. J.*, **104**, 110–132. [DOI], [URL]

Chandrasekhar, S., 1947, "On the Radiative Equilibrium of a Stellar Atmosphere. XV.", *Astrophys. J.*, **105**, 424–434. [DOI], [URL]

Chandrasekhar, S., 1950, *Radiative Transfer*, Clarendon Press, Oxford, first edn.

Chapman, R. D., 1966, "Radiative Transfer in Extended Stellar Atmospheres", *Astrophys. J.*, **143**, 61–74. [DOI], [URL]

Charvin, P., 1965, "Étude de la polarisation des raies interdites de la couronne solaire. Application au cas de la raie verte λ 5303", *Annales d'Astrophysique*, **28**, 877–934. [URL]

Chevallier, L., Paletou, F. and Rutily, B., 2003, "On the accuracy of the ALI method for solving the radiative transfer equation", *Astron. Astrophys.*, **411**, 221–227. [DOI], [URL], [arXiv:astro-ph/0601341 [astro-ph]]

Collett, E., 1993, *Polarized Light: Fundamentals and Applications*, Marcel Dekker, Inc., New York, first edn.

Daniel, F. and Cernicharo, J., 2008, "Solving radiative transfer with line overlaps using Gauss-Seidel algorithms", *Astron. Astrophys.*, **488**, 1237–1247. [DOI], [URL], [arXiv:0807.1845 [astro-ph]]

de la Chevrotière, A., St-Louis, N., Moffat, A. F. J. and MiMeS Collaboration, 2014, "Searching for Magnetic Fields in 11 Wolf-Rayet Stars: Analysis of Circular Polarization Measurements from ESPaDOnS", *Astrophys. J.*, **781**, 73 (20 pages). [DOI], [URL]

de Wijn, A. G., Socas-Navarro, H. and Vitas, N., 2017, "First Detection of Sign-reversed Linear Polarization from the Forbidden [O I] 630.03 nm Line", *Astrophys. J.*, **836**, 29 (4 pages). [DOI], [URL], [arXiv:1701.08793 [astro-ph.SR]]

del Pino Alemán, T., Casini, R. and Manso Sainz, R., 2016, "Magnetic Diagnostics of the Solar Chromosphere with the Mg II h-k Lines", *Astrophys. J. Lett.*, **830**, L24 (6 pages). [DOI], [URL], [arXiv:1607.05683 [astro-ph.SR]]

del Pino Alemán, T., Trujillo Bueno, J., Casini, R. and Manso Sainz, R., 2020, "The Magnetic Sensitivity of the Resonance and Subordinate Lines of Mg II in the Solar Chromosphere", *Astrophys. J.*, **891**, 91 (15 pages). [DOI], [URL]

Derouich, M., Auchère, F., Vial, J. C. and Zhang, M., 2010, "Hanle signatures of the coronal magnetic field in the linear polarization of the hydrogen Lα line", *Astron. Astrophys.*, **511**, A7 (7 pages). [DOI], [URL], [arXiv:0912.5068 [astro-ph.SR]]

Dima, G., Kuhn, J. and Berdyugina, S., 2016, "Infrared Dual-line Hanle diagnostic of the Coronal Vector Magnetic Field", *Frontiers in Astronomy and Space Sciences*, **3**, 13 (9 pages). [DOI], [URL]

Domke, H. and Hubeny, I., 1988, "Scattering of Polarized Light in Spectral Lines with Partial Frequency Redistribution: General Redistribution Matrix", *Astrophys. J.*, **334**, 527–538. [DOI], [URL]

Dopita, M. A., Seitenzahl, I. R., Sutherland, R. S., Vogt, F. P. A., Winkler, P. F. and Blair, W. P., 2016, "Forbidden Iron Lines and Dust Destruction in Supernova Remnant Shocks: The Case of N49 in the Large Magellanic Cloud", *Astrophys. J.*, **826**, 150-164. [DOI], [URL], [arXiv:1605.02385 [astro-ph.GA]]

Doschek, G. A., Warren, H. P., Laming, J. M., Mariska, J. T., Wilhelm, K., Lemaire, P., Schühle, U. and Moran, T. G., 1997, "Electron Densities in the Solar Polar Coronal Holes from Density-Sensitive Line Ratios of Si VIII and S X", *Astrophys. J. Lett.*, **482**, L109–L112. [DOI], [URL]

Dumont, S., Omont, A., Pecker, J. C. and Rees, D., 1977, "Resonance line polarization: the line core.", *Astron. Astrophys.*, **54**, 675–681. [URL]

Fabiani Bendicho, P. and Trujillo Bueno, J., 1999, "Three-dimensional radiative transfer with multilevel atoms", in *Solar Polarization*, (Eds.) Nagendra, K. N., Stenflo, J. O., Astrophysics and Space Science Library, **243**, 219-230, Kluwer Academic Publishers, Boston, Mass. [DOI], [URL]

Fabiani Bendicho, P., Trujillo Bueno, J. and Auer, L., 1997, "Multidimensional radiative transfer with multilevel atoms. II. The non-linear multigrid method.", *Astron. Astrophys.*, **324**, 161–176. [URL]

Faurobert, M., 1987, "Linear polarization of resonance lines in the absence of magnetic fields. I - Slabs of finite optical thickness", *Astron. Astrophys.*, **178**, 269–276. [URL]

Faurobert, M., 1988, "Linear polarization of resonance lines in the absence of magnetic fields. II - Semi-infinite atmospheres", *Astron. Astrophys.*, **194**, 268–278. [URL]

Faurobert, M., Arnaud, J., Vigneau, J. and Frisch, H., 2001, "Investigation of weak solar magnetic fields. New observational results for the Sr I 460.7 nm linear polarization and radiative transfer modeling", *Astron. Astrophys.*, **378**, 627–634. [DOI], [URL]

Faurobert, M., Derouich, M., Bommier, V. and Arnaud, J., 2009, "Hanle effect in the solar Ba II D2 line: a diagnostic tool for chromospheric weak magnetic fields", *Astron. Astrophys.*, **493**, 201–206. [DOI], [URL], [arXiv:0811.1180 [astro-ph]]

Faurobert-Scholl, M., 1991, "Hanle effect with partial frequency redistribution. I. Numerical methods and first applications.", *Astron. Astrophys.*, **246**, 469–480. [URL]

Faurobert-Scholl, M., 1992, "Hanle effect with partial frequency redistribution. II - Linear polarization of the solar CA I 4227 A line", *Astron. Astrophys.*, **258**, 521–534. [URL]

Faurobert-Scholl, M., 1993, "Investigation of microturbulent magnetic fields in the solar photosphere by their Hanle effect in the Sr I 4607 angstroms line.", *Astron. Astrophys.*, **268**, 765–774. [URL]

Faurobert-Scholl, M., 1996, "Diagnostics with the Hanle Effect", *Solar Phys.*, **164**, 79–90. [DOI], [URL]

Faurobert-Scholl, M., Frisch, H. and Nagendra, K. N., 1997, "An operator perturbation method for polarized line transfer. I. Non-magnetic regime in 1D media.", *Astron. Astrophys.*, **322**, 896–910. [URL]

Ferrière, K., 2009, "Interstellar magnetic fields in the Galactic center region", *Astron. Astrophys.*, **505**, 1183–1198. [DOI], [URL], [arXiv:0908.2037 [astro-ph.GA]]

Fluri, D. M., Nagendra, K. N. and Frisch, H., 2003, "An operator perturbation method for polarized line transfer. VI. Generalized PALI method for Hanle effect with partial frequency redistribution and collisions", *Astron. Astrophys.*, **400**, 303–317. [DOI], [URL]

Frisch, H., 1988, "Radiative Transfer with Frequency Redistribution - Asymptotic methods scaling laws and approximate solutions", in *Saas-Fee Advanced Course 18: Radiation in Moving Gaseous Media*, p. 339, Geneva Observatory, Switzerland. [URL]

Frisch, H., 1996, "Partial Frequency Redistribution of Polarized Radiation", *Solar Phys.*, **164**, 49–66. [DOI], [URL]

Frisch, H., 2007, "The Hanle effect. Decomposition of the Stokes parameters into irreducible components", *Astron. Astrophys.*, **476**, 665–674. [DOI], [URL]

Frisch, H., Faurobert, M. and Nagendra, K. N., 2001, "The Hanle Effect with Angle Dependent Redistribution Functions", in *Advanced Solar Polarimetry – Theory, Observation, and Instrumentation*, (Ed.) Sigwarth, M., Astronomical Society of the Pacific Conference Series, **236**, pp. 197–204, Astronomical Society of the Pacific, San Francisco. [URL]

Frisch, H., Anusha, L. S., Sampoorna, M. and Nagendra, K. N., 2009, "The Hanle effect in a random magnetic field. Dependence of the polarization on statistical properties of the magnetic field", *Astron. Astrophys.*, **501**, 335–347. [DOI], [URL]

Gandorfer, A., 2000, *The Second Solar Spectrum: A high spectral resolution polarimetric survey of scattering polarization at the solar limb in graphical representation. Volume I: 4625 Å to 6995 Å*, vdf Hochschuverlag, Zürich

Gandorfer, A., 2002, *The Second Solar Spectrum: A high spectral resolution polarimetric survey of scattering polarization at the solar limb in graphical representation. Volume II: 3910 Å to 4630 Å*, vdf Hochschuverlag, Zürich. [URL]

Gandorfer, A., 2005, *The Second Solar Spectrum: A high spectral resolution polarimetric survey of scattering polarization at the solar limb in graphical representation. Volume I: 3160 Å to 3915 Å*, vdf Hochschuverlag, Zürich

Gelfreikh, G. B., 1994, "Radio Measurements of Coronal Magnetic Fields", in *IAU Colloq. 144: Solar Coronal Structures*, (Eds.) Rusin, V., Heinzel, P., Vial, J.-C., 21-28, VEDA Publishing Company, Bratislava, Slovakia. [URL]

Gibson, S., Kucera, T., White, S., Dove, J., Fan, Y., Forland, B., Rachmeler, L., Downs, C. and Reeves, K., 2016, "FORWARD: A toolset for multiwavelength coronal magnetometry", *Frontiers in Astronomy and Space Sciences*, **3**, 8-29. [DOI], [URL]

Gouttebroze, P., 1990, "Radiative transfer in cylindrical objects by the discrete ordinate method", *Astron. Astrophys.*, **228**, 295–298. [URL]

Gouttebroze, P., 2004, "Radiative transfer in cylindrical threads with incident radiation", *Astron. Astrophys.*, **413**, 733–743. [DOI], [URL]

Gouttebroze, P., 2005, "Radiative transfer in cylindrical threads with incident radiation. II. 2D azimuth-dependent case", *Astron. Astrophys.*, **434**, 1165–1171. [DOI], [URL]

Gouttebroze, P., Vial, J. C. and Tsiropoula, G., 1986, "Emission of Lyman alpha radiation by solar coronal loops. I - General synopsis", *Astron. Astrophys.*, **154**, 154–170. [URL]

Grant, L. P. and Peraiah, A., 1972, "Spectral line formation in extended stellar atmospheres", *Mon. Not. Roy. Astron. Soc.*, **160**, 239–247. [DOI], [URL]

Grotrian, W., 1939, "Zur Frage der Deutung der Linien im Spektrum der Sonnenkorona", *Naturwissenschaften*, **27**, 214–214. [DOI], [URL]

Habbal, S. R., Druckmüller, M., Morgan, H., Daw, A., Johnson, J., Ding, A., Arndt, M., Esser, R., Rušin, V. and Scholl, I., 2010, "Mapping the Distribution of Electron Temperature and Fe Charge States in the Corona with Total Solar Eclipse Observations", *Astrophys. J.*, **708**, 1650–1662. [DOI], [URL]

Habbal, S. R., Druckmüller, M., Morgan, H., Ding, A., Johnson, J., Druckmüllerová, H., Daw, A., Arndt, M. B., Dietzel, M. and Saken, J., 2011, "Thermodynamics of the Solar Corona and Evolution of the Solar Magnetic Field as Inferred from the Total Solar Eclipse Observations of 2010 July 11", *Astrophys. J.*, **734**, 120 (18 pages). [DOI], [URL]

Hackbush, W., 1985, *Multi-Grid Methods and Applications*, Springer, Germany, first edn.

Hale, G. E., 1908, "On the Probable Existence of a Magnetic Field in Sun-Spots", *Astrophys. J.*, **28**, 315–343. [DOI], [URL]

Hamann, W. R., 2003, "Basic ALI in Moving Atmospheres", in *Stellar Atmosphere Modeling*, (Eds.) Hubeny, I., Mihalas, D., Werner, K., Astronomical Society of the Pacific Conference Series, **288**, pp. 171–184, Astronomical Society of the Pacific, San Francisco, CA. [URL]

Hanle, W., 1923, "Über den Zeemaneffekt bei der Resonanzfluoreszenz", *Naturwissenschaften*, **11**, 690–691. [DOI], [URL]

Hanle, W., 1924, "Über magnetische Beeinflussung der Polarisation der Resonanzfluoreszenz", *Zeitschrift für Physik*, **30**, 93–105. [DOI], [URL]

Hanle, W., 1925, "Die magnetische Beeinflussung der Resonanzfluoreszenz", *Ergebnisse der exakten naturwissenschaften*, **4**, 214–232. [URL]

Hauschildt, P. H., 1992, "A fast operator perturbation method for the solution of the special relativistic equation of radiative transfer in spherical symmetry.", *J. Quantitative Spectroscopy and Radiative Transfer*, **47**, 433–453. [DOI], [URL]

Hauschildt, P. H. and Baron, E., 2004, "Improved discretization of the wavelength derivative term in CMF operator splitting numerical radiative transfer", *Astron. Astrophys.*, **417**, 317–324. [DOI], [URL], [arXiv:astro-ph/0401164 [astro-ph]]

Hauschildt, P. H. and Baron, E., 2009, "A 3D radiative transfer framework. IV. Spherical and cylindrical coordinate systems", *Astron. Astrophys.*, **498**, 981–985. [DOI], [URL], [arXiv:0903.1949 [astro-ph.IM]]

Hauschildt, P. H. and Wehrse, R., 1991, "Solution of the special relativistic equation of radiative transfer in rapidly expanding spherical shells.", *J. Quantitative Spectroscopy and Radiative Transfer*, **46**, 81–98. [DOI], [URL]

Hauschildt, P. H., Best, M. and Wehrse, R., 1991, "Relativistic effects in supernova photospheres", *Astron. Astrophys.*, **247**, L21–L24. [URL]

Hauschildt, P. H., Störzer, H. and Baron, E., 1994, "Convergence properties of the accelerated Λ-iteration method for the solution of radaitive transfer problems.", *J. Quantitative Spectroscopy and Radiative Transfer*, **51**, 875–891. [DOI], [URL]

Heinzel, P., 1981, "Non-coherent scattering in subordinate lines: a unified approach to redistribution functions", *J. Quantitative Spectroscopy and Radiative Transfer*, **25**, 483–499. [DOI], [URL]

Heinzel, P. and Hubeny, I., 1982, "Non-coherent scattering in subordinate lines: II. Collisional redistribution", *J. Quantitative Spectroscopy and Radiative Transfer*, **27**, 1–14. [DOI], [URL]

Heinzel, P. and Hubeny, I., 1983, "Non-coherent scattering in subordinate lines: IV. Angle-averaged redistribution functions.", *J. Quantitative Spectroscopy and Radiative Transfer*, **30**, 77–88. [DOI], [URL]

Hillier, D. J., 1996, "The calculation of line polarization due to scattering by electrons in multi-scattering axisymmetric envelopes.", *Astron. Astrophys.*, **308**, 521–534. [URL]

House, L. L., 1972, "Coronal Emission Line Polarization", *Solar Phys.*, **23**, 103–119. [DOI], [URL]

House, L. L., 1977, "Coronal emission-line polarization from the statistical equilibrium of magnetic sublevels. I. Fe XIII.", *Astrophys. J.*, **214**, 632–652. [DOI], [URL]

Hubeny, I., 1982, "Non-coherent scattering in subordinate lines: III. Generalized redistribution functions", *J. Quantitative Spectroscopy and Radiative Transfer*, **27**, 593–609. [DOI], [URL]

Hubeny, I., 1985, "General aspects of partial redistribution and its astrophysical importance.", in *Progress in stellar spectral line formation theory*, (Eds.) Beckman, J. E., Crivellari, L., NATO Advanced Science Institutes (ASI) Series C, **152**, pp. 27–58, D. Reidel Publishing Co., Dordrecht. [URL]

Hubeny, I., 1992, "Accelerated Lambda Iteration", in *The Atmospheres of Early-Type Stars*, (Eds.) Heber, U., Jeffery, C. S., **401**, pp. 375–392, Springer-Verlag, Berlin, Heidelberg. [DOI], [URL]

Hubeny, I., 2003, "Accelerated Lambda Iteration: An Overview", in *Stellar Atmosphere Modeling*, (Eds.) Hubeny, I., Mihalas, D., Werner, K., Astronomical Society of the Pacific Conference Series, **288**, pp. 17–34, Astronomical Society of the Pacific, San Francisco, CA. [URL]

Hubeny, I. and Cooper, J., 1986, "Redistribution of Radiation in the Presence of Velocity-changing Collisions", *Astrophys. J.*, **305**, 852–862. [DOI], [URL]

Hubeny, I. and Heinzel, P., 1984, "Non-coherent scattering in subordinate lines - V. Solutions of the transfer problem.", *J. Quantitative Spectroscopy and Radiative Transfer*, **32**, 159–168. [DOI], [URL]

Hubeny, I. and Lites, B. W., 1995, "Partial Redistribution in Multilevel Atoms. I. Method and Application to the Solar Hydrogen Line Formation", *Astrophys. J.*, **455**, 376–388. [DOI], [URL]

Hubeny, I. and Mihalas, D., 2014, *Theory of Stellar Atmospheres: An Introduction to Astrophysical Non-equilibrium Quantitative Spectroscopic Analysis*, Princeton University Press, Princeton, New Jersey, first edn.

Hubeny, I., Oxenius, J. and Simonneau, E., 1983a, "Absorption and emission line profile coefficients of multilevel atoms - I. Atomic profile coefficients.", *J. Quantitative Spectroscopy and Radiative Transfer*, **29**, 477–493. [DOI], [URL]

Hubeny, I., Oxenius, J. and Simonneau, E., 1983b, "Absorption and emission line profile coefficients of multilevel atoms - II. Velocity-averaged profile coefficients", *J. Quantitative Spectroscopy and Radiative Transfer*, **29**, 495–506. [DOI], [URL]

Hummer, D. G., 1962, "Non-coherent scattering: I. The redistribution function with Doppler broadening", *Mon. Not. Roy. Astron. Soc.*, **125**, 21–37. [DOI], [URL]

Hummer, D. G. and Rybicki, G. B., 1971, "Radiative transfer in spherically symmetric systems. The conservative grey case", *Mon. Not. Roy. Astron. Soc.*, **152**, 1–19. [DOI], [URL]

Hummer, D. G., Kunasz, C. V. and Kunasz, P. B., 1973, "Numerical evaluation of the formal solution of radiative transfer problems in spherical geometries.", *Computer Physics Communications*, **6**, 38–57. [DOI], [URL]

Hyder, C. L., 1965, "The Polarization of Emission Lines in Astronomy. III. The Polarization of Coronal Emission Lines.", *Astrophys. J.*, **141**, 1382–1389. [DOI], [URL]

Ignace, R., 2001, "The Hanle Effect as a Diagnostic of Magnetic Fields in Stellar Envelopes. III. Including the Finite Star Depolarization Effect", *Astrophys. J.*, **547**, 393–401. [DOI], [URL]

Ignace, R. and Brimeyer, A., 2006, "Models of forbidden line emission profiles from axisymmetric stellar winds", *Mon. Not. Roy. Astron. Soc.*, **371**, 343–355. [DOI], [URL], [arXiv:astro-ph/0605259 [astro-ph]]

Ignace, R., Nordsieck, K. H. and Cassinelli, J. P., 1997, "The Hanle Effect as a Diagnostic of Magnetic Fields in Stellar Envelopes. I. Theoretical Results for Integrated Line Profiles", *Astrophys. J.*, **486**, 550–570. [DOI], [URL]

Ignace, R., Hole, K. T., Cassinelli, J. P. and Henson, G. D., 2011, "Time-dependent behavior of linear polarization in unresolved photospheres, with applications for the Hanle effect", *Astron. Astrophys.*, **530**, A82 (5 pages). [DOI], [URL], [arXiv:1103.4155 [astro-ph.IM]]

Inoue, S., 2016, "Magnetohydrodynamics modeling of coronal magnetic field and solar eruptions based on the photospheric magnetic field", *Progress in Earth and Planetary Science*, **3**, 19 (28 pages). [DOI], [URL]

Ivanov, V. V., 1991, "Analytical methods of line formation theory - Are they still alive", in *Stellar atmospheres: Beyond classical models*, (Eds.) Crivellari, L., Hubeny, I., Hummer, D. G., NATO ASI Ser. C, **341**, p. 81, Kluwer Academic Publishers, Dordrecht

Jefferies, J., Lites, B. W. and Skumanich, A., 1989, "Transfer of Line Radiation in a Magnetic Field", *Astrophys. J.*, **343**, 920–935. [DOI], [URL]

Jess, D. B., Reznikova, V. E., Ryans, R. S. I., Christian, D. J., Keys, P. H., Mathioudakis, M., Mackay, D. H., Krishna Prasad, S., Banerjee, D., Grant, S. D. T., Yau, S. and Diamond, C., 2016, "Solar coronal magnetic fields derived using seismology techniques applied to omnipresent sunspot waves", *Nature Physics*, **12**, 179–185. [DOI], [URL], [arXiv:1605.06112 [astro-ph.SR]]

Jones, R. C., 1941, "New calculus for the treatment of optical systems. I. Description and discussion of the calculus", *Journal of the Optical Society of America*, **31**, 488–493. [DOI], [URL]

Judge, P. G., 1998, "Spectral Lines for Polarization Measurements of the Coronal Magnetic Field. I. Theoretical Intensities", *Astrophys. J.*, **500**, 1009–1022. [DOI], [URL]

Judge, P. G. and Casini, R., 2001, "A Synthesis Code for Forbidden Coronal Lines", in *Advanced Solar Polarimetry – Theory, Observation, and Instrumentation*, (Ed.) Sigwarth, M., Astronomical Society of the Pacific Conference Series, **236**, pp. 503–510, Astronomical Society of the Pacific, San Francisco. [URL]

Judge, P. G., Casini, R., Tomczyk, S., Edwards, D. P. and Francis, E., 2001, "Coronal Magnetometry: A Feasibility Study", pp. 1–79, NASA STI/Recon Technical Report N, High Altitude Observatory, Boulder. [URL]

Kazantsev, S. A., 1983, "REVIEWS OF TOPICAL PROBLEMS: Astrophysical and laboratory applications of self-alignment", *Soviet Physics Uspekhi*, **26**, 328–351. [DOI], [URL]

Kosirev, N. A., 1934, "Radiative equilibrium of the extended photosphere", *Mon. Not. Roy. Astron. Soc.*, **94**, 430–443. [DOI], [URL]

Kramar, M., Lin, H. and Tomczyk, S., 2016, "Direct Observation of Solar Coronal Magnetic Fields by Vector Tomography of the Coronal Emission Line Polarizations", *Astrophys. J. Lett.*, **819**, L36 (6 pages). [DOI], [URL], [arXiv:1502.07200 [astro-ph.SR]]

Kraus, M., Borges Fernandes, M. and de Araújo, F. X., 2010, "Neutral material around the B[e] supergiant star LHA 115-S 65. An outflowing disk or a detached Keplerian rotating disk?", *Astron. Astrophys.*, **517**, A30 (13 pages). [DOI], [URL], [arXiv:1005.4511 [astro-ph.SR]]

Kunasz, P. B. and Hummer, D. G., 1974a, "Radiative transfer in spherically symmetric systems-III. Fundamentals of line formation", *Mon. Not. Roy. Astron. Soc.*, **166**, 19–56. [DOI], [URL]

Kunasz, P. B. and Hummer, D. G., 1974b, "Radiative transfer in spherically symmetric systems-IV. Solution of the line transfer problem with radial velocity fields", *Mon. Not. Roy. Astron. Soc.*, **166**, 57–78. [DOI], [URL]

Landi Degl'Innocenti, E., 1982, "The determination of vector magnetic fields in prominences from the observations of the Stokes profiles in the D3 line of helium", *Solar Phys.*, **79**, 291–322. [DOI], [URL]

Landi Degl'Innocenti, E., 1983a, "Polarization in Spectral Lines: II A Classification Scheme for Solar Observations", *Solar Phys.*, **85**, 33–40. [DOI], [URL]

Landi Degl'Innocenti, E., 1983b, "Polarization in spectral lines I: A Unifying Theoretical Approach", *Solar Phys.*, **85**, 3–31. [DOI], [URL]

Landi Degl'Innocenti, E., 1984, "Polarization in Spectral Lines III: Resonance Polarization in the Non-Magnetic, Collisionless Regime", *Solar Phys.*, **91**, 1–26. [DOI], [URL]

Landi Degl'Innocenti, E., 1985, "Polarization in spectral lines. IV: Resonance polarization in the Hanle effect, collisionless regime.", *Solar Phys.*, **102**, 1–20. [DOI], [URL]

Landi Degl'Innocenti, E., 1987, "Transfer of Polarized Radiation, using 4 x 4 Matrices", in *Numerical Radiative Transfer*, (Ed.) Kalkofen, W., pp. 265–278, Cambridge University Press, Cambridge, UK. [URL]

Landi Degl'Innocenti, E., 2002, "The physics of polarization", in *Astrophysical Spectropolarimetry*, (Eds.) Trujillo-Bueno, J., Moreno-Insertis, F., Sánchez, F., pp. 1–53, Cambridge University Press, Cambridge, UK. [URL]

Landi Degl'Innocenti, E. and Landolfi, M., 2004, *Polarization in Spectral Lines*, Kluwer Academic Publishers, Dordrecht, The Netherlands (LL04), first edn.

Landi Degl'Innocenti, E., Bommier, V. and Sahal-Bréchot, S., 1987, "Linear polarization of hydrogen Balmer lines in optically thick quiescent prominences", *Astron. Astrophys.*, **186**, 335–353. [URL]

Landi Degl'Innocenti, E., Bommier, V. and Sahal-Bréchot, S., 1991, "Resonance line polarization for arbitrary magnetic fields in optically thick media. I - Basic formalism for a 3-dimensional medium.", *Astron. Astrophys.*, **244**, 391–400. [URL]

Landi Degl'Innocenti, E., Landi Degl'Innocenti, M. and Landolfi, M., 1997, "Density matrix and polarized radiative transfer : A heuristic approach to the problem of frequency redistribution", in *Science with THÉMIS*, (Eds.) Mein, N, Sahal-Bréchot, S., Proc. Forum THÉMIS, p. 59, Obs. Paris-Meudon, Paris

Landi Degl'Innocenti, M. and Landi Degl'Innocenti, E., 1988, "An analytical expression for the Hanle-effect scattering phase matrix", *Astron. Astrophys.*, **192**, 374–378. [URL]

Landstreet, J. D., 2015, "Surface magnetic fields across the HR Diagram", in *Polarimetry: From the Sun to Stars and Stellar Environments*, (Eds.) Nagendra, K. N., Bagnulo, S., Centeno, R., Martínez González, M. J., IAU Symposium, **305**, pp. 12–21, Cambridge University Press, Cambridge. [DOI], [URL]

Léger, L., Chevallier, L. and Paletou, F., 2007, "Fast 2D non-LTE radiative modelling of prominences. Numerical methods and benchmark results", *Astron. Astrophys.*, **470**, 1–9. [DOI], [URL], [arXiv:astro-ph/0703689 [astro-ph]]

Leroy, J. L., 1977, "On the intensity of magnetic field in quiescent prominences.", *Astron. Astrophys.*, **60**, 79–84. [URL]

Leroy, J. L., 1985, "The Hanle effect applied to magnetic field measurements", in *Measurements of Solar Vector Magnetic Fields*, (Ed.) Hagyard, M. J., **2374**, pp. 121–140, NASA Conference Publication, NASA Marshall Space Flight Center. [URL]

Leroy, J. L., Ratier, G. and Bommier, V., 1977, "The polarization of the D3 emission line in prominences.", *Astron. Astrophys.*, **54**, 811–816. [URL]

Leroy, J. L., Bommier, V. and Sahal-Bréchot, S., 1983, "The Magnetic Field in the Prominences of the Polar Crown", *Solar Phys.*, **83**, 135–142. [DOI], [URL]

Li, H., Landi Degl'Innocenti, E. and Qu, Z., 2017, "Polarization of Coronal Forbidden Lines", *Astrophys. J.*, **838**, 69 (15 pages). [DOI], [URL]

Lin, H. and Casini, R., 2000, "A Classical Theory of Coronal Emission Line Polarization", *Astrophys. J.*, **542**, 528–534. [DOI], [URL]

Lin, H., Penn, M. J. and Tomczyk, S., 2000, "A New Precise Measurement of the Coronal Magnetic Field Strength", *Astrophys. J. Lett.*, **541**, L83–L86. [DOI], [URL]

Lin, H., Kuhn, J. R. and Coulter, R., 2004, "Coronal Magnetic Field Measurements", *Astrophys. J. Lett.*, **613**, L177–L180. [DOI], [URL]

Liu, Y. and Lin, H., 2008, "Observational Test of Coronal Magnetic Field Models. I. Comparison with Potential Field Model", *Astrophys. J.*, **680**, 1496–1507. [DOI], [URL], [arXiv:0710.3223 [astro-ph]]

Lockyer, J. N., 1866, "Spectroscopic Observations of the Sun", *Proceedings of the Royal Society of London Series I*, **15**, 256–258. [URL]

López Ariste, A., Asensio Ramos, A. and González Fernández, C., 2011, "Photospheric Hanle diagnostic of weak magnetic dipoles in stars", *Astron. Astrophys.*, **527**, A120 (5 pages). [DOI], [URL], [arXiv:1011.6288 [astro-ph.SR]]

Lyot, B., 1939, "The study of the solar corona and prominences without eclipses ", *Mon. Not. Roy. Astron. Soc.*, **99**, 580–594. [DOI], [URL]

Mackay, D. H. and Yeates, A. R., 2012, "The Sun's Global Photospheric and Coronal Magnetic Fields: Observations and Models", *Living Reviews in Solar Physics*, **9**, 6 (50 pages). [DOI], [URL], [arXiv:1211.6545 [astro-ph.SR]]

Magain, P., 1986, "Contribution functions and the depths of formation of spectral lines", *Astron. Astrophys.*, **163**, 135–139. [URL]

Manso Sainz, R. and Martínez González, M. J., 2012, "Hanle Effect for Stellar Dipoles and Quadrupoles", *Astrophys. J.*, **760**, 7 (10 pages). [DOI], [URL], [arXiv:1209.6187 [astro-ph.SR]]

Manso Sainz, R. and Trujillo-Bueno, J., 1999, "The Hanle effect in 1D, 2D and 3D", in *Solar Polarization*, (Eds.) Nagendra, K. N., Stenflo, J. O., Astrophysics and Space Science Library, **243**, pp. 143–156, Kluwer Academic Publishers, Boston, Mass. [DOI], [URL]

Manso Sainz, R. and Trujillo Bueno, J., 2003, "A Multilevel Radiative Transfer Program for Modeling Scattering Line Polarization and the Hanle Effect in Stellar Atmospheres", in *Solar Polarization*, (Eds.) Trujillo-Bueno, J., Sanchez Almeida, J., Astronomical Society of the Pacific Conference Series, **307**, pp. 251–262, Astronomical Society of the Pacific, San Francisco. [URL]

Manso Sainz, R. and Trujillo Bueno, J., 2011, "Scattering Polarization and Hanle Effect in Stellar Atmospheres with Horizontal Inhomogeneities", *Astrophys. J.*, **743**, 12 (27 pages). [DOI], [URL], [arXiv:1108.2958 [astro-ph.SR]]

Mariani, F. and Neubauer, F. M., 1990, "The Interplanetary Magnetic Field", in *Physics of the Inner Heliosphere I*, (Eds.) Schwenn, R., Marsch, E., pp. 183–206, Springer-Verlag, Berlin, Heidelberg. [URL]

McCrea, W. H., 1928, "A note on Dr. P. A. Taylor's paper "The equilibrium of the calcium chromosphere,"", *Mon. Not. Roy. Astron. Soc.*, **88**, 729–740. [DOI], [URL]

McCrea, W. H. and Mitra, K. K., 1936, "Schuster's Problem for a Moving Atmosphere", *Z. Astrophys.*, **11**, 359–378. [URL]

McKenna, S. J., 1984, "The Transfer of Polarized Radiation in Spectral Lines - Solar Type Stellar Atmospheres", *Astrophys. Space Sci.*, **106**, 283–297. [DOI], [URL]

McKenna, S. J., 1985, "The Transfer of Polarized Radiation in Spectral Lines - Formalism and Solutions in Simple Cases", *Astrophys. Space Sci.*, **108**, 31–66. [DOI], [URL]

Megha, A., Sampoorna, M., Nagendra, K. N. and Sankarasubramanian, K., 2017, "Hanle-Zeeman Scattering Matrix for Magnetic Dipole Transitions", *Astrophys. J.*, **841**, 129 (14 pages). [DOI], [URL]

Megha, A., Sampoorna, M., Nagendra, K. N. and Sankarasubramanian, K., 2018, "Coronal magnetic field measurements using forbidden emission lines", in *Long term datasets for the understanding of solar and stellar magnetic cycles*, (Eds.) Banerjee, D., Jiang, J., Kusano, K., Solanki, S., IAU Symposium, **340**, 61-62, Cambridge University Press, Cambridge. [DOI], [URL]

Megha, A., Sampoorna, M., Nagendra, K. N., Anusha, L. S. and Sankarasubramanian, K., 2019a, "Resonance Line Polarization in Spherically Symmetric Moving Media: a Parametric Study", in *Proceedings of 9th Solar Polarization workshop SPW9*, (Eds.) Gandorfer, A., Lagg, A., Raab, K., 14, MPS, Göttingen. [DOI], [URL], [arXiv:2001.06201 [astro-ph.SR]]

Megha, A., Sampoorna, M., Nagendra, K. N., Anusha, L. S. and Sankarasubramanian, K., 2019b, "Polarized Line Formation in Spherically Symmetric Atmospheres with Velocity Fields", *Astrophys. J.*, **879**, 48 (18 pages). [DOI], [URL]

Megha, A., Sampoorna, M., Nagendra, K. N., Anusha, L. S. and Sankarasubramanian, K., 2020a, "Highly Convergent Iterative Techniques for Solving Polarized Line Formation in Spherically Symmetric Atmospheres", *Astrophys. J.*, (Under preparation)

Megha, A., Sampoorna, M., Nagendra, K. N., Anusha, L. S. and Sankarasubramanian, K., 2020b, "Polarized Line Formation in Spherically Symmetric Expanding Atmospheres with Weak Field Hanle Effect", *Astrophys. J.*, (Under preparation)

Megha, A., Sampoorna, M., Nagendra, K. N. and Sankarasubramanian, K., 2020c, "Polarized Scattering Matrix for Magnetic Dipole Transitions", in *Solar Polarization 8*, (Eds.) Belluzzi, L., Trujillo Bueno, J., Casini, R., Romoli, M., (In press),

Mihalas, D., 1978, *Stellar Atmospheres*, W. H. Freeman and Company, San Francisco, second edn.

Mihalas, D., 1980, "Solution of the comoving-frame equation of transfer in spherically symmetric flows. VII - Angle-dependent partial redistribution", *Astrophys. J.*, **238**, 1034–1041. [DOI], [URL]

Mihalas, D., Kunasz, P. B. and Hummer, D. G., 1975, "Solution of the comoving-frame equation of transfer in spherically symmetric flows. I. Computational method for equivalent-two-level-atom source functions.", *Astrophys. J.*, **202**, 465–489. [DOI], [URL]

Mihalas, D., Kunasz, P. B. and Hummer, D. G., 1976a, "Solution of the Comoving-Frame Equation of Transfer in Spherically Symmetric Flows. III. Effect of Aberration and Advection Terms", *Astrophys. J.*, **206**, 515–524. [DOI], [URL]

Mihalas, D., Kunasz, P. B. and Hummer, D. G., 1976b, "Solution of the comoving-frame equation of transfer in spherically symmetric flows. IV. Frequency-dependent source functions for scattering by atoms and electrons.", *Astrophys. J.*, **210**, 419–433. [DOI], [URL]

Milić, I., 2013, "Transfer of polarized line radiation in 2D cylindrical geometry", *Astron. Astrophys.*, **555**, A130 (11 pages). [DOI], [URL]

Milić, I. and Faurobert, M., 2012, "Modeling scattering polarization in molecular solar lines in spherical geometry", *Astron. Astrophys.*, **539**, A10 (8 pages). [DOI], [URL]

Mitchell, A. C. G. and Zemansky, M. W., 1934, *Resonance radiation and excited atoms*, Cambridge University Press, Cambridge

Moruzzi, G. and Strumia, F., 1991, *The Hanle Effect and Level-Crossing Spectroscopy*, Plenum Press, New York

Mueller, H., 1948, "The foundation of optics", *Journal of the Optical Society of America*, **38**, 661–663

Nagendra, K. N., 1988, "Resonance Line Polarization in Spherical Atmospheres", *Astrophys. J.*, **335**, 269–289. [DOI], [URL]

Nagendra, K. N., 1989, "Polarization of Resonance Lines Formed in Extended Spherical Atmospheres", *Astrophys. Space Sci.*, **154**, 119–142. [DOI], [URL]

Nagendra, K. N., 1994, "Resonance Line Polarization in Spherical Atmospheres: Partial Redistribution Effects Studied with the Domke-Hubeny Redistribution Matrix", *Astrophys. J.*, **432**, 274–295. [DOI], [URL]

Nagendra, K. N., 1995, "Collisional redistribution effects on line polarization in spherical atmospheres", *Mon. Not. Roy. Astron. Soc.*, **274**, 523–543. [DOI], [URL]

Nagendra, K. N., 1996, "Partial Redistribution Effects on Line Polarization in the Presence of Velocity Fields", *Solar Phys.*, **164**, 67–78. [DOI], [URL]

Nagendra, K. N., 2003, "Numerical Solutions of Polarized Line Transfer Equations", in *Stellar Atmosphere Modeling*, (Eds.) Hubeny, I., Mihalas, D., Werner, K., Astronomical Society of the Pacific Conference Series, **288**, pp. 611–615, Astronomical Society of the Pacific, San Francisco. [URL]

Nagendra, K. N., 2014, "Partial Redistribution Theory and its Applications in the Interpretation of the Second Solar Spectrum", in *Solar Polarization 7*, (Eds.) Nagendra, K. N., Stenflo, J. O., Qu, Q., Samooprna, M., Astronomical Society of the Pacific Conference Series, **489**, pp. 179–193, Astronomical Society of the Pacific, San Francisco. [URL]

Nagendra, K. N., 2015, "On the importance of partial frequency redistribution in modeling the scattering polarization", in *Polarimetry: From the Sun to Stars and Stellar Environments*, (Eds.) Nagendra, K. N., Bagnulo, S., Centeno, R., Martínez González, M. J., IAU Symposium, **305**, pp. 351–359, Cambridge University Press, Cambridge. [DOI], [URL]

Nagendra, K. N., 2019, "Polarized Line Scattering Theory With Applications in Astrophysical Radiative Transfer: A Historical Perspective", in *Radiative Signatures from the Cosmos*, (Eds.) Werner, K., Stehle, C., Rauch, T., Lanz, T.,

Astronomical Society of the Pacific Conference Series, **519**, pp. 51–58, Astronomical Society of the Pacific, San Francisco. [URL]

Nagendra, K. N., 2020, "Polarized Line Formation: Methods and Solutions", in *Solar Polarization 8*, (Eds.) Belluzzi, L., Trujillo Bueno, J., Casini, R., Romoli, M., (In press),

Nagendra, K. N. and Sampoorna, M., 2009, "Numerical Methods in Polarized Line Formation Theory", in *Solar Polarization 5: In Honor of Jan Stenflo*, (Eds.) Berdyugina, S. V., Nagendra, K. N., Ramelli, R., Astronomical Society of the Pacific Conference Series, **405**, pp. 261–274, Astronomical Society of the Pacific, San Francisco. [URL]

Nagendra, K. N., Frisch, H. and Faurobert-Scholl, M., 1998, "An operator perturbation method for polarized line transfer. III. Applications to the Hanle effect in 1D media", *Astron. Astrophys.*, **332**, 610–628. [URL]

Nagendra, K. N., Paletou, F., Frisch, H. and Faurobert-Scholl, M., 1999, "An operator perturbation method for polarized line transfer IV: Applications to the Hanle effect with partial frequency redistribution", in *Solar Polarization*, (Eds.) Nagendra, K. N., Stenflo, J. O., Astrophysics and Space Science Library, **243**, pp. 127–142, Kluwer Academic Publishers, Boston, Mass. [DOI], [URL]

Nagendra, K. N., Frisch, H., Faurobert-Scholl, M. and Paletou, F., 2000, "An Operator Perturbation Method of Polarized Line Transfer V. Diagnosis of Solar Weak Magnetic Fields", *Journal of Astrophysics and Astronomy*, **21**, 255–258. [DOI], [URL]

Newkirk, G. J., Dupree, R. G. and Schmahl, E. J., 1970, "Magnetic Fields and the Structure of the Solar Corona. II: Observations of the 12 November 1966 Solar Corona", *Solar Phys.*, **15**, 15–39. [DOI], [URL]

Noerdlinger, P. D. and Rybicki, G. B., 1974, "Transfer of line radiation in differentially expanding atmospheres, IV: The two-level atom in plane parallel geometry solved by the Feautrier method.", *Astrophys. J.*, **193**, 651–676. [DOI], [URL]

Noerdlinger, P. D. and Scargle, J. D., 1972, "Transfer of Resonance-Line Radiation in Differentially Expanding Atmospheres. II. Analytic Solution for the Case of Coherence in the Frame of the Fluid", *Astrophys. J.*, **176**, 463–478. [DOI], [URL]

Öhman, Y., 1929, "Astronomical Consequences of the Polarization of Fluorescence,", *Mon. Not. Roy. Astron. Soc.*, **89**, 479–483. [DOI], [URL]

Olson, G. L. and Kunasz, P. B., 1987, "Short characteristic solution of the non-LTE transfer problem by operator perturbation. I. The one-dimensional planar slab.", *J. Quantitative Spectroscopy and Radiative Transfer*, **38**, 325–336. [DOI], [URL]

Olson, G. L., Auer, L. H. and Buchler, J. R., 1986, "A rapidly convergent iterative solution of the non-LTE radiation transfer problem.", *J. Quantitative Spectroscopy and Radiative Transfer*, **35**, 431–442. [DOI], [URL]

Omont, A., Smith, E. W. and Cooper, J., 1972, "Redistribution of Resonance Radiation. I. The Effect of Collisions", *Astrophys. J.*, **175**, 185–199. [DOI], [URL]

Omont, A., Smith, E. W. and Cooper, J., 1973, "Redistribution of Resonance Radiation. II. The Effect of Magnetic Fields", *Astrophys. J.*, **182**, 283–300. [DOI], [URL]

Oxenius, J., 1965, "Emission and absorption profiles in a scattering atmosphere", *J. Quantitative Spectroscopy and Radiative Transfer*, **5**, 771–781. [DOI], [URL]

Paletou, F. and Auer, L. H., 1995, "A new approximate operator method for partial frequency redistribution problems.", *Astron. Astrophys.*, **297**, 771–778. [URL]

Paletou, F. and Faurobert-Scholl, M., 1997, "An operator perturbation method for polarized line transfer. II. Resonance polarization with partial frequency redistribution effects", *Astron. Astrophys.*, **328**, 343–348. [URL]

Paletou, F. and Léger, L., 2007, "Fast multilevel radiative transfer", *J. Quantitative Spectroscopy and Radiative Transfer*, **103**, 57–66. [DOI], [URL]

Penn, M. J., 2014, "Infrared Solar Physics", *Living Reviews in Solar Physics*, **11**, 2 (66 pages). [DOI], [URL]

Peraiah, A., 1978, "Effects of partial frequency redistribution with dipole scattering on the formation of spectral lines in expanding media.", *Kodaikanal Observatory Bulletins*, **2**, 115–160. [URL]

Peraiah, A., 1984, "Discrete space theory of raidative transfer", in *Numerical Radiative Transfer*, (Ed.) Kalkofen, W., pp. 281–306, Cambridge University Press, Cambridge, UK

Peraiah, A., 2002, *An Introduction to Radiative Transfer: Methods and Applications in Astrophysics*, Cambridge University Press, Cambridge, first edn.

Peraiah, A. and Grant, I. P., 1973, "Numerical solution of the radiative transfer equation in spherical shells.", *J. Int. Math. Appl*, **12**, 75–90. [URL]

Pierce, K., 2000, *Allens Astrophysical Quantities, ed. A. N. Cox*, Springer, Newyork, fourth edn.

Plowman, J., 2014, "Single-point Inversion of the Coronal Magnetic Field", *Astrophys. J.*, **792**, 23 (8 pages). [DOI], [URL]

Povel, H., 1995, "Imaging Stokes polarimetry with piezoelastic modulators and charge-coupled-device image sensors", *Optical Engineering*, **34**, 1870–1878. [DOI], [URL]

Povel, H., Aebersold, H. and Stenflo, J. O., 1990, "Charge-coupled device image sensor as a demodulator in a 2-D polarimeter with a piezoelastic modulator", *Applied Optics*, **29**, 1186–1190. [DOI], [URL]

Querfeld, C. W., 1982, "The formation and interpretation of the Fe XIII 10747 A coronal emission line", *Astrophys. J.*, **255**, 764–773. [DOI], [URL]

Querfeld, C. W., Smartt, R. N., Bommier, V., Landi Degl'Innocenti, E. and House, L. L., 1985, "Vector Magnetic Fields in Prominences - Part Two He I D3 Stokes Profiles Analysis for Two Quiescent Prominences", *Solar Phys.*, **96**, 277–292. [DOI], [URL]

Rangarajan, K. E., 1997, "Resonance line polarization in the presence of wave motion.", *Astron. Astrophys.*, **320**, 265–272. [URL]

Raouafi, N. E., Riley, P., Gibson, S., Fineschi, S. and Solanki, S. K., 2016, "Diagnostics of Coronal Magnetic Fields Through the Hanle Effect in UV and IR Lines", *Frontiers in Astronomy and Space Sciences*, **3**, 20 (10 pages). [DOI], [URL], [arXiv:1606.08493 [astro-ph.SR]]

Rayleigh, L., 1922, "Polarisation of the Light Scattered by Mercury Vapour Near the Resonance Periodicity", *Proceedings of the Royal Society of London Series A*, **102**, 190–196. [DOI], [URL]

Rees, D. E., 1978, "Non-LTE resonance line polarization in the absence of magnetic fields.", *Pub. Astron. Soc. Japan*, **30**, 455–466. [URL]

Rees, D. E. and Saliba, G. J., 1982, "Non-LTE resonance line polarization with partial redistribution effects", *Astron. Astrophys.*, **115**, 1–7. [URL]

Reynolds, S. P., Gaensler, B. M. and Bocchino, F., 2012, "Magnetic Fields in Supernova Remnants and Pulsar-Wind Nebulae", *Space Sci. Rev.*, **166**, 231–261. [DOI], [URL], [arXiv:1104.4047 [astro-ph.GA]]

Rybicki, G. B., 1971, "A modified Feautrier method.", *J. Quantitative Spectroscopy and Radiative Transfer*, **11**, 589–595. [DOI], [URL]

Rybicki, G. B. and Hummer, D. G., 1991, "An accelerated lambda iteration method for multilevel radiative transfer.", *Astron. Astrophys.*, **245**, 171–181. [URL]

Rybicki, G. B. and Hummer, D. G., 1992, "An accelerated lambda iteration method for multilevel radiative transfer. II. Overlapping transitions with full continuum.", *Astron. Astrophys.*, **262**, 209–215. [URL]

Rybicki, G. B. and Lightman, A. P., 1979, *Radiative Processes in Astrophysics*, Wiley-Interscience Publication, New York, first edn.

Sahal-Bréchot, S., 1974, "Role of collisions in the polarization degree of the forbidden emission lines of the solar corona. II. Depolarization by electron impact and calculation of the polarization degree of the green line of Fe XIV.", *Astron. Astrophys.*, **36**, 355–363. [URL]

Sahal-Bréchot, S., 1977, "Calculation of the polarization degree of the infrared lines of Fe XIII of the solar corona.", *Astrophys. J.*, **213**, 887–899. [DOI], [URL]

Sahal-Bréchot, S., 1981, "The Hanle effect applied to magnetic field diagnostics.", *Space Sci. Rev.*, **29**, 391–401. [URL]

Sahal-Bréchot, S., Bommier, V. and Leroy, J. L., 1977, "The Hanle effect and the determination of magnetic fields in solar prominences.", *Astron. Astrophys.*, **59**, 223–231. [URL]

Sahal-Bréchot, S., Malinovsky, M. and Bommier, V., 1986, "The polarization of the O VI 1032 Å line as a probe for measuringthe coronal vector magnetic field via the Hanle effect.", *Astron. Astrophys.*, **168**, 284–300. [URL]

Saito, K., Makita, M., Nishi, K. and Hata, S., 1970, "A non-spherical axisymmetric model of the solar K corona of the minimum type", *Annals of the Tokyo Astronomical Observatory*, **12**, 51–173. [URL]

Sakurai, T. and Spangler, S. R., 1994, "The Study of Coronal Plasma Structures and Fluctuations with Faraday Rotation Measurements", *Astrophys. J.*, **434**, 773–785. [DOI], [URL]

Sampoorna, M., 2011, "m-state Interference with Partial Frequency Redistribution for Polarized Line Formation in Arbitrary Magnetic Fields", *Astrophys. J.*, **731**, 114 (13 pages). [DOI], [URL]

Sampoorna, M. and Nagendra, K. N., 2015a, "Partial Redistribution Effects on Polarized Lines Formed in Moving Media in the Presence of a Weak Magnetic Field", in *Polarimetry: From the Sun to Stars and Stellar Environments*, (Eds.) Nagendra, K. N., Bagnulo, S., Centeno, R., Martínez González, M. J., IAU Symposium, **305**, pp. 387–394, Cambridge University Press, Cambridge. [DOI], [URL]

Sampoorna, M. and Nagendra, K. N., 2015b, "Polarized Line Formation in Moving Atmospheres with Partial Frequency Redistribution and a Weak Magnetic Field", *Astrophys. J.*, **812**, 28 (18 pages). [DOI], [URL]

Sampoorna, M. and Nagendra, K. N., 2016, "Polarized Line Formation in Non-monotonic Velocity Fields", *Astrophys. J.*, **833**, 32 (10 pages). [DOI], [URL]

Sampoorna, M. and Trujillo Bueno, J., 2010, "Gauss-Seidel and Successive Over-relaxation Methods for Radiative Transfer with Partial Frequency Redistribution", *Astrophys. J.*, **712**, 1331–1344. [DOI], [URL], [arXiv:1002.4179 [astro-ph.SR]]

Sampoorna, M., Nagendra, K. N. and Stenflo, J. O., 2007a, "Hanle-Zeeman Redistribution Matrix. II. Comparison of Classical and Quantum Electrodynamic Approaches", *Astrophys. J.*, **670**, 1485–1503 (SNS07). [DOI], [URL]

Sampoorna, M., Nagendra, K. N. and Stenflo, J. O., 2007b, "Hanle-Zeeman Redistribution Matrix. I. Classical Theory Expressions in the Laboratory Frame", *Astrophys. J.*, **663**, 625–642. [DOI], [URL]

Sampoorna, M., Nagendra, K. N. and Frisch, H., 2008, "The Hanle effect with partial frequency redistribution. Construction of a frequency-dependent polarization matrix and numerical solution by a PALI method", *J. Quantitative Spectroscopy and Radiative Transfer*, **109**, 2349–2363. [DOI], [URL]

Sampoorna, M., Trujillo Bueno, J. and Landi Degl'Innocenti, E., 2010, "On the Sensitivity of Partial Redistribution Scattering Polarization Profiles to Various Atmospheric Parameters", *Astrophys. J.*, **722**, 1269–1289. [DOI], [URL], [arXiv:1008.2585 [astro-ph.SR]]

Sampoorna, M., Nagendra, K. N. and Frisch, H., 2011, "Spectral line polarization with angle-dependent partial frequency redistribution. II. Accelerated lambda iteration and scattering expansion methods for the Rayleigh scattering", *Astron. Astrophys.*, **527**, A89 (15 pages). [DOI], [URL]

Scharmer, G. B., 1983, "A Linearization Method for Solving Partial Redistribution Problems", *Astron. Astrophys.*, **117**, 83–88. [URL]

Sengupta, S., 1993, "Resonance Line Polarization in a Moving Medium - Solution in the Comoving Frame with Complete Frequency Redistribution", *Mon. Not. Roy. Astron. Soc.*, **265**, 513–523. [DOI], [URL]

Smitha, H. N., Sampoorna, M., Nagendra, K. N. and Stenflo, J. O., 2011, "Polarized Line Formation with J-state Interference in the Presence of Magnetic Fields. I. Partial Frequency Redistribution in the Collisionless Regime", *Astrophys. J.*, **733**, 4 (10 pages). [DOI], [URL]

Smitha, H. N., Sowmya, K., Nagendra, K. N., Sampoorna, M. and Stenflo, J. O., 2012, "Polarized Line Transfer with F-state Interference in a Non-magnetic Medium: Partial Frequency Redistribution Effects in the Collisionless Regime", *Astrophys. J.*, **758**, 112 (7 pages). [DOI], [URL], [arXiv:1208.6369 [astro-ph.SR]]

Smitha, H. N., Nagendra, K. N., Sampoorna, M. and Stenflo, J. O., 2013, "Polarized line formation with J-state interference in the presence of magnetic fields: A Heuristic treatment of collisional frequency redistribution", *J. Quantitative Spectroscopy and Radiative Transfer*, **115**, 46–59. [DOI], [URL], [arXiv:1209.0243 [astro-ph.SR]]

Soleillet, P., 1929, "Sur les paramètres caractérisant la polarization partielle de la lumière dans les phénomènes de fluorescence", *Annales de Physique*, **12**, 23–97

Sowmya, K., Nagendra, K. N., Sampoorna, M. and Stenflo, J. O., 2014a, "Polarized Light Scattering with the Paschen-Back Effect, Level-crossing of Fine Structure States, and Partial Frequency Redistribution", *Astrophys. J.*, **793**, 71 (9 pages). [DOI], [URL], [arXiv:1407.5457 [astro-ph.SR]]

Sowmya, K., Nagendra, K. N., Stenflo, J. O. and Sampoorna, M., 2014b, "Polarized Scattering with Paschen-Back Effect, Hyperfine Structure, and Partial Frequency Redistribution in Magnetized Stellar Atmospheres", *Astrophys. J.*, **786**, 150 (7 pages). [DOI], [URL], [arXiv:1512.07731 [astro-ph.SR]]

Sowmya, K., Nagendra, K. N., Sampoorna, M. and Stenflo, J. O., 2015, "Polarized Scattering of Light for Arbitrary Magnetic Fields with Level-crossings from the Combination of Hyperfine and Fine Structure Splittings", *Astrophys. J.*, **814**, 127 (17 pages). [DOI], [URL], [arXiv:1512.07736 [astro-ph.SR]]

Stenflo, J. O., 1976, "Resonance-line polarization. I. A non-LTE theory for the transport of polarized radiation in spectral lines in the case of zero magnetic field.", *Astron. Astrophys.*, **46**, 61–68. [URL]

Stenflo, J. O., 1978, "Resonance-line polarization. III. The Hanle effect in a compact non-LTE radiative transfer formulation.", *Astron. Astrophys.*, **66**, 241–248. [URL]

Stenflo, J. O., 1982, "The Hanle Effect and the Diagnostics of Turbulent Magnetic Fields in the Solar Atmosphere", *Solar Phys.*, **80**, 209–226. [DOI], [URL]

Stenflo, J. O., 1991, "Applications of the Hanle Effect in Solar Physics", in *The Hanle Effect and Level-Crossing Spectroscopy*, (Eds.) Moruzzi, G., Strumia, F., pp. 237–279, Plenum Press, New York. [URL]

Stenflo, J. O., 1994, *Solar Magnetic Fields*, Kluwer Academic Publishers, Dordrecht, The Netherlands (S94), first edn.

Stenflo, J. O., 1996, "Scattering Physics", *Solar Phys.*, **164**, 1–20. [DOI], [URL]

Stenflo, J. O., 1998, "Hanle-Zeeman scattering matrix", *Astron. Astrophys.*, **338**, 301–310 (S98). [URL]

Stenflo, J. O., 2002, "Polarized radiation diagnostics of solar magnetic fields", in *Astrophysical Spectropolarimetry*, (Eds.) Trujillo-Bueno, J., Moreno-Insertis, F., Sánchez, F., pp. 55–100, Cambridge University Press, Cambridge, UK. [URL]

Stenflo, J. O., 2005, "Polarization of the Sun's continuous spectrum", *Astron. Astrophys.*, **429**, 713–730. [DOI], [URL]

Stenflo, J. O., 2013, "Solar magnetic fields as revealed by Stokes polarimetry", *Astron. Astrophys. Rev.*, **21**, 66 (58 pages). [DOI], [URL], [arXiv:1309.5454 [astro-ph.SR]]

Stenflo, J. O., 2015, "Physics of Polarized Scattering at Multi-level Atomic Systems", *Astrophys. J.*, **801**, 70 (13 pages). [DOI], [URL], [arXiv:1501.02259 [astro-ph.SR]]

Stenflo, J. O., 2016, "The D_1 enigma and its physical origin", *arXiv e-prints*, arXiv:1610.09861. [URL], [arXiv:1610.09861 [physics.atom-ph]]

Stenflo, J. O., 2017, "History of Solar Magnetic Fields Since George Ellery Hale", *Space Sci. Rev.*, **210**, 5–35. [DOI], [URL], [arXiv:1508.03312 [astro-ph.SR]]

Stenflo, J. O. and Keller, C. U., 1996, "New window for spectroscopy", *Nature*, **382**, 588. [DOI], [URL]

Stenflo, J. O. and Keller, C. U., 1997, "The second solar spectrum. A new window for diagnostics of the Sun.", *Astron. Astrophys.*, **321**, 927–934. [URL]

Stenflo, J. O. and Stenholm, L., 1976, "Resonance-line polarization. II. Calculations of linear polarization in solar UV emission lines.", *Astron. Astrophys.*, **46**, 69–79. [URL]

Stenflo, J. O., Twerenbold, D. and Harvey, J. W., 1983a, "Coherent scattering in the solar spectrum - Survey of linear polarization in the range 3165-4230 A", *Astron. Astrophys. Suppl.*, **52**, 161–180. [URL]

Stenflo, J. O., Twerenbold, D., Harvey, J. W. and Brault, J. W., 1983b, "Coherent scattering in the solar spectrum - Survey of linear polarization in the range 4200-9950 A", *Astron. Astrophys. Suppl.*, **54**, 505–514. [URL]

Stokes, G. G., 1852, "On the Composition and Resolution of Streams of Polarized Light from different Sources", *Transactions of the Cambridge Philosophical Society*, **9**, 399–416. [URL]

Supriya, H. D., Nagendra, K. N., Sampoorna, M. and Ravindra, B., 2012, "The effect of electron scattering redistribution on atomic line polarization", *Mon. Not. Roy. Astron. Soc.*, **425**, 527–539. [DOI], [URL]

Trujillo Bueno, J., 1999, "Towards the modelling of the second solar spectrum", in *Solar Polarization*, (Eds.) Nagendra, K. N., Stenflo, J. O., Astrophysics and Space Science Library, **243**, pp. 73–96, Kluwer Academic Publishers, Boston. [DOI], [URL]

Trujillo Bueno, J., 2001, "Atomic Polarization and the Hanle Effect", in *Advanced Solar Polarimetry – Theory, Observation, and Instrumentation*, (Ed.) Sigwarth, M., Astronomical Society of the Pacific Conference Series, **236**, pp. 161–195, Astronomical Society of the Pacific, San Francisco. [URL]

Trujillo Bueno, J., 2020, in *Solar Polarization 8*, (Eds.) Belluzzi, L., Trujillo Bueno, J., Casini, R., Romoli, M., (In press),

Trujillo Bueno, J. and Fabiani Bendicho, P., 1995, "A Novel Iterative Scheme for the Very Fast and Accurate Solution of Non-LTE Radiative Transfer Problems", *Astrophys. J.*, **455**, 646–657. [DOI], [URL]

Trujillo Bueno, J. and Landi Degl'Innocenti, E., 1996, "The polarization-free approximation", *Solar Phys.*, **164**, 135–153. [DOI], [URL]

Trujillo Bueno, J. and Landi Degl'Innocenti, E., 1997, "Linear Polarization Due to Lower Level Depopulation Pumping in Stellar Atmospheres", *Astrophys. J. Lett.*, **482**, L183–L186. [DOI], [URL]

Trujillo Bueno, J. and Manso Sainz, R., 1999, "Iterative Methods for the Non-LTE Transfer of Polarized Radiation: Resonance Line Polarization in One-dimensional Atmospheres", *Astrophys. J.*, **516**, 436–450. [DOI], [URL]

Trujillo Bueno, J., Shchukina, N. and Asensio Ramos, A., 2004, "A substantial amount of hidden magnetic energy in the quiet Sun", *Nature*, **430**, 326–329. [DOI], [URL], [arXiv:astro-ph/0409004 [astro-ph]]

Trujillo Bueno, J., Štěpán, J. and Casini, R., 2011, "The Hanle Effect of the Hydrogen Lyα Line for Probing the Magnetism of the Solar Transition Region", *Astrophys. J. Lett.*, **738**, L11 (5 pages). [DOI], [URL], [arXiv:1107.4787 [astro-ph.SR]]

Trujillo Bueno, J., Landi Degl'Innocenti, E. and Belluzzi, L., 2017, "The Physics and Diagnostic Potential of Ultraviolet Spectropolarimetry", *Space Sci. Rev.*, **210**, 183–226. [DOI], [URL]

Uitenbroek, H., 2001, "Multilevel Radiative Transfer with Partial Frequency Redistribution", *Astrophys. J.*, **557**, 389–398. [DOI], [URL]

van Blerkom, D. and Hummer, D. G., 1968, "A Non-LTE Theory of Overlapping Lines Near the Series Limit", *Astrophys. J.*, **154**, 741–750. [DOI], [URL]

van Noort, M., Hubeny, I. and Lanz, T., 2002, "Multidimensional Non-LTE Radiative Transfer. I. A Universal Two-dimensional Short-Characteristics Scheme for Cartesian, Spherical, and Cylindrical Coordinate Systems", *Astrophys. J.*, **568**, 1066–1094. [DOI], [URL]

Vardavas, I. M. and Cannon, C. J., 1976, "Non-isotropic redistribution in chromospheric-type stellar atmospheres.", *Astron. Astrophys.*, **53**, 107–114. [URL]

Štěpán, J. and Trujillo Bueno, J., 2013, "PORTA: A three-dimensional multilevel radiative transfer code for modeling the intensity and polarization of spectral lines with massively parallel computers", *Astron. Astrophys.*, **557**, A143 (15 pages). [DOI], [URL], [arXiv:1307.4217 [astro-ph.SR]]

Waldmeier, M., 1957, *Die Sonnenkorona I, II*, Birkhaüser, Basel, Switzerland, first edn.

Wiegelmann, T., Thalmann, J. K. and Solanki, S. K., 2014, "The magnetic field in the solar atmosphere", *Astron. Astrophys. Rev.*, **22**, 78 (106 pages). [DOI], [URL], [arXiv:1410.4214 [astro-ph.SR]]

Wilson, S. J. and Sen, K. K., 1965, "Modified spherical harmonic method and spherical geometry. III. Transfer problem in spherically symmetric finite shell of planetary nebula", *Annales d'Astrophysique*, **28**, 855–859. [URL]

Wood, R. W., 1905, "Shadow Bands and the Polarizarion of the Corona", *Pub. U.S Naval Obs*, **4**, D112–D116

Wood, R. W., 1908, "On the emission of polarized light by fluorescent gases", *The London, Edinburgh, and Dublin Philosophical Magazine and Journal of Science*, **16**, 184–189. [DOI], [URL]

Wood, R. W., 1912, "Diffraction gratings with controlled groove form and abnormal distribution of intensity", *The London, Edinburgh, and Dublin Philosophical Magazine and Journal of Science*, **23**, 689–714. [DOI], [URL]

Wood, R. W. and Ellett, A., 1923a, "Destruction of the Polarisation of Resonance Radiation by weak Magnetic Fields", *Nature*, **111**, 255. [DOI], [URL]

Wood, R. W. and Ellett, A., 1923b, "On the Influence of Magnetic Fields on the Polarisation of Resonance Radiation", *Proceedings of the Royal Society of London Series A*, **103**, 396–403. [DOI], [URL]

Wood, R. W. and Ellett, A., 1924, "Polarized Resonance Radiation in Weak Magnetic Fields", *Physical Review*, **24**, 243–254. [DOI], [URL]

Yan, H. and Lazarian, A., 2006, "Polarization of Absorption Lines as a Diagnostics of Circumstellar, Interstellar, and Intergalactic Magnetic Fields: Fine-Structure Atoms", *Astrophys. J.*, **653**, 1292–1313. [DOI], [URL], [arXiv:astro-ph/0611281 [astro-ph]]

Zanstra, H., 1941a, "On the weakening of the polarisation effect by collision damping", *Mon. Not. Roy. Astron. Soc.*, **101**, 273–280. [DOI], [URL]

Zanstra, H., 1941b, "Theory of a polarisation effect in Fraunhofer lines due to oscillator scattering", *Mon. Not. Roy. Astron. Soc.*, **101**, 250–265. [DOI], [URL]

Zeeman, P., 1897, "On the Influence of Magnetism on the Nature of the Light Emitted by a Substance.", *Astrophys. J.*, **5**, 332–347. [DOI], [URL]

Zirin, H., 1976, "Fe XIII line in R Aquarii", *Nature*, **259**, 466–467. [DOI], [URL]